# Benefit of air intake optimization for new turbocharged gasoline engine

Vincent Raimbault



UNIVERSITE BRETAGNE SCIENCES LOIRE POUR L'INGENIEUR

CENTRALE NANTES

# THESE DE DOCTORAT DE

L'ÉCOLE CENTRALE DE NANTES
COMUE UNIVERSITE BRETAGNE LOIRE

ECOLE DOCTORALE N° 602
*Sciences pour l'Ingénieur*
Spécialité : « *Energétique, Thermique, Combustion* »

Par
## « Vincent RAIMBAULT »

# « Benefit of air intake optimization for new turbocharged gasoline engine »

**Thèse présentée pour une soutenance à « Nantes », le « 11 septembre 2019 »**
**Unité de recherche : Laboratoire de recherche en Hydrodynamique, Énergétique et Environnement Atmosphérique**

**Rapporteurs avant soutenance** :

| | |
|---|---|
| Pascal Stouffs | Professeur des Universités, Université de Pau et des Pays de l'Adour |
| Antonio Sciaretta | Docteur HDR, IFP Energies Nouvelles |

**Composition du Jury :**

| | | |
|---|---|---|
| Présidente : | Céline Morin | Professeur des Universités, Université de Valenciennes et du Hainaut-Cambrésis |
| Examinateurs : | Pascal Stouffs | Professeur des Universités, Université de Pau et des Pays de l'Adour |
| | Antonio Sciarretta | Docteur HDR, IFP Energies Nouvelles |
| | Stéphane Guilain | Docteur, Renault |
| Dir. de thèse : | David Chalet | Professeur des Universités, Ecole Centrale de Nantes |
| Co-dir. de thèse : | Michael Bargende | Professeur des Universités, IKV Allemagne |

**Invité**

| | | |
|---|---|---|
| | Jérôme Migaud | Ingénieur, Mann+Hummel |

# *Acknowledgment*

*This PhD Thesis, entitled "Benefit of Air Intake optimization for new turbocharged gasoline engine", has been integrated in a joined International Teaching and Research Chair between Ecole Centrale de Nantes and MANN+HUMMEL. It has been handled with a collaboration with Forschungsinstitut für Kraftfahrwesen und Fahrzeugmotoren Stuttgart.*

*I would like to express my recognition to Pr.* ***David CHALET****, Full Professor in the LHEEA laboratory of Ecole Centrale de Nantes. I greatly appreciated the effort he puts to support me on the writing of this thesis. His guidance has been a key point to drive through all this process.*

*I would like also to express my gratitude to the MANN+HUMMEL management who gave me the chance to start this thesis. Firstly* ***Jérôme MIGAUD****, Director Innovation Transportation in MANN+HUMMEL Group, for all the effort he brought to set up the whole project from the beginning. I am grateful for his help not only with the technical aspect but with all difficulties I faced. I will not forget* ***Charles Vaillant****,* ***Cedric Dackam*** *and* ***Christopher Sturgess*** *who have been so supportive too.*

*My stay in Germany within the Forschungsinstitut für Kraftfahrwesen und Fahrzeugmotoren Stuttgart has been a real chance for this PhD Thesis. It would not have been possible without Pr.* ***Michael Bargende****, Full professor and managing director of the Institute, and Dr.* ***Michael Grill****, Doctor and head of the department 0D/1D simulation.*

*I would also like to take this opportunity to thank* ***Torsten Günther*** *and* ***Lukas Urban*** *for the countless and very constructive discussions we had and for their friendship. This thesis would not have been possible without* ***Quentin Montaigne*** *and* ***Vincent Berthome*** *for all the tests they carried out and the challenging discussion and fun we had. I would like to tell my consideration to Dr.* ***Hanna Sara*** *who welcomed me in the office and* ***Antoine Bouedec*** *who has fixed everything on the engine.*

*And last, but not the least; I would like to thank* ***my family*** *and* ***my friends*** *who continuously followed me during this adventure, their kindness has been the best support ever. Thank you.*

*I will become old when I will stop learning*

*Hopefully I will die young*

# Table of Content

# Notations

Latin letters:

| | |
|---|---|
| $A$ | Progressive wave amplitude [Pa] |
| $A_{fl}$ | Flame front area [m$^2$] |
| $A_v$ | Vehicle front surface [m$^2$] |
| $A_w$ | Wall surface [m$^2$] |
| $B$ | Regressive wave amplitude [Pa] |
| $C$ | Progressive wave amplitude [Pa] |
| $c_0$ | Sound speed [m/s] |
| $C_1$ | Calibration constant |
| $C_2$ | Calibration constant |
| $C_k$ | Turbulence start coefficient |
| $c_m$ | Mean piston speed [m/s] |
| $C_\tau$ | Empirical constants for ignition delay modeling |
| $C_{\tau 1}$ | Empirical constants for ignition delay modeling |
| $C_{\tau 2}$ | Empirical constants for ignition delay modeling |
| $C_p, C_v$ | Specific heat capacity under constant pressure or volume [J/K/kg] |
| $C_w$ | Drag coefficient |
| $d$ | Bore [m] |
| $d_{IV}$ | Diameter inlet valves [m] |
| $D$ | Regressive wave amplitude [Pa] |
| $Displ$ | Engine displacement volume [m$^3$] |
| $E_{out}$ | Energy required on WLTC cycle [kWh] |
| f | Frequency [Hz] |
| $f_0$ | Friction coefficient |
| $f_1$ | Friction coefficient |
| $f_2$ | Friction coefficient |
| $\vec{F}$ | Force [N] |
| $F_{Engine}$ | Engine force request [N] |
| $F_{Road}$ | Road related force [N] |
| $F_{Friction}$ | Friction force [N] |
| $F_{Drag}$ | Aerodynamic drag [N] |
| $g$ | Standard acceleration [m/s²] |
| $H_u$ | Enthalpy of the unburned zone [J] |
| $h_{IV}$ | Maximum lift inlet valve [m] |
| $k$ | Wave number |
| $k_e$ | Kinetic energy [J] |
| $k_{e,start}$ | Starting kinetic energy [J] |
| $k_{e,q}$ | Specific kinetic energy produced by squish [J] |
| $l$ | Expansion chamber length [m] |

| | |
|---|---|
| $l_h$ | Helmholtz resonator neck length [m] |
| $l_{sc}$ | Length scale [m] |
| LD1 | Side branch length to Air Intake Manifold length [m] |
| LD2 | Charge Air Cooler to side branch duct [m] |
| LV | Side branch duct length [m] |
| $m$ | Vehicle mass [kg] |
| $m_E$ | Entrained mass [kg] |
| $m_f$ | Fuel mass [kg] |
| $m_t$ | Mixture mass moving from unburned to burned zone [kg] |
| $\dot{m}_1$ | Measured mass flow rate [kg] |
| $\dot{m}_a$ | Air mass flow at intake [kg/s] |
| $\dot{m}_f$ | Fuel mass flow rate [kg/s] |
| $\dot{m}_c$ | Corrected air mass flow [kg/s] |
| M | Molar mass [kg/mole] |
| $M_{LET}$ | Low End Torque [Nm] |
| N | Engine speed [RPM] |
| $n_{LET}$ | Minimum engine speed where maximum torque is reach [RPM] |
| Ncylinder | Number of cylinder [-] |
| $n_{IV}$ | Number inlet valves [-] |
| $p$ | Acoustic pressure [Pa] |
| $P$ | Pressure [bar] |
| $p_O$ | Motored pressure [Pa] |
| $P_0$ | Pressure at the reference point [K] |
| $P_{out}$ | Output Power [kW] |
| $P1$ | Compressor outlet pressure [Pa] |
| $P2$ | Air Intake Manifold pressure [Pa] |
| $P3$ | Exhaust manifold pressure [Pa] |
| $P_{1_{ref}}$ | Pressure at the reference point [Pa] |
| $p_{cyl}$ | Cylinder pressure [bar] |
| $p_h$ | Acoustic pressure in the Helmholtz cavity [Pa] |
| $Phi$ | Fuel to air equivalence ratio |
| $P_{i,c}$ | Inlet compressor pressure [bar] |
| $P_{i,t}$ | Inlet turbine pressure [bar] |
| $P_{intake}\ Cyl1$ | Upstream intake valve pressure at cylinder 1 [bar] |
| $P_{intake}\ Cyl2$ | Upstream intake valve pressure at cylinder 2 [bar] |
| $P_{o,c}$ | Outlet compressor pressure [bar] |
| $P_{o,t}$ | Outlet turbine pressure [bar] |
| $P_{ref}$ | Reference pressure [bar] |
| $q$ | Heat transfer [J/s] |
| $q_1$ | Measured mass Flow rate [kg/s] |
| $q_c$ | Corrected mass Flow rate [kg/s] |
| $q_h$ | Mass flow in the Helmholtz resonator [kg/s] |
| $Q_B$ | Heat released [J/s] |
| $Q_{HV}$ | Heating value of the fuel [J/kg] |
| $Q_w$ | Wall heat transfer [J/s] |
| $r$ | Ideal specific gas constant [J/kg/K] |

| | |
|---|---|
| $r_c$ | Geometrical compression ratio |
| $R$ | Ideal gas constant [J/mole/K] |
| $S_1$ | Upstream duct section [m$^2$] |
| $S_2$ | Expansion section [m$^2$] |
| $S_3$ | Downstream duct section [m$^2$] |
| $S_h$ | Helmholtz neck surface [m$^2$] |
| $S_q$ | Quarter lambda tube cross section [m$^2$] |
| $t$ | Time [s] |
| $t_k$ | End of combustion time [s] |
| $T$ | Air intake temperature [K] |
| $T_0$ | Temperature at the reference point [K] |
| $T_1$ | Measured temperature [K] |
| $T_{1_{ref}}$ | Temperature at the reference point [K] |
| $T_b$ | Bulk temperature [K] |
| $T_{i,c}$ | Inlet compressor temperature [K] |
| $T_{is,o,c}$ | Isentropic outlet compressor temperature [K] |
| $T_{i,t}$ | Inlet turbine temperature [K] |
| $T_{is,o,t}$ | Isentropic outlet turbine temperature [K] |
| $T_{intake}\ Cyl1$ | Upstream intake valve temperature at cylinder 1 [K] |
| $T_{intake}\ Cyl2$ | Upstream intake valve temperature at cylinder 2 [K] |
| $T_{o,c}$ | Outlet compressor temperature [K] |
| $T_{o,t}$ | Outlet turbine temperature [K] |
| $T_{Out}$ | Output Torque [N.m] |
| $T_{ref}$ | Reference temperature [K] |
| $T_{ub}$ | Unburnt zone temperature [K] |
| $T_w$ | Wall temperature [K] |
| $u$ | Acoustic velocity [m/s] |
| $u_1$ | Acoustic velocity in domain 1[m/s] |
| $u_2$ | Acoustic velocity in domain 2 [m/s] |
| $u_L$ | Laminar flame speed [m/s] |
| $u_{L,0}$ | Laminar flame velocity in reference condition [m/s] |
| $u_E$ | Total flame front speed [m/s] |
| $u_h$ | Acoustic velocity in Helmholtz resonator [m/s] |
| $u_q$ | Acoustic velocity in the quarter lambda tube [m/s] |
| $u_{Turb}$ | Turbulent flame speed [m/s] |
| v | Vehicle speed [m/s] |
| $\dot{v}$ | Vehicle acceleration [m/s²] |
| v0 | Reference vehicle speed [m/s] |
| $V$ | Volume [m$^3$] |
| $V_{1_{ref}}$ | Instantaneous cylinder volume at reference point [m$^3$] |
| $V_{cyl}$ | Instantaneous cylinder volume [m$^3$] |
| $V_D$ | Cylinder displacement volume [m$^3$] |
| $V_h$ | Helmholtz resonator volume [m$^3$] |
| $V_p$ | Piston speed [m/s] |
| $Vol_{eff}$ | Volumetric efficiency |

| | |
|---|---|
| $W$ | Work [J] |
| $w_c$ | Compressor work [J] |
| $w_{is,c}$ | Isentropic Compressor work [J] |
| $w_{is,t}$ | Isentropic Turbine work [J] |
| $w_t$ | Turbine work [J] |
| $W_{th}$ | Theoretical work over the cycle [J] |
| $x_{r,st}$ | Residual gas fraction |
| Z | Acoustic impedance [Pa.s/m$^3$] |

Greek letters:

| | |
|---|---|
| $\alpha_w$ | Heat exchange coefficient |
| $\alpha$ | Laminar flame velocity parameter |
| $\beta$ | Laminar flame velocity parameter |
| $\gamma$ | Ratio of specifics heat $\frac{C_p}{C_v}$ $\psi$ |
| $\psi$ | Road slope rate |
| $\eta_{f,i}$ | Indicated fuel conversion efficiency [J/kg] |
| $\eta$ | Volumetric efficiency with pressure in Air Intake Manifold |
| $\eta_c$ | Isentropic compressor efficiency |
| $\eta_m$ | Mechanical efficiency |
| $\eta_r$ | Number of crank revolution for each power stroke per cylinder |
| $\eta_t$ | Isentropic turbine efficiency |
| $\rho_{uv}$ | Density of the unburned zone [kg/m$^3$] |
| $\rho_a$ | Air Density [kg/m$^3$] |
| ∅ | Crank angle [°CA] |
| Ø AIM | Air Intake Manifold diameter [m] |
| Ø Volume | Added Volume diameter [m] |
| Ø V | Side branch duct diameter [m] |
| $\lambda$ | Air-fuel equivalence ratio |
| $\rho$ | Air density [kg/m3] |
| $\tau$ | Turbine expansion ratio |
| $\tau_i$ | Ignition delay |
| $\varepsilon_{Diss}$ | Dissipation coefficient |
| $\varepsilon_q$ | Coefficient kinetic energy produced by squish |
| $\varphi$ | Compressor pressure ratio |
| $\chi_S$ | Isentropic compressibility coefficient [m$^3$/J] |
| $\xi$ | Laminar flame parameter |
| ω | Pulsation [rad/s] |

Acronyms:

| | |
|---|---|
| 1D | *One-dimensional* |
| 3D | *Three-dimensional* |

| | |
|---|---|
| *AFR* | *Air Fuel Ratio* |
| *AI* | *Auto-Ignition* |
| *AIM* | *Air Intake Manifold* |
| *AIS* | *Air Intake System* |
| *BDC* | *Bottom Dead Center* |
| *BEV* | *Battery Electric Vehicle* |
| *BMEP* | *Brake Mean Effective Pressure* |
| *BSFC* | *Brake Specific Fuel Consumption* |
| *CAC* | *Charge Air Cooler* |
| *CO* | *Carbon monoxide* |
| *$CO_2$* | *Carbone dioxide* |
| *COP* | *Conference of the Parties* |
| *DOE* | *Design Of Experiment* |
| *DRS* | *Double Resonance System* |
| *E.O* | *Engine Order* |
| *ECU* | *Electronic Control Unit* |
| *EGR* | *Exhaust Gas Recirculation* |
| *EIVC* | *Early Intake Valve Closing* |
| *EV* | *Electric Vehicle* |
| *EVC* | *Exhaust Valve Closing* |
| *FFT* | *Fast Fourier Transform* |
| *GHG* | *Green House Gases* |
| *HC* | *HydroCarbon* |
| *HEV* | *Hybrid Electric Vehicle* |
| *HVAC* | *Heating Ventilation and Air Conditioning* |
| *ICE* | *Internal Combustion Engine* |
| *IVC* | *Intake Valve Closing* |
| *IVO* | *Intake Valve Opening* |
| *Lambda* | *Air-fuel equivalence ratio* |
| *LIVC* | *Late Intake Valve Closing* |
| *M* | *Molar mass* |
| *MAPO* | *MAximum Pressure Oscillation* |
| *MBT* | *Maximum Brake Torque* |
| *MEP* | *Mean Effective Pressure* |
| *MFB50* | *50% of Mass Fraction Burnt* |
| *MLET* | |
| *NEDC* | *New European Driving Cycle* |
| *NOx* | *Nitrogen oxide* |
| *OEM* | *Original Equipment Manufacturer* |
| *PV* | *Pressure Volume* |
| *PM* | *Particulate Matter* |
| *PME* | *Pression Moyenne Effective* |
| *PMEP* | *Pumping Mean Effective Pressure* |
| *PMH* | *Point Mort Haut* |
| *RCM* | *Rapid Compression Machine* |
| *RDE* | *Real Drive Emission* |
| *RON* | *Research Octane Number* |
| *RPM* | *Revolutions Per Minute* |
| *SCR* | *Selective Catalystic Reduction* |
| *SI* | *Spark ignition* |
| *TDC* | *Top Dead Center* |
| *TDCF* | *Top Dead Center Firing* |
| *TWC* | *Three Way Catalyst* |
| *VCR* | *Variable Compression Ratio* |

| | |
|---|---|
| *VTG* | *Variable turbine geometry* |
| *VVT* | *Variable Valve Timing* |
| *WLTC* | *Worldwide harmonized Light vehicles Test Cycle* |
| *WOT* | *Wide Open Throttle* |
| *WG* | *Waste Gate* |

# 1 Introduction

Worldwide transportation is reaching a breakthrough point. Public concern for climate change, greenhouse gases (GHGs), and respiratory illness due to poor air quality is increasing. As such, the automotive industry faces an important paradigm shift.
The main contribution from light duty vehicles to global warming is related to Carbone dioxide ($CO_2$) emissions not only on the road, but also from the well to the tank and because vehicle construction. Today, air quality regulations requires cars to limit emissions of Nitrogen Oxide (NOx), Particulate Matter (PM), Carbon mOnoxide (CO), and HydroCarbon (HC). While there are different ways to approach this problem, Heywood *et al* [1] described this complex issue with the equation ( 1.1 ).

$$GHG = Person\ Miles \frac{Vehicle\ Miles}{Person\ Miles} \frac{Energy}{Vehicle\ Miles} \frac{GHG}{Energy} \quad (1.1)$$

This equation sequences not only the efficiency of the engine, the occupancy rate of the vehicle, but also the mileage per person and the greenhouse effect of the energy.
Following the Paris climate talks' Conference of the Parties 21 (COP21), the upcoming regulations in Europe Euro 7 (€7) regulations are pushing to reach 90g/km of $CO_2$ or paid taxes around 95€/(g($CO_2$)*sold vehicle) [2] [3] for each gram exceeding 93g/km. The European commission agreed to target a $CO_2$ reduction of 30% in 2030 and 50% by 2050 compared to 1990.
At the same time, new transportation solutions are slowly growing. Today, electric cars are directly emitting less $CO_2$. However, when considering the complete vehicle lifetime the situation is more complicated. First, new electric cars are using rare earth elements which are neither renewable nor $CO_2$ free [4] and mainly the Cobalt extraction and market could be a bottle neck for this technology [5]. Second, the recycling of electric batteries and motors poses a difficult challenge. Third, the main difficulty will be to produce the electricity in a "clean" way. Coal and Diesel-electric generation are not providing many benefits [6] and nuclear energy is still under debate. Lastly, the issue of how to transport and even store this electric energy remains unresolved. While some renewable sources may provide a large quantity, this energy cannot be properly controlled for today's demands. For instance, if considering only solar and wind energy, a windy and sunny day would be perfect for the production of energy, but households typically require more energy in the evenings, and not during the day when energy production is at its peak. In addition, energy production can decrease during critical times, such as dark winter months when houses require even more electrical power.
The replacement of the complete pure Internal Combustion Engine (ICE) fleet by electric cars would require more advanced development of infrastructure and bigger battery capacity. Conventional engine car drivers are used to filling their tank every 1000km or more with a filling time of few minutes. The current electric cars carry heavy batteries to reach 500km for the heaviest. The battery electric vehicle distance capacity is highly dependent on the driving conditions such as the temperature, which can alter the mean

velocity from mean speed 50km/h to 100km/h. Renault [7] demonstrated a driving range dropping down from 342km to 200km. The charging time was still higher even with the fastest charging system. The remaining questions about the battery lifetime and the replacement cost are still an area of concern for the end customer. This is the reason why today there are a lot of small electric cars for short trips in cities. Those cars don't require high range and thus the heavy battery can be lowered and the cost of their replacement reduced.

The power density is a key quantity for the aeronautic industry where the increase of the weight means an increase of power to take off and so a further weight increase to cope with it. The cars don't need to take off but the low energy density of the battery compared to the current fuel (depicted in the Figure 1), discussed by Amirante *et al* [8] and Shih *et al* [9], leads Electric Vehicle (EV) to bring more weight than a current ICE driven vehicle to travel lower distance. Furthermore the fuel tank mass decreases during driving whereas it stays high with the battery. High vehicle weight is correlated with higher energy consumption during acceleration and braking. Furthermore the non-exhaust emissions such as particulate matter from tires wear was linked to vehicle weight by Timmers *et al* [10].

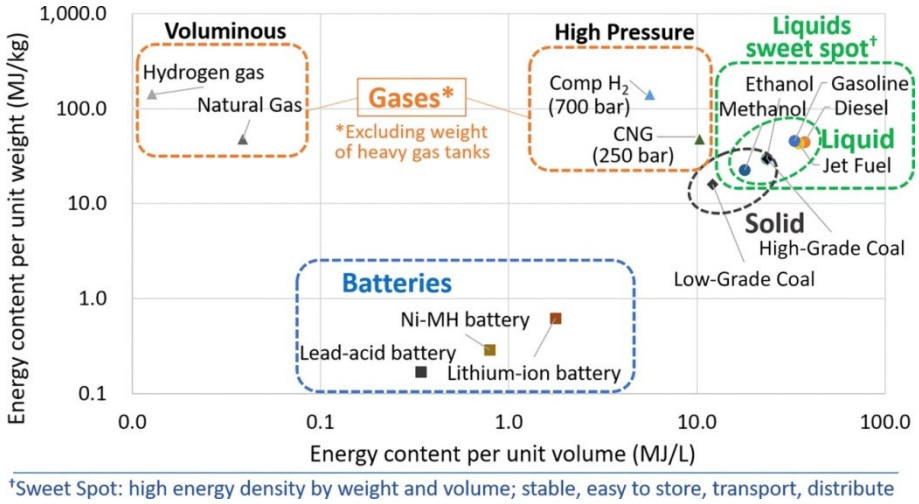


**Figure 1: Power density of battery compared to fuel and hydrogen** [9]

Some other technologies are under investigation with working prototypes. The fuel cells are like the Battery Electric Vehicle (BEV) with no local $CO_2$, NOx or HC production. Alstom [11] launched a program to replace Diesel powered trains with hydrogen powered versions. As hydrogen can be explosive, the challenge stands in the production, transport and storage of this gas. The higher driving range, higher energy storage and fast charging could make this technology competitive with ICE. Nevertheless this technology is not yet ready for large market share because of the missing infrastructure to fill the hydrogen tank. At the same time, because of the political decision to ban Diesel cars for some major cities in Europe, the market shifted from Diesel to gasoline engines. This decision has been motivated by the NOx and particles emissions of the old Diesel cars. The effect of this consumer shift is an increase of $CO_2$. Indeed the fuel consumption of the Diesel engine is still lower than gasoline especially in urban driving because of the pumping losses. This pushes the Original Equipment Manufacturers (OEM) to enhance the gasoline engine to fulfill the upcoming sold fleet $CO_2$ emissions limits. The project for the upcoming

regulations is to evaluate the average $CO_2$ emissions of the total sold cars. Then the reduction of the market share of the Diesel cars [12] puts more pressure on the gasoline to reduce $CO_2$ emissions. Part of the effort will be assumed by the different hybridization levels. The hybridization starts from stop and start (micro hybrids), which are nowadays commonly installed, to 48V hybrid powertrain able to run the vehicle till 50km/h for few tens of kilometers. Depending of the driving style and the driving environment, Schudeleit *et al* [13] have shown a potential of 6.8% $CO_2$/km saving with 48 V Hybrid Electric Vehicle (HEV). Further improvement could become from the vehicle connectivity [14].
The hybrid powered vehicles market share will increase as the pressure on the fuel savings gets higher. Nevertheless the cost will also have to be considered as mentioned by Harter *et al* [15] and shown in Figure 2.

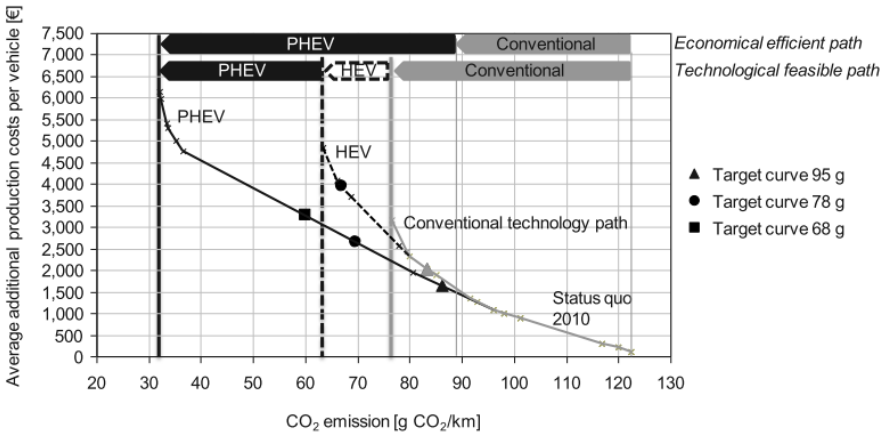


**Figure 2: Technology path for the defined small car OEM in 2025** [15]

The hybrid powertrain will provide $CO_2$ savings when the conditions in load and speed vary. When cruising on the highway, there will be much less energy to recover from the brake and the additional weight, as well as the extra packaging volume required by the electric part remains a drawback. The hybridization allows changing the ICE operating conditions. Indeed, the idle condition can be avoided and torque demands increase toward engine operating point with higher efficiency. The Figure 3 shows the conventional engine operates around 45N.m and lower and around 2000RPM with the efficiency between 10 to 30%. The full hybrid version runs at higher engine speed around 2500RPM and mainly at torque higher than 40N.m to 80N.m where the efficiency remains above 30% and 35%.

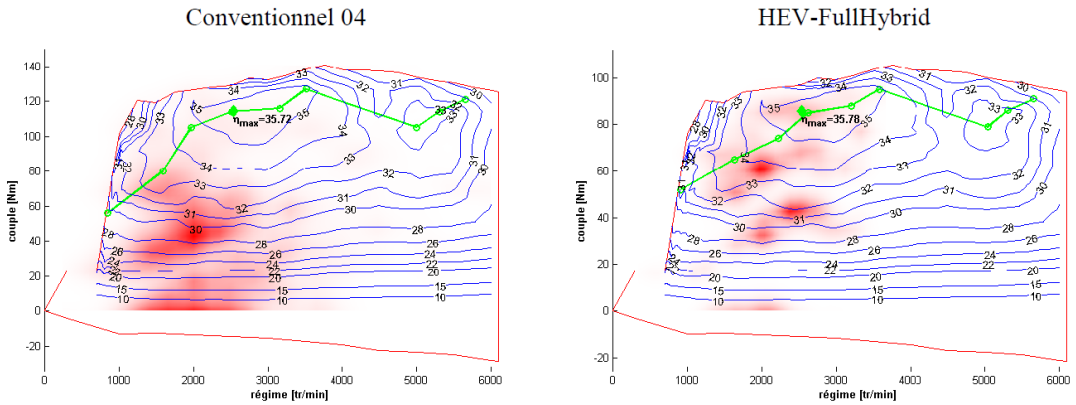


**Figure 3 : Comparison of the operating conditions of a conventional ICE (left) and Full Hybrid (right)** [16]

Many research activities are focusing on the forecast of future transportation. Indeed the current occupancy rate [17] is only about 1.5 in Europe. Over the last years, car sharing has grown, as well as the carpooling, this gives the chance to use the dedicated car to the specific usage. This opens the question of the driving conditions to estimate the fuel consumption and emissions. With the new regulations, the so called Real Drive Emissions (RDE) is to be launched with the responsibility for the Original Equipment Manufacturers (OEMs) to fulfill the emissions limitation not only on the standard driving cycle, but on wider range of driving conditions. The Figure 4 illustrates the important steps from New European Driving Cycle (NEDC) to Worldwide harmonized Light vehicles Test Cycle (WLTC) and to RDE as it enlarges the area in the engine map which needs to control the tailpipe emissions toward higher engine load and speed.

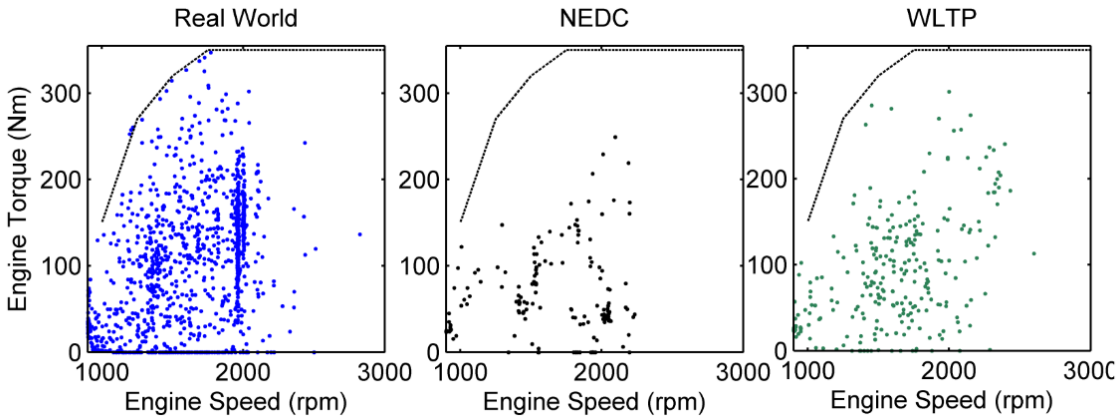


**Figure 4: Engine operating conditions for different engines driving cycles** [18]

A basic evaluation of the fuel consumption can be done on a cycle to better understand what are the vehicle and the engine contributions. The dynamic fundamental principal gives equality between the required force from the vehicle running on the cycle and the force provided by the engine as written in equation ( 1.2 ).

$$F_{Engine} = F_{Road} + F_{Drag} + m\,\dot{\mathrm{v}} \qquad (1.2)$$

In this equation the losses from the gear and transmission are neglected.
The aerodynamic drag force is commonly written as equation ( 1.3 ).

$$F_{Drag} = \frac{1}{2}\rho_a\, A_v\, C_w\, \mathrm{v}^2 \qquad (1.3)$$

$A_v$ denotes the frontal area of the considered car, $\rho$ indicates the air density, v represents the car velocity and $C_w$ consists of the drag coefficient.
The friction can be related to the vehicle velocity [19] [20] with equation ( 1.4 )

$$F_{Road} = m\, g \cos(\psi)\,(f_0 + f_1 \frac{\mathrm{v}}{\mathrm{v0}} + f_2 \left(\frac{\mathrm{v}}{\mathrm{v0}}\right)^2 \qquad (1.4)$$

The coefficients$f_0$, $f_1$ and $f_2$ are friction coefficients for road force tuning, m is the vehicle mass and g stands for gravity.
The equation ( 1.5 ) defines the engine output power.

$$P_{out} = F_{Engine}\,\mathrm{v} \qquad (1.5)$$

The WLTC gives the vehicle velocity, Horiba company [19] gives 0.13 as an example value for $f_0$.
The Brake Specific Fuel Consumption (BSFC) is defined at the ratio between the output power and the fuel rate as stated in the equation ( 1.6 ).

$$BSFC = \frac{\dot{m}_f}{P_{out}} \qquad (1.6)$$

With the hypothesis of a mean BSFC of 220 g/kW which is already challenging, it is possible to calculate the fuel consumption for different vehicle drag coefficients and mass as reported on the Table 1.

**Table 1: Consumption Assessment on WLTC for constant BSFC**

| | M=1225kg Av=2.25m² | M=500 kg Av=2.25m² | M=1225kg Av = 1m² | M= 500kg Av=1m² |
|---|---|---|---|---|
| **Energy [kWh]** | 3.7 | 2.4 | 3.0 | 1.7 |
| **BSFC [g/kW]** | 220 | 220 | 220.0 | 220 |
| **Distance [km]** | 23.3 | 23.3 | 23.3 | 23.3 |
| **fuel density [g/L]** | 750 | 750 | 750 | 750 |
| **consumption [l/100km]** | 4.7 | 3.0 | 3.8 | 2.1 |
| **$CO_2$ g/km** | 121.3 | 78.0 | 98.1 | 54.8 |

As depicted in Table 1, even with the low and hypothetical constant BSFC, it is quite difficult to reach the target of 90 g($CO_2$)/km. The ICE efficiency needs to be enhanced and also the car weight and drag to fulfill further $CO_2$ reduction. The weight reduction and the frontal area provide possibilities for $CO_2$ emissions drop. Pavlovich *et al* [21] have reported the $CO_2$ emissions share with about 20% in rolling resistance, about 28% in drag and the rest in inertia. Going in the same direction, the Figure 5 discloses the consumption vs the vehicle weight of sold cars from 2012 and 2013 and shows a high number of heavy vehicle with $CO_2$ emissions higher than 150 g/100km.

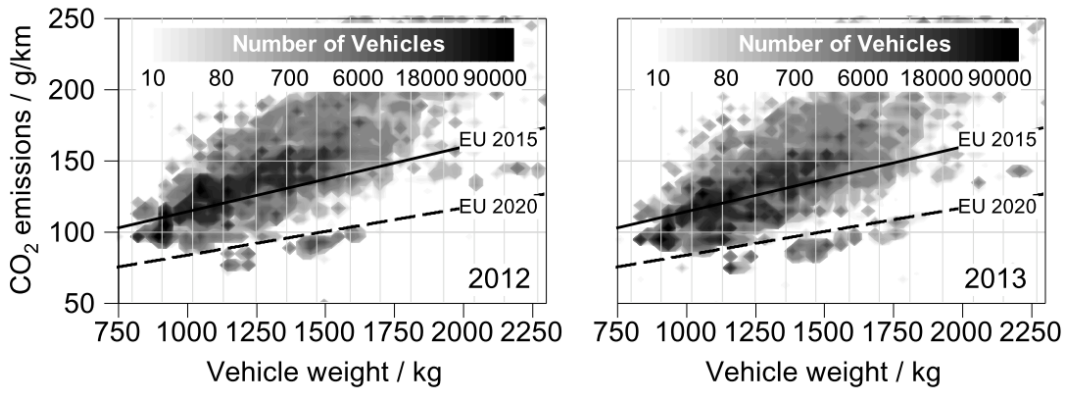


**Figure 5: Fleet mass vs $CO_2$ emissions in 2012 and 2013 [22]**

The $CO_2$ reduction is not only a challenge for the engine, but for all parts of the vehicle. Nevertheless it seems that the car will be driven for some time by the Internal Combustion Engine for still a few years. During this time its efficiency needs to be increased. The proposed study aims to find some ways to improve the efficiency or contribute to improve the efficiency of the turbocharged direct injection gasoline engine. Those improvements consist of stretching the area of the lowest BSFC and reducing the area where the BSFC is very high such as idle and very low load area.

After this first chapter which introduces the PhD Thesis, the second chapter presents a literature survey. It discusses the ways to make a gasoline engine efficient and the main associated challenges, in regard of the next regulations. Some technologies will be listed and discussed.
The third chapter presents the tools used during the PhD Thesis studies. First the acoustic formulation and the dedicated test bench are described. Then the 1D simulation code is presented with the models' set up and tuning methodology.
The fourth chapter investigates the increase of the torque at low engine speed. As new regulations aim to keep the catalyst efficient, the stoichiometric mixture has to be maintained at all engine operating conditions. This will restrain the torque at low engine speed. A concept aiming to improve the cylinder air filling will be presented and evaluated through simulation and then via engine tests.
The fifth chapter concentrates on the power side. The power of a gasoline engine is mainly driven by the combustion and the temperature at the exhaust. The development of a new device is discussed to reduce the intake temperature which leads to enabling an earlier combustion and reduction of the exhaust gas temperature. The device is simulated in a complete engine and then validated on a test bench.
Finally, the conclusion presents the main results for the different evaluated solutions. Perspectives for the upcoming work are then listed.

# 2 Literature survey

The internal combustion engine is a converter of potential calorific energy coming from the fuel to mechanical energy. The goal of the engine development is either to get more engine output mechanical power and/or to reduce the consumption for the same output power. The last years the Spark Ignition (SI) engines gained in popularity from the politics. Mainly because of the issue related to the NOx emissions of Diesel engines.
The Diesel engine has the advantage of lower $CO_2$ emissions. The challenge for SI engine is to increase its efficiency to be relevant not only to reduce NOx emissions but also the $CO_2$ emissions.
The first part of this chapter is dedicated to present the thermodynamic process which allow the conversion of the chemical potential to the mechanical torque or power of the SI engine. At first the ideal cycle first defined by Beau de Rochas and applied by Otto will be presented. The real cycle will be then discussed at its lower pressure side defining the gas exchange process. The high pressure part is then analyzed. This will demonstrate the benefit to the boosting system. The second part describes the main boosting technologies and their behaviors. The third part focuses on the tail pipe emissions, first the parameters influencing the raw emissions and later the after treatment system. The conclusion will define the strategy to be adopted by the future SI engines. This strategy is a challenge for different processes such as the combustion which can present some abnormal ignition due to the in-cylinder conditions. The fourth section will describe the knocking and some strategies to control it.

## 2.1 Beau de Rochas / Otto Cycle

The development of the 4 strokes engine has been developed more than 150 years ago. Discussions are still ongoing the real father of the SI engine but it seems that Alphonse Beau de Rochas has been the first one to patent the principle of the SI 4 stroke engine in 1862. But the same year Nikolaus Otto produced its first engine and wrote a patent the next year. Nevertheless these two allowed this breakthrough technology emergence.
The Beau de Rochas / Otto cycle is the focus of this section.

### 2.1.1 Ideal Beau de Rochas / Otto cycle

The ideal Beau de Rochas / Otto cycle, described in Figure 6, starts at the Top Dead Center (TDC) of the piston at the point A. From this point the intake valve is opened, the cylinder volume increases until the Bottom Dead Center (BDC) when the valve closed at the point B. The now closed cylinder reduce in volume because of the piston rising to the TDC and the pressure increases until the point C. The combustion occurs without volume change between C and D. Then the expansion stroke is described by the portion D to E. At the E point the exhaust valve opens so that the in-cylinder pressure drop to ambient at the TDC, point B, and stay constant until reaching the BDC at the point A. The cycle is then completed and can start again.

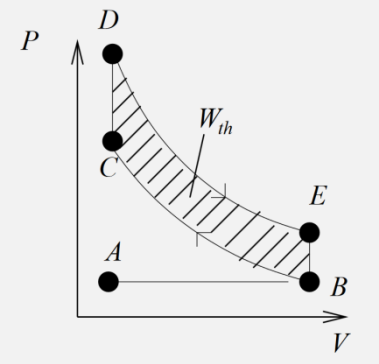


**Figure 6: Ideal Beau de Rochas / Otto cycle** [23]

The output work is defined as the hatched surface. Beau de Rochas explained the needs for largest expansion as possible and so reduce the pressure at the point E, leading to reduce the heat losses in the exhaust and thus the greatest output work.
Heywood [24] and Costa *et al* [25] have presented the direct relationship between the compression ratio and the fuel conversion efficiency. The geometrical compression ratio $(r_c)$ is defined as the ratio between the volume of the cylinder at the TDC and the volume at the BDC. For ideal gas the indicated fuel conversion efficiency $(\eta_{f,i})$ is written as the equation ( 2.1 )

$$\eta_{f,i} = \frac{W_{th}}{m_f Q_{HV}} = 1 - \frac{1}{r_c^{\gamma-1}} \qquad (2.1)$$

In this respect, the new engine are tending to increase this compression ratio. For part load operating conditions, the increase of compression ratio directly improves the BSFC [25].

The ideal Beau de Rochas / Otto cycle uses simplification to make it easy to calculate. The actual SI engine process presents some differences which are explained on the following sequences. The first on the low pressure side of the cycle (A↔B) and the others on the high pressure side (B-C-D-E).

### 2.1.2 Real Low Pressure Beau de Rochas / Otto cycle

The lower pressure parts of the Pressure / Volume (PV) diagrams stands for the pumping work. This pumping work can be evaluated with a 1D simulation, for instance on Figure 7, by calculating the area between the exhaust stroke and intake stroke mean pressure.

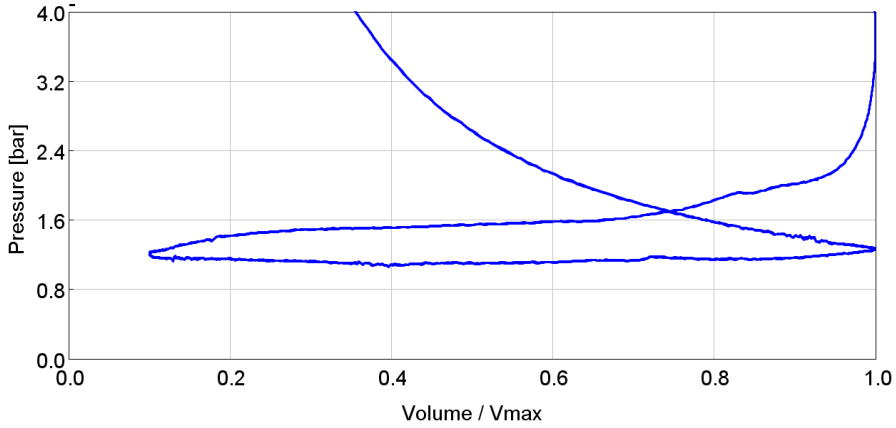


**Figure 7: Low pressure PV Diagram – Pumping losses example from GT Power simulation**

This pumping work corresponds to the mechanical work provided by the piston to ensure the cylinder air filling and cylinder gases extraction after the combustion. The pressure drop upstream the intake valve leads to increase the pumping work. In exhaust side the increase of pressure yields also to increase the required work to push the gases to the exhaust line. The reduction of the pressure losses at the intake and exhaust reduces the pumping work and increase the overall performance.
This pumping work is particularly sensitive for gasoline engine working in stoichiometric mixture. The stoichiometric mixture corresponds to theoretical air to fuel ratio for a complete combustion. The Air Fuel Ratio (AFR) can be calculated through the mass flow in equation ( 2.2 ). Depending the actual gasoline properties this value is about 14.7 meaning that air mass in the cylinder is supposed to be 14.7 times higher than gasoline.

$$AFR = \frac{\dot{m}_a}{\dot{m}_f} \qquad (2.2)$$

The lambda, equation ( 2.3 ), gives the air fuel ratio with stoichiometry as reference and thus $\lambda = 1$ describes the stoichiometric mixture with $AFR_{stoïc} = 14.7$.

$$\lambda = \frac{AFR_{actual}}{AFR_{stoïc}} \qquad (2.3)$$

Whereas the Diesel engine working in excess of air, the gasoline engine mainly controls the air quantity provided to the cylinder to ensure that all fuel will be burnt during the combustion process. For the low torque demand, the air quantity is controlled thanks to a

throttle body in the intake system. The throttle body controls the quantity of air reaching the cylinder. Depending on the air quantity the fuel quantity is injected in the cylinder to reach the driver torque demanded. If the torque request is not reached the throttle body opens giving more air to the cylinder and so more fuel is injected. The Figure 8 describes the effect of this throttling on the pumping work through a 1D simulation. The Brake Mean Effective Pressure (BMEP) assesses the output performance of the engine independently from its displacement volume as defined in the equation ( 2.4 ).

$$BMEP = \eta_r \frac{W}{Displ} = \frac{4\pi\, T_{Out}}{Displ} \qquad (2.4)$$

For three different BMEP demands the pressure is recorded over the cylinder volume to maximum cylinder volume ratio. The Volume/Vmax ratio equals to 1 denotes the BDC, the TDC is reached when this ratio is the invert of $r_c$.

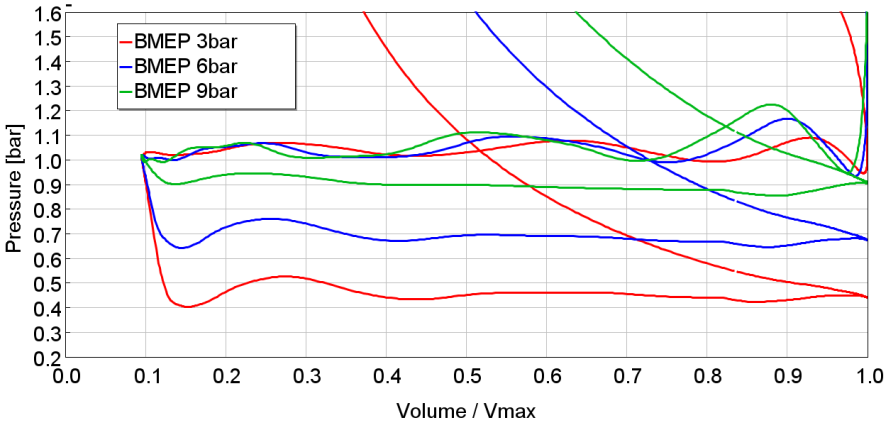


**Figure 8: Low pressure PV Diagram – Pumping losses example from GT Power simulation**

For low BMEP demand, the fuel to be burnt stays low; as a consequence the air quantity required in the cylinder is low. The engine can be represented as a volumetric pump and the throttle body controlled the vacuum to reduce the air density. The pumping work increases because in the same time the exhaust pressure remain above ambient. Part of this issue is addressed by the stop and start system which limits the idle conditions of the engine where the torque request is almost null and the throttle body is almost closed. The downsizing goes also to that direction. Indeed giving the rough assumption that the fuel quantity injected in the engine is linearly related to the torque output, a smaller engine requires to open more the throttle body for the same output torque as soon as the maximum torque is not reached. So that the pumping works is lower with the smaller engine for the same low torque level. The BSFC is then better for this operating condition with the smaller engine than with the bigger one.
The pumping work can be evaluated through the pumping mean effective pressure (PMEP) defined as the difference between mean exhaust pressure during exhaust stroke and mean intake pressure during intake stroke.

**Table 2: Pumping work for different load**

| BMEP [bar] | 3 | 6 | 9 |
|---|---|---|---|
| Mean pressure in the intake manifold [bar] | 0.46 | 0.71 | 0.93 |
| PMEP [bar] | 0.57 | 0.35 | 0.16 |
| BSFC [g/kWh] | 330 | 264 | 241 |

The Table 2 sums up the results coming from the Figure 8. Low BMEP induces low intake manifold pressure. This vacuum increases the pumping losses and thus increase the BSFC. The Figure 9 represents the engine operating point in a torque vs engine speed map. The presented results are obtained for the NEDC and WLTC class3. The bubbles size represents the operating duration over the cycle. The Full Load and Motoring curves are represented in dot line. The driving cycles are mainly using the left bottom side of the engine map. This area is mainly low load and low engine speed where the pumping work is sensitive.

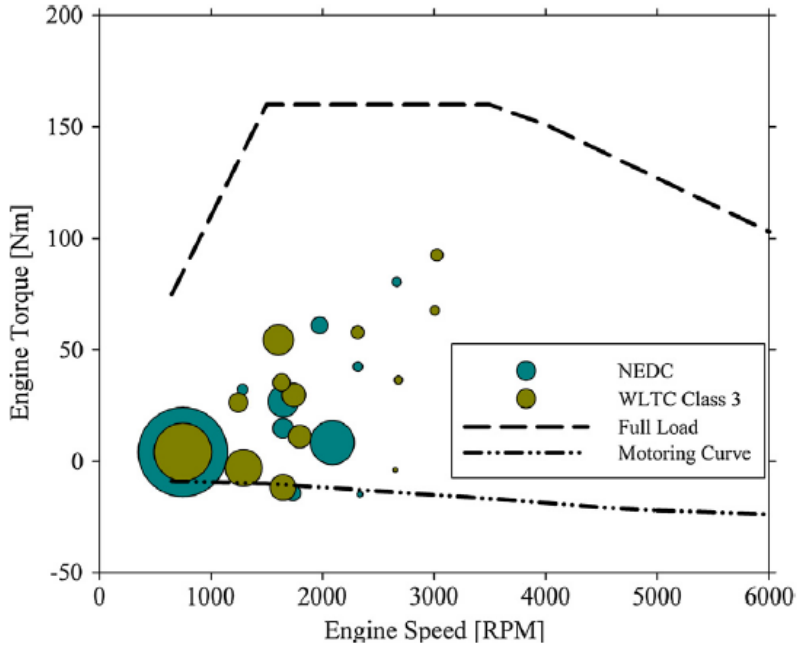


**Figure 9: Operating point for NEDC and WLTC on 1,2L gasoline engine** [26]

A smaller displacement volume engine is not able to provide as much power and torque as the bigger engine in full load conditions. This could lead to damage the drivability of the car and the fun to drive. This is the reason why there has been a massive usage of the boosting systems. The aim of the boosting system is to maintain a low BSFC on the running conditions involved in the standard driving cycles while enabling the engine to perform high power and torque when the driver wants it. The torque is provided by the high pressure part of the Beau de Rochas / Otto cycle.

### 2.1.3 Full load operation

In the Beau de Rochas / Otto cycle the work is provided by the high pressure side of the cycle. The area between the compression stroke and the expansion gives the actual work. With a boosting system the compression starts with higher pressure and ends up with higher pressure and temperature. The increased in air mass trap in the cylinder allows more burning fuel. The equation ( 2.5 ) demonstrates the increase of heat release with higher fuel mass burnt.

$$\frac{dm_t}{dt} = \frac{dQ_B}{d\emptyset} \cdot \frac{1}{H_u} \frac{d\emptyset}{dt} \qquad (2.5)$$

The heat release increase is beneficial for the work because it gives the chance to increase the pressure in the cylinder as described by the equation ( 2.6 ).

$$dQ_B = \frac{\gamma}{\gamma - 1}\, p\, dV_{cyl} + \frac{1}{\gamma - 1}\, VdP \qquad (2.6)$$

In the Figure 6, this increases the distance CD and increases the high pressure Beau de Rochas cycle.

It can also be mentioned that the downsizing tends to reduce the cylinders volumes and thus decrease the cylinders wall surface. Indeed the cylinder wall is partly responsible of heat losses to the coolant or to the oil. The compression and expansion in the cylinder are not adiabatic represented as the segment BC and DE in Figure 6. The insulation has been early investigated by Bryzik *et al* [27] on a Diesel engine. The investigation has consisted of a ceramic coating of piston cylinder head, valve and piston with high insulation properties. The heat losses to the cooling fluid have been drastically reduced from 30% to 17%. Fukui *et al* [28] have explained the consequence of heat insulation on the cylinder wall temperature which increases. This leads to decrease the charging efficiency as the air density during the intake stroke decrease. Another proposal is to provide a thin insulation layer with a low heat capacity so that the one side of the layer follow the in-cylinder gas temperature while keeping the heat exchange low. The Figure 10 describes this layer which insulate the cylinder wall to the cylinder volume. With hypothetical constant heat exchange with the coolant ("Water"), the insulation avoids the warm up of the air during intake stroke and during combustion, the insulation reduces the cooling effect which increases the inner wall temperature.

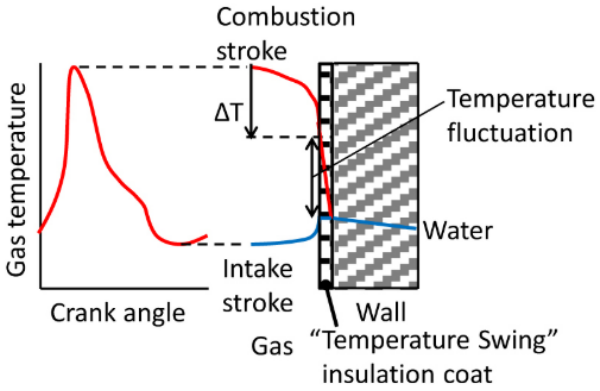


**Figure 10: Temperature swing Heat Insulation** [29]

This results in higher indicated work and higher exhaust energy which can be a risk on engine under severe conditions. Hölz *et al* [30] have shown the potential of an improved coolant fluid flow controlled. The wall heat transfer can be described as ( 2.7 ).

$$\frac{Q_w}{dt} = \alpha_w \, A_W \, (T_w - T) \qquad (2.7)$$

And Woschni [31] gives the heat transfer coefficient ( 2.8 )

$$\alpha_w = \; 110 \, d^{-0.2} \, p_{cyl}^{0.8} \, T_b^{-0.53} (C_1 Vp + C_2 \frac{V_{Cyl} T_{1_{ref}}}{P_{1_{ref}} V_{1_{ref}}} (p_{cyl} - p_0))^{0.8} \qquad (2.8)$$

Le Guen *et al* [32] reviewed different other models such as Bargende or Hohenberg showing how the k-Ɛ turbulence model can affect the results. The heat losses need to be considered to evaluate properly the power and the torque of the engine. The heat exchange can affect the air density and has to be considered during the gas exchange process too. This latter effect is considered through the volumetric efficiency $Vol_{eff}$ defined in the equation ( 2.9 ). This criterion is defined as the actual air mass trapped in the cylinder compared to the air mass which would be trapped for a steady intake atmospheric pressure.

$$Vol_{eff} = \frac{\dot{m}_a}{\rho \, V_D \frac{N}{2}} \qquad (2.9)$$

$\rho$ is defined at atmospheric pressure.
For turbocharged engine this value can be higher than 1 as the turbocharger provides a boost pressure higher than ambient. In order to reject the effect of the turbocharger in the analysis and compare the intake system as for naturally aspirated engines the volumetric efficiency with pressure and temperature reference in the air intake manifold, equation ( 2.10 ), can be used.

$$\eta = \; \frac{\dot{m}_a \, T \cdot r}{V_D \cdot \frac{N}{2} \cdot P} \qquad (2.10)$$

## 2.2 Boosting systems

The last generation of the SI engines is mainly using boosting system as it gives the chance to increase the power density. The boosting and more specifically the turbocharger gives the chance to increase strongly the intake pressure and so increase the density of the air trapped in the cylinder. The turbocharger allows using part of the energy which could be wasted in the exhaust gases otherwise. The intake pressure increase allows to burn more fuel. Thus for a defined engine displacement volume the turbocharged engine provide more output power.

### 2.2.1 Turbocharger

The turbocharger is built of two main elements in one side a turbine is placed in the exhaust ducts and uses the exhaust enthalpy. The recovered energy is converted in mechanical energy. This last one is transmitted to the compressor side through a shaft. The compressor will increase the pressure in the intake side.
The exhaust gas, going through the turbine, expands until it reaches the atmospheric pressure. Salameh [33] describes the power provided by the turbine in adiabatic condition as written in equation ( 2.11 ).

$$w_t = \dot{m}_a \, C_p \, (T_{i,t} - T_{o,t}) \qquad (2.11)$$

The equation ( 2.12 ) defines isentropic efficiency.

$$\eta_t = \frac{w_t}{w_{is,t}} \approx \frac{T_{i,t} - T_{o,t}}{T_{i,t} - T_{is,o,t}} \qquad (2.12)$$

The equations ( 2.13 ) and ( 2.14 ) defines the power and the isentropic efficiency at the compressor side.

$$w_c = \dot{m}_a \, C_p \, (T_{o,c} - T_{i,c}) \qquad (2.13)$$

$$\eta_c = \frac{w_{is,c}}{w_c} \approx \frac{T_{is,o,c} - T_{i,c}}{T_{o,c} - T_{i,c}} \qquad (2.14)$$

$$\tau = \frac{P_{i,t}}{P_{o,t}} = \left(\frac{T_{is,o,t}}{T_{i,t}}\right)^{\frac{\overline{\gamma}}{1-\overline{\gamma}}} \qquad (2.15)$$

$$\varphi = \frac{P_{o,c}}{P_{i,c}} = \left(\frac{T_{is,o,c}}{T_{i,c}}\right)^{\frac{\overline{\gamma}}{\overline{\gamma}-1}} \qquad (2.16)$$

The efficiency of the power transmission from turbine to compressor is defined in equation ( 2.17 ).

$$\eta_m = \frac{w_c}{w_t} \qquad (2.17)$$

The equations ( 2.15 ) and ( 2.16 ) define $\tau$ the expansion ratio at the turbine and $\varphi$ the compression ratio from the compressor in function of the pressure and temperature at their inlet and outlet. Because of ideal gas and adiabatic transformation assumption, the equation ( 2.18 ) relates the compression ratio at the compressor with the temperature at the compressor and turbine inlet and the expansion ratio at the turbine.

$$\varphi = \left(1 + \frac{T_{i,t}}{T_{i,c}} \eta_c \, \eta_m \, \eta_t \left(1 - \tau^{\frac{1-\overline{\gamma}}{\overline{\gamma}}}\right)\right)^{\frac{\overline{\gamma}}{\overline{\gamma}-1}} \qquad (2.18)$$

The adiabatic assumption prevents from considering the heat exchanges which are actually happening within the turbocharger between the turbine and compressor and with the ambient and oil. Furthermore a finer analysis should take into account the variation of $\gamma$ with the temperature and with the gas contents. It is higher for pure air than fuel.

Nevertheless the equation ( 2.18 ) shows the relationship between the intake compression ratio and the expansion ratio and the inlet temperature at the turbine. Then, the performance is influenced by the compressor, turbine and mechanical efficiencies. The increase of boost pressure requires enough exhaust temperature and pressure. In another hand the temperature ratio at the turbine denotes the heat recovering from the exhaust gases.

The Figure 11 shows a LHEEA measurement of the efficiency and mass flow rate sensitivity to the expansion ratio at the turbine. The equation ( 2.19 ) defines how the air mass flow is corrected to reject the measurement conditions effects.

$$\dot{m}_c = \dot{m}_1 \frac{\sqrt{T_1 / T_{ref}}}{P / P_{ref}} \qquad (2.19)$$

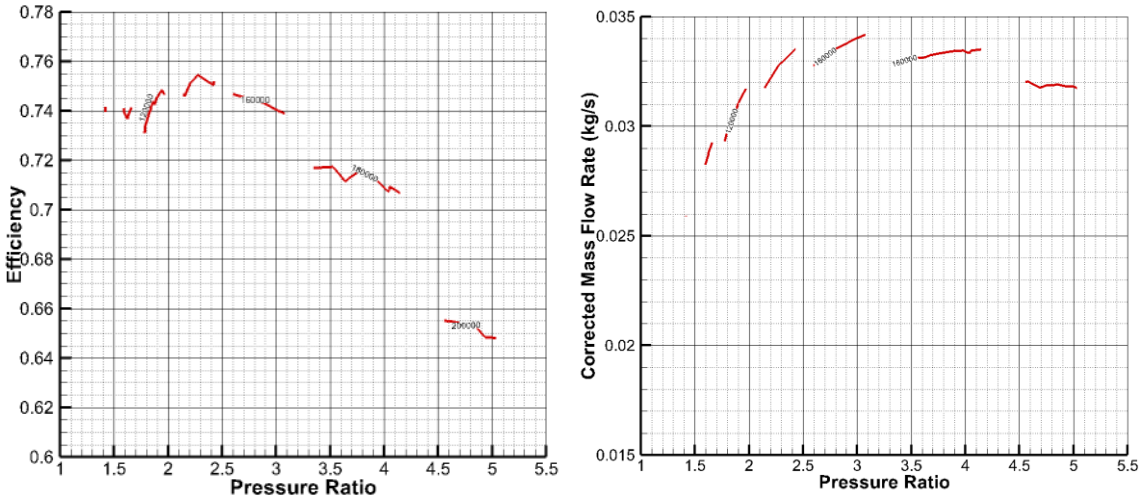


(a) (b)

**Figure 11: Example turbine maps with efficiency (a) and corrected mass flow (b)**

The turbine is layout to ensure that the maximum efficiency is obtained at the most sensitive operating conditions, such as the maximum torque where the air flow is low and the expansion ratio high. On another hand, the turbine has to be big enough to maintain low back pressure at maximum power. This layout needs to be adapted to the compressor behavior too.

The measurements from LHEEA, presented on Figure 12, characterize the compressor side. The middle part represents the best efficiency area. The surge line limits the left end. The surging appears for high pressure ratio and low air flow which limits the boost pressure at low engine speed. Deep surging leads mechanical damaged on the compressor wheel. A light surge is characterize by reverse air flow and low frequency pressure oscillations. The highest pressure ratio is limited by the maximum rotational speed which is usually around 250 000RPM. This limit depends on the compressor wheel diameter. The linear velocity at the blade should too high to avoid very high centrifugal force. Thus small compressor can reach higher speed. The right limitation corresponds to choke. This limitation is reached when the flow at the inlet impeller or at the diffuser vanes blocks the compression [34].

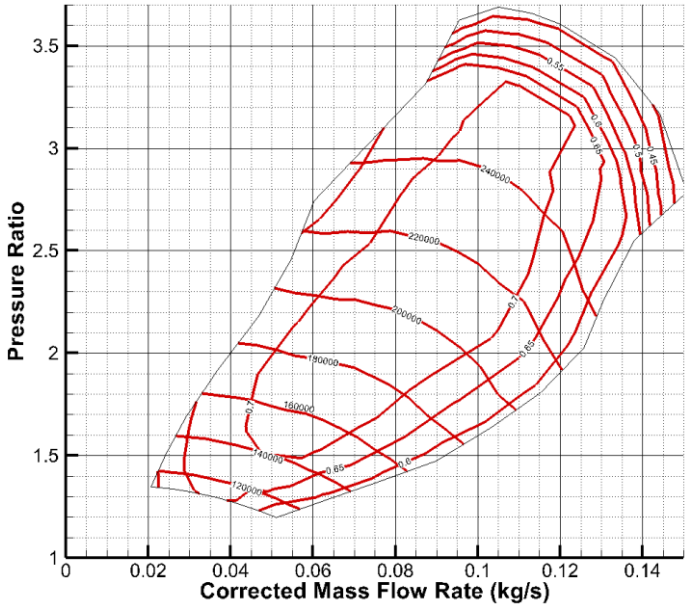


**Figure 12: Compressor map example**

The turbocharger requires an adaptation to engine and the expectations. For instance a small displacement engine requires less air mass flow so a smaller compressor would be preferred to avoid the surging and thus improve the low end torque. Some engines are equipped with 2 turbochargers so that the boost pressure can be enhanced at lower engine speed with a smaller compressor and the choke can be shift toward higher air flow with a bigger compressor. Watson *et al* [35] have shown how the boost pressure allows a higher output torque. Nevertheless the higher boost pressure increases the risk of abnormal combustion. Furthermore the charge air cooling is required to lower the effect on the knock and to increase the air density.

At high engine speed the late combustion leads to high exhaust temperature. The material temperature limitations can be reached and yield to mechanical risk for the exhaust line components. The temperature of the turbine is usually limited to 1200K otherwise the oxidation (showed on Figure 13) can occur.

**Figure 13: Turbine damaged due to temperature excess** [36]

The turbocharger needs to be controlled in order to obtain the desired boost pressure or to be deactivated. As already mentioned, the engine is mainly driving part load where the boosting is not required. The turbocharger can then be deactivated or controlled through a bypass channel on the turbine where the flow is controlled by a valve so called the waste gate (WG). Another technology well known for Diesel engine consists of a Variable Turbine Geometry (VTG). Christmann *et al* [37] have explained the different technologies developed over the years and the benefit on the turbine efficiency presented on Figure 14. Morand *et al* [36] complemented the benefit of a lower back pressure at the exhaust which reduces the pumping work and decreases the residual gases.

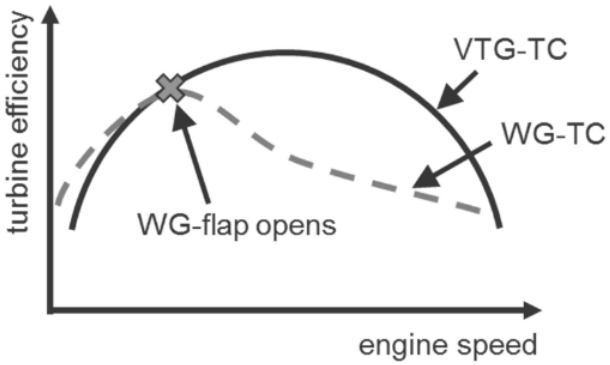


**Figure 14: Variable turbine geometry compared to waste gate** [37]

One main well known drawback of the turbocharger is the delay between the torque demand and the engine respond. The turbocharger requires time to achieve the speed able to provide the boost pressure: this is known as turbocharger lag. This is mainly driven by the turbocharger mechanical inertia and the thermal inertia especially at the turbine. Steady state conditions need to be reached to provide the maximum power at the compressor. This has been highlighted by Lefevre *et al* [38] who have proposed an experimental methodology to assess the transient performance of a turbocharged engine with 5 consecutive tips in (full load request) at a given engine speed. The performance is specified by the time to reach 90% of the maximum BMEP.
Over the years different solutions have been considered to overcome this matter as well as the surging issue happening for low air mass flow and high compression ratio. The next session deal with the supercharger and e-booster.

### 2.2.2 Superchargers and e-boosters

The increase output torque and the time to torque has been addressed through different ways. The naturally aspirated engine provides fast response but need large displacement for high output which is detrimental to the BSFC. The turbocharger requires time to reach the high output level. The roots supercharger presented on Figure 15 has been used for many years to increase the output torque from very low engine speed to maximum power operating point.

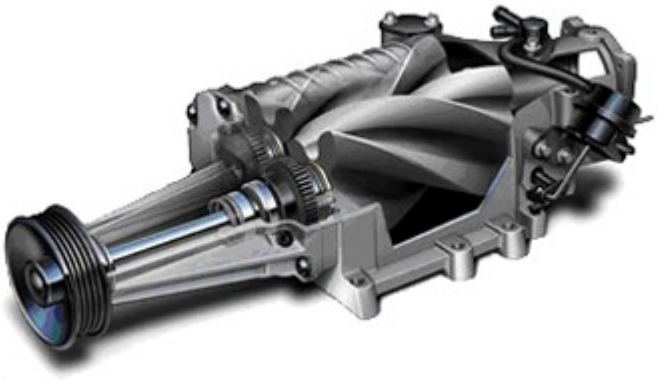

**Figure 15: Roots supercharger design** [39]

The supercharger is driven by the crankshaft giving the chance to provide a fast and relatively high boosting from the very low engine speed. Different OEM used this device alone on the entire engine speed range or only for low engine speed to compensate the lack of boosting coming from the turbocharger in this area. The supercharger alone reduce the chance to recover part of the exhaust gases energy and is not going in the direction of the BSFC improvement. The most recent development went toward a supercharger coupled with a turbocharger with aim to improve the low end torque and the transient response of the engine. The benefit has been demonstrated and applied for different mass production engines (i.e. 2.0L gasoline engine Volvo or 1.4L gasoline engine VW). It has been mainly used upstream the turbocharger's compressor. This position allows both the turbocharger faster spin on acceleration and a boost pressure increase and thus a direct torque increase. However the energy used by the supercharger could be provided directly to the wheel. Even if the torque reach higher level, the consumption can be affected. Furthermore Lau *et al* [40] have mentioned the high level noise created by the supercharger which is wide frequency range with specific peak at the supercharger order. It requires specific encapsulation devices as well as acoustic dampener in the air path.
The most recent developments for passenger cars move toward centrifugal compressor and electric motor. The Figure 16 shows the centrifugal compressor which is quite similar to the compressor used on turbochargers but driven by an electric motor which prevents from using mechanical energy which could be used by the wheels when the electricity has been previously stored in a battery. The compressor map is then adapted to obtain high boost pressure at low engine speed.

**Figure 16: E-Booster concept** [42]

Aymanns *et al* [41] have tested e-booster with two voltage supplies, the current 12V and the ongoing 48V. The Figure 17 demonstrates the performance benefit in transient and steady state conditions with further benefit of the 48V with lower current demand. The steady state BMEP can be attained much faster with e-booster with almost 2 seconds gain with the 48V e-booster over the 2.5 second ramp up with the turbocharger alone.

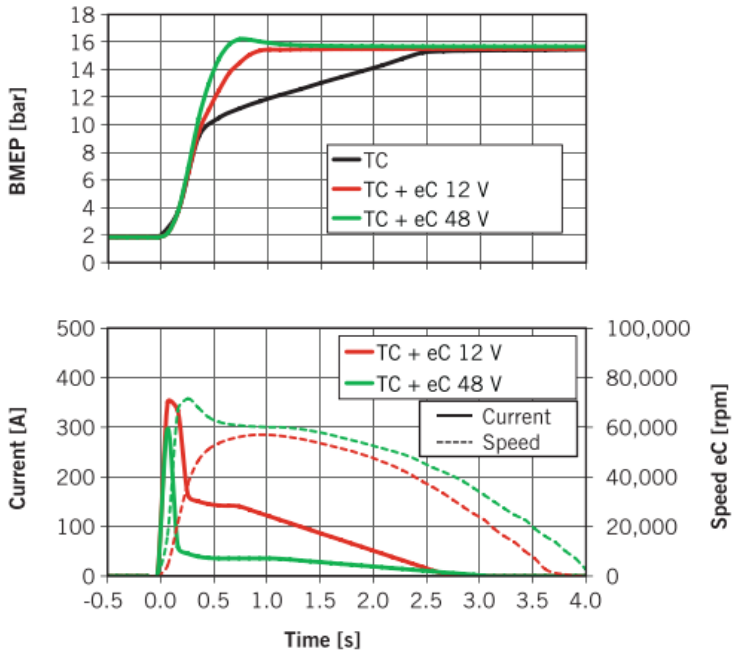


**Figure 17: Benefit of the e-booster on transient condition** [41]

The Figure 18 gives a translation of the torque benefit in vehicle performance through a 80 to 120km/h acceleration evaluation [41]. Even if some assumption on gear ratio could provide a bias in the assessment, the results give the potential on covered distance benefit up to 5.8%. But this results is obviously largely depending on the gear ratio and can significantly reduce with lower gear ratio or the automatic gear box.

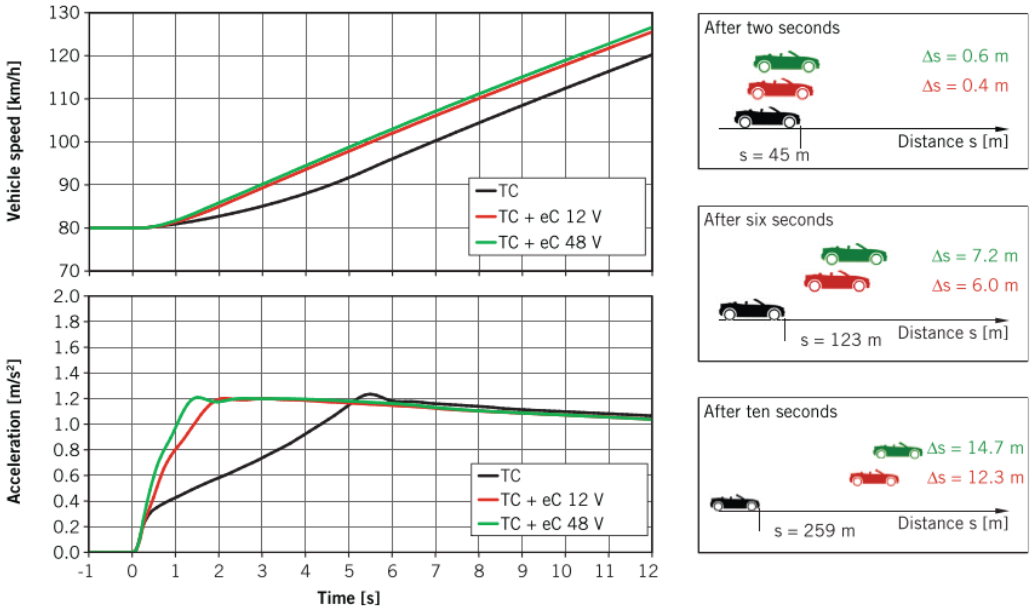


**Figure 18: E-boosting effect on the vehicle acceleration** [41]

Basset *et al* [42] have discussed further the new matching possibility of the current turbocharger with e-booster. Indeed the turbocharger is then mainly dedicated to power benefit at higher engine speed. It can be bigger and provides the best efficiency at higher air flow while the e-booster can supply the boost pressure at lower air flow for higher low end torque. Droulez [43] proposed to complement the e-booster by a cooling system using the Heating Ventilation and Air Conditionning (HVAC) evaporator to increase the air density.

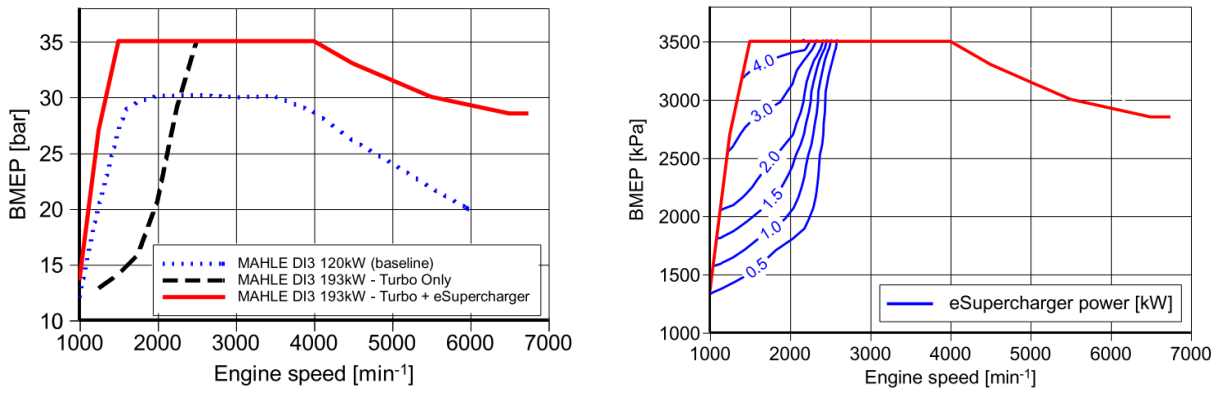


**Figure 19: E-booster effect on BMEP (a) and power consumption (b)** [44]

The Figure 19 compares baseline configuration with only a turbocharger and a resized turbocharger giving more power above 2000RPM and an e-booster providing BMEP at lower engine speed. The overall benefit is about 5 bar BMEP. The power requested by the e-booster is also presented and shows a variation over BMEP and reached more than 4kW at the maximum torque and 1500RPM.
For fuel saving, the competition with hybrid battery electric vehicle can be discussed as the e-booster permits the extreme downsizing and so reduces the pumping losses whereas a hybrid vehicle can use directly the recovered electricity to the wheel.

Fleiss *et al* [45] have presented another indirect boosting system using a compressor driven by the crankshaft to compress air in a tank. The stored pressurized air can be released at the turbine to faster acceleration. The time to torque can then be enhanced. There is a loop effect as a faster turbine acceleration allows faster increase in boost pressure and so increased airflow through the engine and thus energy available at the turbine.

The main issue with all those technologies is the energy consumption which can be used to drive the wheel and quite complex devices to implement. The acoustic charging doesn't need extra power supply.

### 2.2.3 Acoustic charging

The acoustic charging has been applied for many years, it was a well-known enabler to increase the air mass trapped in the cylinder and thus the power of internal combustion engine. The aim is to use the variation of the pressure created at the intake. In 1929 Capetti

[46] attempted to determine theoretically the length providing the best volumetric efficiency and its variation with the engine speed and explained the importance of the wave phasing. The prediction of the wave action has been largely discussed and optimized over the year using linear acoustic theories, some others uses thermodynamic approach [47][24]. The thermodynamic approach requires more computational effort where the acoustic theory make the calculation fast. The other main advantage of the acoustic theory is possible analysis in frequency domain which makes easier the analysis but can give less accuracy in regards of the quantifications.

In 1982, Tabaczynski [48] has presented the effect of the intake pipe on the volumetric efficiency. The comparison of different length shows that the intake pipe length permits to increase the volumetric efficiency at different engine speed as depicted on Figure 20. An 826mm length pipe provide a volumetric efficiency higher than 1 at 3500RPM, giving better engine filling than the intake process without any pressure drops.

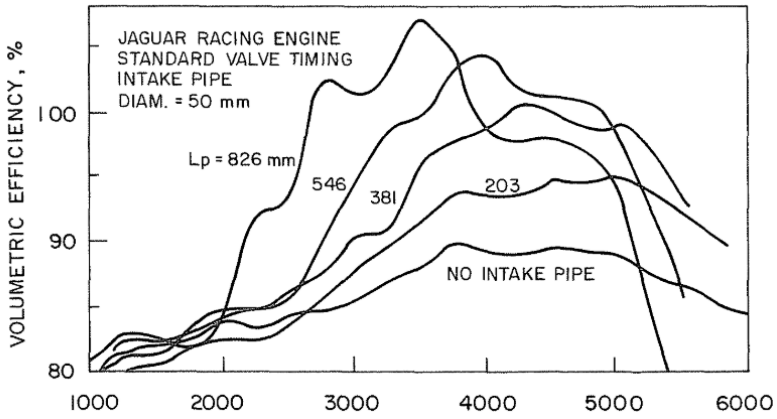


**Figure 20: Effect of the intake pipe length on the volumetric efficiency** [48]

In 1986, Matsumoto *et al* [49] have proposed an innovative air intake manifold design with different flap allowing to open or close different section. The Figure 21 shows the benefit on the volumetric efficiency in a large engine speed range.

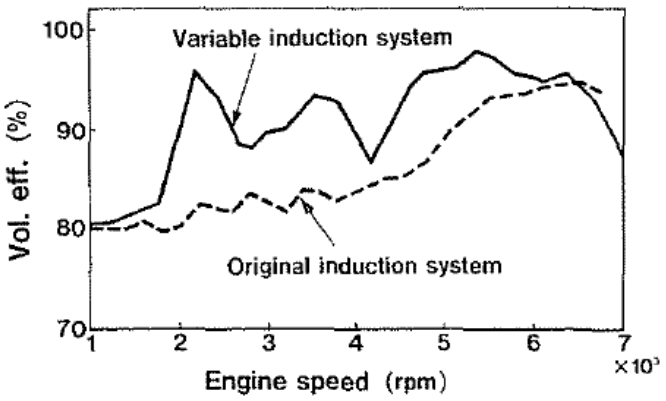


**Figure 21: Volumetric efficiency enhancement using variable induction system** [49]

Bühl *et al* [50] have used active systems to tune the resonance with long and short routes giving the chance to reduce the fuel consumption through de-throttling process. Basically

the right length allows to reduce the volumetric efficiency without high effect on the pumping losses. The pressure waves are used to generate a backflow and thus reduce the air quantity in the cylinder without reducing the mean intake pressure. The test handles on naturally aspirated 3 cylinder gasoline engine showed 1g/km fuel reduction on NEDC. Migaud *et al* [51] have proposed to use not only the intake manifold but the reflection on a dedicated volume to increase the low end torque of a Diesel engine. The system allows to move from a short duct dedicated to increase the maximum power. While the long path provides high pulsation level at lower engine speed to increase the low end torque.

### 2.2.4 Conclusion

The turbocharger is an efficient boosting system to reduce the fuel consumption of SI engine as a key enabler for downsizing. The main drawback of this solution is the so called turbocharger lag and the risk of induced back pressure at the exhaust. The supercharger and e-booster can address those issues and improve the output performance of the engines but are consuming energy which can otherwise be used directly at the wheel and then starts to compete with hybrids.
The acoustic charging could be a way to enhance the output performance of the engine without consuming useful energy. A further downsizing as also to be considered in regard of the tail pipe emissions discussed in the next section.

## 2.3 Tail pipe emissions

The tail pipe emissions have been part of concerned since early 1970's. In the 1990's, the Europe defined the Euro standard since Euro1, sum up in the Table 3, the main concerns are related to HC, CO and NOx.

**Table 3: European union emissions regulations overview [2]**

| | date | CO [g/km] | HC [g/km] | HC+NOx [g/km] | NOx [g/km] | PM [mg/km] | PN |
|---|---|---|---|---|---|---|---|
| **Euro 1** | jul.-92 | 2.72 | - | 0.97 | - | - | - |
| **Euro 2** | jan.-96 | 2.2 | - | 0.5 | - | - | - |
| **Euro 3** | jan.-00 | 2.3 | 0.20 | - | 0.15 | - | - |
| **Euro 4** | jan.-05 | 1.0 | 0.10 | - | 0.08 | - | - |
| **Euro 5** | sept.-09 | 1.0 | 0.10 | - | 0.06 | 0.005 | - |
| **Euro 6 d temp** | sept.-19 | 1.0 | 0.10 | - | 0.06 | 0.0045 | $6.0\times10^{11}$ |
| **Euro 6** | jan.-21 | | | | | | |

The CO and HC emissions limitations stays at the same level since Euro 4. The NOx specific limitations started with the Euro 3 standard and has been lowered ever since. It is

even more stringent since Euro 6 d temp, as a new driving cycle, has been adopted and requires higher load and engine speed.
This has been effective on the reduction of the NOx emissions, in Europe and the US, as depicted by the Figure 22. The EU NOx has been halved between 1990 and 2010, they are still going down.

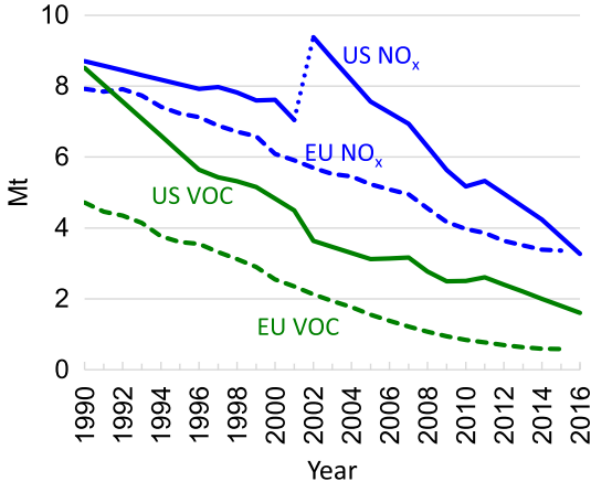


**Figure 22: Total NOx emissions from High way vehicle (LDV, HDV, commercial vehicle and motorcycle) in the US and Europe** [52]

The new regulations and the public concerns about the pollutant emissions and more specifically on NOx. Its control is a major challenge for engine development. The first step is to understand the mechanism of the NOx formation.

### 2.3.1 NOx raw emissions

The NOx emissions results from the atmospheric nitrogen reaction. Heywood [24] cites Zeldovic governing equations ( 2.20 ), ( 2.21 ) and ( 2.22 ) of production and destruction of nitrogen monoxide.

$$O + N_2 \leftrightarrow NO + N \quad (2.20)$$

$$N + O_2 \leftrightarrow NO + O \quad (2.21)$$

$$N + OH \leftrightarrow NO + H \quad (2.22)$$

The production and destruction of NO is not working at the same temperature range and the same rate which explains that the combustion can produce variation of the nitrogen oxide.
The NO formation rate can be written using equation ( 2.23 ).

$$\frac{d[NO]}{dt} = \frac{6 \times 10^6}{T^{1/2}} \exp\left(\frac{-69\,090}{T}\right)[O_2]^{1/2}[N_2] \quad (2.23)$$

$[O_2]$ and $[N_2]$ are the oxygen and nitrogen equilibrium concentration. The equation ( 2.23 ) illustrates the exponential increase of NO production when the temperature increases. This sensitivity to the temperature is reported in the Figure 23.

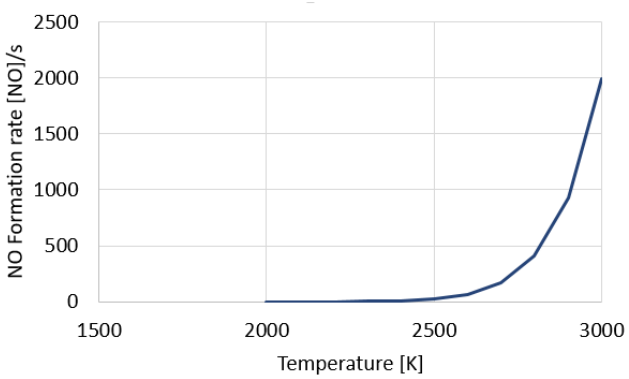


**Figure 23: [NO] formation dependency with the Temperature**

The conversions between nitrogen monoxide and nitrogen dioxide are governed by the equation ( 2.24 ) and ( 2.25 ).

$$NO + HO_2 \leftrightarrow NO_2 + OH \quad (2.24)$$

$$NO_2 + O \leftrightarrow NO + O_2 \quad (2.25)$$

Thus the combustion timing influences the $NO_x$ raw emissions as Zschutschke *et al* [53] have shown in the Figure 24. The Mass Fraction Burnt 50 (MFB50) is defined as the crank angle position when fifty percent of the fuel mass injected has been burnt.

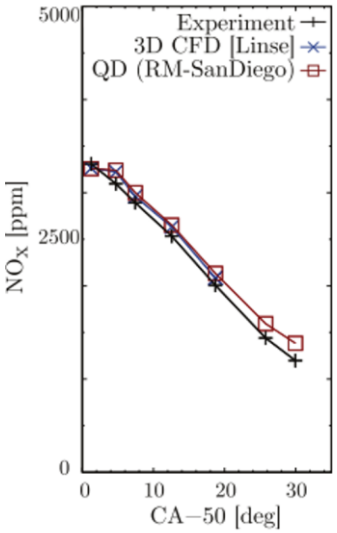


**Figure 24: NOx raw emissions in function of MFB50** [53]

The effect of the air fuel ratio is also observable as well as the effect of the combustion timing. Giansetti [54] evaluated the effect of the influence of the mixture on the 3 main pollutant emissions HC, CO and NOx. The HC and CO stays low for lean mixture whereas the NOx tends to increase in this condition (as depicted in Figure 25).

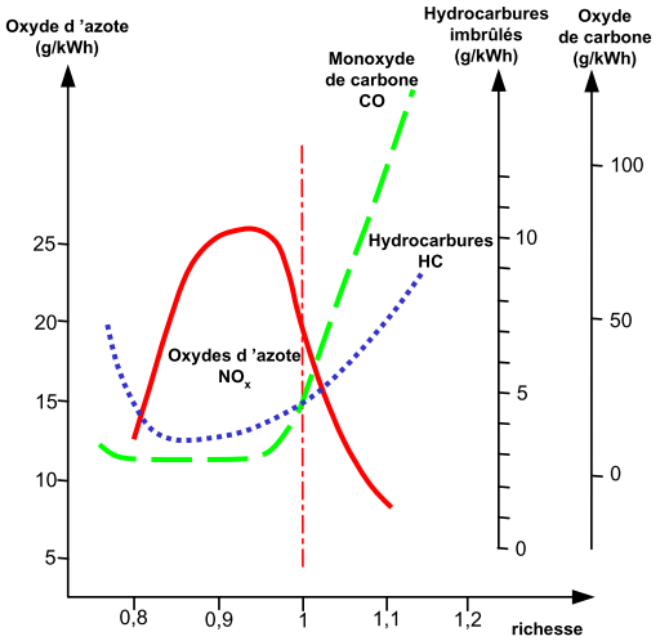


**Figure 25: Raw emissions overview in function of the fuel to air ratio** [54]

The raw emissions for the three main pollutant emissions are quite low for stoichiometric mixture. However the current SI engine are all equipped with three ways catalyst. Thus the emissions is not evaluated at the exhaust valve but at the end of exhaust line and thus downstream this after treatment device.

### 2.3.2 Three way catalyst

Three ways catalyst (TWC) allows to reduce the NOx and to oxidize the HC and CO. The technology has been developed intensively over the past 60 years as described by Keenan [55] and presented in the Table 4. It has been first an oxidation catalyst, for only HC and CO, and then moved to a TWC still in use today.

**Table 4: Catalyst technology evolution over the past 60 years** [55]

| Technology | Date | Company |
|---|---|---|
| Single Cylinder Oxidation Catalyst | 1957 | Ford |
| Oxidation Catalyst | 1959 | GM |
| Pellets | 1971 | Ford |
| Diesel Oxidation Catalyst | 1971 | Cummins |
| Three Way Catalyst | 1972 | EPA |
| Monolith | 1974 | Corning |
| Diesel Particulate Filter | 1980 | Esso |
| Selective Catalytic Reduction | 1986 | Degussa |
| Electrically Heated Catalyst | 1989 | EPA |
| Methane Oxidation Catalyst | 1991 | GM |
| Hydrocarbon Adsorber | 1992 | SwRI |
| NOx Storage Catalyst | 1995 | Toyota & JM/Daimler |
| Ammonia Oxidation Catalyst | 1998 | MAN |
| Diesel Particulate NOx Reduction | 2000 | Toyota |
| Pre Turbo Catalyst | 2000 | Emitec/MAN |
| Partial Oxidation Catalyst | 2001 | Emitec |
| SCR on Filter | 2003 | Engelhard |
| Gasoline Particulate Filter | 2009 | Ricardo |
| Passive NOx Adsorber | 2011 | JM/Cummins |
| Three Way NOx Storage Catalyst | 2012 | Daimler/Umicore |

The TWC are usually made of ceramic honey comb structure giving high thermal resistance and low thermal expansion. The main active part is made of noble metals. The platinum (Pt), palladium (Pd) and rhodium (Rh) are mainly used in the current technologies. Usually two are used jointly such as Pt/Pd or Pt/Rh. The usage of the noble metals is the reason of the high cost of this after treatment device.

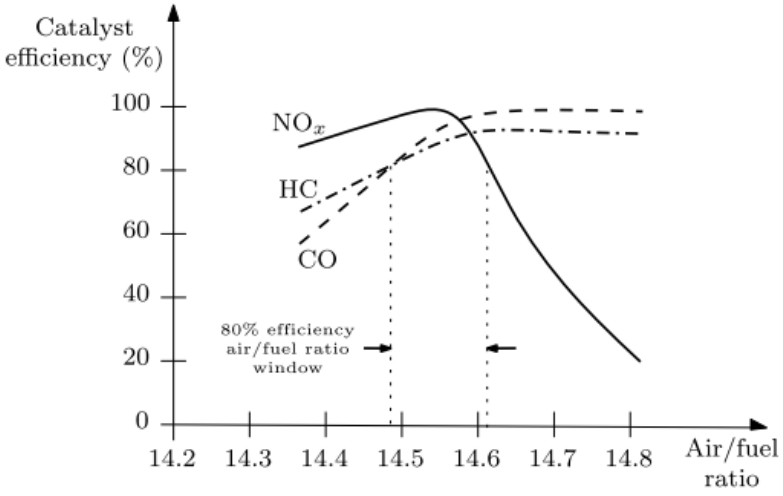


**Figure 26: Three way catalyst efficiency** [56]

When running close to stoichiometric mixture the NOx, HC and CO are converted in the TWC on $N_2$, $CO_2$ and $H_2O$ at the same time. The Figure 26 shows the sensitivity of the TWC to the mixture. In stoichiometric conditions the TWC ensures the best conversion tradeoff between the HC, CO and NOx at tail pipe outlet. This is the reason why even if the raw emissions in lean (excess air) mixture are lower, the stoichiometric mixture has to be maintained.

### 2.3.3 Conclusion

The tail pipe emissions are driving the technologies developed for the new engines. Not only the raw emissions has to be considered but also the possibility for the three way catalyst to convert them in none pollutant species. The Figure 27 shows the different driving cycle in the engine map. The NEDC was located at the bottom left side of the engine map and so at low engine speed and low load. The real driving cycle covers all the operating condition. This actually means that the tail pipe has to be well controlled on the complete engine operating conditions and so the mixture has to be maintained stoichiometric upstream the TWC to make it efficient. The figure does represent two main areas where the lambda one is not yet applied which is the scavenging area where the mixture is lean (excess of air). The enrichment consists of fuel excess compared to stoichiometric. The engine strategy will have to change to comply with the new regulation.

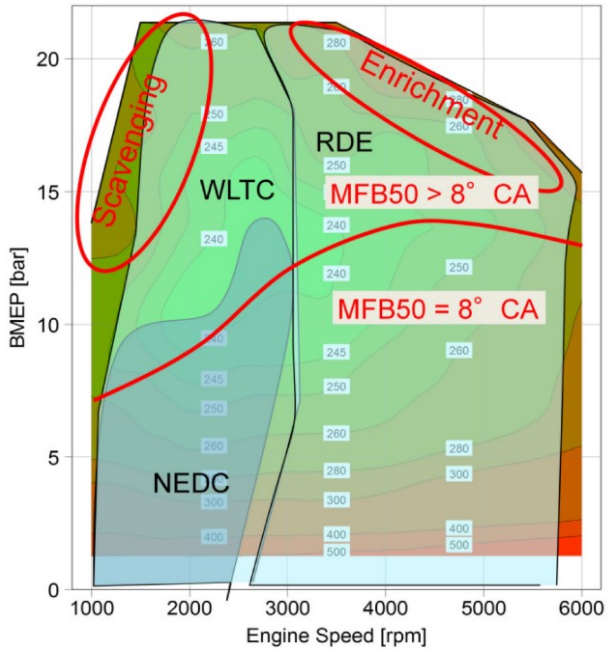


**Figure 27: Engine map and current GTDI engines strategies** [57]

The Figure 27 exhibits a delimitation between the low load of MFB50 at 8°CA and the higher load where the MFB50 is higher than 8°CA. The shift in combustion is due to the abnormal combustion known as knocking, discussed in the next section.

## 2.4 Knocking

The combustion is usually modeled as a spherical flame separating the burnt zone from the unburnt mixture. This front flame starts at the spark plug position and propagates with the flame speed in the combustion chamber until the whole mixture is burnt. In ideal situation the combustion is instantaneous and takes place at the top dead center. In real situation the front flame velocity is not infinite and the combustion duration is few tens CA.

The MFB50 has been experimentally shown to be optimum when positioned between 6 and 16° after top dead center [24] [58] [59] [60] [61]. This optimum depends on the combustion duration and wall heat transfer. As the combustion is not instantaneous, part of it takes place before the Top Dead Center (TDC) which is increasing the compression work from the piston. In the same time a late combustion means lower expansion until the Bottom Dead Center (BDTC) which lowers the engine efficiency. The tradeoff between those two effects goes for a fast combustion process. The combustion duration is shorten when the temperature, pressure and the turbulence increase. The maximum pressure in the cylinder is limited by the mechanical criterion on the mobile part which would need to withstand higher constraint. Indeed the increase of compression ratio raises the maximum in-cylinder pressure as well. Nevertheless this has been faced by the Diesel engine where the maximum in-cylinder pressure is much higher than for gasoline engines. The combustion binds also the compression ratio. High compression ratio leads to high pressure and temperature and thus more risk for knocking. This knocking is defined as the ignition ahead of the spark plug ignited flame front [62]. The Figure 28 shows the engine map where the knock limits is usually met. This is a large area above a BMEP limit depending of the compression ratio.

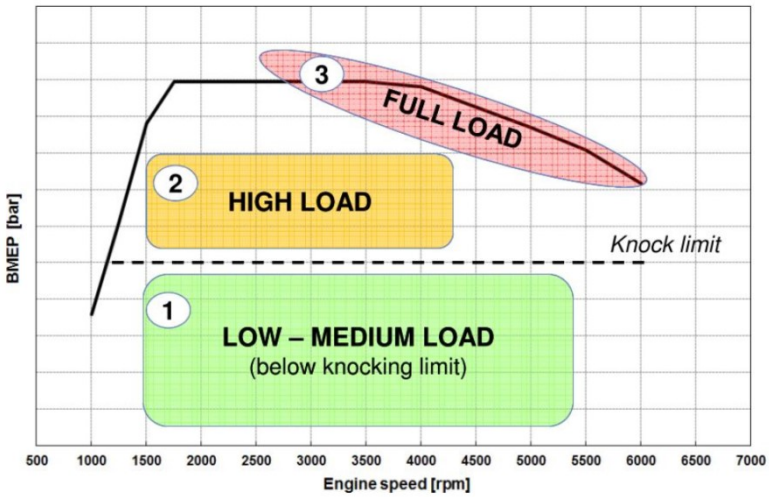


**Figure 28: Knock risk position in engine operating map** [63]

The up to date engines are running knock controlled in high load. It can be controlled through spark timing delay but this measure is not always enough. The next section defines the knock occurrence conditions and effect. The next part presents different solutions to improve the knock resistance.

### 2.4.1 Knock occurrence conditions and effect

The auto ignition exists because in some area of the unburned zone, the mixture reaches the conditions of self-ignition. The mixture auto-ignites when a combination of temperature and pressure threshold is reached. Robert *et al* [64] and Töpfer *et al* [65] have located the most usual self-ignition area close to the exhaust valve as depicted in the Figure 29. Qi *et al* [66] have located also possible auto ignition near the cylinder wall. Peters *et al* [67] have mentioned the effect of the wall temperature by simulation and demonstrated that the increase of 30K is enough to increase the pre-ignition risk.

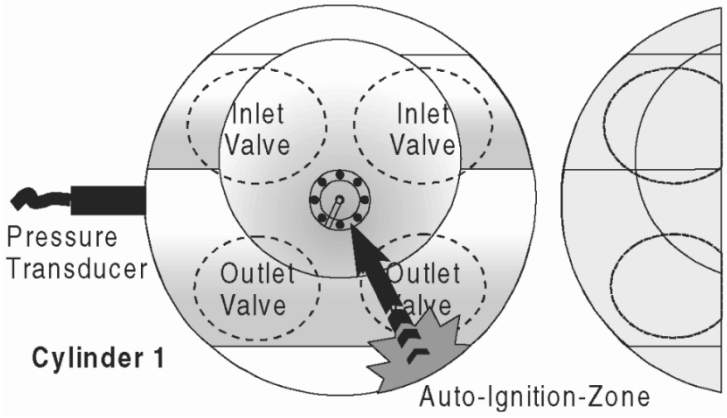


**Figure 29: Auto ignition location and propagation direction** [65]

Rothe *et al* [68] have shown how the swirl enhances the temperature homogeneity and contributes to rise knock resistance. Dahnz *et al* [69] have highlighted the risk related to the lubricant droplets and the fuel properties with the variation of the Research Octane Number (RON) or on the ethanol concentration [25]. The Figure 30 shows some condition limits that bounds the possibility of knocking in regard of the mixture temperature and air to fuel ratio (A/F).

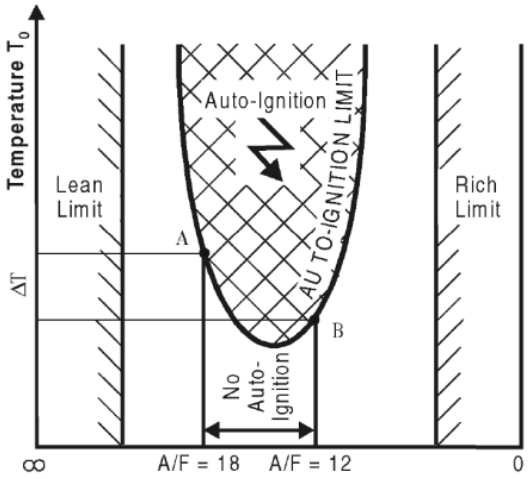


**Figure 30: Knocking conditions** [65]

Because of the knock risk the compression ratio is limited and thus the thermal efficiency expressed in equation ( 2.1 ). When knock is detected the spark timing is delayed tending to reduce the maximum temperature and pressure of the unburnt zone and thus limit the knock risk. Nevertheless this later combustion reduces the thermal efficiency as the expansion is reduced and increases the exhaust temperature.
The knock can be detected through the cylinder pressure as it induced high frequency oscillation [70]. The Figure 31 shows the effect on the in-cylinder pressure and the result of band pass filtering post processing.

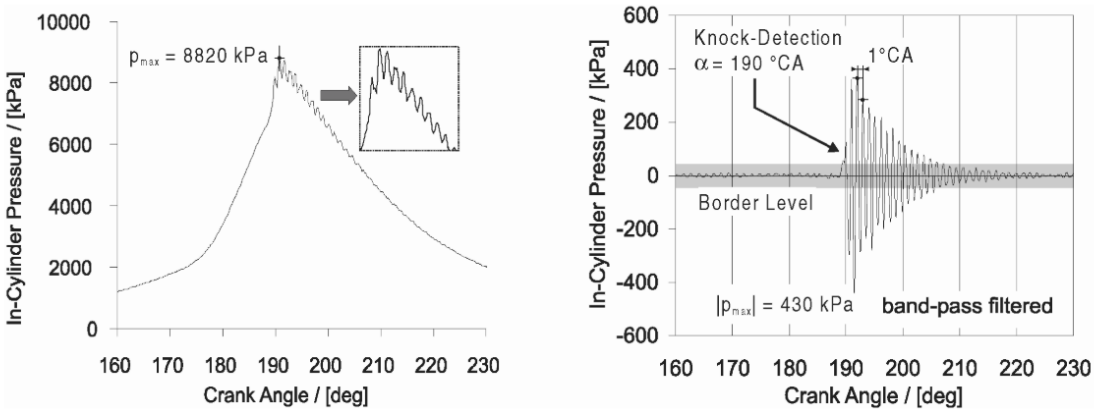


**Figure 31: Mitsubishi GDI S.I engine. In-cylinder pressure (left) non filtered signal, (right) band pass filtered f=4-14 kHz** [71]

A common way consists in the evaluation of the Maximum Pressure Oscillation (MAPO) as defined by the equation ( 2.26 ) [72] [73] [74] [75].

$$MAPO = \max\left(\left|P_{cyl\_filt}\right|\right) \qquad (2.26)$$

$P_{cyl\_filt}$ is the high frequency pass filtered (above 4 kHz) in-cylinder pressure signal.
The MAPO characterizes the knock intensity. Kawahara *et al* [76] have linked the knock intensity to the mass fraction of the unburned mixture before the auto-ignition appears. The mass burnt by the auto ignited flame defines the knock intensity and the high frequency pressure signal amplitude.
Robert *et al* [64] have shown that using LES simulation tools is possible to model the knocking and properly located the auto-ignition area. Furthermore the presented pre-ignition is described as an early auto-ignition which generate pressure wave causing additional auto ignitions. This creates detonation with very high temperature. Qi *et al* [66] have well observed those phenomena with rapid compression machine (RCM).
In mass production, Businaro *et al* [59] described a reliable solution to evaluate the knock, which consists to record the engine block shell acceleration. Indeed the high frequency in-cylinder pressure pulsation radiates to the engine block and can be sensed with an accelerometer measurement of the outside shell.
The knock leads to higher temperature in the cylinder and higher pressure which could be beneficial for the output torque. These increases in pressure and temperature have negative consequences on the cylinder, piston and pin axis material. Ceschini *et al* [77] and Balducci *et al* [72] have carried out a quantitative and qualitative evaluation of the knock impacts. The high temperature induced by the knock softens the aluminum alloy of the piston, it has been observed wear, roughness changed and abrasion. It can wear out the anodized layer which leads to degrade the sealing function. In extreme cases the piston can be destroyed.
The current engine combustion strategy is mainly driven by the knocking, reason why the combustion can be delayed. The modeling and the influencing parameters will be discussed in the section 3.2.2. The knock can be partly controlled through a spark timing calibration. Indeed retarding the spark timing make the combustion happening when the expansion is already ongoing. The pressure and temperature during the combustion are lower which reduces the risk of auto ignition. The Figure 32 shows the effect of the spark timing variation on the PV diagram. The surface covered between the compression and

the expansion defines the work. For high torque/BMEP the spark timing is delayed thus the combustion pressure peak happens later, nevertheless the output work is increased as pressure is higher.

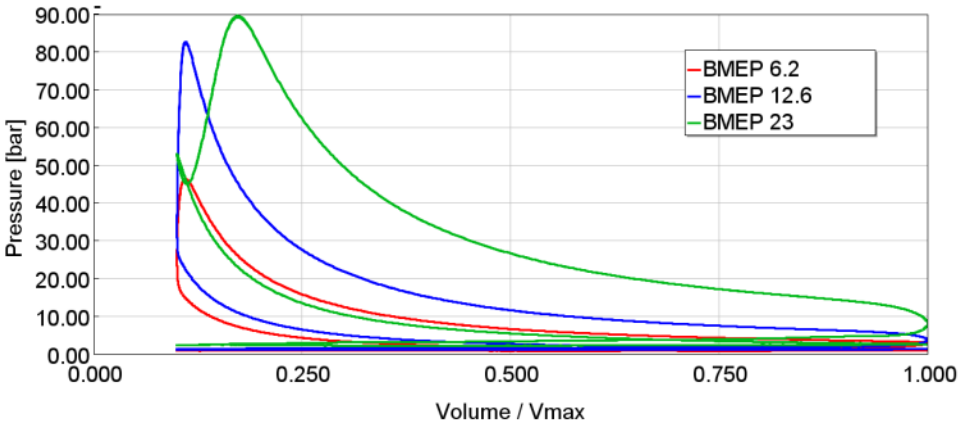


**Figure 32: Pressure Volume diagram for 3 different loads**

### 2.4.2 Current technologies for knocking mitigation

The high compression ratio improves the overall specific fuel consumption. For high load it tends to increase the knock tendency. It can partially be overtaken through a delayed combustion. For high engine speed and full load the overfueling/enrichment has been adopted for years but needs now to be rejected for the next regulations.
Thewes *et al* [22] have listed some technical solutions such as the cooled Exhaust Gas Recirculation (EGR), Miller cycle or cylinder deactivation. Some others have presented the water injection and jet ignition as an alternative. Those technologies are discussed in the following parts.

#### 2.4.2.1 Miller and Late or Early intake valve closing

The Miller and Atkinson cycles have been presented as an extended expansion in the cylinder [78]. Atkinson patented a mechanism allowing for higher expansion than compression [79]. This allows expanding the in-cylinder gases until the pressure reach the exhaust pressure and thus reduces the remaining energy in the exhaust gases. The proposed mechanism increased the complexity of the mobile parts such as the crank shaft and rods. The Figure 33 shows the effect of the extended expansion on the high pressure loop surface which defines the output work.

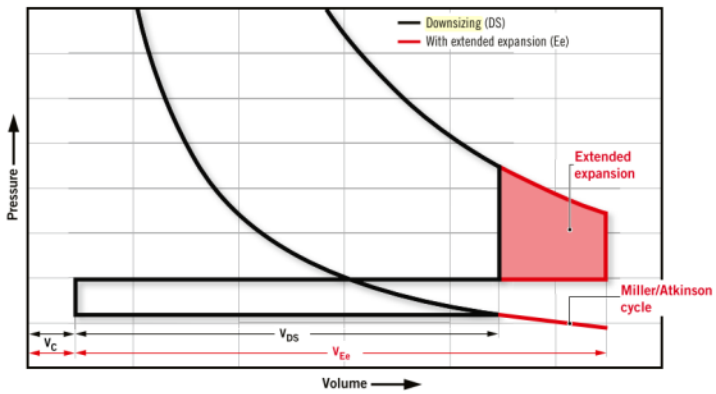


**Figure 33: Effect of extended expansion** [80]

Based on the Miller and Atkinson cycles many studies have been carried out to decrease the compression stroke through the valve timing variation [63] [81] [82]. The Figure 34 shows the valve lift corresponding to an early intake valve closing (EIVC) and late intake valve closing (LIVC). In case of EIVC the intake process ends before the piston reached the bottom dead center (BDC) which leads to an expansion of the gas until BDC.

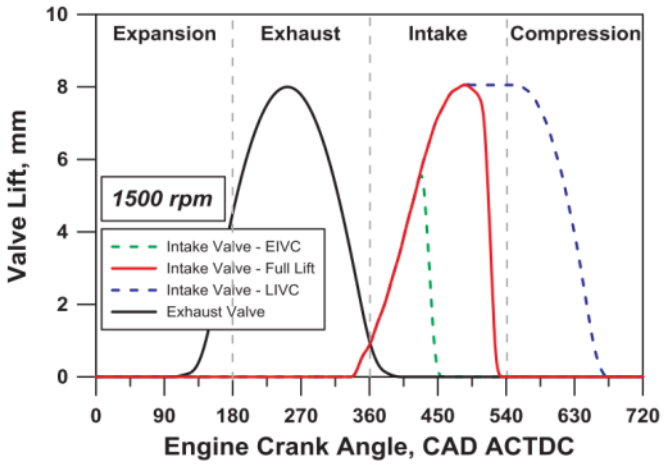


**Figure 34: Valve timing expansion for Miller cycle** [83]

For the LIVC the intake valve closes after the BDC so that part of the flow can go back in the intake manifold before the compression starts. Thus in both case the compression is reduced compare to the expansion. Teodosio *et al* [83] have simulated both strategies at low load and conclude with 5.6% BSFC reduction potential from the EIVC. The EIVC gives a better potential BSFC than the LIVC. Doria *et al* [63] have evaluated also EIVC and LIVC at high load and conclude on a better potential of the latter because of the turbulence effect. Both strategies give a benefit for the combustion as it allows an earlier combustion. The resulting lower temperature gives the possibility to reduce the over fueling and goes in the direction of the stoichiometric mixture required by the new regulation. Both EIVC and LIVC have obvious negative effect on the engine air filling which needs to be compensated by the boosting system.

This solution aims to reduce the effective compression stroke while maintaining the expansion in the cylinder. The knock resistance can be improved. The output power tends to be reduced as the volumetric efficiency is reduced. This can be compensated by an

increased boost pressure, Demmelbauer-Ebner *et al* [84] have used a variable turbine geometry to maintain high output power.

#### 2.4.2.2 Exhaust Gas Recirculation (EGR)

The intake and exhaust valve closing timing plays also an important role in the burnt gas quantity remaining in the cylinder. This is largely used at part load. The exhaust gases can also be introduced in the cylinder via an external loop. The gas is picked from the exhaust line and redistributed in the intake after having been cooled.
The main advantage of the EGR, described by Maiboom *et al* [85], is the heat capacity increase of the in-cylinder mixture and reduction of the combustion speed.
Potteau *et al* [86] have evaluated the different external EGR architectures represented on Figure 35. The most well-known consists on the high pressure EGR where the gas is picked up at the exhaust manifold and cooled down before release in the intake manifold. And the low pressure EGR loop connecting the turbine outlet and the compressor inlet.

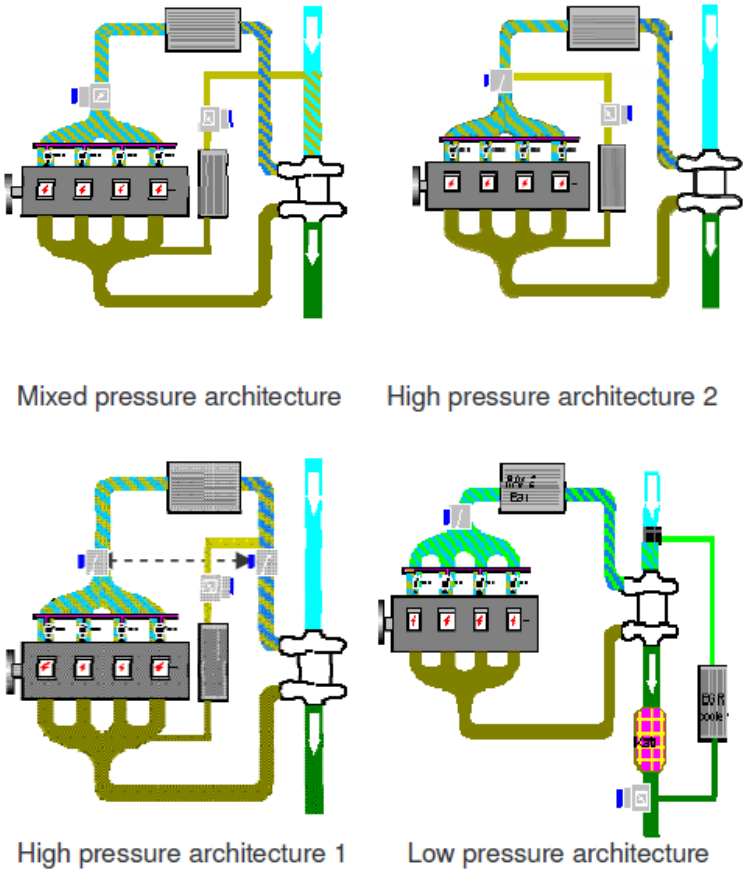


**Figure 35: EGR loop architectures** [86]

The EGR has been largely considered to reduce the pumping work during low load operation. The EGR is then used to open the throttle body while the Oxygen quantity remains the same [87]. This improves the BSFC. At higher load it can also be used to improve the knock resistance.
Kumano *et al* [88] have evaluated the EGR to reduce the knock tendency. The high pressure (HP) and low pressure (LP) are mentioned and the latter usually preferred. The

high pressure EGR requires pressure difference between the intake valve and the exhaust pre turbine favorable to gas circulation from the exhaust to the intake. With the addition of a cooler pressure drop this situation is not reached for all operating conditions.
Alger *et al* [89] have compared the SI cooled low pressure EGR concept with Diesel engine. The SI engine with high EGR rate up to 30% gives good potential in BSFC. It has been mentioned the effect on the combustion speed and the risk of misfire. Furthermore the EGR increase the pumping losses and the back pressure due to the increase turbine inlet temperature. The exhaust temperature has decreased by 100°C. Alger *et al* [90], Bozza *et al* [91] and Fontana *et al* [92] have explained the temperature reduction by the advantageous combustion phasing and in-cylinder temperature reduction.
Bozza *et al* [93] have expressed The low pressure EGR is an efficient solution for knock mitigation. One challenge lies in the difficulty to properly know the EGR rate. Liu *et al* [94] proposed a way to solve it through a pressure measurement in the EGR route. Nevertheless the estimation of the actual EGR rate sucks by the engine remains a challenge mainly during highly transient operating conditions and because of the high pressure fluctuation appearing in the intake and exhaust manifolds. This could partially explain the observed increase in the cycle to cycle variation when using low pressure EGR.

#### 2.4.2.3 Water injection

Going in the same direction as the EGR, another fluid can do the same kind of action.
The water injection has been widely investigating to improve BSFC. Hoppe *et al* [95] investigated the water injection as complement measure to cooled EGR and Millerization. The investigation demonstrated the cooling effect of the water vaporization in the cylinder as depicted in the Figure 36.

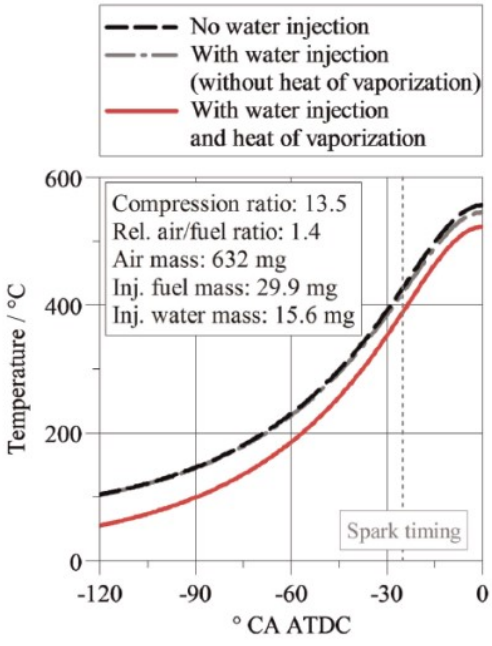


**Figure 36 Cooling effect of the water injection** [95]

Thus the water injection permits a better combustion phasing because the better knock resistance reduces also the exhaust temperature. The benefit is moderated by resulting slower combustion. The water quantity has been tested until 60% of water to fuel ratio by

Kappner *et al* [96] when Hoppe *et al* [95] have estimated the best configuration lower than 50% in the Figure 37. The contours represent the water to air ratio.

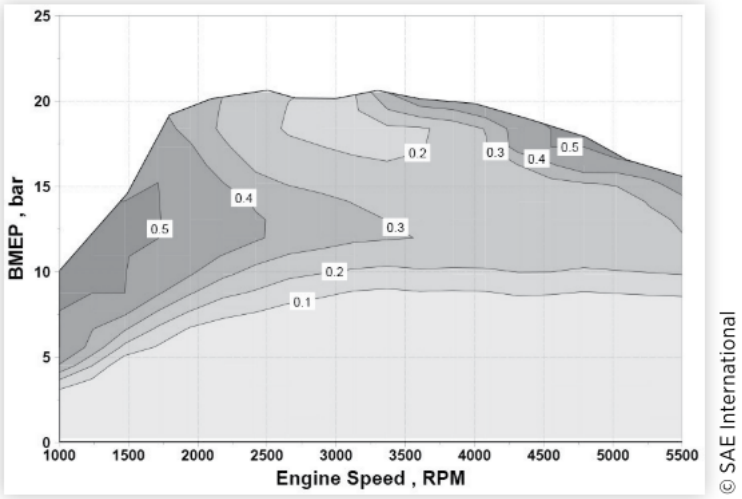


**Figure 37: Water to fuel ratio map** [93]

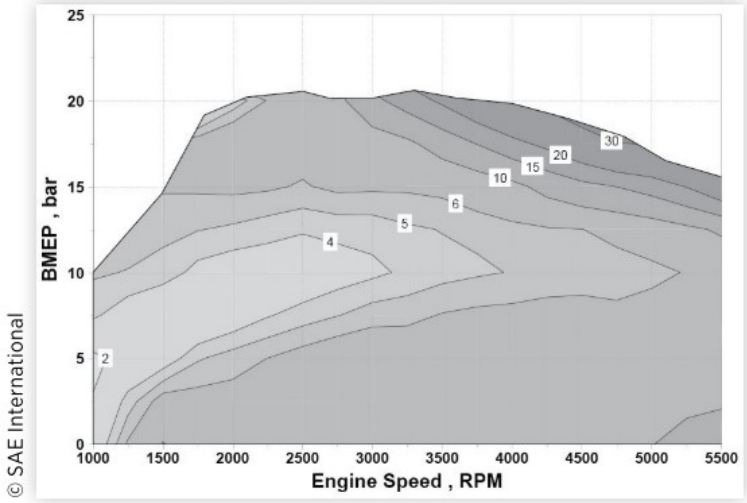


**Figure 38: BSFC gain with water injection** [93]

The Figure 38 shows equivalent BSFC improvement with water injection around the maximum power area. The contours symbolize the BSFC benefit. It seems this solution does not give so high potential at low engine speed and high load. The Figure 39 shows the effect of the water injection on the in-cylinder pressure and on the heat release. The high frequency part of the signal disappear with the injection of water. This reveals the reduction of knock which is confirmed by the heat release which presents a peak without water.

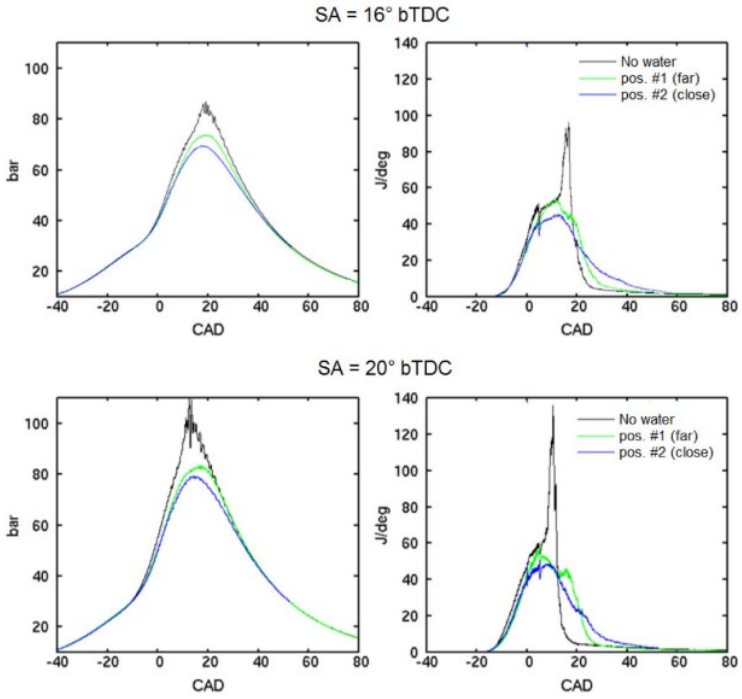


**Figure 39: Effect of the water injection on there and heat release** [97]

Käppner *et al* [96] have presented the different possible water injection location such at the intake manifold used in the mass production M4 GTS car. Compared to EGR the injected water quantity is easier to control and the experience with the fuel injection provides strong and longtime experience for engineers.

**Table 5: Architecture of the water injection** [98]

| (Port) Water Injection | (Direct) Water Injection | |
|---|---|---|
| 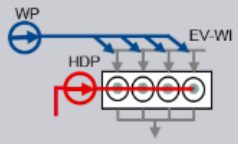  | 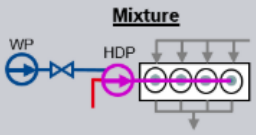  | 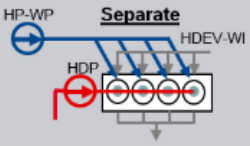  |
| **Low Costs:** Components + Integration | **High Costs:** Development of corrosion and freezing robust HS-Steels (+ components) | |
| **Robust:** Against freezing and corrosion | **Complex:** Requires *reversible HP pumps* | |
| **Modular & Compact:** Add-on system to existing DI system | **Non-modular:** Requires major overhaul of existing HP fuel system | **Packaging:** Extra HP water injector + HP water pump |
| **Energy-efficient:** LP system -> Low energy-requirement | **Start-stop incompatibility:** Requires water-fuel mixture to be replaced with pure fuel | **Energy-inefficient:** Requires additional HP water pump |
| Higher water consumption | Lower water consumption | Lower water consumption |

The Table 5 summarizes the different water injection locations and the associated challenges. The port injection is the easiest to install and cheaper but the water consumption is higher than direct in-cylinder injection. This latter requires either a water

fuel emulsion or another injector which can be difficult to implement because of the small space available in this area.
The main issue is to supply the water. Indeed different solutions have been considered such as the EGR gases condensation or collecting the water from the passenger compartment air conditioning. They need further systems to collect the required water quantity and store it. Some other are thinking for an additional tank for the demineralized water such as it is for the Selective Catalitic Reducetion (SCR). The usage of tap water would require further water treatment to maintain the water quality.

#### 2.4.2.4 Variable Compression Ratio

The Variable Compression Ratio (VCR) has been discussed for years. In principle it is a good way to optimize the trade-off between the knock risk and the efficiency. Indeed at low load the compression ratio can be high and thus greatly increase the efficiency as expressed in the equation ( 2.1 ). Reducing the compression ratio at high load allows reducing pressure and temperature which is beneficial for knock resistance.
Tomazic *et al* [99] have proposed a complete concept with a two stage variable compression ratio varying from a compression ratio at 14 at low BMEP to a compression ratio at 10 at higher load where the knock risk is higher. The Figure 40 (a) shows BMEP point of shifting over the engine speed. This is about 8 bar BMEP under the Full Load curve. The figure exhibits the main operating point used by the US06 cycle and shows that most of the operating point are in the CR14 area. US06 is a high speed high load cycle US standard. The Figure (b) shows that this shifting line can be moved toward higher BMEP for fuel with higher RON. The authors proposed to control the compression with the fuel quality via a knock recognition. They exhibited potential of 5-7% fuel consumption saving depending on the driving cycle.

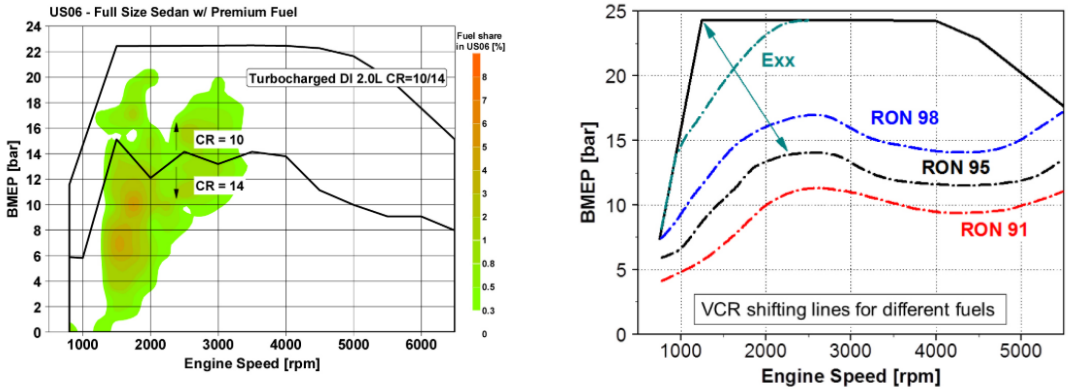


(a) (b)

**Figure 40: Compression ratio strategy** [99]

Walther *et al* [100] have combined the EIVC and VCR at 2000RPM and 2bar BMEP and exhibited a significant BSFC reduction with a compression ratio at 18. For a BMEP of 5bar the optimal compression ratio is about 16. Schwaderlapp *et al* [101] have discussed the opportunity of VCR to increase the internal EGR.
The BSFC enhancement is valuable but the complexity of the installation as well as the mass increase makes this solution quite difficult to apply in mass production. Nevertheless

Kiga *et al* [102] have presented the first mass production engine equipped with VCR and turbocharger.

#### 2.4.2.5 Jet ignition

All the previous solutions aim to change the in-cylinder conditions so that the knock can be controlled. The other way is to change the combustion process so that the knock cannot take place. The jet ignition already in use in Formula One [103] goes in that direction. The Figure 41 shows the pre-chamber at the spark plug. In this pre-chamber the mixture is kept at stoichiometric and when ignited the mixture go through few holes and so ignites the rest of the cylinder. Bunce *et al* [104] have described the concept with only 3% of the fuel flow going through the prechamber for the ignition. The measurements, carried out on a single cylinder, has demonstrated the possibility for a faster and earlier combustion. The knock risk can be then reduced because of the lower time available for auto ignition. Furthermore the authors described the potential for lean mixture combustion. Lean mixture defined as excess of air compared to stoichiometric. In this condition the NOx raw emissions decrease because of cooler combustion.
This better knock resistance would help to increase the compression ratio and thus improve the efficiency.

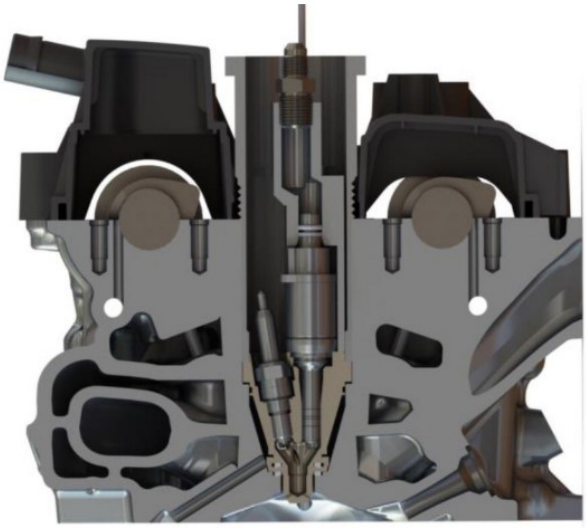

**Figure 41: Jet ignition design** [104]

The main drawback of the lean combustion is the incapacity of the three way catalyst to convert the NOx in air excess. The lean combustion would lead to the same difficulties as the Diesel engines. Alvarez *et al* [105] have mentioned the needs for additional EGR.

## 2.5 Conclusion

An efficiency enhancement of the SI engine has been discussed in this Literature Survey Chapter. The high compression ratio with a small displacement turbocharged engine allows the reduction of the $CO_2$ emissions while keeping high specific power. The turbocharger is an efficient way to improve the engine performance however its performance at low engine speed and response time gives room for improvement. Different technologies have been discussed. The acoustic charging mainly used at high

engine speed and for naturally aspirated engine presents the advantage of low energy consumption and fast response. The Chapter 4 will adapt it for a 3 cylinder turbocharged gasoline engine at low engine speed.
In the same time the control of the pollutant emissions requires to maintain the stoichiometric upstream to the three way catalyst. This latter challenges the combustion with knocking risk. The knocking has been demonstrated to be related to the mixture temperature. The Chapter 5 will be dedicated to reduce the intake temperature with the pressure waves.
The next sections will use the effect of the pressure wave in the air intake systems. The following Chapter 3 will focus on the facilities to assess the pressure wave propagation and the engine behavior.

# 3 Wave propagation and engine simulations

The Literature Survey has shown different ways to improve the engine performances whether at low engine speed or maximum operating points. One of them is the acoustic boosting using the pressure wave action in the intake system. The development of new solutions using those pressure wave requires to understand the pressure wave propagation and behavior. The effect of the pressure wave's actions has then to be evaluated with the rest of the engine components to understand the possible interaction and quantify the resulting output performance.
This chapter starts with the presentation of different tools to model and evaluate the pressure wave propagation through the linear acoustic approach. The effect of some geometries are discussed and characterized. The second part evaluates the complete engine system. The GT Power software is used to emulate the engine. The complete air intake and exhaust has to be modeled as well as the turbocharger. The 0D UserCylinder combustion model is described and finally the knocking evaluation is discussed.

## 3.1 Acoustic wave propagation

The intake system is the air provider of the engine, doing so it can affect its behavior in different ways. The pressure drop affects the air density during the intake stroke and so will contribute to change the trapped air mass in the cylinder. The ideal gas law equation ( 3.1 ) gives the direct relation between the pressure reduction and the gas density knowing that the engine cylinder stays constant.

$$\rho = \frac{P}{rT} \qquad (3.1)$$

The intake flow is unsteady and highly dynamic. The motion of the piston during the intake stroke creates a sinus shape flow velocity. This phenomenon is combined with the opening and closing of valve which abruptly shut down the flow, induce pressure pulses upstream the intake valve. The air intake system contributes to the wave propagation allowing increasing or damping them. Mezher *et al* [106] have shown that a well-tuned length between the cooler and the valve for a Diesel engine can increase the wave amplitude (Figure 42). With the presented configuration, the pressure wave amplitude increases for length of 1.5m whereas with 0.9m and 2.9m the pressure variation stays lower. Furthermore the phasing of the pressure varies. The maximum is at about 180°CA with 1.5m whereas maximum occurs at about 150°CA for 0.9m and with the 2.9mm the maximum is at about 210°CA. In each cases there is 180°CA between two maximum.

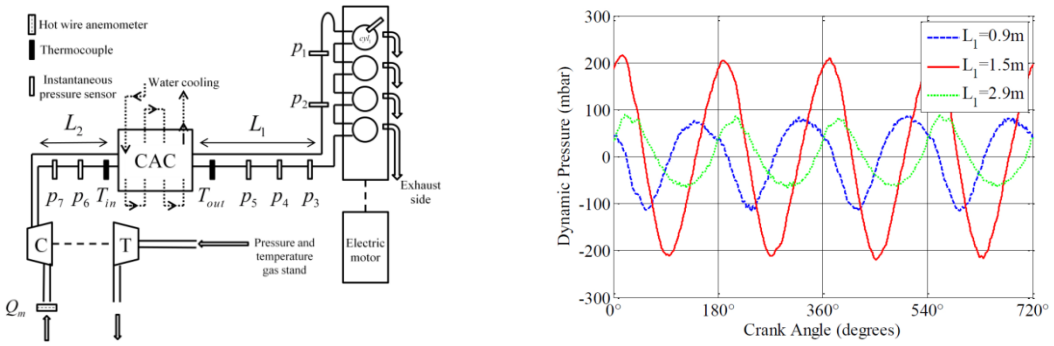


**Figure 42: Wave amplitude for different length ($L_1$) between the cooler and the intake manifold** [106]

### 3.1.1 Linear acoustic

The influence of pressure wave on the volumetric efficiency has been studied during many years. Winterbone *et al* [107] [108] have largely assessed the influence of the air intake system design and mainly the air intake system.
The pressure wave propagation without dissipation can be written with the fundamental principle of the dynamics equation ( 3.2 ) [109].

$$\rho \frac{d\vec{u}}{dt} = -\overrightarrow{grad}\, P + \rho \vec{F} \qquad (3.2)$$

The mass conservation is defined by the equation ( 3.3 ).

$$\frac{\partial \rho}{\partial t} + div(\rho \vec{u}) = \rho \dot{m}_a \quad (3.3)$$

Considering an isentropic transformation of ideal gas, the density variation can be linked to pressure through the equation ( 3.4 ).

$$dP = \frac{1}{\rho \chi_S} d\rho \quad (3.4)$$

The linearization at first order without viscosity gives the equation ( 3.5 )

$$\Delta p - \frac{1}{{c_0}^2} \frac{\partial^2}{\partial t^2} p = \rho_0 \left[ div \overrightarrow{F} - \frac{\partial \dot{m}_a}{\partial t} \right] \quad (3.5)$$

The lower case variable represents the first order linearized variation around the average ambient.

Munjal [110] has written the propagation equation ( 3.6 ), for a one dimensional approach and without source. The linear acoustic assumption implies low amplitude fluctuation meaning for instance pulsation amplitude much smaller than ambient.

$$\left( \frac{\partial^2}{\partial t^2} - {c_0}^2 \frac{\partial^2}{\partial x^2} \right) p = 0 \quad (3.6)$$

${c_0}^2$ corresponds to the sound speed and is defined in the equation ( 3.7 ).

$${c_0}^2 = \frac{\gamma R T}{M} \quad (3.7)$$

The solutions to this equation can be written with equation ( 3.8 )

$$p\,(x,t) = \left( A\, e^{-jkx} + B\, e^{jkx} \right) e^{j\omega t} \quad (3.8)$$

$A$, conventionally, represents the amplitude of the wave propagating in positive x direction and $B$ the amplitude of the wave propagating in the opposite direction.
If considering linear acoustic at one frequency the equation ( 3.8 ) is only depending on the position as defined in equation ( 3.9 ).

$$p\,(x) = A\, e^{-jkx} + B\, e^{jkx} \quad (3.9)$$

Using the two distant sensors in the ducts it is then possible to calculate those amplitudes and evaluate the reflection coefficient.
The pressure and the particle velocity are linked through the impedance as expresses in the equation ( 3.10 ).

$$Z = \frac{p}{u} \quad (3.10)$$

Winterbone *et al* [108] have explained the effect of an open end and closed end in the wave propagation. The first one reflects the wave while the sign shifts from positive to negative. The second one also produces a reflection but the reflected wave keeps the same sign. The impedance of a closed end is quite easy to evaluate as the velocity at the wall is null which means infinite impedance. For the open end, the impedance is supposed

to be null as the acoustic pressure will be null. The wave cannot pressurized the outside volume. Dalmont *et al* [111] have shown that the reflection with opened end does not happen directly at the boundary. Indeed an extension of the actual duct length allows to fit the theoretical wave reflection to the measurement. The added length depends mainly on the end shape and duct diameter.
Some other boundaries can be evaluated through linear acoustic theory such as the expansion, expansion chamber or the Helmholtz resonator presented in the next section.

### 3.1.2 Wave propagation at geometry changes

#### 3.1.2.1 Expansion

Pascal [112], Munjal [110] and [113] described the expansion influence in wave propagation. The Figure 43 represents an expansion from a cross section $S_1$ to a section $S_2$.

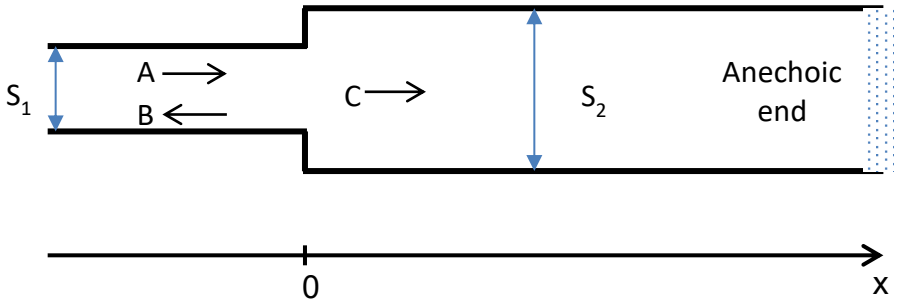


**Figure 43: Expansion Scheme** [112]

The pressure in the section upstream x=0 (section 1) is described by the equation ( 3.9 ). In the region downstream x=0 (section 2), the anechoic end (none reflective) allows to write the pressure as equation ( 3.11 ).

$$p_2\,(x) = C\,e^{-jkx} \qquad (3.11)$$

At the junction the x=0 the conservative mass can be applied and the air mass flow from one side equal the other side as shown in equation ( 3.12 ).

$$\rho S_1 u_1 = \rho S_2 u_2 \qquad (3.12)$$

The equations ( 3.3 ) can be used to write the velocity $u_1$ with equation ( 3.13 ).

$$u_1 = \frac{A}{\rho_0 c_0} e^{-jkx} - \frac{B}{\rho_0 c_0} e^{jkx} \qquad (3.13)$$

In the same way the equation ( 3.14 ) gives an expression of the velocity $u_2$.

$$u_2 = \frac{C}{\rho_0 c_0} e^{-jkx} \qquad (3.14)$$

The equation ( 3.15 ) is a combination of ( 3.12 ), ( 3.13 ) and ( 3.14 ) at $x = 0$.

$$S_1(A - B) = S_2\,C \qquad (3.15)$$

There is continuity of pressure at the junction too.

$$A + B = C \qquad (3.16)$$

Finally it is possible to express the reflection coefficient as defined in equation ( 3.17 ).

$$\frac{B}{A} = \frac{S_1 - S_2}{S_1 + S_2} \qquad (3.17)$$

The transmission coefficient is expressed in ( 3.18 ).

$$\frac{C}{A} = \frac{2\,S_1}{S_1 + S_2} \qquad (3.18)$$

The transmission and reflection reflect the sensitivity of pressure wave to the variation of cross section in the duct. Each cross section change results in a reflection and loss in transmission. In the intake system, it can be beneficial to create some reflections so that part of the energy can get back to the cylinder and so improve the engine air filling.
The muffler and air cleaner are also using this kind of phenomena to reduce the transmitted acoustic power. The volume of the air cleaner and sometimes of the muffler can be considered as an expansion chamber, with an expansion and a restriction, as depicted in the Figure 44. The expansion chamber is defined as a cylindrical volume, with two connected ducts with smaller cross section than the volume.

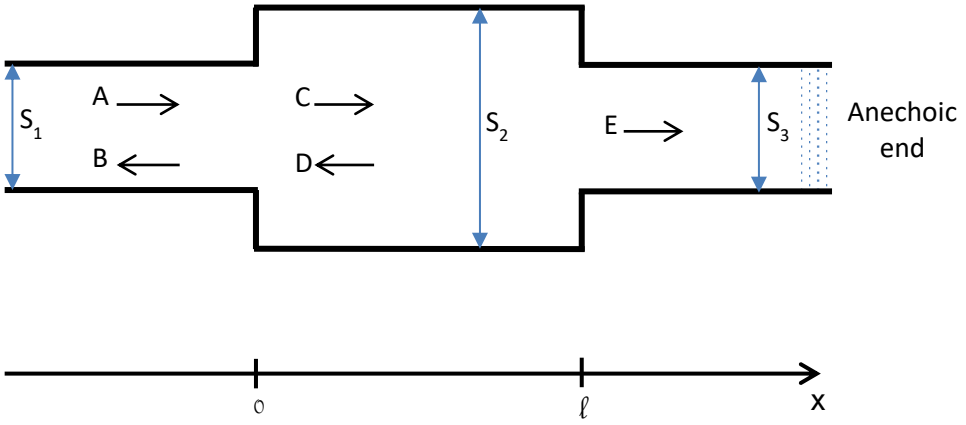


**Figure 44: Expansion chamber** [112]

The pressure can be written in all section as described in equation ( 3.19 ).

$$\begin{aligned} p\,(x) &= A\,e^{-jkx} + B\,e^{jkx},\ \ x < 0 \\ p(x) &= C\,e^{-jkx} + D\,e^{jkx},\ \ 0 < x < l \\ p\,(x) &= E\,e^{-jkx},\ \ l < x \end{aligned} \qquad (3.19)$$

The air mass flow and the pressure continuity can be then written for the expansion $x = 0$ and the restriction $x = l$.

$$S_1(A - B) = S_2\,(C - D),\ \ x = 0 \qquad (3.20)$$

$$A + B = C + D,\ x = 0$$

$$S_2\left(C\, e^{-jkl} - D\, e^{jkl}\right) = S_3 E\, e^{-jkl},\ x = l$$

$$C\, e^{-jkl} + D\, e^{jkl} = E\, e^{-jkl},\ x = l$$

If $S_1 = S_3$, it is possible to combine the equations ( 3.20 ) to find the reflection coefficient ( 3.21 ) and transmission coefficient ( 3.22 ).

$$\frac{B}{A} = \frac{j\left(\frac{S_1}{S_2} - \frac{S_2}{S_1}\right) sin(kl)}{2\cos(kl) + j\left(\frac{S_1}{S_2} + \frac{S_2}{S_1}\right) sin(kl)} \qquad (3.21)$$

$$\frac{E}{A} = \frac{2\, e^{jkl}}{2\cos(kl) + j\left(\frac{S_1}{S_2} + \frac{S_2}{S_1}\right) sin(kl)} \qquad (3.22)$$

The equation ( 3.21 ) and ( 3.22 ) can be applied to a variation duct from 0.05m to 0.15m diameters with a chamber length of 0.5 m.
The frequency can be introduced with wave number as given in the equation ( 3.23 ).

$$k = 2\,\pi\,\mathrm{f} \qquad (3.23)$$

The resulting coefficient magnitude is represented in Figure 45 and shows high reflection coefficient until the Eigen mode of the chamber which is 342Hz so that the wave length is twice the chamber length. The Eigen mode is characterized by a high transmission coefficient and low reflection.

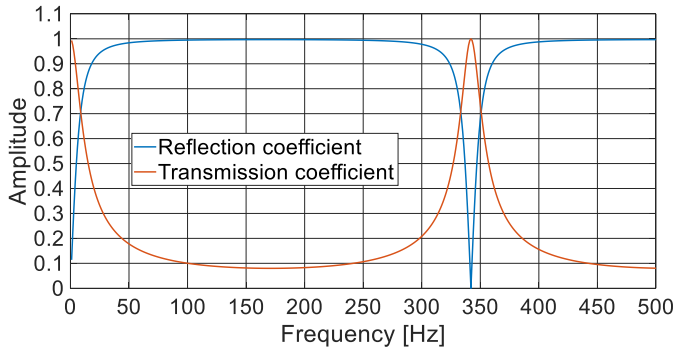


**Figure 45: Expansion chamber reflection and transmission coefficients magnitude**

The angle is represented in Figure 46. The transmission coefficient angle increases because of the propagation time through the volume, then there is an abrupt change at the Eigen mode. The reflection shows a variation between the incident wave and reflected wave of $\pi$ which denotes opposite values. The reflection coefficient shows also a step at the Eigen mode frequency.

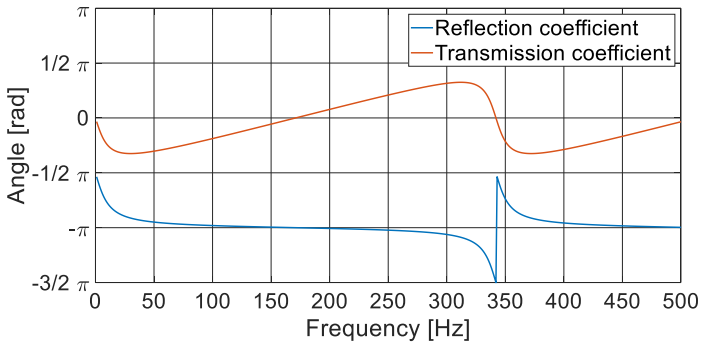


**Figure 46: Expansion chamber reflection and transmission coefficients angle**

The expansion chamber is quite efficient to reduce the wave transmission but also to obtain a reflection.

#### 3.1.2.2 The Helmholtz resonator

The Helmholtz resonator is one of the most used in acoustic. It is composed of a connecting duct and a volume as depicted in Figure 47.

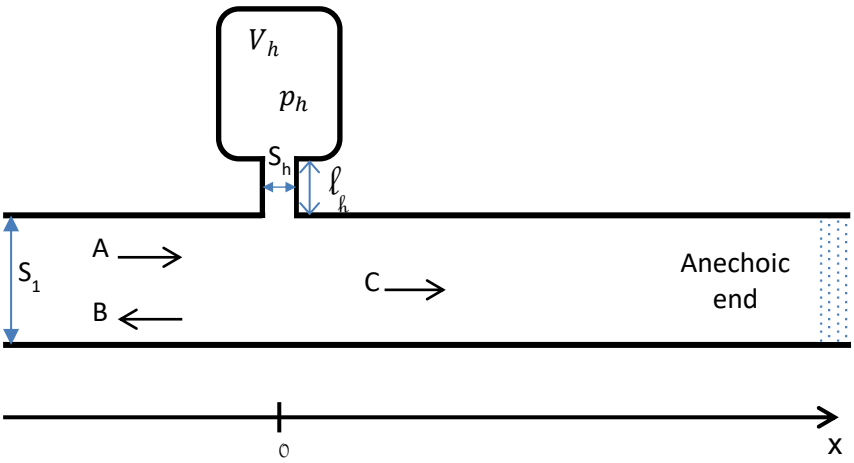


**Figure 47: Duct equipped with a Helmholtz resonator** [112]

At the Helmholtz resonator neck the air mass flow can be written through a variation of density in the volume.

$$q_h = j\,\omega\,\rho\,V_h \qquad (3.24)$$

So that the cavity pressure in the volume can be expressed as ( 3.25 ).

$$p_h = \frac{{c_0}^2 q_h}{j\omega V_h} \qquad (3.25)$$

For low frequency, the wave length is big in comparison to the neck length and the air mass in the neck can be assumed as incompressible. The volume can be considered as a spring.

$$p - p_h = j\omega\rho_0 l_h u_h \qquad (3.26)$$

The air mass flow continuity leads to the variation of the mass in the neck equal to the volume air flow.

$$\rho_0 u_h S_h = q_h \qquad (3.27)$$

$$u_h = \frac{q_h}{\rho_0 S_h} \qquad (3.28)$$

$$p - p_h = \frac{j\omega l_h q_h}{S_h} \qquad (3.29)$$

By combining ( 3.25 ), ( 3.26 ) and ( 3.29 ) the pressure at the intake neck can be written as following.

$$p_h = \left(\omega^2 - \frac{c^2 S_h}{V l_h}\right)\frac{j l_h Q_h}{\omega S_h} = \left(\frac{{c_0}^2}{j\omega V} + \frac{j\omega l_h}{S_h}\right)p_h \qquad (3.30)$$

$$q_h = \frac{-j\omega p}{\left(\omega^2 - \frac{{c_0}^2 S_h}{V l_h}\right)\frac{l_h}{S_h}} \qquad (3.31)$$

The equation ( 3.31 ) shows a maximum when the $\omega^2 = \frac{c^2 S}{Vl}$ becomes null. The corresponding frequency is the Helmholtz resonator resonance frequency. Some minor adjustment can be adapted to correct the length as the radiation length is not fully represented by the geometrical length of the neck as already mentioned in the previous section.

Using the continuity equation of the pressure and air mass flow for $x = 0$ the amplitude of the reflected wave and transmitted wave can be evaluated.

The pressure at $x = 0$ is the pressure at the resonator neck and the pressure from the upstream side and downstream side so that the equation ( 3.32 ) can be written.

$$p_h = A + B = C \qquad (3.32)$$

The air flow coming from upstream is equivalent to the air flow in the resonator combined with the air flow downstream as depicted in the equation ( 3.33 ).

$$\frac{S_1}{c_0}(A - B) = q_h + \frac{S_1}{c_0}C \qquad (3.33)$$

The reflection coefficient can be written as equation ( 3.34 ).

$$\frac{B}{A} = \frac{j c_0 \omega S_h}{2 S_1 l_h \left(\omega^2 - \frac{{c_0}^2 S_h}{V l_h}\right) - j c_0 \omega S_h} \qquad (3.34)$$

And the transmission coefficient can be written as ( 3.35 ).

$$\frac{C}{A} = \frac{1}{1 - j\dfrac{\omega c_0 S_h}{2S_1 l_h\left(\omega^2 - \dfrac{{c_0}^2 S_h}{V l_h}\right)}} \qquad (3.35)$$

The Figure 48 shows the Helmholtz resonator ability to reduce the wave transmission at its resonance frequency. The resonance frequency of 150Hz is obtained for a volume of 1L, a neck radius of 15mm and length of 100mm.

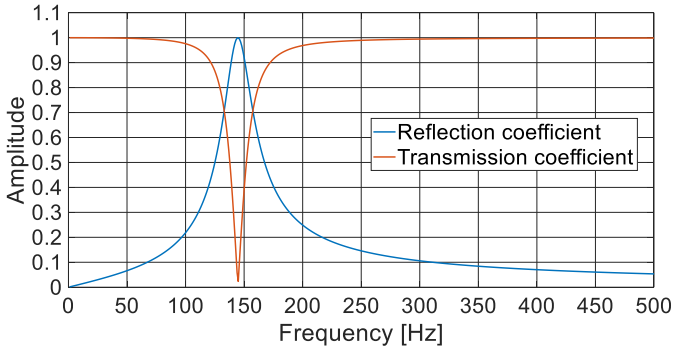


**Figure 48: Helmholtz resonator reflection and transmission coefficients magnitude**

Those simple geometries can influence the engine air filling as shown by Winterbone [107] where the reflection can help to increase the pressure at the intake valve closing. In the same time Munjal [110] has illustrated the interest of the transmission on the acoustic emissions either at the air inlet or the exhaust pipes which contributes the overall noise production of a car.

The application of this methodology for complex geometry is difficult. For this reason, the simulation tools, such as GT Power, are used and can be compared to impedance measurements.

### 3.1.3 Dynamic flow bench / Impedance measurement

A dedicated test bench has been built up to evaluate the impedance of an air intake system. The so called dynamic flow bench has been widely explained by Chalet *et al* [114]. The Figure 49 shows the mounting of the intake system. At first an air flow is initiated with a vacuum pump. The air flow is chosen and controlled as close as possible to the in situ conditions which depends on the engine application at the maximum power operating condition. After stabilization time the air mass flow $\dot{m}_a(t)$ is abruptly and linearly shut down to zero in 0.5ms and the pressure $p(t)$ is recorded at each runner of the air intake manifold.

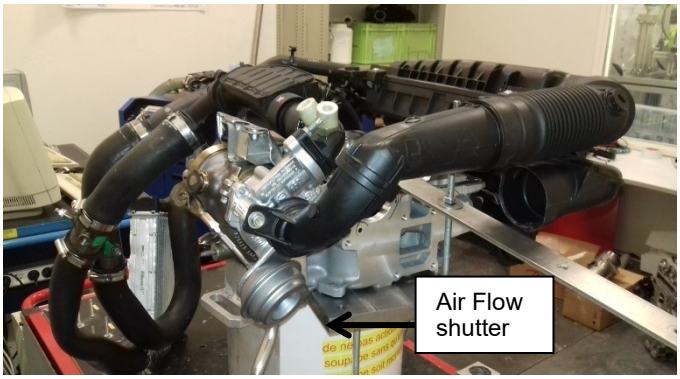


**Figure 49: Complete AIS mounted on the so called "Dynamic Flow Bench**

The pressure is measured with a Kistler 4045A2 piezo resistive transducers. The output signal is amplified and prefiltered with a National Instruments PCI-6071E board.
The stabilized air mass flow is measured with Sierra 780 S air mass flow meter. The dedicated shutting system, presented on Figure 50, allows a linear air flow reduction in short controlled time. The shutting component position is evaluated with a laser sensor. The instantaneous air mass flow can thus be estimated with a direct relationship between the airflow decrease and the shutting component position

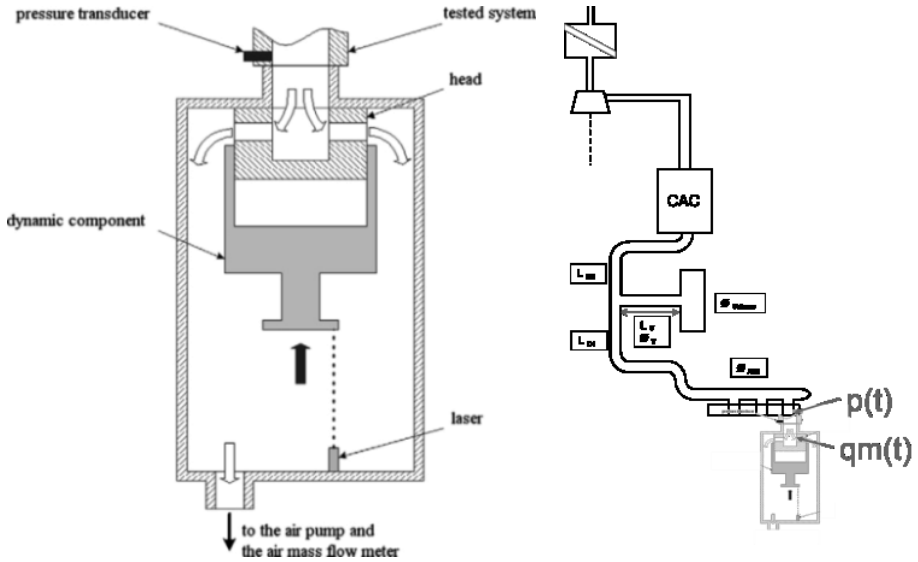


**Figure 50: Shutting system allowing a linear air decrease in 0.5 ms and air intake description** [115]

The Figure 51 shows the simulated dynamic flow bench air flow starting at the chosen 90kg/h. The pressure is recorded in the duct close to the shutting device. The example is applied to a 2,5m length duct with 40mm diameter and an opened end. The pressure signal presents an oscillation with a period of 3ms which corresponds to the quarter length tube resonance. For more complex intake system the frequency analysis is preferred.

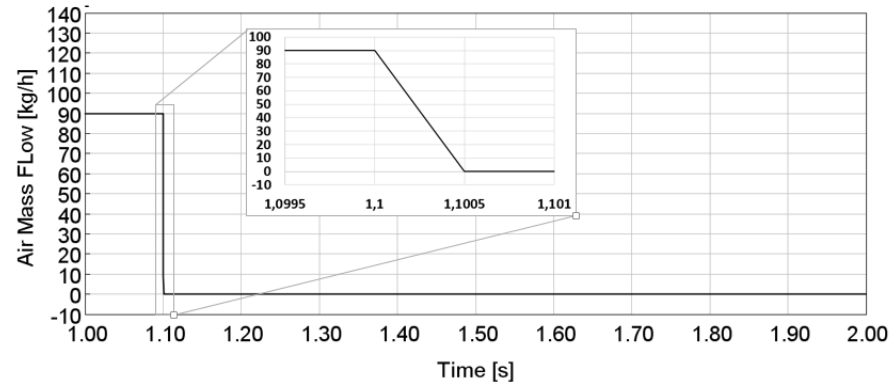


(a)

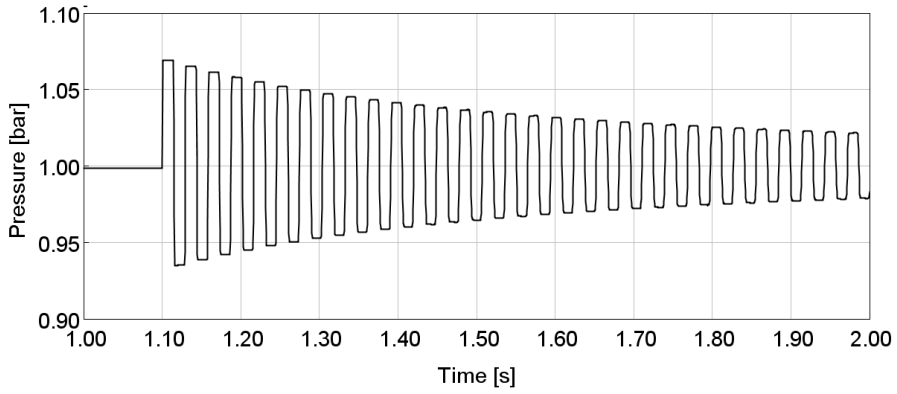


(a)

**Figure 51: GT Power simulation of dynamic flow bench, estimated air flow $\dot{m}_a$(t) (a) and pressure p(t) (b)**

The calculation of the transfer function is reported in the equation ( 3.36 ).

$$Z(j\omega) = \frac{FFT\ [p(t)]}{FFT[\dot{m}_a(t)]} = \frac{P(j\omega)}{\dot{m}_a(j\omega)} \qquad (3.36)$$

Z(jω) named transfer function is the ratio between the recorded pressure and the air mass flow in frequency domain. It gives an evaluation of the pressure response to an air mass flow excitation. The transfer function magnitude of the previous example is reported on the Figure 52.

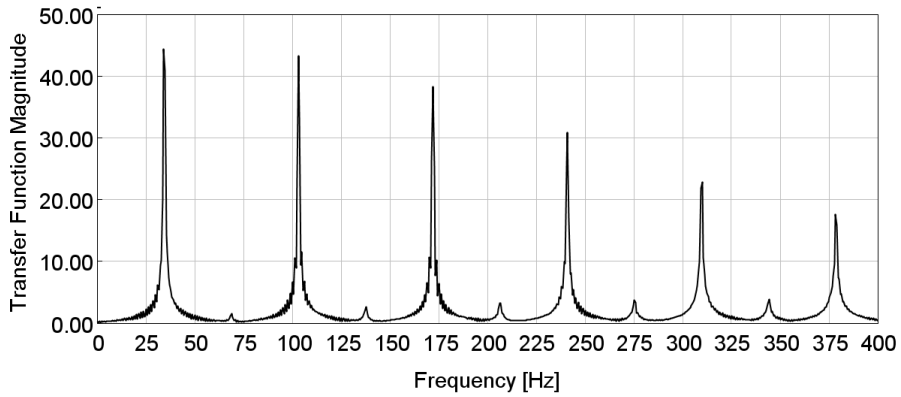


**Figure 52: Calculated transfer function**

This has been validated through various comparison between the measurement and simulation [116]. This methodology can be used as soon as a prototype is available for a quick checked of intake system simulation models.

## 3.2 Engine simulation tools

This PhD thesis aims to consider not only the intake system but the effect of the intake on the engine system. As an example the increase of pressure drop will be compensated by the turbocharger which will require higher pressure at the turbine and thus increase the back pressure at the exhaust valve. A tool allowing to take into account the complete engine is required at least to give the trend and gives a ranking of the different configuration which will be evaluated.
The commercial software GT Power has been used to simulate the complete system. First the methodology to model the intake and exhaust line is described. The second part presents the combustion model, using an add-on integrated in GT Power. The knocking evaluation is explained in the last part.

### 3.2.1 GT Power models

GT Power offers opportunities to generate a lot of variation either for intake or exhaust dimensions. There is different ways to fit the model to the measurement. The first one consists in tuning each component for the pressure drop, thermal conditions and the dynamic behavior. For instance, to adapt the pressure drop it is possible to introduce a local pressure drop at the connection between ducts (OrificeConn). Another way is to have them induced in the duct using losses coefficient (Forward and Revers Loss Coefficient), the pressure drop is then distributed over the length. The temperature can be easily defined using an imposed wall temperature so that the intake temperature fits the expected value.
During this PhD thesis, the geometry had to be changed drastically and the model should react accordingly. Following the previously described method, the model would not react properly. In order to cope this target and ensure the complete system to be well described, all parts are meshed using GEM 3D tool and all the bend and size are modelled as accurately as possible. Then the pressure drops are kept as “def” in GT Power meaning no additional pressure drop is integrated. Thus a duct addition or new bend will be reacting properly. To ensure a well described model, the intake system is mounted on the dynamic test bench.
The compressor and the turbine thermodynamic performances are defined through maps giving the rotation speed, the compression or expansion ratio and the air flow as well as the inertia and friction. Torregrosa *et al* [117] have developed a model of a compressor able to reflect its acoustic behavior. Some ducts are added at the inlet and outlet of the compressor and the turbine to reflect the actual internal geometry.

### 3.2.2 Combustion models - User cylinder tool

The combustion plays a key role as it converts the chemical potential in mechanical work. The literature discusses a lot the different possibility to evaluate it. The 3D simulation seems to provide the best accuracy but is not the easiest to set up neither the fastest. The

zero dimensional or quasi-dimensional combustion modeling requires less modeling effort and computational time. Kaprielian [118] has listed different models used to simulate the combustion. The Wiebe law can describe the combustion but all the parameters should be adapted for each operating conditions. This cannot fit the expectation of the proposed investigation. Then the main models are using entrainment model to describe the flame propagation and energy release process.

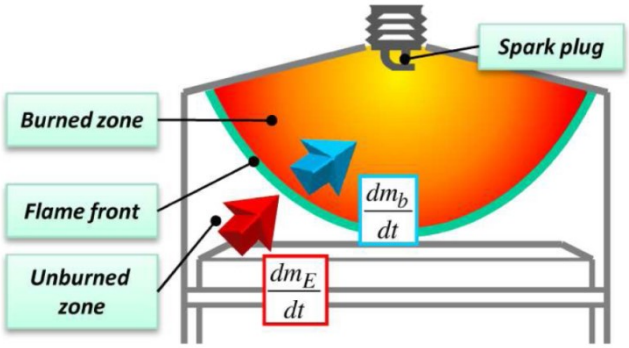


**Figure 53: 2 zones models description** [119]

The Figure 53 shows how the model splits the in-cylinder volume in 2 zones. The first zone contains the burnt gases and stays at high temperature. The second zone contains the unburned gases. Those two zones are separated by the moving flame where the combustion energy is released. The energy released from the combustion will depend of the mass of unburned gas going to the burned zone. Grill *et al* [120] have explicited the flame speed, equation ( 3.37 ) as a combination of laminar speed and turbulent speed.

$$u_E = u_{Turb} + u_L \qquad (3.37)$$

The turbulent velocity $u_{Turb}$ is directly related to the turbulence induced during the intake process. The laminar velocity $u_L$ can be related to the in-cylinder thermal condition as shown in equation ( 3.38 ).

$$u_L = u_{L,0}\left(\frac{T_{ub}}{T_0}\right)^{\alpha}\left(\frac{P_{cyl}}{P_0}\right)^{\beta}\left(1 - 2.06\ {x_{r,st}}^{\xi}\right) \qquad (3.38)$$

$\alpha$, $\beta$ and $u_{L,0}$ are given for each fuel. $x_{r,st}$ refers to residual gas fraction and is set to 0.97. The user manual [121] advices to set $\xi$ at 0.973. Grill *et al* [120] have given an estimation of $\alpha$, $\beta$ and $u_{L,0}$ which are fuel dependent and can be defined with the equation ( 3.39 ), ( 3.40 ) and ( 3.41 ) for gasoline.

$$\alpha = 2.18 - 0.8\left(\frac{1}{\lambda} - 1\right) \qquad (3.39)$$

$$\beta = -0.16 + 0.22\left(\frac{1}{\lambda} - 1\right) \qquad (3.40)$$

$$u_{L,0} = 0.305 - 0.549\left(\frac{1}{\lambda} - 1.21\right)^2 \qquad (3.41)$$

The equation ( 3.42 ) defines the turbulence speed as a function of the turbulence kinetic energy.

$$u_{Turb} = C_k \sqrt{\frac{2}{3} \cdot k_e} \qquad (3.42)$$

$C_u$ is the parameter to be set and $k_e$ the kinetic energy. The kinetic energy is defined at 20°CA upstream the TDCF with the equation ( 3.43 ).

$$k_{e,start} = C_k \left( \frac{c_m \, d^2}{n_{IV} \, d_{IV} \, h_{IV}} \right)^2 \qquad (3.43)$$

Its dissipation and variation over time is then estimated through an isotropic k-Ɛ model expressed in the equation ( 3.44 ).

$$\frac{dk_e}{dt} = \frac{2}{3} \frac{k_e}{V_{cyl}} \frac{dV_{cyl}}{dt} - \varepsilon_{Diss} \frac{k_e^{1.5}}{l_{sc}} + \left( \varepsilon_q \frac{k_{e,q}^{1.5}}{l_{sc}} \right) \qquad (3.44)$$

$l_{sc}$ the length scale is the sphere diameter equivalent to cylinder volume. $C_k$ has to be set in order to fit the best the experiment. The cylinder pressure trace can be used to find its right value. It is supposed to be in the range from 0.02 and 5, with preference for 0.35 when there is no more information. The dissipation coefficient $\varepsilon_{Diss} = 0.09$.
This is comparable to the parameters used in SI Turb model proposed by Gamma Technologies [122].

The cylinder geometry is partly taken into account through the flame front surface. The Figure 54 and Figure 55 demonstrate how it varies over the burned volume. The surface depends of the position of the flame front, starting as spherical it will hit the cylinders wall and change in shape and thus varies in surface. The shift of the spark have also a great influence on the flame front surface as it will change the way the flame front hits the wall.

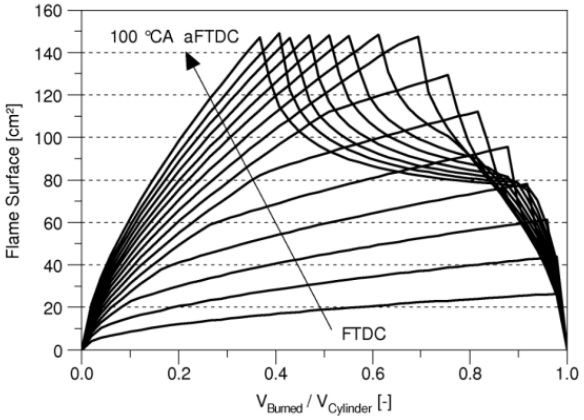


**Figure 54: Flame surface with centered spark vs the burned volume. Different piston positions are shown** [120]

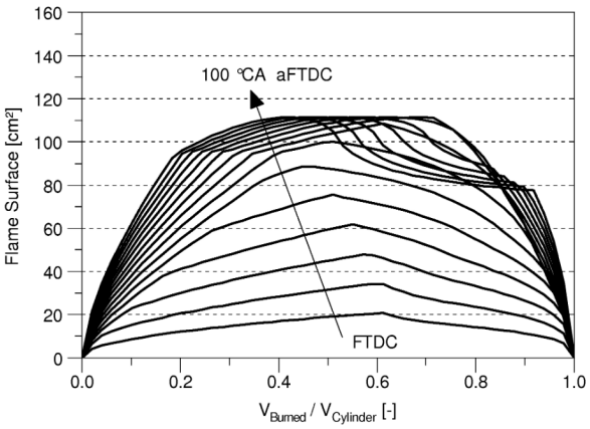


**Figure 55: Flame surface with non-centered spark plug (10mm) vs burned volume. Different pistons positions are shown** [120]

Knowing the surface and the velocity it is then possible to calculate with the equation ( 3.45 ) the air/fuel mixture mass flow brought into the flame [121].

$$\frac{dm_E}{dt} = \rho_{uv} \cdot A_{fl} \cdot u_E \qquad (3.45)$$

Then first law of thermodynamic gives energy balance in the relation ( 3.46 ) which links the heat rate to variation of the mass of the burned / unburned $m_{uv}$ zone.

$$\frac{dQ_B}{d\emptyset} \cdot \frac{1}{H_u} \frac{d\emptyset}{dt} = \frac{dm_f}{dt} \qquad (3.46)$$

The heat losses through the cylinder wall are evaluated through a Woschni model presented in the section 2.1.3. The actual geometry of the coolant circuit is taken into account into the GT Power wall solver.

This model is efficient to evaluate the heat release in fast manner. Nevertheless this is a 0D model so there is no possibility to take into account any local heat source or hotspot. The model is nevertheless able to evaluate the burnt and the unburnt zone temperature. The unburnt zone temperature and pressure are used to evaluate the knock risk.

### 3.2.3 Knock modeling

The knocking occurs when part of the unburnt zone ignites before the main flame front reaches this area. The knock modeling aims to evaluate when the unburnt zone reaches the conditions of the auto ignition. The fuel influences the self-ignition. As an example Hann *et al* [123] have described the influence with added hydrogen in methane which greatly speed up the ignition at low temperature. The EGR can also be used to mitigate the knocking, Fandakov *et al* [124] have presented, in the Figure 56, the ignition delay ($\tau_i$) in function of the inverse temperature for different pressure, air fuel mixture ratio (lambda).

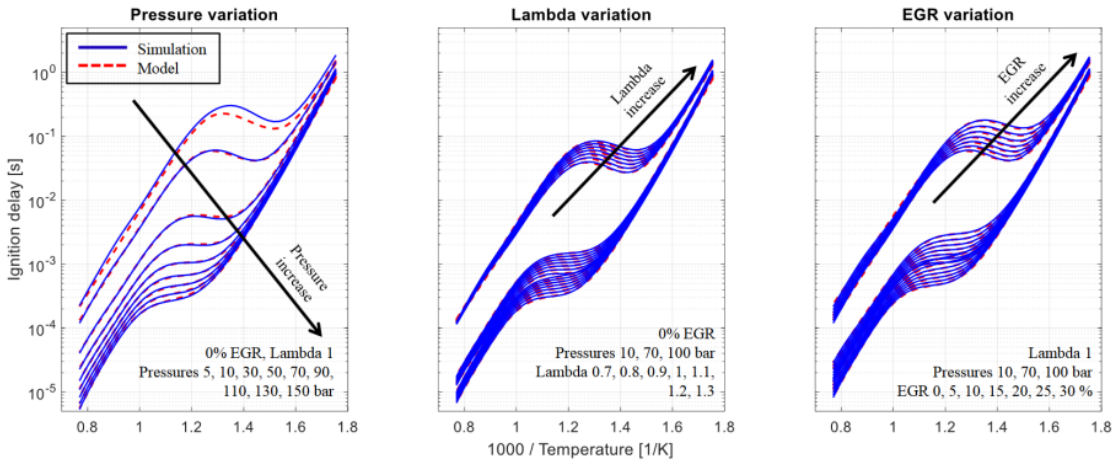


**Figure 56: High-temperature ignition delay times at various boundary conditions**

Such curves show the time needed to ignite in steady state conditions. It is the possible to show how parameters affect the knock tendency, thus the pressure rise tends to decrease the ignition delay, so increase the knock tendency. Lambda and EGR rate go in an opposite way and tend to improve the knock resistance. This is the reason why they can be used for knock mitigation.
The ignitin delay can be modeled through the Arrhenius equation ( 3.47 ) expressed by Fandakov *et al* [124].

$$\tau_i = C_\tau \, p^{C_{\tau 1}} e^{C_{\tau 2}/T_{ub}} \qquad (3.47)$$

The equation ( 3.48 ) defines the knock integral as the invert of ignition delay integral.

$$I_k = \int_{t=0}^{t=t_k} \frac{1}{\tau_i} dt \qquad (3.48)$$

The integral has to be evaluated in the unburnt zone during the moving in-cylinder condition during the combustion. If the ignition delay is then lower than the complete combustion this value exceed 1 and the ignition is supposed to happen. This limit value can be set differently to cope with measurements.
This modeling has been has been developed for small volume, this has been extended for the complete cylinder volume because the changes applied during this thesis do not change the position of the hot spots nor their intensity. The $I_k$ target is set accordingly.

### 3.2.4 Conclusion

The pressure wave modeling has been considered in different ways allowing to understand unsteady phenomena and layout air intake systems. The benefit will be evaluated through GT Power model sets in order to react to intake geometry changes. The combustion model is able to take into account the variation in the intake, such as temperature, pressure or air flow. The knocking model will allow to evaluate the knock risk or to control the spark timing to maintain a constant knock risk.
It has been first apply to increase the low engine speed torque, so called the low end, torque and response time of a three cylinder turbocharged engine.

# 4 Low End Torque Enhancement thanks to Double Resonance System

There has been a strong trend during the last decade to use smaller displacement engine on heavier cars. The so called downsizing is shown to give potential fuel saving through higher load operating conditions, lower weight and reduced pumping losses [125]. This increase in specific power and torque has been possible through an intensive use of efficient boosting systems.

The last generation of high performance engines, with high BMEP, largely uses turbocharger to increase the specific power and reduce fuel consumption. These turbochargers cannot give the maximum benefit at low engine speed when the exhaust gas enthalpy is not high enough and because of the surge limit [126]. With the last evolution of turbocharger and engine strategies the torque edge has been moved toward low engine speed allowing for downspeeding and thus fuel saving [127]. Nevertheless there is still an engine speed range where the torque is lower and an opportunity exists for improvement. This would allow a faster acceleration of the vehicle, mainly for heavy vehicles or vehicles with trailers running uphill in high slope. The trade-off between the output power and the low end torque is illustrated in the Figure 57, where the trend shows an increase of both. The borderline TC engines show the possibility to have high specific low end torque or high specific power but the necessary compromise to maintain both of them at high level.

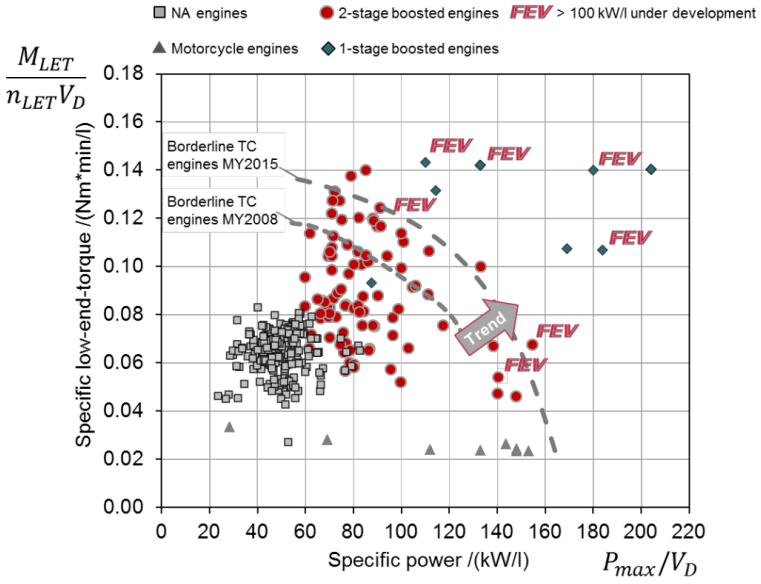


**Figure 57: Trade-off between output power and low end torque** [128]

The resonance charging could be a way for further improvement. Electric boosting system aims to address the same target with higher output potential but the cost and the adaptation effort is also higher.

The internal combustion engines valves opening and closing generate pressure waves which are propagated into the inlet and exhaust manifolds [129] [107]. As a consequence, the engine performance and the volumetric efficiency can be affected by this phenomenon [130]. The air intake design of a naturally aspirated engine results from a tradeoff between the pressure losses and the acoustic resonance at the intake [131] [132] [133]. Manufacturers have proposed active intake parts, such as variable intake manifolds or resonant volumes and plenums in order to use pressure waves.

The proposed concept aims to increase the torque at very low engine speed using pressure waves from the air intake system. Some solutions have been already presented, Taylor *et al* [134] have demonstrated a good potential. Nevertheless the increase in air intake manifold runner length up to 1100mm is difficult to place in a real engine compartment.

The proposed concept consists of a side volume and an additional duct between the charge air cooler and the air intake manifold. The induced enhancement of the pressure wave amplitude at the air inlet runners provides a higher volumetric efficiency at low engine speed. The wave action should provide higher air density at the intake valve closing and thus increases the mass flow and thus the torque in steady and transient conditions.

The concept is first described. Then a GT Power model has first been set to evaluate the potential of the solution. Then a frequency analysis gives more explanation on the actual behavior of the device. The validation has been carried out through engine test bench evaluation in steady state and transient conditions.

## 4.1 The concept description

The concept consists of a side branch including a volume at the end which will give a location for wave reflection. The system can be tuned by varying the length and the diameter from the Charge Air Cooler (CAC) to the Air Intake Manifold (AIM). A schematic drawing of the base line Air Intake System (AIS) is presented in Figure 58. In this configuration, a duct directly connects the CAC to the AIM. A pressure sensor $P_2$ is placed in the AIM to evaluate the boost pressure and the pressure wave amplitude. A pressure sensor mounted on the spark plug gives the in-cylinder pressure. This signal allows to evaluate the MFB50 and the possible knock which may occur during testing.

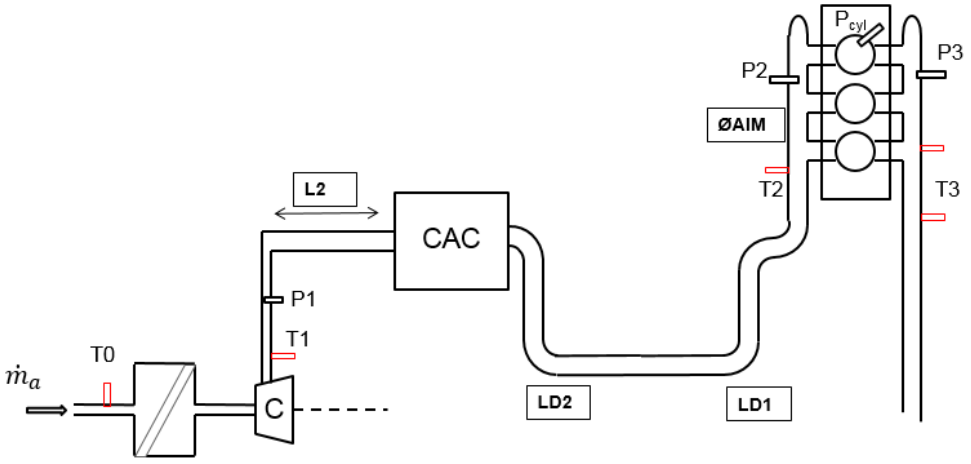


**Figure 58: Schematic drawing of the air intake system (AIS) on the base line**

The Figure 59 shows the concept equipped with an added volume. The Figure 60 shows the cylindrical shape with a length of 440mm and a diameter ØVolume. The connected duct has a diameter ØV and length LV. The position of the connection is defined by upstream length LD2 and downstream LD1.

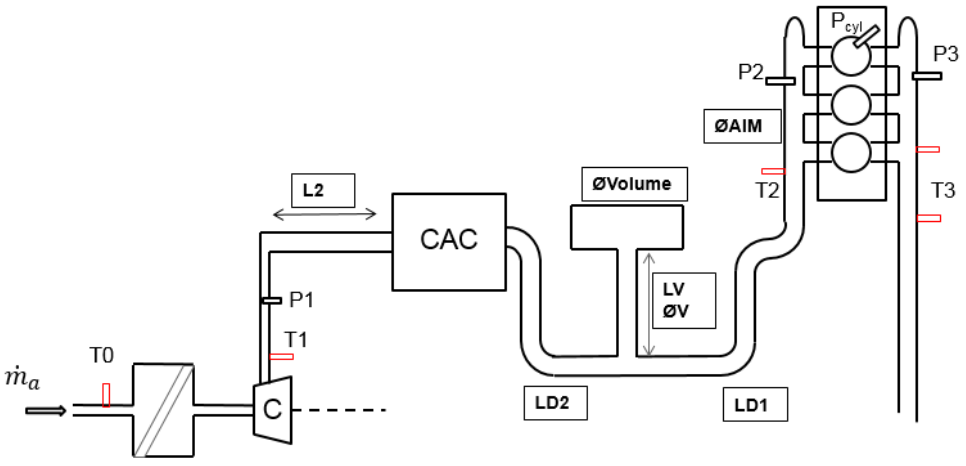


**Figure 59: Schematic drawing of the air intake system (AIS) with double resonance system**

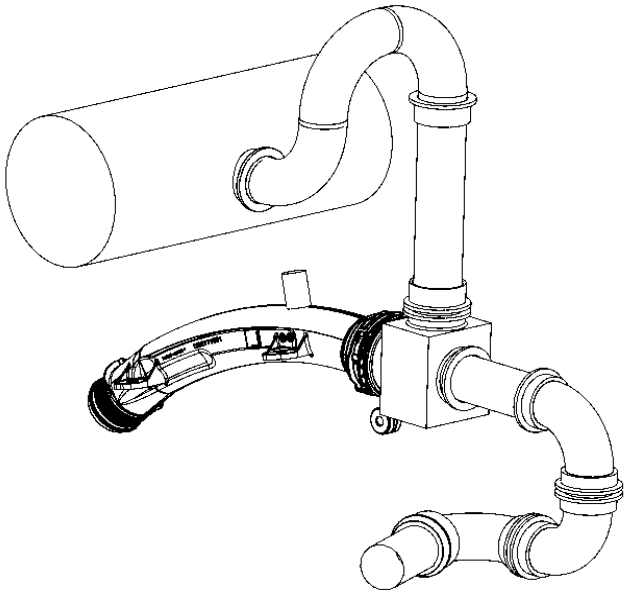

**Figure 60: Drawing of the prototype**

The aim of the present study consists to evaluate if this concept allows increasing the volumetric efficiency and how this benefit can result in higher output torque.

## 4.2 1D simulation to evaluate the potential

The simulation tool gives the chance to layout the concept and evaluates the effect on the complete system including the turbocharger. The results are not used to provide an absolute value but a comparison with the base line.

### 4.2.1 3 cylinder engine model set up

The evaluation is done on an gasoline turbocharged 3 cylinder engine [135] [136]. Its main characteristics are reported in Table 6. This engine will be also used for engine test bench validation.

**Table 6: Engine characteristics** [135]

| | |
|---|---|
| Compression Ratio | 10.5 |
| Number of Cylinder | 3 |
| Displacement | 1199 $cm^3$ |
| Bore | 75mm |
| Stroke | 90.5 mm |
| Intake valves | 2 / cylinder |
| Exhaust valves | 2 / cylinder |
| Valve timing | Variable |
| Conrod Length | 143mm |
| Crankshaft / Liner offset | 7.5mm |
| Specific Power | 80 kW/l |
| Specific torque | 191 N.m/l |

Using the engine characteristic and the full load curve represented on Figure 61, a simulation model has been set up.

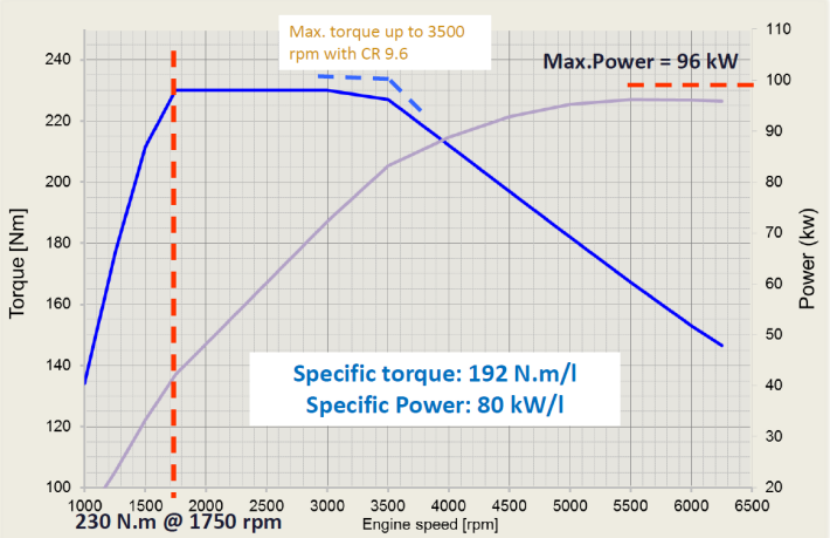


**Figure 61: Full load curve** [135]

The Figure 62 shows the full load curve coming from the model and the first measurement carried out on the engine. The tests set up will be presented in the paragraph 4.4. The torque is slightly lower than on the Figure 61 but the trend is very similar.

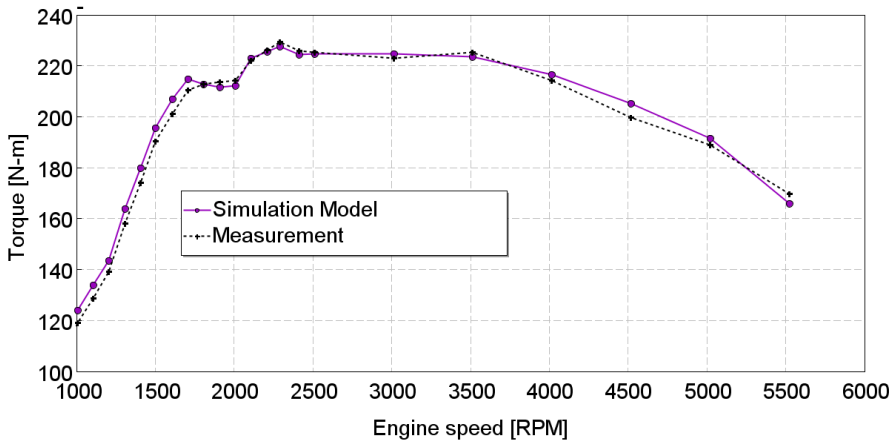


**Figure 62: Full Load curve**

The intake air mass flow and the turbocharger speed have been also checked, the Figure 63 and Figure 64 show the good agreement between the simulation and the measurements.

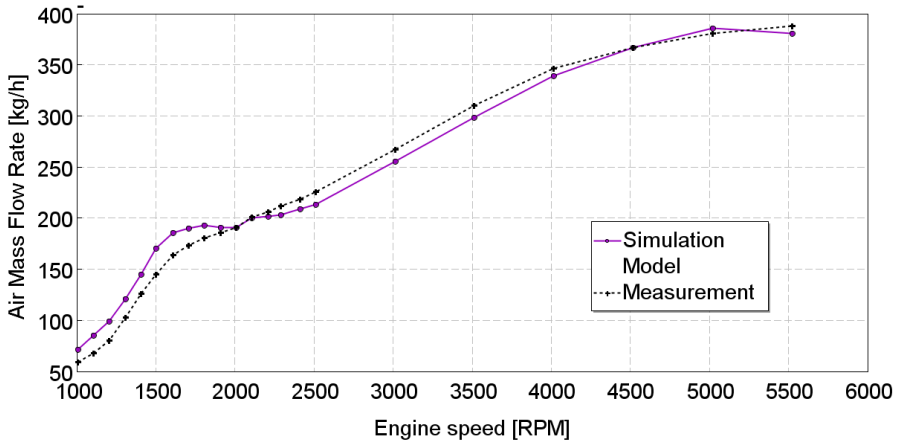


**Figure 63: Air mass flow**

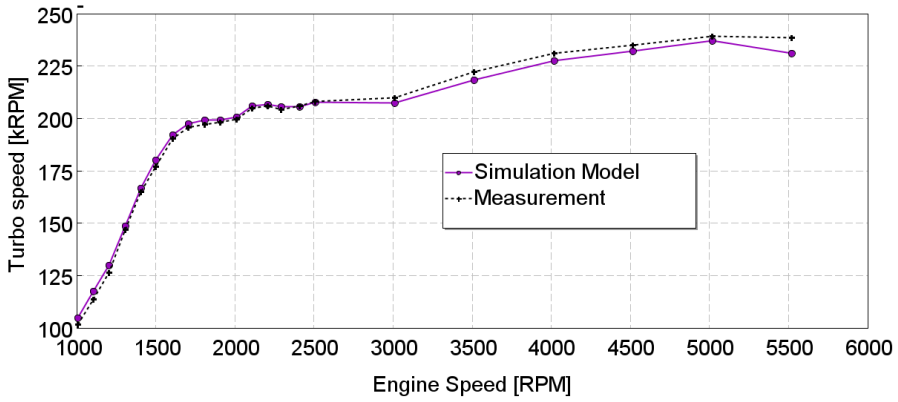


**Figure 64: Turbocharger speed**

The valve timing and the geometry modeling quality can be checked with the pressure comparison at the intake and exhaust valve. The Figure 65 and Figure 66 represent the

pressure signal at the intake and exhaust valve and show good agreement between the model and the simulation.

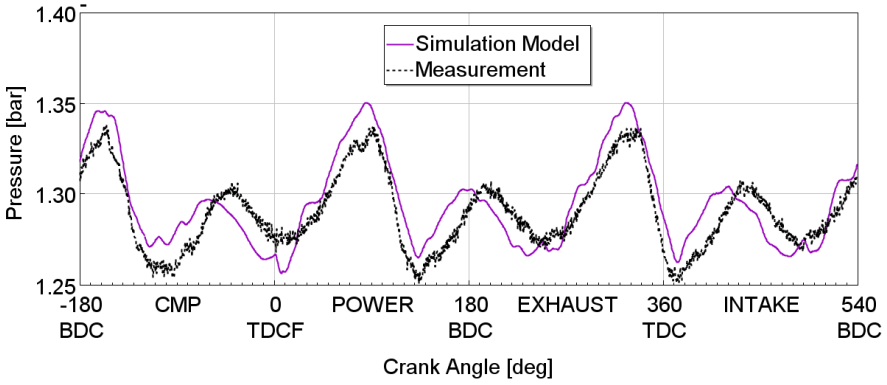


**Figure 65: Intake valve pressure at 1000RPM**

At the same engine speed, the Figure 66 present no difference between the measured exhaust valve pressure and the simulation results.

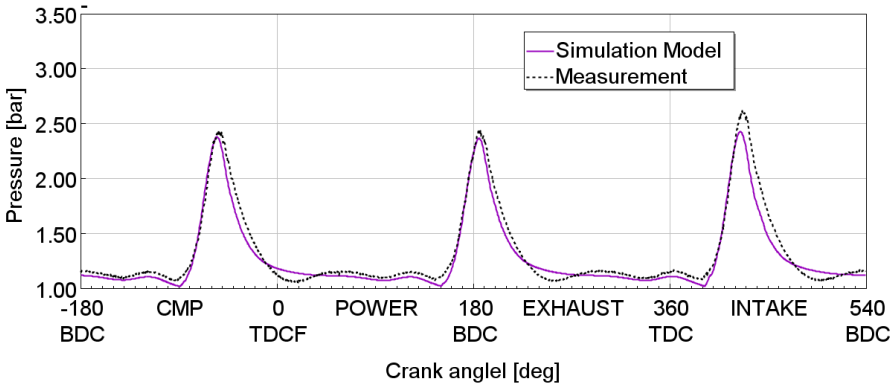


**Figure 66: Exhaust valve pressure at 1000 RPM**

The turbulence value used to calculate the flame propagation speed is set to reach the full load curve and to be consistent with the in-cylinder pressure measurements available as depicted on Figure 67.

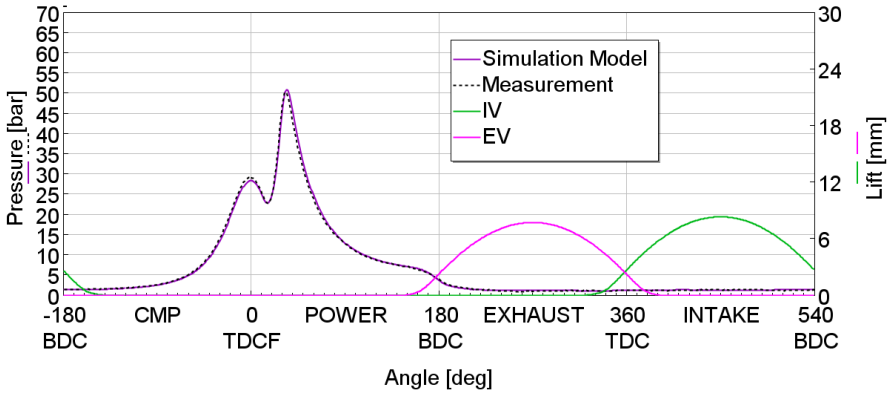


**Figure 67: Cylinder 1 pressure at 1000RPM.**

Heat losses, friction, turbine and compressor maps have been assumed from previous models. Those uncertainties can affect the absolute output torque and power but should not change the trend on the output torque benefits from the proposed architecture.
The model is used only for full load evaluation and in comparison between the different configurations.

### 4.2.2 Parametric analysis

The different components of the geometry downstream the Charge air cooler are tested to assess their influence on the resulting output torque. This preliminary study aimed to evaluate a torque increase potential. A more detailed frequency analysis is carried out later and the validation on engine test bench has been handled to evaluate the actual benefit.
The effect of the added volume is evaluated with a diameter going from 60mm to 160 (ØVolume) and length of 440mm. The connection length between the volume and the intake manifold varies from 2000 to 4000mm (LV + LD1). The length between the volume and the T junction (LV) is 60% and the length between the T junction and the air intake manifold (LD1) is 40%. This ratio have been demonstrated as best from primarly simulation and will be confirmed later. The diameter of the ducts going to the volume varies (ØV) from 25 mm to 35mm. The MFB50 is set constant at 15.9°CA like the base line version. The turbocharger has to provide the highest boost pressure possible and thus the WG is kept closed. The air fuel ratio is maintained stoichiometric. The first evaluation is carried out for 1000RPM because the torque is the lowest and because lower engine speed involves lower frequency and thus bigger resonators and thus defined the maximum packaging volume required.
The Figure 68 shows the torque variation resulting from the different geometry changed with a full factorial Design Of Experiment (DOE).

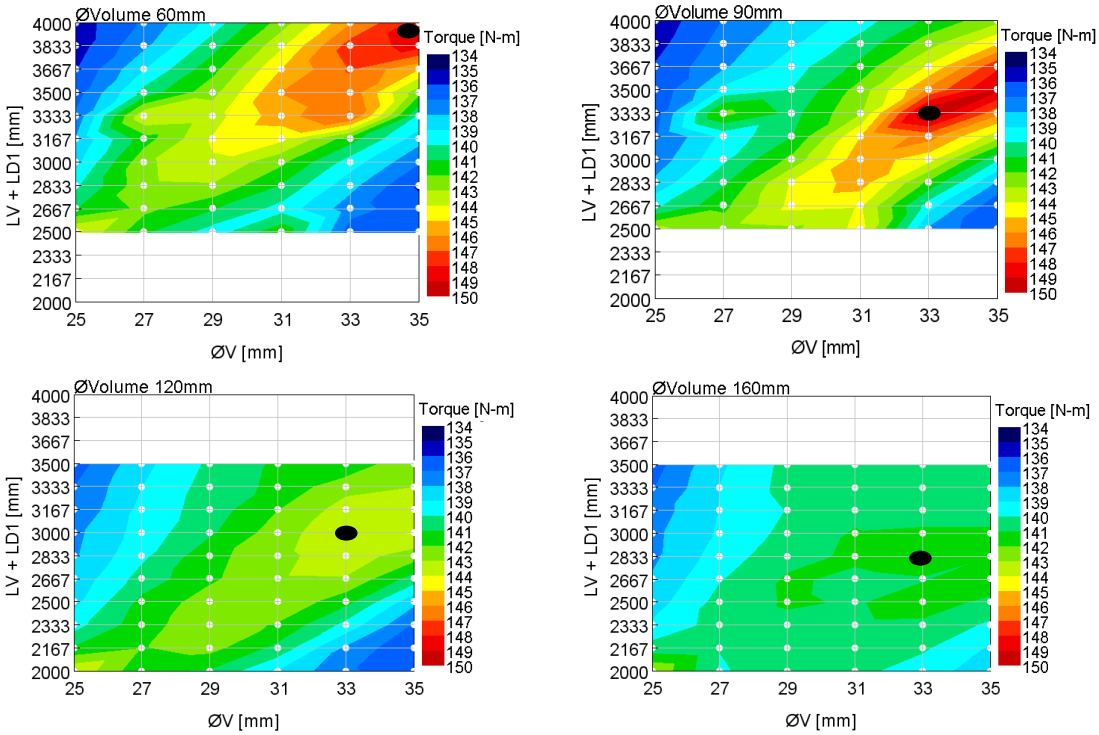


**Figure 68: Torque output for different volume diameters and connection ducts length and diameter at 1000RPM**

With a smaller volume the optimum duct length and diameter is bigger. For instance, with the volume diameter of 120mm, the optimal duct is about 33mm diameter and 3000mm length while with the volume diameter of 60mm the optimal seems to be with a 35mm diameter and length at 4000mm. The base line configuration provides an output torque of 130N.m. The best configuration provides 18N.m increase.
The intake absolute pressure (P2) where the output torque has been maximum for each DRS volume size, depicted in Figure 68, has been drawn in Figure 69 with dimension reported in the Table 7.

**Table 7 : Optimum point for each volume diameter**

| Ø Volume | LV + LD1 | Ø V |
|---|---|---|
| 60 mm | 4000 mm | 35 mm |
| 90 mm | 3333 mm | 33 mm |
| 120 mm | 3000 mm | 33 mm |
| 160 mm | 2833 mm | 33 mm |

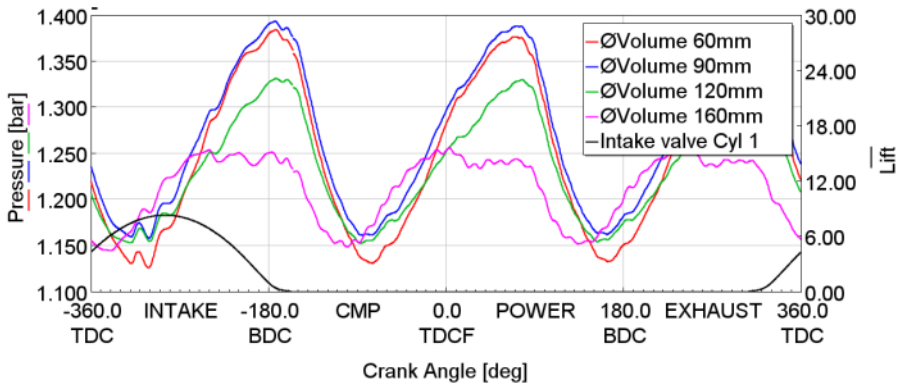


**Figure 69: Static absolute pressure upstream the intake valve for maximum output torque point from DOE**

For all these optimum points, the AIM plenum pressure presents high pressure wave amplitude with almost a sinus shape. As expected when the maximum of the pressure wave is well synchronized with the intake valve closing, the air trapped in the cylinder increases in density.

The interaction with the upstream line has been evaluated through a DOE. The different length LD1, LD2 and LV have been tested. The reference corresponds to the Ø Volume = 90mm.

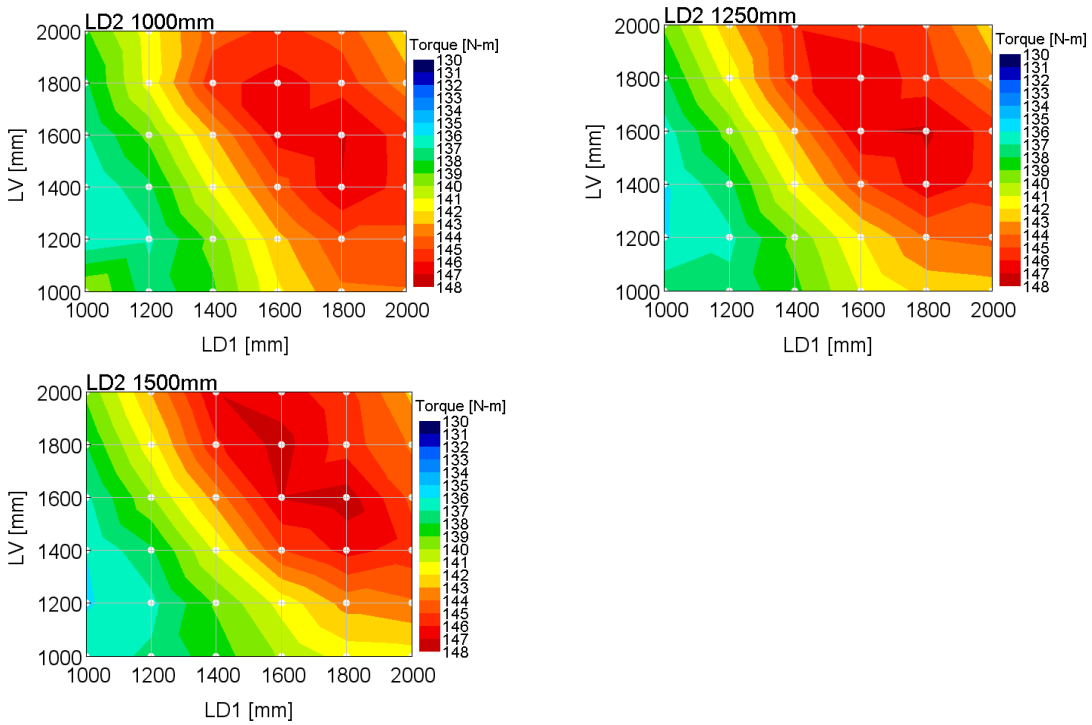


**Figure 70 : Torque response for different length set up**

The Figure 70 shows the colormap resulting from the length variation on the output torque. The three figures show almost the same scheme with a maximum for LD1 about 1800mm and LV at 1600mm. The length LD2 which has been tested from 1000mm to 1500mm does not influence much the tuning. The length upstream the volume side branch does not affect the tuning. The position of the CAC can be modified and so the adaptation on different vehicle can be handled easily.

This first study shows clearly the potential of the added volume to increase the pressure wave amplitude and so the output torque.
The pressure wave main frequency is related to the engine order. The pressure signal presents 3 peaks in the 720°CA. As the number of cylinder is 3 in this example the frequency is related to 1.5 Engine Order (E.O) with the frequency calculated through the equation ( 4.1 ).

$$f = \frac{N}{60} * Ncylinder/2 \qquad (4.1)$$

The frequency is 25Hz for the E.O 1.5 at 1000RPM.

The main frequency created at the intake system is mainly composed of the frequency described by the equation ( 4.1 ). It reflects the frequency of intake valve events. Higher order frequencies are also produced. An evaluation of a volume which would benefit the double wave frequency has been tested and is so called E.O 3. The added volume behaves as a resonator with a volume depending on the Eigen mode frequency. With higher frequency the volume required is smaller and the length shorter.

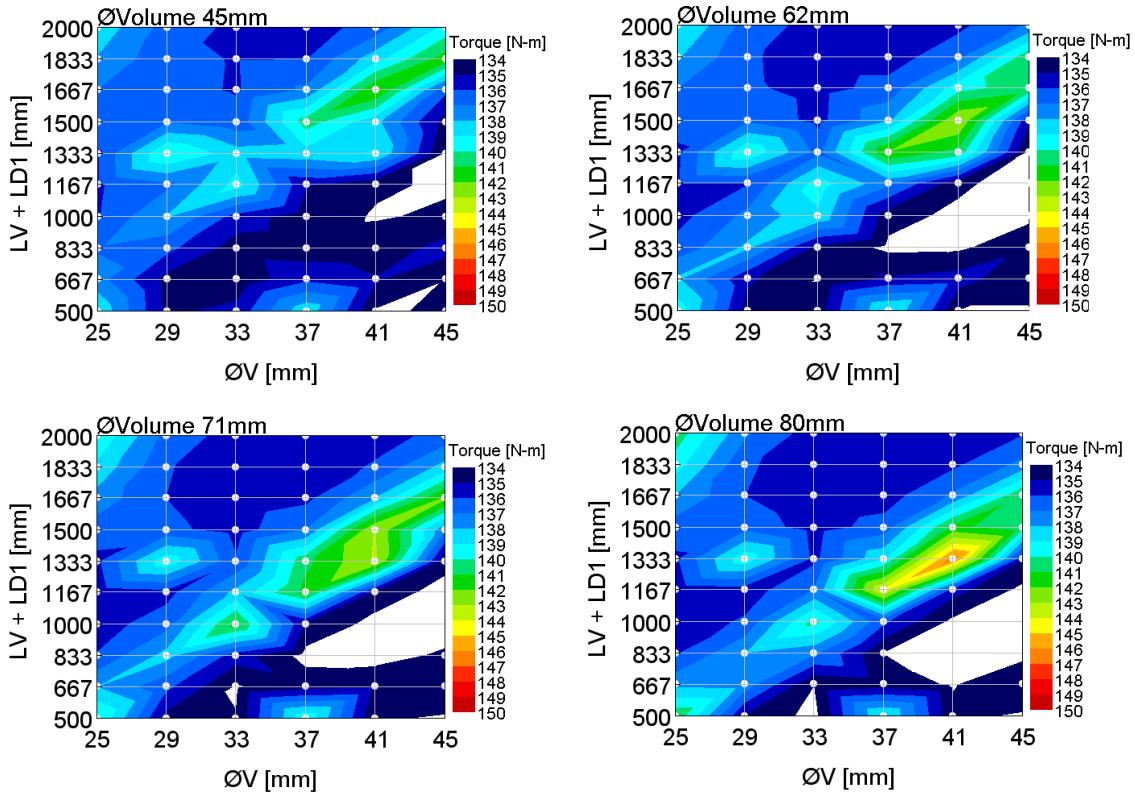


**Figure 71: Torque output for different volume diameters and connection ducts length and diameters**

The Figure 71 depicts the colormap of the output torque for a variation of the ØV and the length between the AIM and the added volume. Four different volumes size have been tested. Each diagram reveals some areas where the output torque can be increased thanks to the added volume. As previously observed, the length can be shorter when the added volume is bigger. Overall the volume required is much smaller and the length shorter but the areas with torque increase are smaller. This is giving a hint that the tuning

has to be finer and the engine speed range where the system can provide benefit will be reduced.
The intake pressure where the output torque has been maximum for each added volume size depicted in Figure 71 has been drawn in Figure 72. The different optimum point are reported in the Table 8.

**Table 8 : Optimum point for each volume diameter**

| ØVolume | LV + LD1 | ØV |
|---|---|---|
| Ø 45 mm | 1667 mm | Ø41 mm |
| Ø 62 mm | 1500 mm | Ø41 mm |
| Ø 71 mm | 1333 mm | Ø41 mm |
| Ø 80 mm | 1333 mm | Ø41 mm |

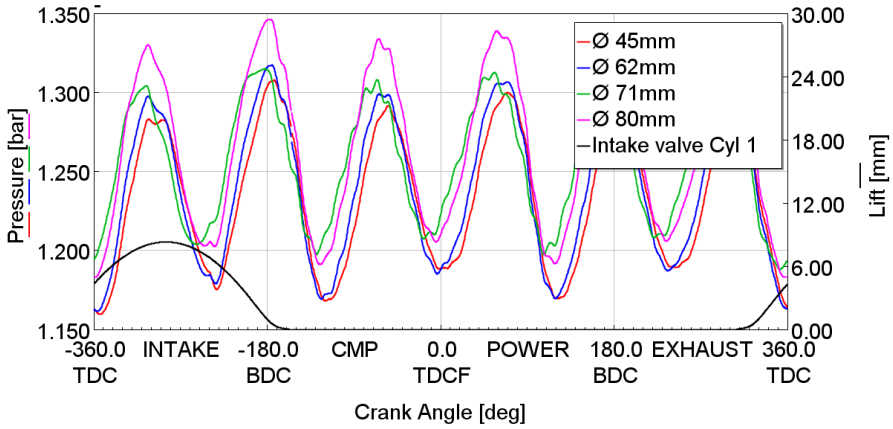


**Figure 72: Static absolute pressure upstream the intake valve for maximum output torque point from DOE**

With the right set of geometries, the intake absolute pressure shows twice the number of peaks presented at the Figure 69. In that case, the frequency is directly 3 times the frequency of the engine crank shaft, and twice the frequency calculated with the equation ( 4.1 ). This frequency is then named E.O 3. When the pressure at the intake valve closing is higher, the volumetric efficiency is enhanced.

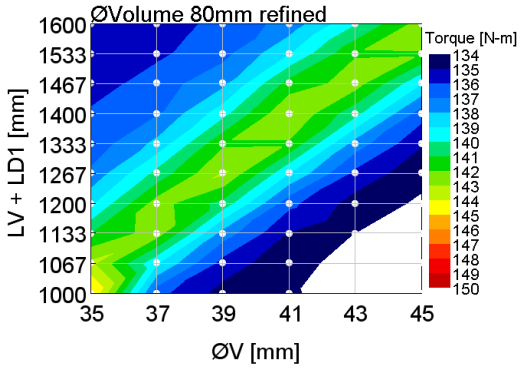


**Figure 73: Refined DOE around the best output torque of the previous model**

The Figure 73 shows a DOE focused on the area where the torque has been shown to provide the highest output torque. It's resulting in an almost straight line where the output

torque is enhanced. This is going from a point with Ø35mm and length of 1000mm to Ø45 mm with 1600mm.

The Figure 74 shows the influence on wider range of engine speed with the 2 first layout for E.O 1.5 and E.O 3. The configuration called E.O 1.5 - LO1 is composed of a duct LD1 with a length 1600mm and LV 1800mm with Ø33.3mm for both. The cylindrical volume 430mm long and Ø90mm is about 2.3l. The configuration named E.O 3 - LO1 is made of cylindrical volume 430mm long and a Ø80mm which is about 1.7l. In this configuration the LD1 is made of tube Ø41mm and a length of 650mm and LV Ø41mm and a length of 750mm.

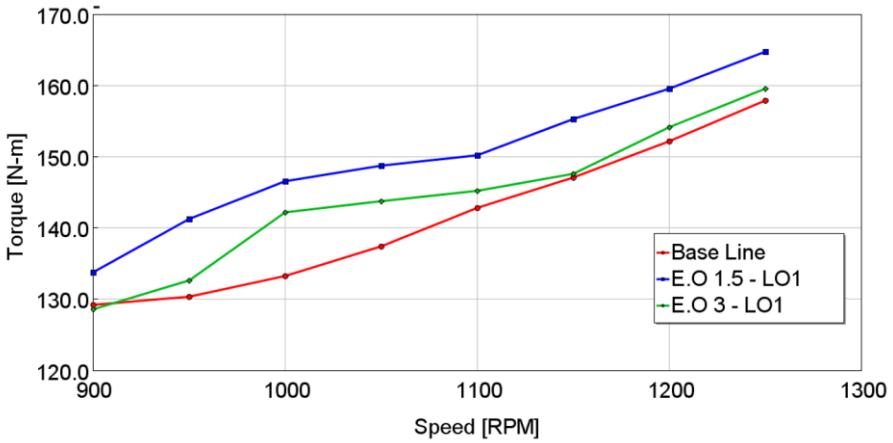


**Figure 74: Full load torque curves with mass production configuration and a set up enhancing EO 1.5 and the other EO 3.**

The Full Load torque shows the increase of engine speed range where the E.O 1.5 - LO1 configuration is beneficial from 900 to 1250RPM. The E.O 3 configuration increases the torque only around 1000RPM, mainly between 950 and 1050RPM.

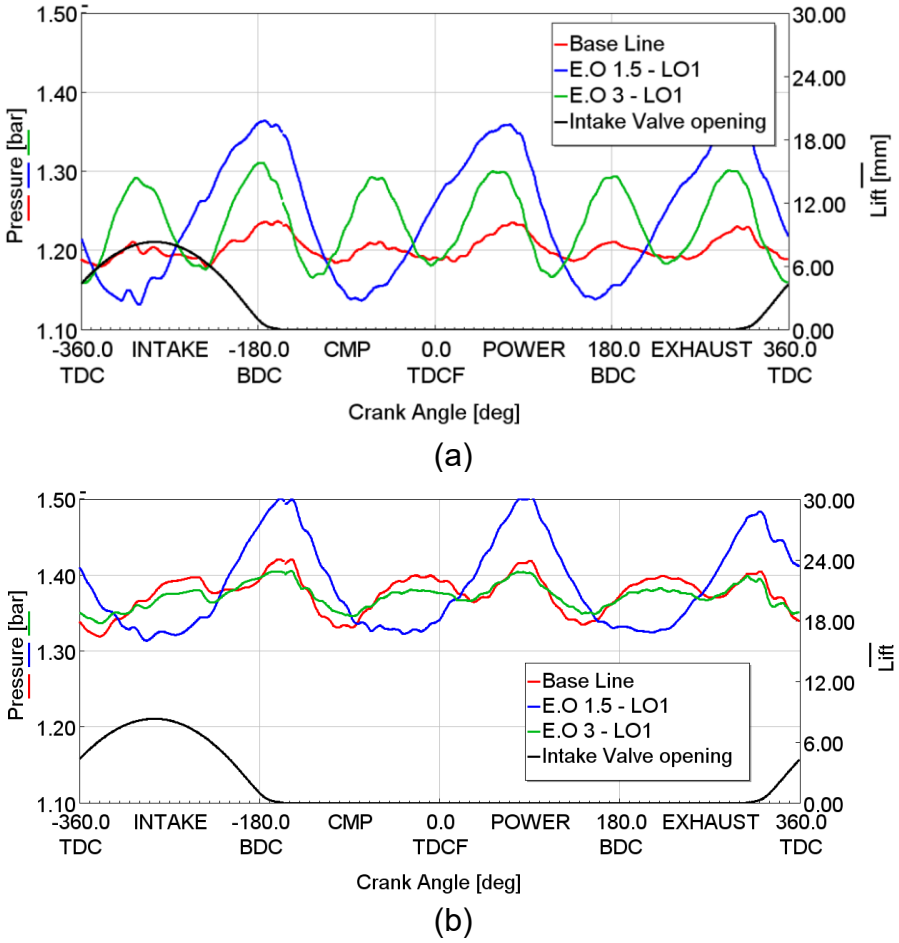


**Figure 75: Pressure upstream the intake valve at 1000RPM (a) and 1250RPM (b)**

The Figure 75 illustrates the relationship between the pressure wave amplitude and the increase of torque observed on Figure 74. The increase of the pressure at the intake valve closing increase the trapped air mass in the cylinder and so give the chance to increase the output torque.

The simulation has demonstrated the potential benefit of acoustic charging for low end torque. Two 440mm long cylindrical volume have been then produced to cover the E.O 1.5 and E.O 3, they have respectively ØVolume 80 mm and 120 mm. The small one corresponds to the setup which demonstrated the highest potential for E.O 3 and the biggest gives the chance to reduce the duct length while maintaining the high output torque for E.O 1.5. The diameter of connecting ducts has been chosen between 33mm and 41mm at 35mm. The length is flexible and can be adjusted during the testing. A fine tuning is carried out with the dynamic flow bench presented at the section 3.1.3.

## 4.3 Frequency analysis

The frequency analysis gives the chance for a fine tuning of the prototype. The frequency analysis is low time consuming. The simulation take only into account the intake line. The test presented in the section 3.1.3 provides results within few minutes.

The first measurement consists in testing the configuration able to reach high amplitude at the E.O 1.5 and so reach peak at 25Hz. Firstly the two volumes diameter 80mm and

120mm are tested, with a length LD1=1380mm and LV=2030mm as depicted on the Figure 76.

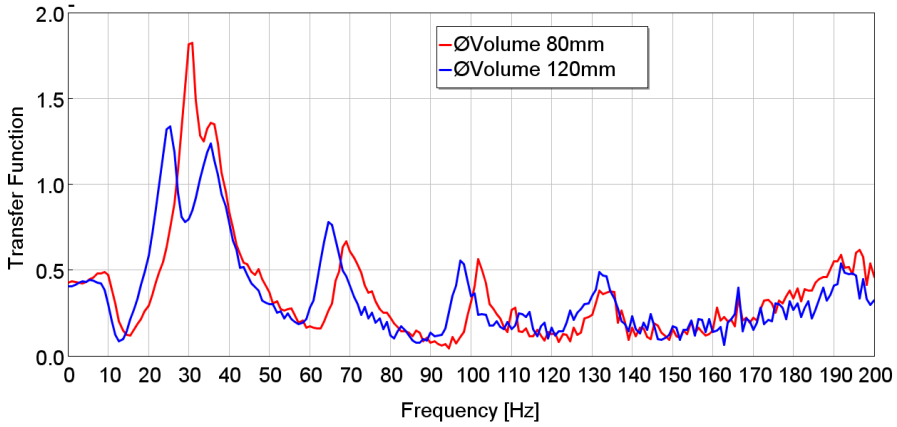


**Figure 76: Transfer function for E.O 1.5 for different volume diameter**

This test reveals that even with long route of a total of 3410mm between the AIM and the added volume the diameter has to be 120mm to reach a maximum at 25Hz. This volume is chosen for this E.O 1.5 configuration.

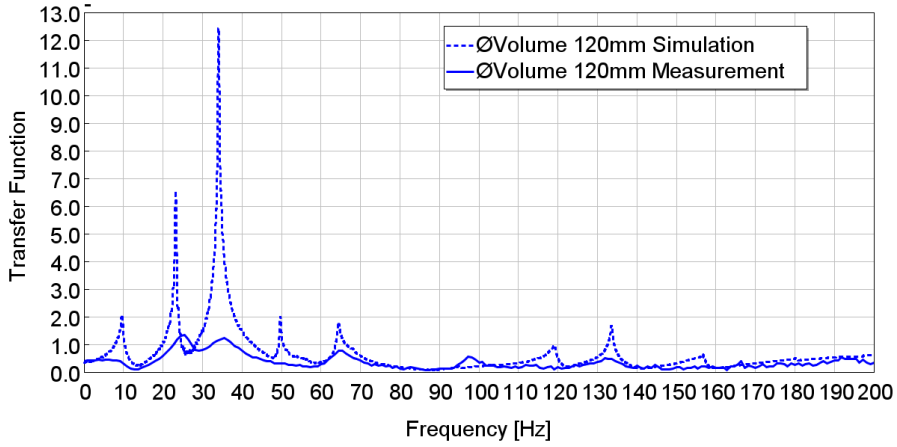


(a)

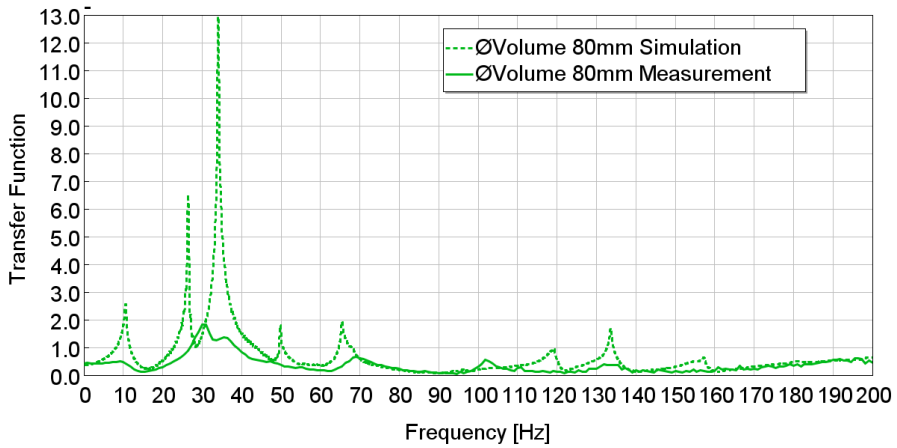


(b)

**Figure 77: Comparison between testing and simulation**

The Figure 77 shows the comparison between the simulation and measurement. The simulation shows resonance at lower frequency than obtained with measurement. This explained the bigger volume will be used to reach the resonance at 25Hz. The model can fit the simulation if the length is shortened. The Figure 78 shows the good frequential agreement when the length in the simulation are reduced for LD1 from 1380mm to 1300mm and for LV from 2030mm to 1850mm. This would be done in case of further analysis required.

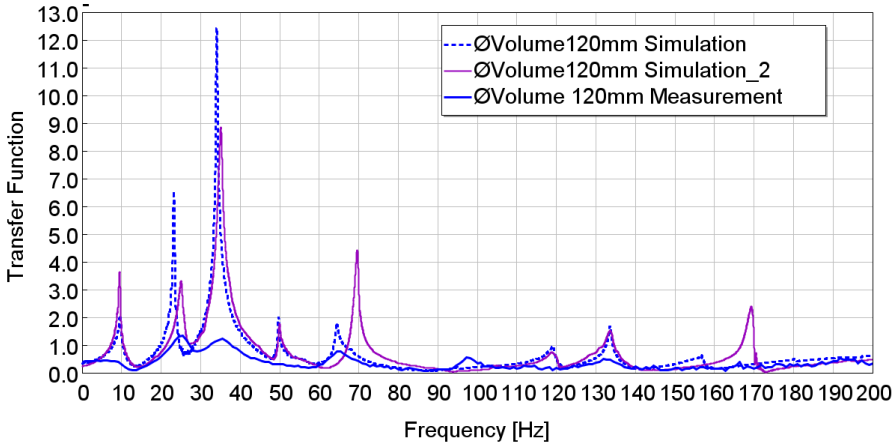


**Figure 78: Tuning of model to fit the measurement**

The testing has also shown that ratio of the length between LD1 and LV can be modified. The Figure 79 shows that the higher transfer function can be obtained with the LD1=1980mm and LV=1430mm and the volume ØVolume=120mm. The amplitude of the transfer function is much lower on measurement than simulation. The viscosity seems to be not well modeled. The increase of this viscosity would increase the pressure drop which is not expected.

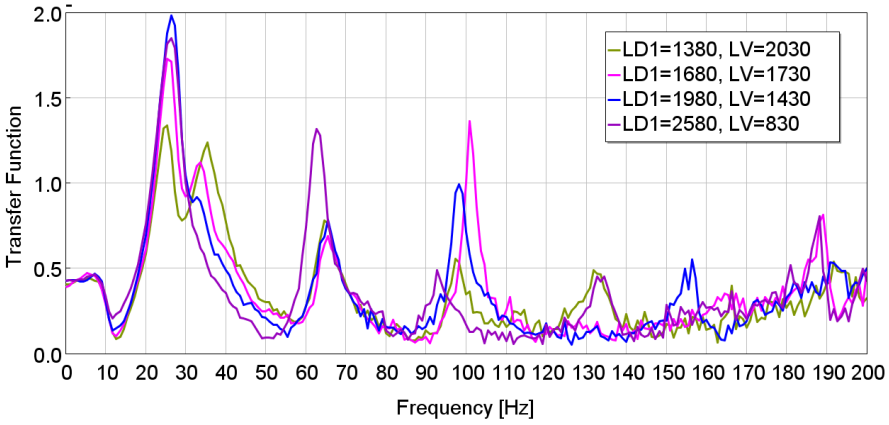


**Figure 79: Variation of the length ratio between LD1 and LV for E.O 1.5**

In the same time the configuration for E.O 3 has been tuned, the Figure 80 shows that the ratio between the LD1 and LV is less sensitive mainly the total length has to be at 1500mm.

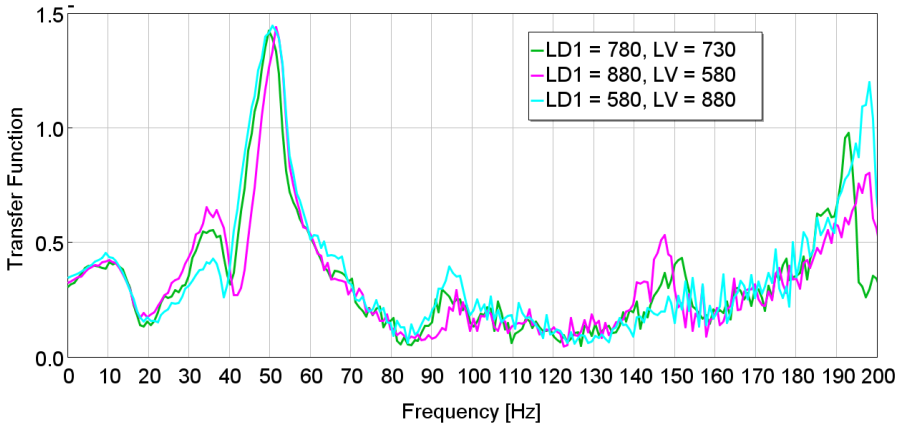


**Figure 80: Variation of the length ratio between LD1 and LV for E.O 3**

The selected configuration are reported and compared to the Base Line on the Figure 81. The version E.O 1.5 is made of an ØVolume=120mm, LD1=1980mm and LV=1430mm and the version E.O 3 is made ØVolume=80mm, LD1=880mm and LV=580mm.

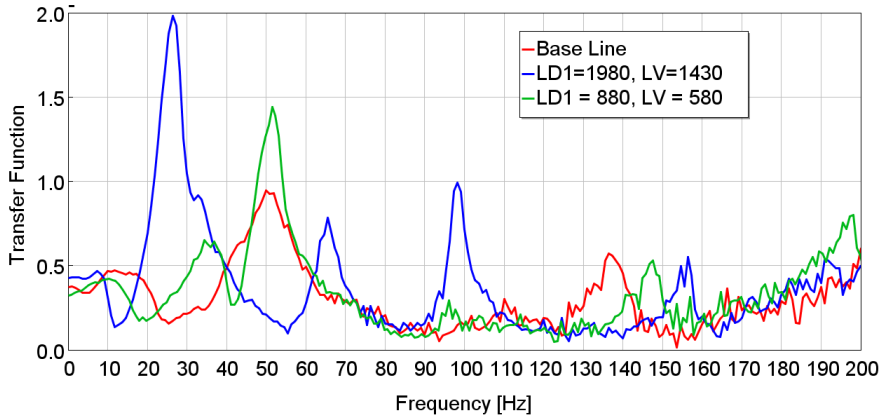


**Figure 81: Selected configurations transfer function**

The dynamic flow bench made possible the fine tuning of the prototypes. The discrepancies between simulation and measurement have been observed. Nevertheless three configurations have been selected to be tested on engine test bench.

## 4.4 Validation on engine test bench

### 4.4.1 Engine test bench set up

The engine has been coupled to a transient dynamometer test bench (as depicted in Figure 82). The gearbox has been removed and replaced with a direct drive to the dynamometer. Pressure and temperature are measured all along the inlet and exhaust air paths of the engine (as depicted on the Figure 58 and Figure 59). Rotational engine speed, torque, fuel consumption, and turbocharger speed are also recorded. To calculate the air fuel ratio, a lambda sensor is used. The in-cylinder pressure is measured with a Kistler spark plug equipped with a pressure sensor type 6115BFD35Q05. The signal is then used in order to calculate the engine heat release and the MFB50. The instantaneous pressures

are measured with Kistler pressure sensors 4049B05DS1-2 with a measurement range from 0 to 5 bar absolute. The torque is obtained with a T40B torque flange.

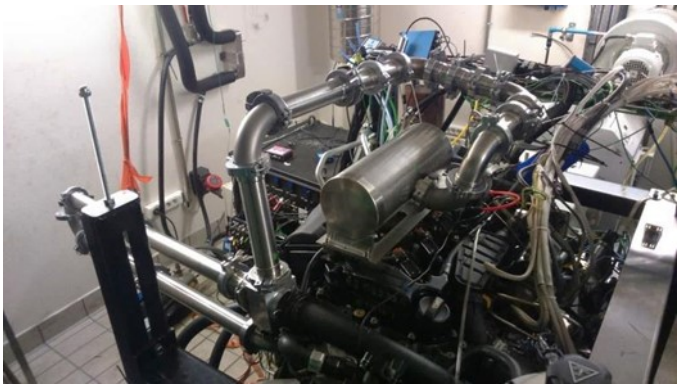

**Figure 82: Test set up on engine**

The temperature is checked in the whole air path at the locations described in the Table 9. The lambda sensor is placed downstream the TWC.

**Table 9: Thermocouples positions in AIS**

| | |
|---|---|
| T0 | Air Cleaner inlet |
| T1 | Compressor outlet |
| T2 | Air Intake Manifold (AIM) |
| T3 | Turbine inlet |
| T4 | Turbine outlet |
| T5 | Catalyst outlet |

This control ensures that each of the five tests done for each configuration starts with the same conditions and allows for a check during operation. As an example the Figure 83 shows the temperatures along the AIS with average, maximum and minimum values of the different runs during a load step at 1200RPM (from 20 Nm to full load).
The test on the engine has been carried out at 1200RPM instead o f

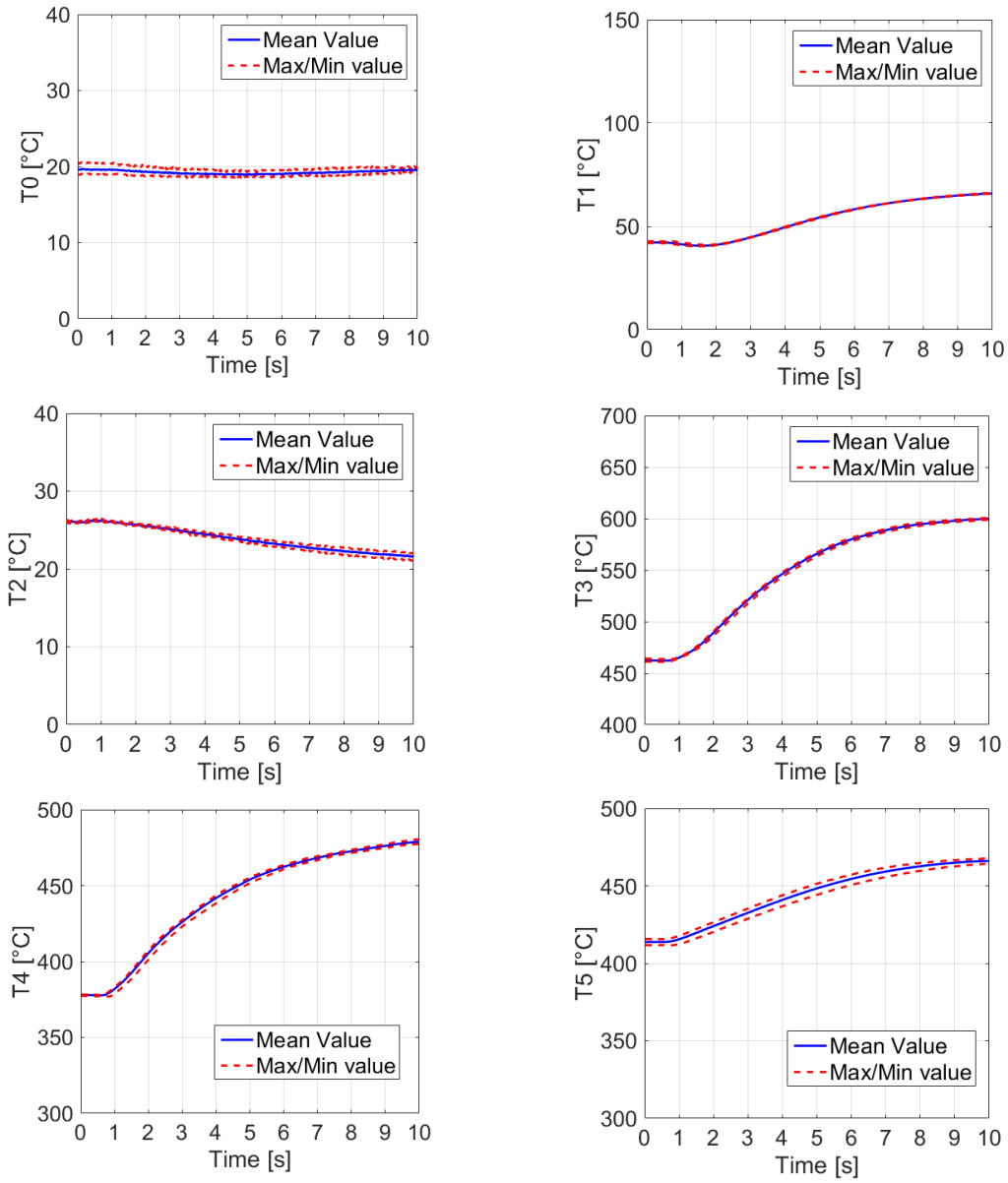


**Figure 83: Temperature evolution along the AIS during the transient test at 1200RPM with Base Line**

The results show that after 10s the thermal conditions are almost stable. Nevertheless a stabilization period of 5 minutes has been imposed for steady state and transient measurements. The turbine thermal conditions are carefully monitored to ensure good reproducibility of all measurements. The temperature at the different location stays low with less than ±1.5%.

Evaluation of the performance of the added system is handled through pressure sensors placed as shown in Table 10 and Figure 59.

**Table 10: Pressure sensors positions in AIS**

| | |
|---|---|
| P1 | Compressor outlet |
| P2 | Intake manifold runner |
| P3 | Exhaust manifold |
| PCyl | Cylinder 1 Pressure |

Fuel consumption is evaluated with a fuel balance AVL 733. To improve the accuracy, the measurement duration has been increased to 30s so that the fuel consumption is high enough to be accurately evaluated.
The torque is measured between the crank shaft of the engine and the brake shaft of the test bench, with a high dynamic inline torque sensor HBM K-T40-001R-MF-S-M-SU2-0-S.

### 4.4.2 Ramp up tests

The first attempt to evaluate the tuning of the air intake with engine speed has been carried through an engine speed run up. The throttle body is maintained opened as well as the waste gate. This aimed to evaluate the wave amplitude without the interaction with turbocharging system. The boost pressure stays almost as the ambient. The run starts from 1000RPM to 5500RPM and the pressure is recorded at the intake manifold (P2 sensor).

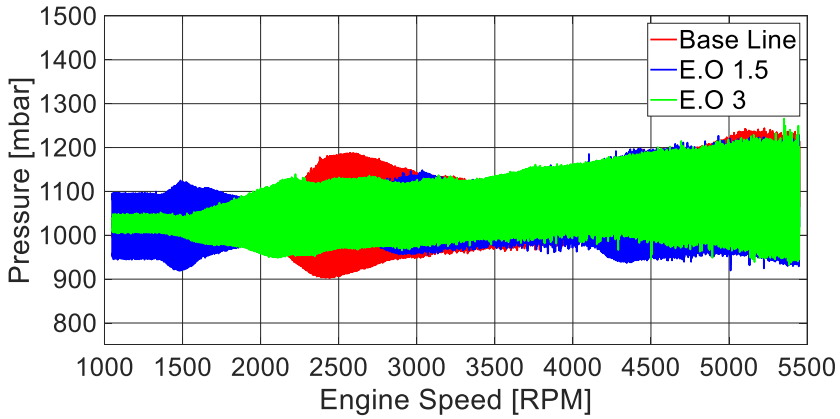


**Figure 84: Manifold pressure during ramp up throttle body and WG opened**

The Figure 84 shows the pressure inside the manifold with much higher oscillations with the configuration E.O 1.5 between 1000 to 2000RPM compared to the two other configurations. The envelop size of the signal, Figure 85, gives a better evaluation of the actual wave amplitude. The E.O 1.5 is well tuned for low engine speed whereas E.O3 and Base Line gives higher amplitude at higher engine speed.

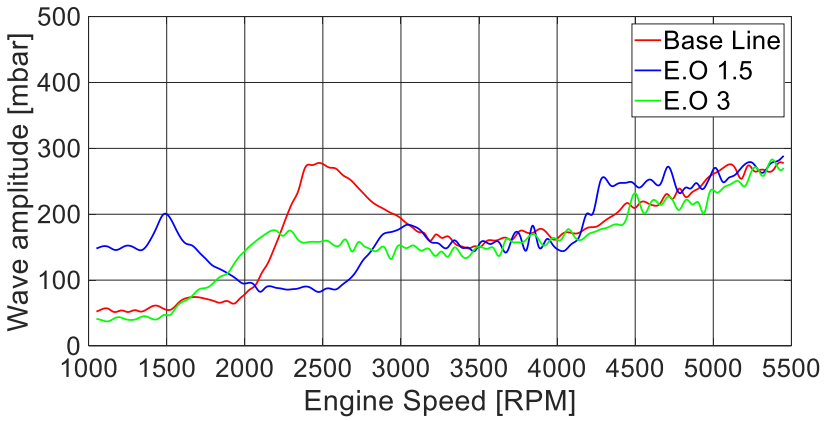


**Figure 85: Wave amplitude during the ramp up**

This test is quite useful to understand the wave propagation in the intake system and gives some hints about the actual tuning of the line. Even if the previous simulation has shown big interest of the E.O 3 configuration, this first results does not reveal high wave amplitude with this configuration at low engine speed.

A tuning of this last E.O 3 version has been performed on the length between the air intake manifold and the volume starting from 1400mm as depicted in Figure 85.

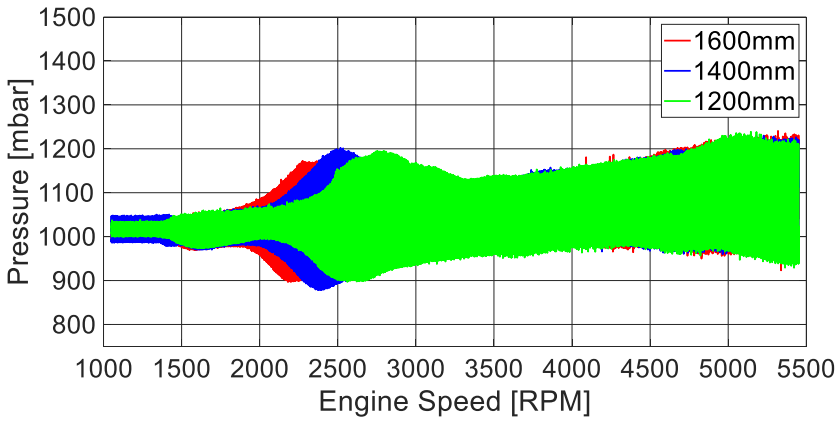


**Figure 86: Wave amplitude during the ramp up with configuration E.O 3 varying the length LV+LD1**

The Figure 87 shows clearly the impact of the length LV+ LD1 on the highest amplitude seeable around 2500RPM. At this engine speed the WG is not closed but controlled to maintain the maximum torque constant from low engine speed to almost maximum power engine speed. The benefit of volumetric efficiency increase at 2500RPM cannot be well used.

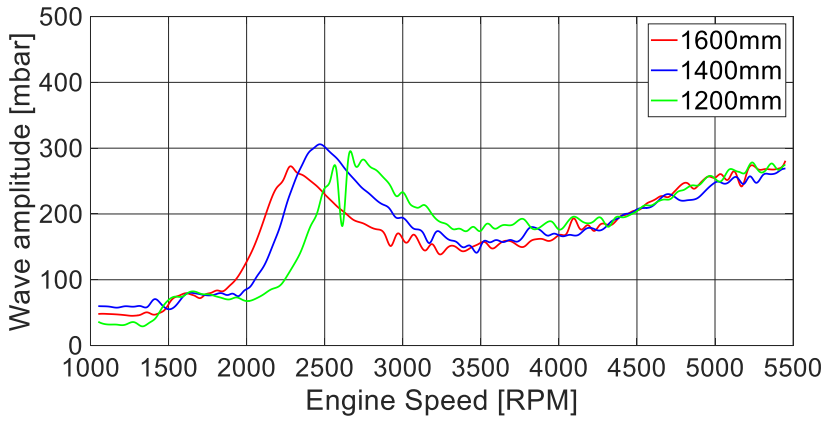


**Figure 87: Wave amplitude during the ramp up with configuration E.O 3 varying the length LV+LD1**

The test of the original configuration E.O 3 with LV+LD1=1400mm will anyway be performed in steady state conditions.

### 4.4.3 Steady state conditions

A first assessment of the relationship between the airflow and the output torque is conducted. The engine runs for different load at constant engine rotational speed (1000RPM in this case). The curve in Figure 88 depicts the engine torque output for different air mass flows. It is noticeable (at this engine speed) that an increase of 1kg/h air flow linearly leads to 3Nm improvement in torque.

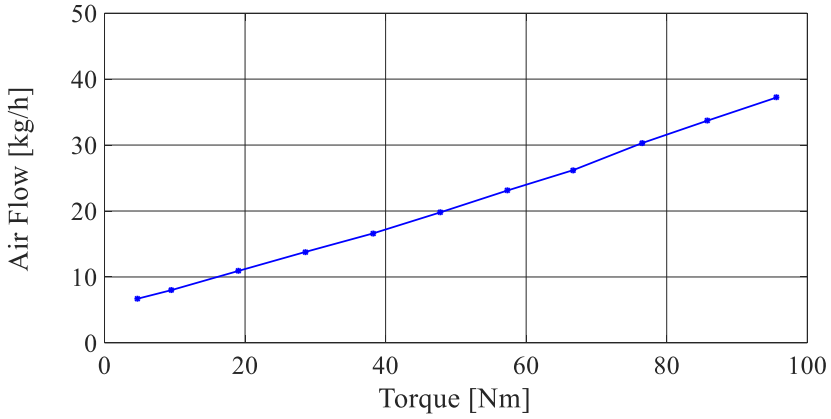


**Figure 88: Torque evolution as function of the air mass flow for a rotational engine speed equal to 1000RPM**

The increase of airflow is handled at low engine speed by activating the throttle body. At full load condition the throttle body is already completely open. The available enthalpy at the exhaust limits the boost pressure which can be provided by the turbocharger. As shown with the simulations, the pressure increase at the intake valve closing can provide increased air mass trapped in the cylinder leading to higher output torque.
In order to understand properly the interaction and keep the parameter under control the first investigations are conducted without overlap between the intake and exhaust valve opening. The overlap creates an air flow which go directly from intake valve to the exhaust as shown on Figure 89, this is so called scavenging.

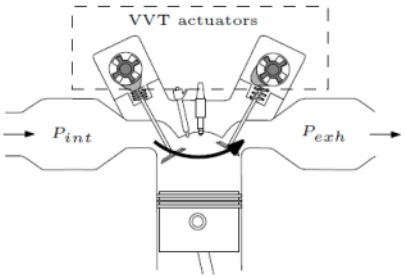


**Figure 89: Scavenging principle** [56]

In the mass production set up, the scavenging is used [136]. This leads to better evacuate the burnt gas out of the cylinder reducing residual burnt gases and cool down the exhaust valve which improve the knock resistance [137]. Furthermore the extra airflow provides more power to the turbine helping to increase the boost pressure.
With the scavenging, the ratio of air trapped in the cylinder is quite difficult to assess. Furthermore the excess of air at the exhaust reduces the capacity of the three way catalyst to reduce nitrogen oxide (NOx) which should be avoided to fulfil the next regulations. The first tests are carried out without scavenging. The intake valve shift later and the exhaust valve earlier so that there is no more overlap. With such setting the air flow is fully trapped in the cylinder and participates to the combustion. The stoichiometric condition is maintained. The ignition timing is adapted to keep the MFB50 at the same crank angle positions.
At 1000RPM it has been observed high torque oscillation. They were related to eigen mode of the transmission between the crankshaft and the test bench brake system. To avoid this issue the following tests are carried out at 1200RPM.
The configuration with the added volume E.O 1.5, with ØVolume=120mm and piping LD1=1980mm, LV=1430mm, is compared to the baseline configuration.
Three main set up are then compared. The first one is the base line, with E.O 1.5 configuration and the waste gate regulated to keep the same boost pressure. In the final version the same added volume is installed and the waste gate remains closed to get the maximum potential of the turbocharger. The results are reported in Table 11.

**Table 11: Comparative engine torque output**

| | Base line | E.O 1.5 iso boost pressure | E.O 1.5 |
|---|---|---|---|
| BMEP (bar) | 12.7 | 13.3 | 14.0 |
| Relative improvement | 0.0 % | 4.4 % | 10.4 % |
| AIM Pressure (bar) | 1.36 | 1.36 | 1.43 |
| Waste gate position | Closed | Regulated | Closed |
| Lambda | 1.02 | 1.02 | 1.02 |
| Airflow (kg/h) | 65.2 | 70.5 | 74.9 |

The aim of this investigation is to quantify the benefit provided by the added volume and the interaction with the turbocharger. The direct benefit of adding the volume is shown through the difference between the two first configurations with an increase of the BMEP of more than 4%. The added volume increases the pressure wave amplitude as shown in Figure 90. There is a further benefit through the turbocharger as the increase of air mass flow leads to higher enthalpy at the turbine which gives higher boost pressure at the intake. This gives another 6% improvement.

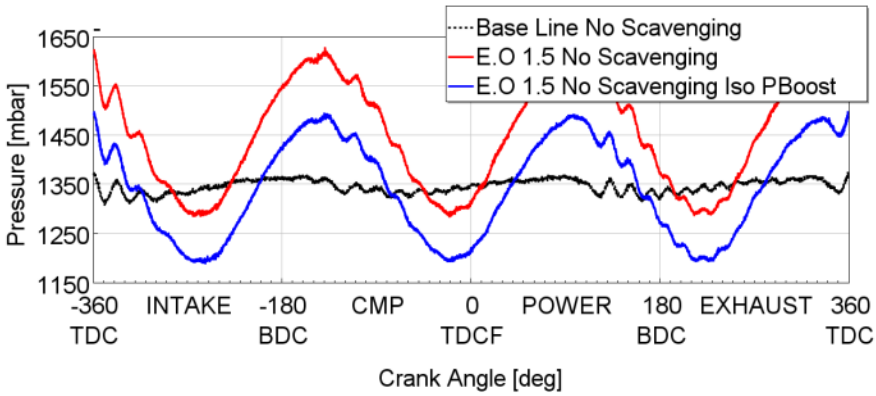


**Figure 90: Runner pressure at 1200RPM**

The benefits summarized in the Table 11 can found an explanation in the Figure 90. The pressure at the end of the intake process (around -180° CA) is higher with the added volume. This pressure increases by more than 120mbar directly with the pressure waves which increases the air flow through the engine and then to the turbine giving another 100mbar higher mean pressure in the intake. The higher mass trapped in the cylinder can be observed in the compression peak at 0° CA in the cylinder pressure signal. This is relevant because the spark timing is almost the same as well as the heat losses through the cylinder wall.

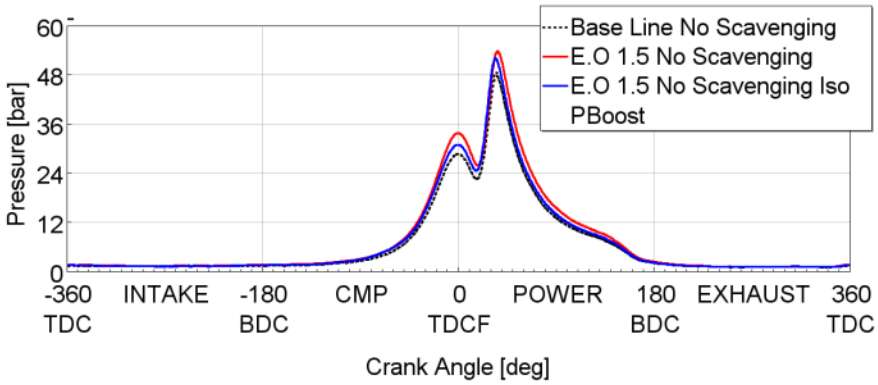


**Figure 91: Cylinder pressure measurement**

This first step shows the potential of this added volume to increase the low end torque without scavenging. This configuration represents a €7 ready set up with stoichiometric pre-catalyst mixture. The increase has been evaluated at 10% which could help a small displacement engine to move a heavy car or a car with a trailer.
Further comparison with the mass production settings have been carried out. This setting includes the scavenging, which can take place when the intake pressure is lower than the exhaust pressure. This is the cyan area on the Figure 92 for the base line configuration. The scavenging can take place after the pressure peak, due to the exhaust valve opening, at 250°CA after the Top Dead Center Firing (TDCF) and latest 310° before the TDCF. This is also possible because of the direct injection. Indeed the air can go through the cylinder but no fuel will be spread directly to the exhaust.

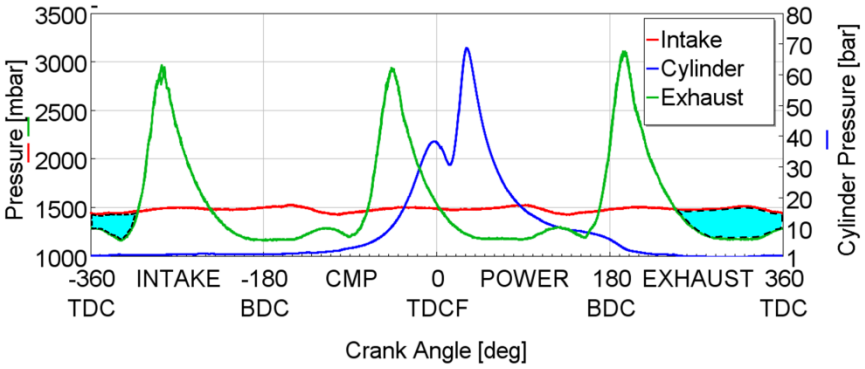


**Figure 92: Potential Scavenging area in base line configuration**

The optimal exhaust valve opening is a tradeoff between the gain providing by the scavenging and the expansion lost in the cylinder. At the intake the drawback is the reduced windows to trap air in the cylinder. The optimal was defined with 10° CA earlier exhaust closing and 10° CA later intake closing.
This setting can also be applied when using the resonance volume as depicted in the Figure 93.

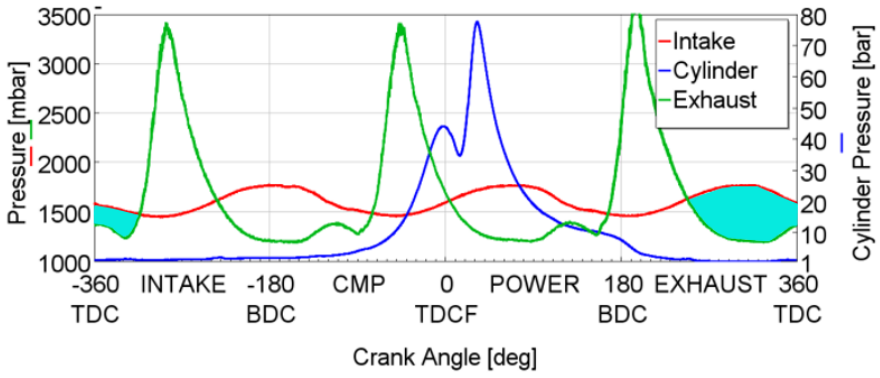


**Figure 93: Pressure signals with the added volume and scavenging**

The Figure 94 compares the intake pressure of the different configurations. The scavenging doesn't reduce the wave amplitude for the configuration aiming to increase the E.O 1.5. For this configuration the mean pressure increase also by 130mbar and pulsation amplitude are at about 155mbar 0 to peak. With scavenging the results are in order of magnitude as without scavenging even slightly higher. With this setting the version with a shorter duct and smaller volume aiming in increasing the engine order 3 has been tested too. The oscillations present clearly more peaks with 6 peaks over 2 engine rotations. Nevertheless the amplitude is much smaller and doesn't show any higher performance than the base line configuration.

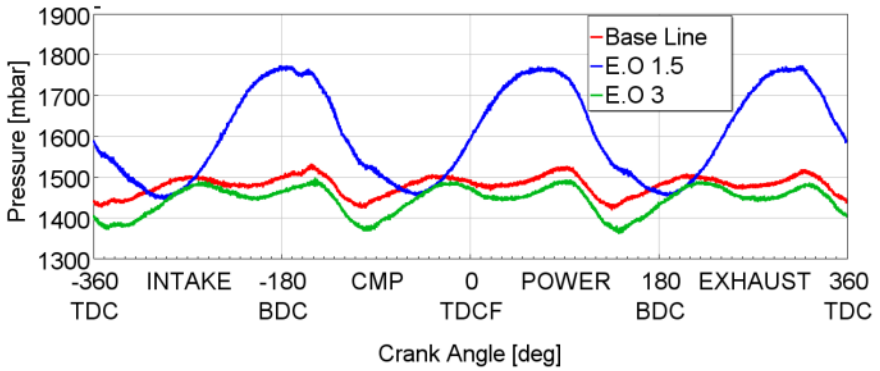


**Figure 94: Intake pressure with scavenging**

The intake pressure signal analysis can be completed through the Figure 95 full load curve with the three different configurations. The torque provided by the different configurations. As already shown the E.O 1.5 configuration allows the increase of the brake torque from 1100 to 1800RPM. The base line configuration and the E.O 3 are giving the same result. The torque at 5500RPM is the same for all configurations. This engine speed corresponds to the maximum power which means that the reduction of the cross section and the increase of the length are not constraining the maximum power.

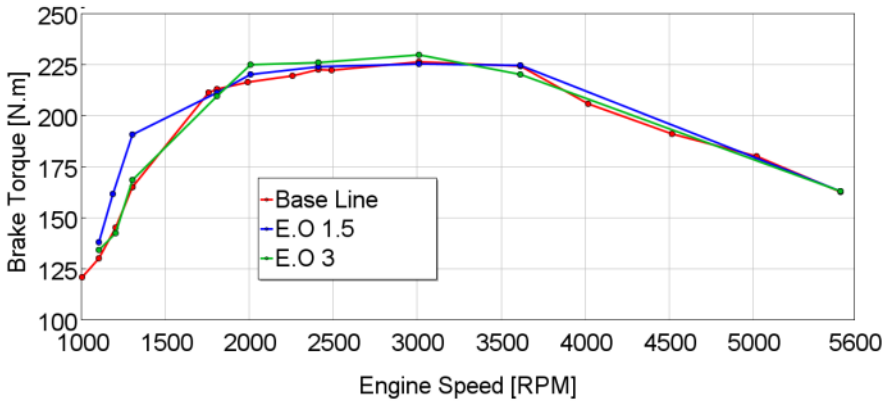


**Figure 95: Full load with mass production setting**

The air fuel mixture has been controlled and regulated to stay constant but the adjustment is not perfect and Figure 96 displays slight difference at 1300RPM.

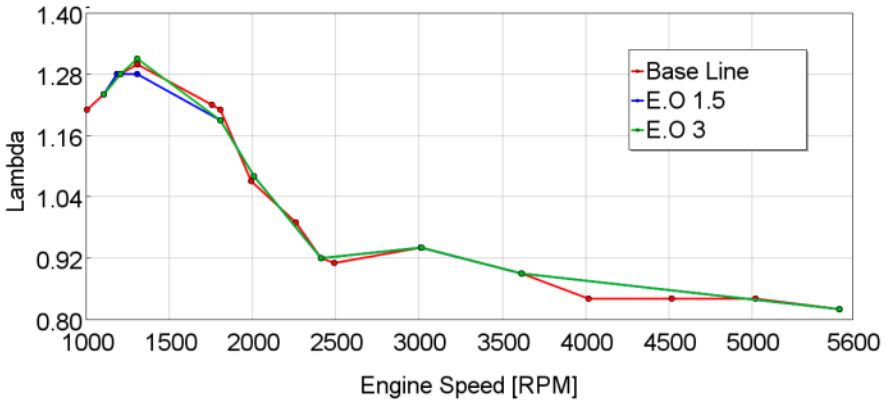


**Figure 96: Full load lambda measurement**

The measurement of lambda at the exhaust gives a hint of the actual airflow being trapped in the cylinder. However this statement relies on the assumption that the trapping ratio stays constant. Actually the lambda gives the resulting effect at the exhaust of what happened in the cylinder and during the valve overlap. The wave effect may have slightly affected the trapping ratio. The Figure 92 and Figure 93 shows that the pressure at the intake is slightly higher during the scavenging process which might be balanced by the higher pressure during intake process as well. However the output torque is consistent with the configuration without scavenging which gives confidence on the assumptions.

The Figure 97 shows the different parameters which have been checked to ensure that the changes do not exceed the limits. At low engine speed, the exhaust and intake pressure stay lower than the maximal pressure defined at higher engine speed and the temperature stays low. The effect at high engine speed are very low.

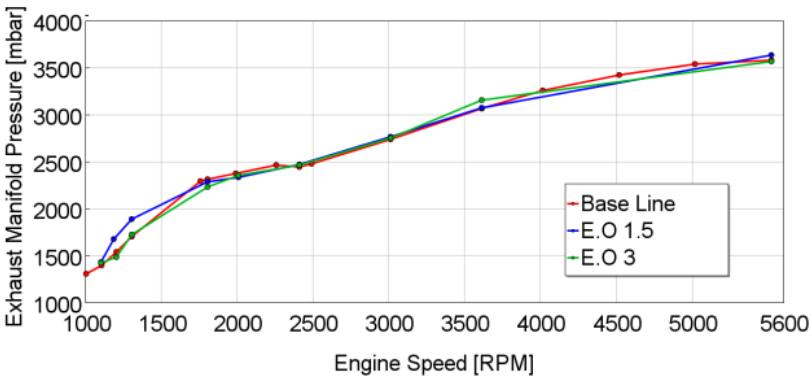


(a)

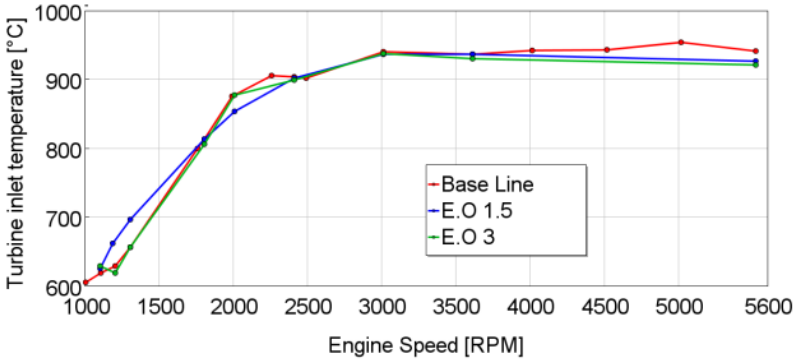


(b)

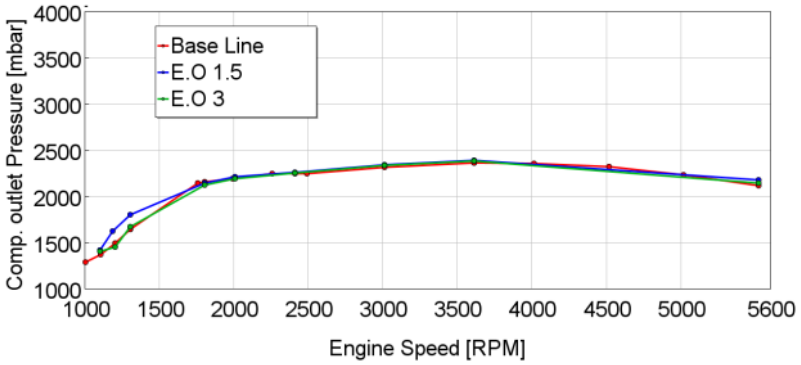


(c)

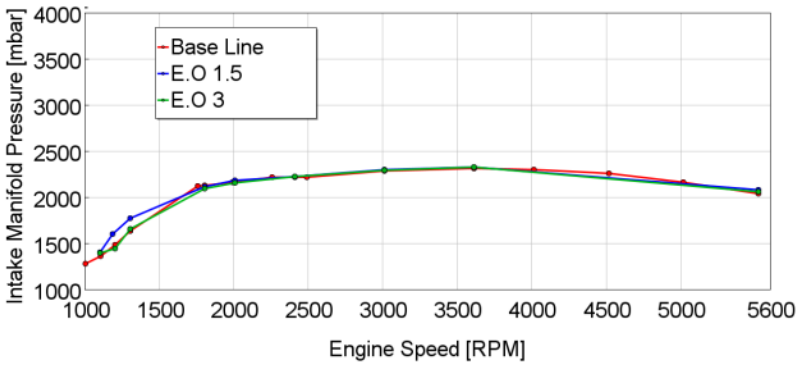


(d)

**Figure 97: Checked parameters (a) Exhaust pressure (b), Exhaust temperature, (c) Compressor outlet pressure and (d) Intake manifold pressure**

The steady state evaluation has shown the torque increase while using an added volume and piping with the right geometry. The benefit has been demonstrated with and without the scavenging. The variation of the acoustic boundary conditions during the scavenging didn't affect the wave amplitude neither the increase boost pressure. Indeed the effect of the direct volumetric efficiency enhancement is doubled through the opportunity to get higher boost pressure resulting from the higher enthalpy at the exhaust.
The evaluation of the smaller packaging volume configuration, E.O 3, didn't show the effect expected from the simulation or the frequency characterization. Further investigation could be carried out to evaluate this set up without scavenging. As the frequency is higher, as well as the number of oscillation during an engine cycle, this configuration may be more sensitive to the variation of the acoustic boundary conditions previously explained.
The packaging volume is an important constrain in the engine development and in possibility to implement innovation in mass production. Further investigation could also be handled to assess the minimum volume able to provide the 10% torque increase.

With the real drive condition as well as the WLTP driving cycle the benefit has to be evaluate not only in steady state but also in transient condition. The following part aims to evaluate the transient behavior of this solution.

### 4.4.4 Fuel consumption impact assessment

The fuel consumption impact is evaluated through 3 operating points which are relevant considering the WLTP cycle. The evaluation has been evaluated at 1200RPM where the device has been tuned. Another evaluation has been carried out at higher engine speed.
The fuel consumption mass has been recorded with an AVL fuel balance type 733S. The acquisition period is about 20s.

The coolant temperature at the engine outlet is kept constant at 92°C ± 3°C. For this operating condition the air fuel mixture remains stoichiometric with lambda=1. The Table 12 lists the parameters used to ensure the repeatability of measurement.

**Table 12: Controlled parameters during fuel consumption evaluation**

| | **Base Line** | **E.O 1.5** | **Base Line** | **E.O 1.5** | **Base Line** | **E.O 1.5** |
|---|---|---|---|---|---|---|
| Engine Speed [RPM] | 1206 | 1206 | 1206 | 1206 | 2010 | 2009 |
| Torque [N.m] | 40,3 | 40,1 | 81,4 | 80,7 | 79,5 | 80,0 |
| Power [kW] | 5,1 | 5,1 | 10,3 | 10,2 | 16,7 | 16,8 |
| BSFC [g/kWh] | 277,9 | 279,4 | 257,2 | 256,0 | 242,6 | 243,5 |
| Accelerator pedal position | 18 | 18 | 34 | 34 | 33 | 33 |
| Turbocharger speed [RPM] | 12437 | 14154 | 25576 | 25410 | 41044 | 42098 |
| PHI [1/λ] | 1,014 | 1,006 | 1,011 | 1,011 | 1,000 | 1,011 |
| IVO [° CA] | -3,0 | -4,4 | 15,7 | 15,1 | 17,2 | 17,2 |
| EVC [° CA] | 28,1 | 27,3 | 10,7 | 14,0 | 9,0 | 8,9 |
| Coolant out temp. [°C] | 92 | 92 | 93 | 92 | 96 | 95 |
| AIM temp. [°C] | 25 | 25 | 25 | 24 | 25 | 25 |
| Atmospheric pressure [mbar] | 1009,1 | 1010,9 | 1009,4 | 1011,3 | 1009,5 | 1011,3 |
| Fuel flow [kg/h] | 1,416 | 1,415 | 2,643 | 2,608 | 4,061 | 4,099 |

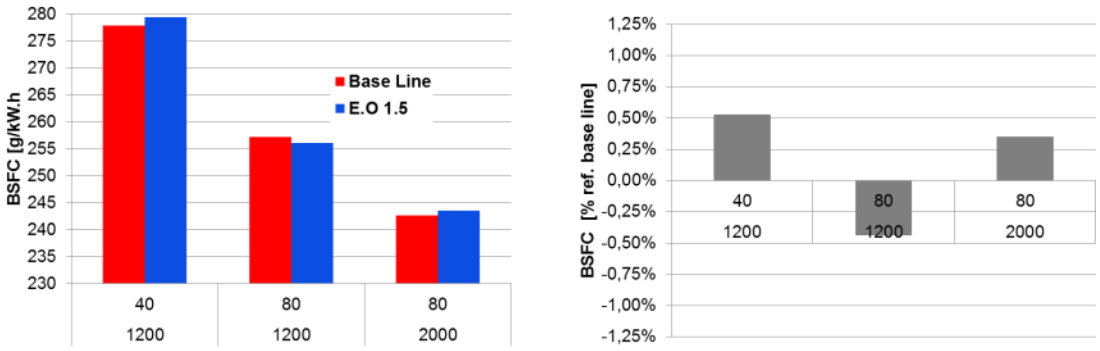


(a) Measurement (b) Relative value

**Figure 98: Impact on BSFC at part load**

The Figure 98 shows the impact of the added volume and smaller cross section. The slight differences shown are smaller than the measurement tool tolerances and don't mean much on the real benefit or drawback for those operating points. The accuracy of the fuel balance is already 1.25% at 1200RPM and 40 N.m and drop to 0.5% with higher load as the fuel flow increase [138].

These results reveal no significant impact of the geometry modification on the part load fuel consumption. These should be anyway confirmed in a larger number of operating point.

### 4.4.5 Load step conditions

The transient behavior is assessed through a load step. Starting at 20Nm the acceleration paddle is pushed to 100% and the throttle body remains open until stabilized conditions are reached. The engine speed is kept constant. To preserve the engine safety, the Electronic Control Unit (ECU) parameters have slightly been changed. First the valve timing has been changed to control the scavenging. The spark timing and the knock control haven't been changed. The ECU original strategy has been maintained. There is an accelerometer on the engine which is used to evaluate the knock. It has been assumed that the knock controller has been able to maintain the knock limit constant for all configuration.

#### 4.4.5.1 With scavenging

The original engine control is set to apply the scavenging as soon as the load increases at this engine speed. The Figure 99 and Figure 100 reports the timing recorded for intake valve and exhaust valve. The exhaust valve timing doesn't vary during the load step whereas the intake which moves to earlier opening creating the condition of the scavenging. The strategy is the same with the base line and with added volume E.O 1.5.

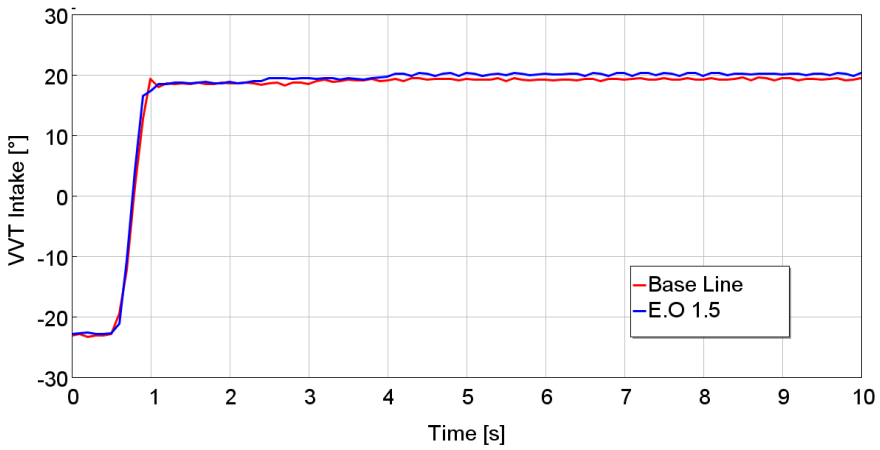


**Figure 99: Intake valve timing**

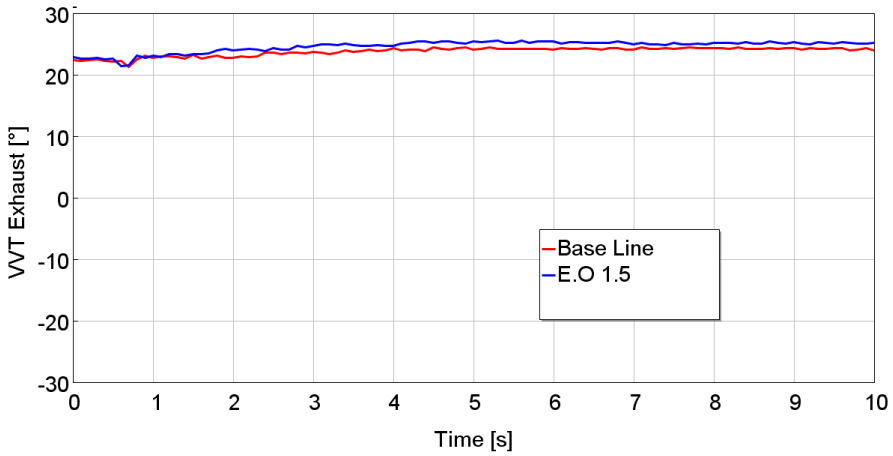


**Figure 100: Exhaust valve timing**

This results in some uncertainties about the actual air fuel ratio in the cylinder during the combustion as the trapping ratio has not been properly evaluated during the measurement. This test anyway gives the chance to evaluate the interaction between the intake, the cylinder and the turbocharger. First it gives the opportunity to evaluate how the modification will impact the turbocharger lag.

The intake pressure is recorded with a high sampling rate at 100 kHz. The signal is filtered with a Butterworth low pass filter and then the envelop function is applied to the resulting signal. The window size for the Matlab envelope operation is about 6 engine cycles. The boost pressure is mean value of the signal and the wave amplitude is the difference between the higher envelope and the lower envelope.

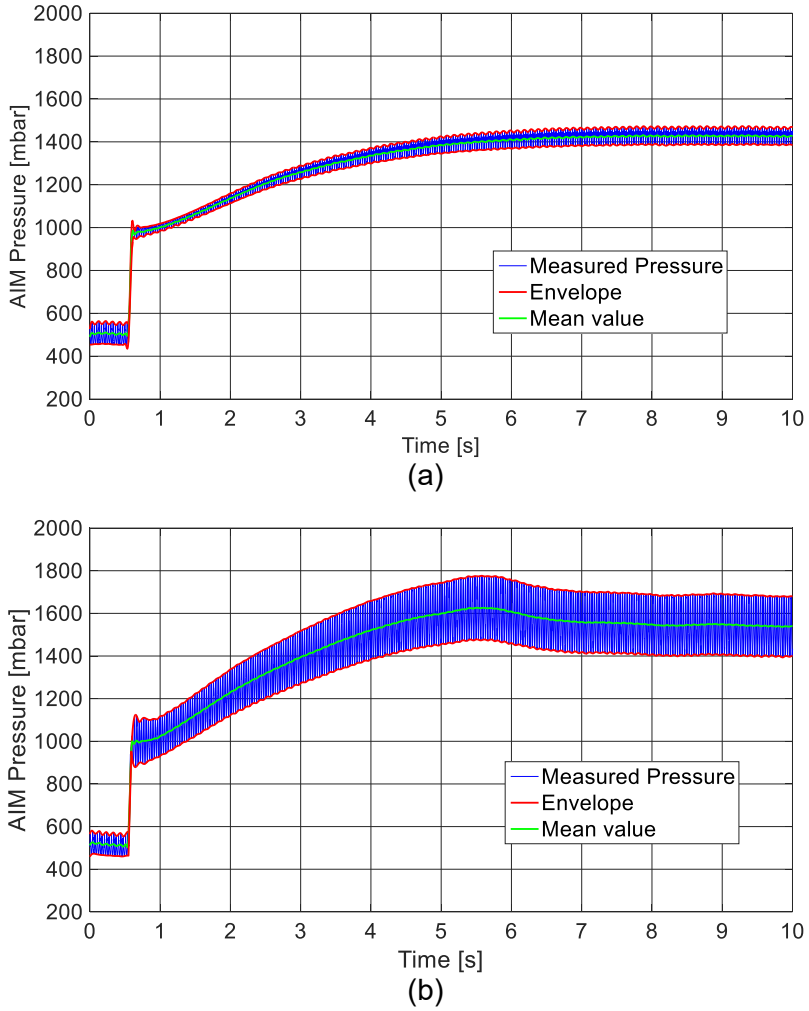


**Figure 101: Base Line (a) and E.O. 1.5 (b) AIM pressure**

The comparison, between Figure 101 (a) and (b), clearly show the increase of pulsation amplitude in the configuration with the added volume. On Figure 101 (b) the pressure wave's amplitude is high directly when the throttle body opens at 0.6s. This demonstrates the very short time needed for the pressure waves to rise in amplitude and thus give instantaneously the associated benefit.

A detailed view is proposed in Figure 102. The sinus shape of the pressure waves demonstrates the Eigen mode at the frequency corresponding to this engine speed. This sinus is obtained directly after the pressure step created at the throttle body opening.

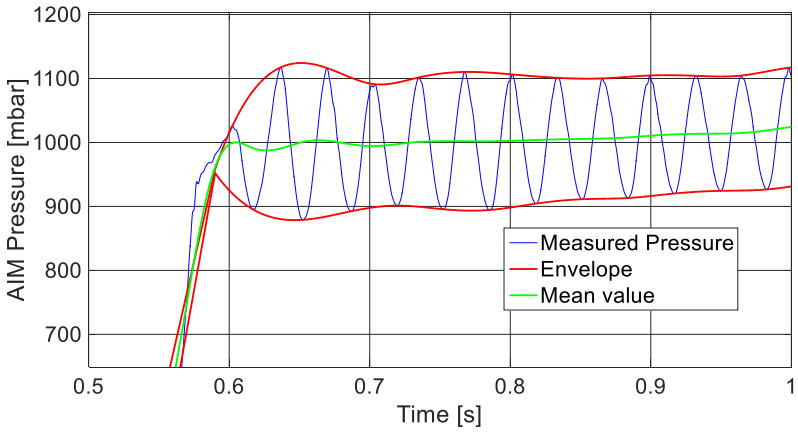


**Figure 102: Zoomed E.O. 1.5 AIM pressure**

In Figure 103, it is noticeable that the wave amplitude is increasing with the boost pressure.

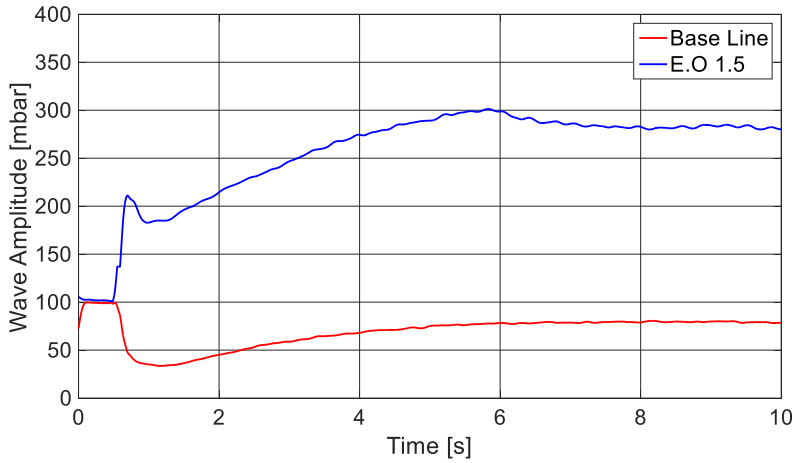


**Figure 103: Wave amplitude during the transient with scavenging**

Not only the wave amplitude increases, but also the boost pressure is increasing with the added volume. Figure 104 shows the increase in boost pressure when the added volume is used. With the added volume, air and fuel flow increase providing then more available enthalpy at the turbine and higher boost pressure.

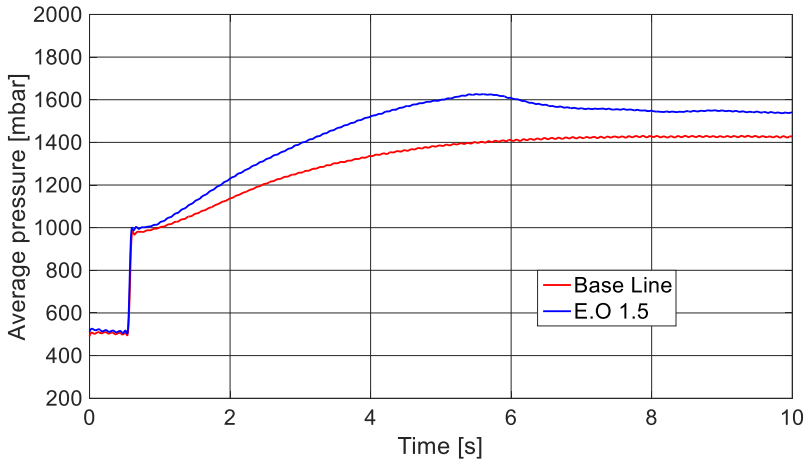


**Figure 104: AIM mean pressure during a load step with scavenging.**

Some concerns can be formulated on the volume increase downstream the compressor, the turbocharger needs to pressurized a bigger volume. The previous curves shows that the step of pressure at 0.6s is greater with added volume, this show no drawback of added volume. This increase in pressure wave amplitude gives an improvement on volumetric efficiency. The main objective is to increase the output torque. This torque is sensed through a torque flange T40B from HBM [139]. The Figure 105 represents the output signal recorded with the same 100 kHz sampling. The signals present high oscillation and cannot be easily analyzed directly. Because of the transient condition it is not possible to just get the average of the complete signal.

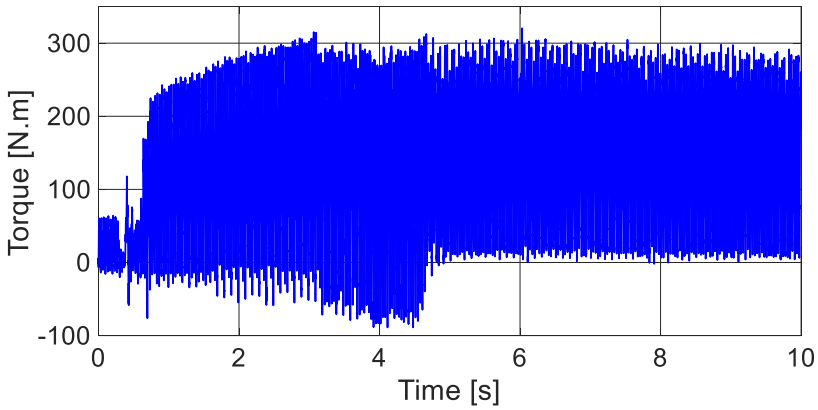


**Figure 105: Torque measurement during load step.**

The Figure 106, with a zoomed torque signal, revealed that the oscillations are corresponding to each cylinder work. The signal can then be post processed through an average sliding windows operation. The windows size is set to cover 6 engine rotations. The presented measurement comes from the average of at least 3 load steps measurements.

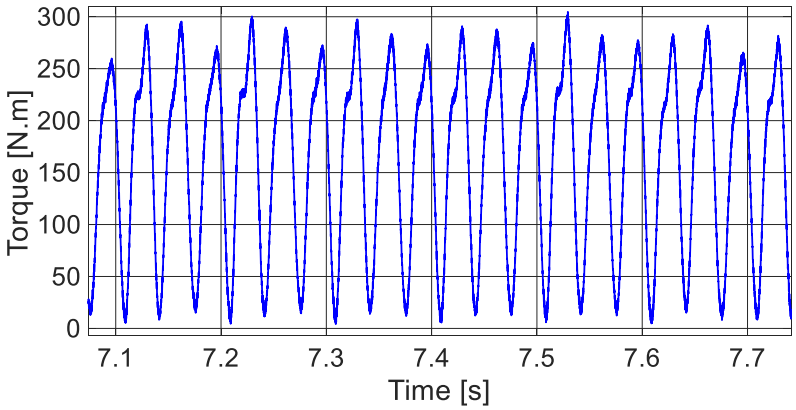


**Figure 106: Zoom in of the torque signal during the load step**

The resulting torque is presented on the Figure 107, where the effect of the added volume can be observed directly after the torque demand at 0.6s which confirms the effect of the pulsation on the volumetric efficiency. Then it seems the torque is close to the base line version at 2.5s and then increases again to reach about 20N.m higher than base line to finish closer. This last part from 7s to the end can be explained by the ECU strategy

reducing the boost pressure because it has hit the limit defined for the base line. Those results reveal that there are some remaining opportunities to enhance the transient behavior by tuning the parameters of the engines.

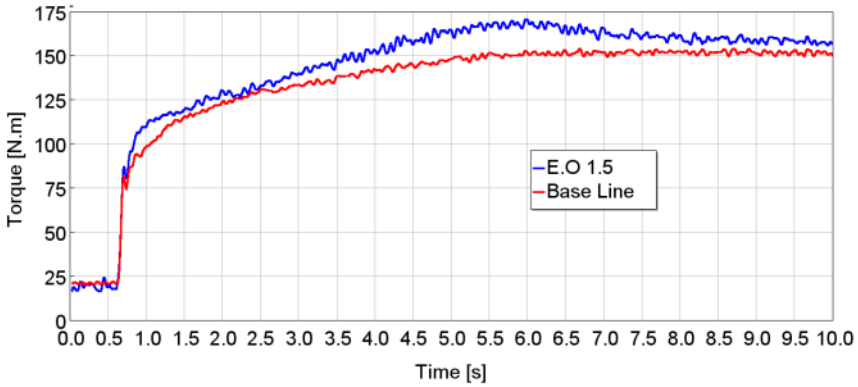


**Figure 107: Torque evolution with the base line and added volume configuration at 1200RPM transient from low 20Nm to full load**

The air flow measurement carried out with a hot wire technology sensor, depicted in the Figure 108, shows that the benefit of the added volume is almost constant during the entire run from the torque demand at 0.6s to the end. The fresh air flow rise at least 15 kg/h from the step to the 6s where the ECU strategy changed. This air flow increase has not been converted in torque as shown previously.

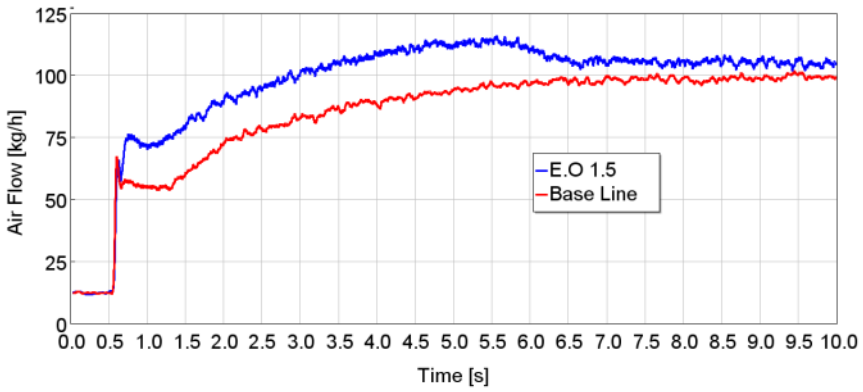


**Figure 108: Air flow evolution**

The mixture at the exhaust is clearly lean after the torque demand and the change in the intake valve timing. The Figure 109 shows the lambda results at the exhaust. This measurement can be delayed compared to the actual condition of the cylinder. Indeed the sensor is not mounted far away downstream the exhaust valve. Furthermore the sensor technology cannot provide instantaneous results. Nevertheless the lambda is clearly lean at the exhaust soon after the torque demand. The result shows a leaner mixture with the added volume. This suggests that the added volume and volumetric efficiency enhancement contributes to increase the scavenging which can partly explained the increase in AIM pressure previously observed.

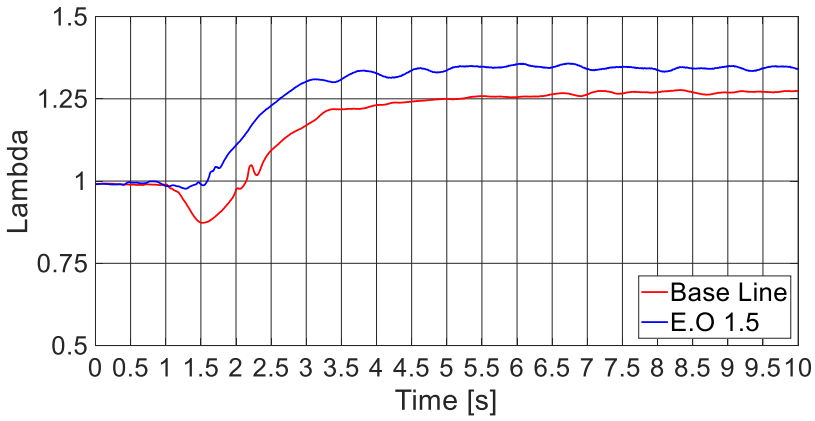


**Figure 109: Lambda measurement at the exhaust with scavenging**

Because of the scavenging it is not possible with this test set up to evaluate the actual in-cylinder mixture during the combustion. A reach mixture in-cylinder and the scavenged flow could lead to a temperature increase in the catalyst because of the oxidation of the unburned fuel. The Figure 110 shows a slight difference between the two configurations which is not enough to conclude on the in-cylinder mixture.

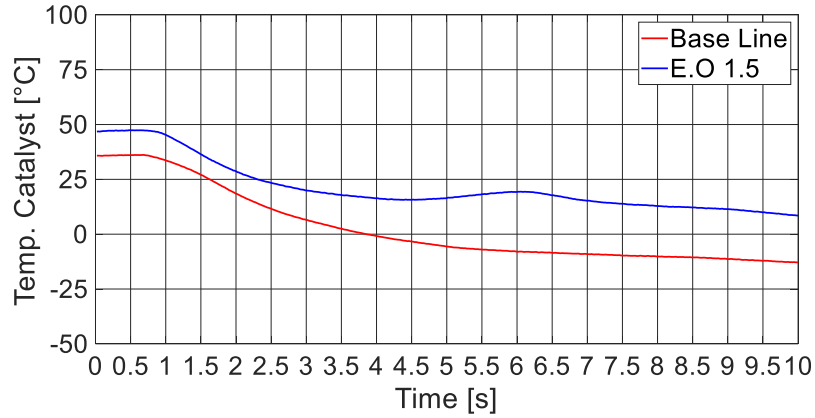


**Figure 110: Temperature difference between the catalyst outlet and the inlet with scavenging**

The Figure 111, showing the turbine inlet temperature, demonstrates an increase with the added volume. This results from a delayed combustion controlled by the spark timing depicted, in Figure 112, also delayed.

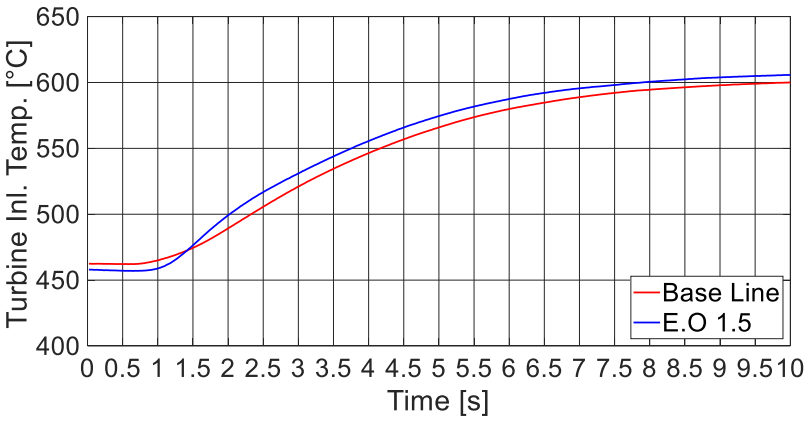


**Figure 111: Inlet turbine temperature with scavenging**

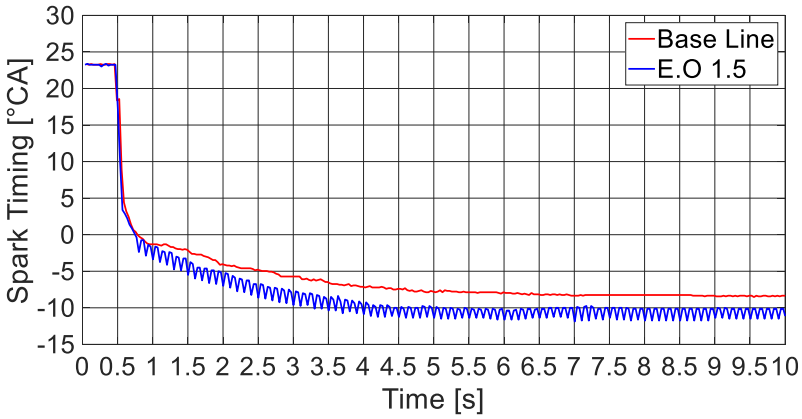


**Figure 112: Spark ignition timing with scavenging**

These tests have shown the positive effect for both the turbocharger as the provided boost pressure can be higher and also the effect on the torque which is directly higher and increase faster than with the base line. The effect on the combustion seems to be a drawback as the spark timing is slightly delayed. This could be explained by the higher pressure at the end of the compression leading more knock tendency.

#### 4.4.5.2 Without scavenging

The load steps have been reproduced while keeping the intake and exhaust valve timing at 0. In this situation the air cannot go directly from the intake to the exhaust as not overlap takes place between the intake and the exhaust valve opening.
Without scavenging the output torque represented in Figure 113 shows lower torque at the end than with scavenging (as depicted on Figure 105). In both cases the torque increases quickly until about 100 N.m directly at the demand. In this case, the gap between the two configurations does not fluctuate and increase slowly until the steady state conditions are reached. The almost 10% torque enhancement are obtained as already shown in steady state conditions.

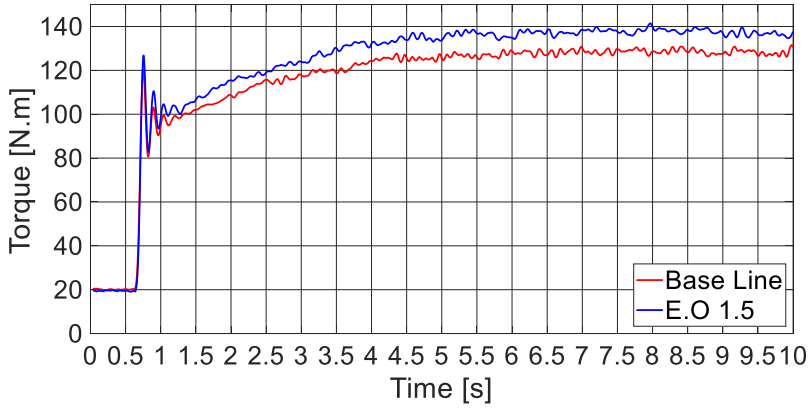


**Figure 113: Output torque without scavenging during load step at 1200RPM.**

At 2 second the torque increased already whereas the intake pressure, in Figure 114, does not increase much. This can again be explained by the direct benefit of the wave amplitude increase when the stabilized torque increase combine with the turbine enthalpy increase provided.

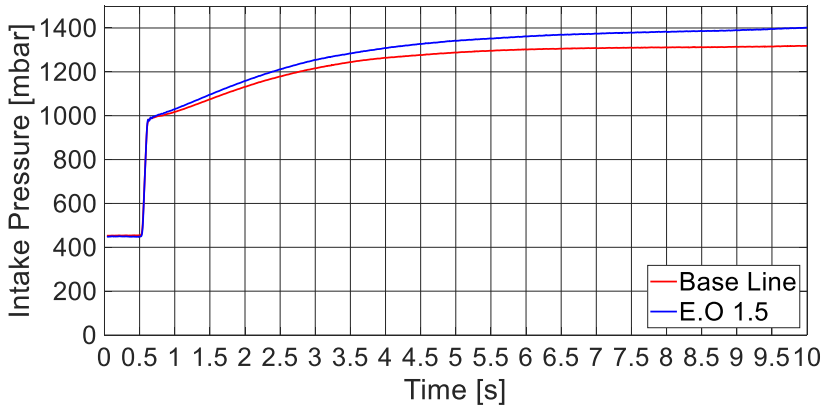


**Figure 114: AIM mean pressure during a load step without scavenging**

The Figure 115 shows the same difference in air flow than what has been observed with torque.

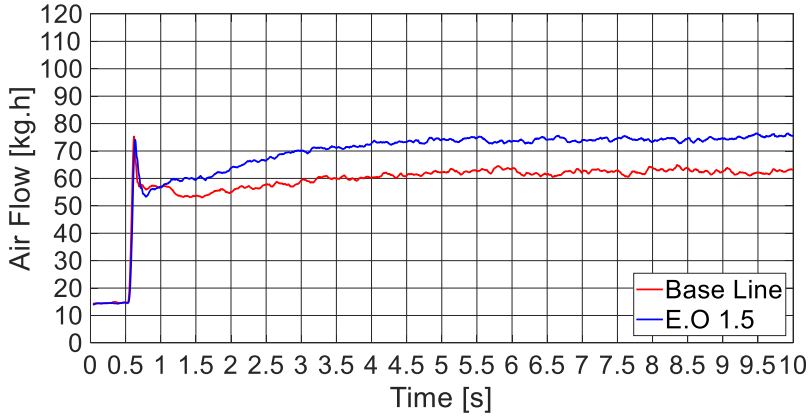


**Figure 115: Intake air flow during the load step without scavenging**

As shown with the scavenging, the Figure 116 reveals the delayed spark ignition with the added volume. The volume increases the pressure and temperature and thus the knock risk. However the output torque is higher with the added volume.

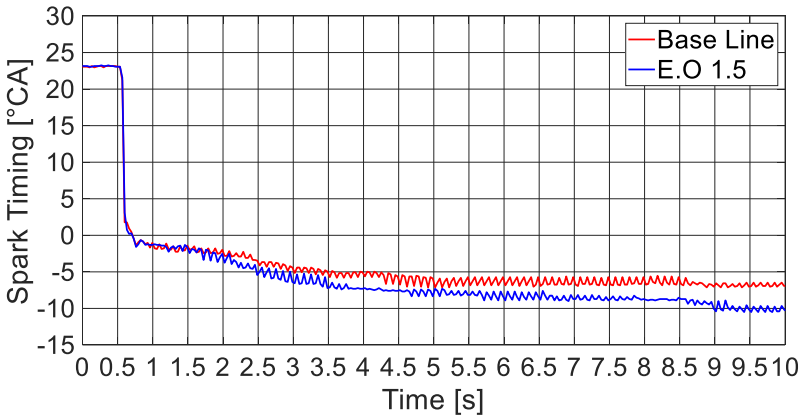


**Figure 116: Spark ignition timing without scavenging**

### 4.4.6 Conclusion and discussion

This study has shown the potential torque increase is permitted by an added volume and length in the intake air path between the charge air cooler and the intake valve. The layout and first benefit assessment carried out with the simulation code is then validated on engine test bench.

With the so called E.O 1.5 version the torque benefit reaches 10% in steady state conditions and the wave action effect has been demonstrated. The fuel consumption has been evaluated through 3 part load operating points and no significant effect has been detected. Nevertheless the volumetric efficiency benefit is not 100% converted in torque has the combustion timing is delayed certainly because of the in-cylinder pressure increase and potentially temperature. Another configuration enhancing the pressure wave at the 3$^{rd}$ Engine Order has shown a good potential with the simulation but not on the engine test bench. First the wave amplitude was lower and the torque enhancement not demonstrated.

The load step evaluation has shown two effects of the volumetric efficiency enhancement. The first enhances the cylinder filling provides a direct torque increase. The second is the loop effect, where the added mass flow through the turbine leads to higher boost pressure or intake pressure to further increase the in-cylinder pressure at the intake valve closing.

The actual acoustic Eigen mode reason has not been completely explained during this study. The effect of the volume and the tube length shows that this is not fully Helmholtz resonator neither a half wave nor quarter wave behavior. Further acoustic calculation could evaluate the actual impedance of the volume and the interaction with the rest of the intake system.

It has to be mentioned at this point that no optimizations were carried out to get the maximum benefit of the device and all results shown on the transient behavior are directly issued with the standard ECU configuration. There are possibilities for even higher potential while adapting the valve timing and the combustion to this specific setup. A tuning

of the spark timing would give a proper evaluation of the knock margin in both base line and E.O 1.5 configurations.
No surge has been observed during the tests. But the effect on surging has been considered through simulations. Figure 117 shows the transient run on the compressor map. The added volume doesn't affect hardly the surge margin as the operating points are moving both higher in pressure ratio and air flow.

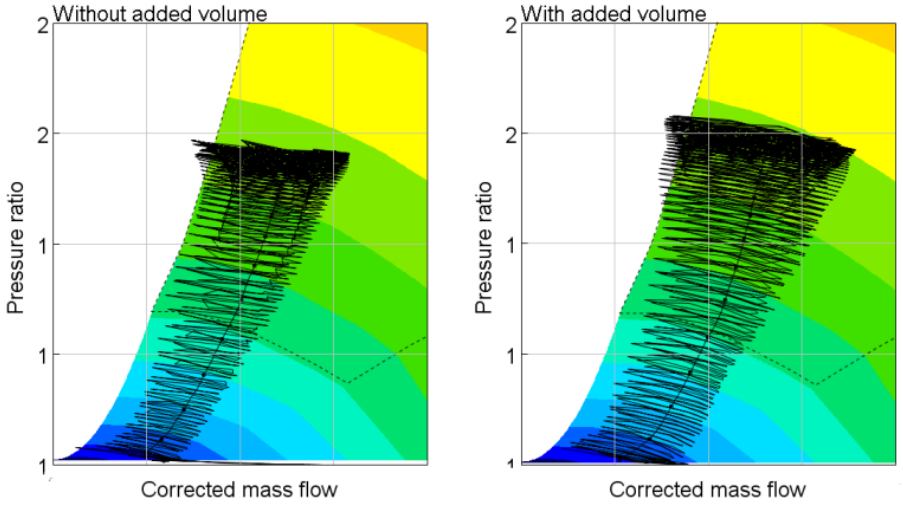


**Figure 117: Results of added volume during transient operation in the compressor map**

This observation would require complementary tests to evaluate the criticality (compressor map accuracy, noise).
The main drawback of the solution is the added required package volume. Nowadays the engine compartment is almost full. Adding 5L of volume and ducts is an important challenge to implement this solution in mass production. For big vehicle using small engine going further with the downsizing this solution will help to maintain the drivability and the fun to drive.

# 5 Intake temperature reduction thanks to wave action

The upcoming regulations and environmental concerns regarding pollutant emissions increase the pressure on OEMs to reduce fuel consumption and emissions. With the RDE evaluation, this will have to be applied not only at low engine speed and low load, but also at full load operating conditions. For instance, the RDE will prevent from some strategies previously adopted to damp the knocking and will impose the stoichiometric mixture upstream the catalyst in all operating conditions. For each operating condition, different challenges limit the engine output power/torque or the BSFC. At the same time the maximum engine power is still a key consideration for the end-consumers' buying decision. In the area of the maximum power, the main drivers are the knocking and the exhaust gas temperature. The knocking precludes from early combustion and decreases its efficiency. One other issue to be taken into account while trying to get a high output power is to limit the exhaust temperature in order to protect its components.
First is a description of the engine used for this study. The second section focuses on the simulations objectives, assumptions and set up. The third part gives an overview of the effect of the intake system on the engine power. The forth part will describe the architecture able to provide an expansion at the intake valve closing. Using this air intake system, the engine simulations are presented in the fifth section and the engine tests are contained in the sixth part before the conclusion and the outlook.

## 5.1 Engine characteristic

The three cylinder engines are dedicated to reach low consumption. The low end torque is a key point, the engine requiring more power are usually using higher displacement and so uses 4 cylinders or more. The considered engine is a downsized turbocharged direct injection engine. This is an Euro 6d-TEMP ready engine. This is a modern developed engine and will have to fulfill the next regulations with the challenge on the maximum output power. It is currently using the enrichment and will have to shift to another strategy. The detailed characteristics are presented in Table 13.

**Table 13. Engine characteristics**

| Aspiration | Turbocharged |
|---|---|
| Injection | Direct |
| Fuel | Gasoline |
| Bore | 72 mm |
| Stroke | 81 mm |
| Compression Ratio | 10.5 |
| Number of Cylinder | 4 |
| Displacement | 1300 $cm^3$ |
| Bore | 72 mm |
| Stroke | 81 mm |
| Intake valves | 2 / cylinder |
| Exhaust valves | 2 / cylinder |
| Valve timing | Variable |
| Specific Power | 92 kW/l |
| Specific torque | 200 N.m/l |

The mass production intake system does not present any specific features and will be used as reference for comparisons. Schnüpke *et al* [140] have given more details on the engine evolution.
The intake base line will be kept constant from the snorkel until the charge air cooler which is a state of the art air to air cooler. The exhaust line also remains the same as the mass production one.

## 5.2 Intake system geometry effects on pressure wave

Intake systems are tuned by suppliers to improve volumetric efficiency. Two levers are used to provide more air to the cylinders. The first aims to reduce pressure losses so that the air density can stay high when trapped in the cylinder. Another, well described method for naturally aspirated engines, consists of using the pressure oscillations to enhance the volumetric efficiency [131] [132].

### 5.2.1 Concept description

For the maximum power operating conditions of turbocharged gasoline engines, the volumetric efficiency is not the most relevant parameter to increase the output power. Indeed in this condition the turbocharger does not provide the maximum output. The knocking and the exhaust temperature are stronger limitations. The proposed idea goes in the same direction as Porsche presented in their patent from Theilemann *et al* [142]. It aims to provide an expansion at the intake valve closing to decrease the air intake temperature. Thus the compression phase will end up with a lower temperature, leading to a lower knocking risk. This will be favorable to an earlier combustion and thus more expansion in the cylinder which leads to a lower exhaust gas temperature.
This target is consistent with the Miller cycle where an earlier intake valve closing creates an expansion in the cylinder before the compression stroke and benefit from the temperature reduction [143].
Basically the intake system has to enable pressure waves to propagate in the intake system so that an expansion happens just upfront the intake valve closing. This is exactly going in the opposite direction as the proposed concepts from Mezher *et al* [106] or Taylor *et al* [134] which try to create a peak of pressure at the valve closing.

Theilemann *et al* [142] have presented the Figure 118 concept which uses volumes to provide reasonance. They have claimed that the right sizing of the volume and the ducts creates the expected expansion well synchronized with the valve closing.

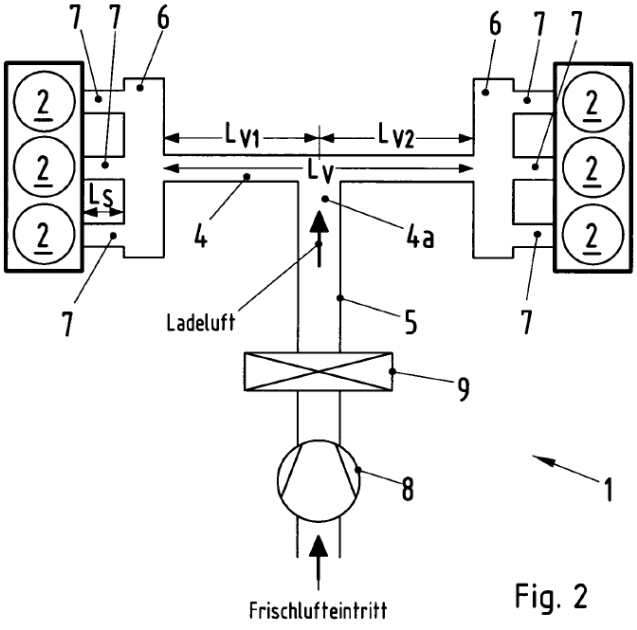


**Figure 118: Theilemann *et al* [142] concept**

The Figure 119 proposed another concept for this study which is closer to the Herschel-Quincke tube principle [144]. In this case, it does not use a single source but each cylinder as a source. In this design there is no volumes and no expansion which avoid any reflection.

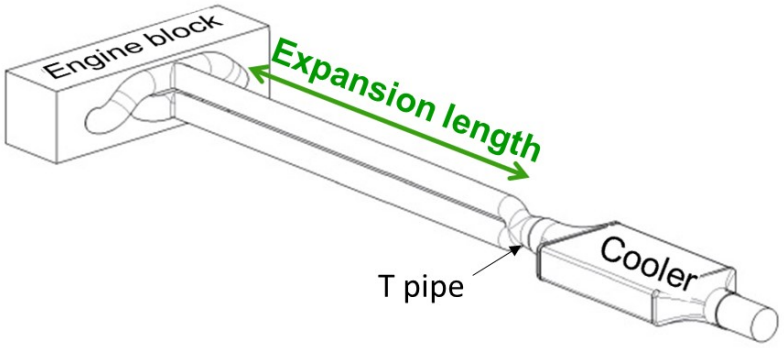


**Figure 119: Description of the concept**

In the Herschel-Quincke concept the duct is divided in two sections, one with a long route and the other with a shorter distance shown on Figure 120. The wave coming from the source at starting end of the duct travels both ways. The two ducts are then reconnected which will have the effect to combine the waves coming from both routes. The waves in the two ducts are travelling with sounds speed. The distance difference between the two routes will end up with a difference in phase between the two waves. For some frequencies the two waves will be in opposition of phase. This results in peaks in the transmission loss diagram has been presented by Poirier *et al* [145].

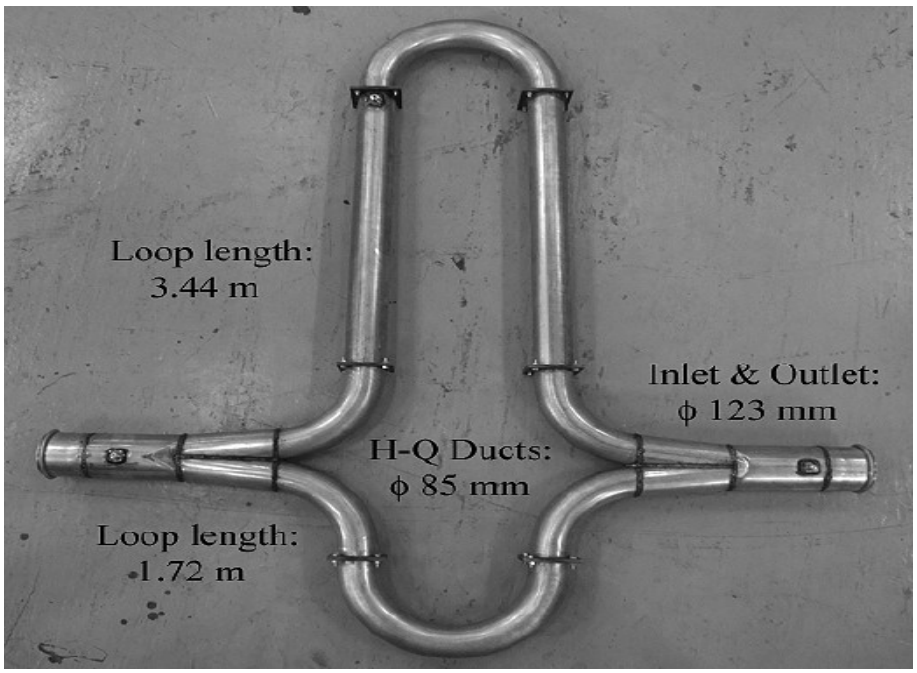


**Figure 120: Herschel Quincke concept** [146]

The engine creates waves at each cylinder. The created waves are approximately the same but delayed by 180° CA.

### 5.2.2 Layout simulation

Using the principle of the Herschel-Quincke principle the length connecting one cylinder to the other can ensure the phase shift between one cylinder to the other and so create the condition for the expansion to take place when the intake valve closes.

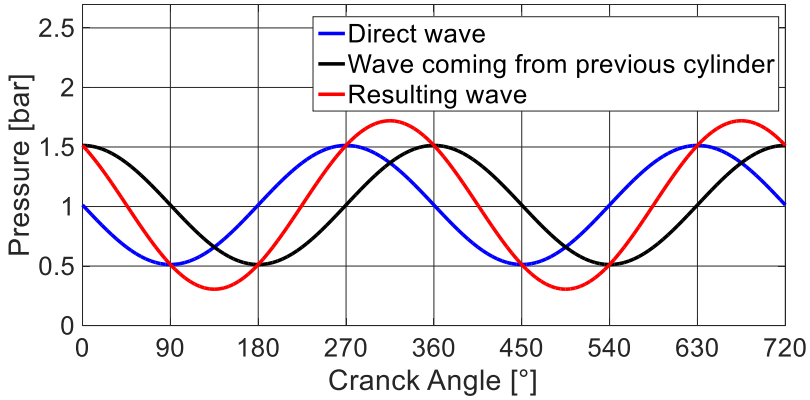


**Figure 121: Example of a wave combination.**

The Figure 121 shows the simplified modeling of the pressure at the cylinder 1 intake valve. Considering two sources, it is possible to draw the pressure signal created at this cylinder (in blue). The red curve describes the wave coming from another cylinder with a phase shift. The combination of those two is a wave with another amplitude and phase (in red).

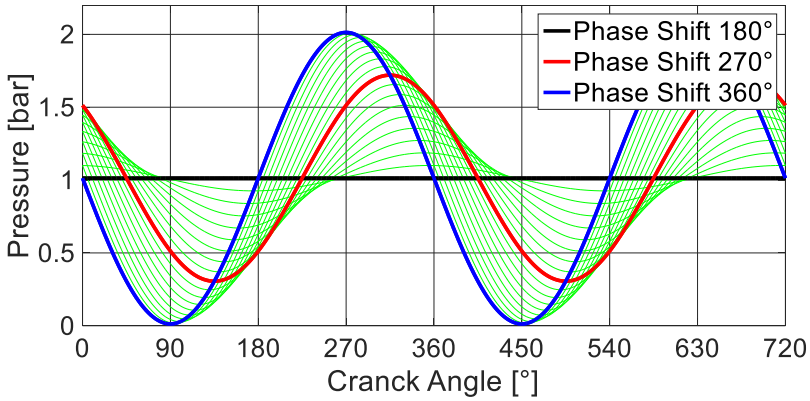


**Figure 122: Resulting pressure from different wave's combination**

The Figure 122 shows the results for several phase shifts. When the two waves are in opposition of phase (Phase Shift 180°) the pulsation is completely damped. The shift of 360° increases the amplitude but does not change the phase. The shift of 270° allows of phase shift of 90° and maintain a quite high amplitude.
For an expansion at the position 0mm of an infinite duct at the time 0s and a wave of 75Hz, the Figure 123 shows that after 6.6ms, the expansion exists at about 2 m.

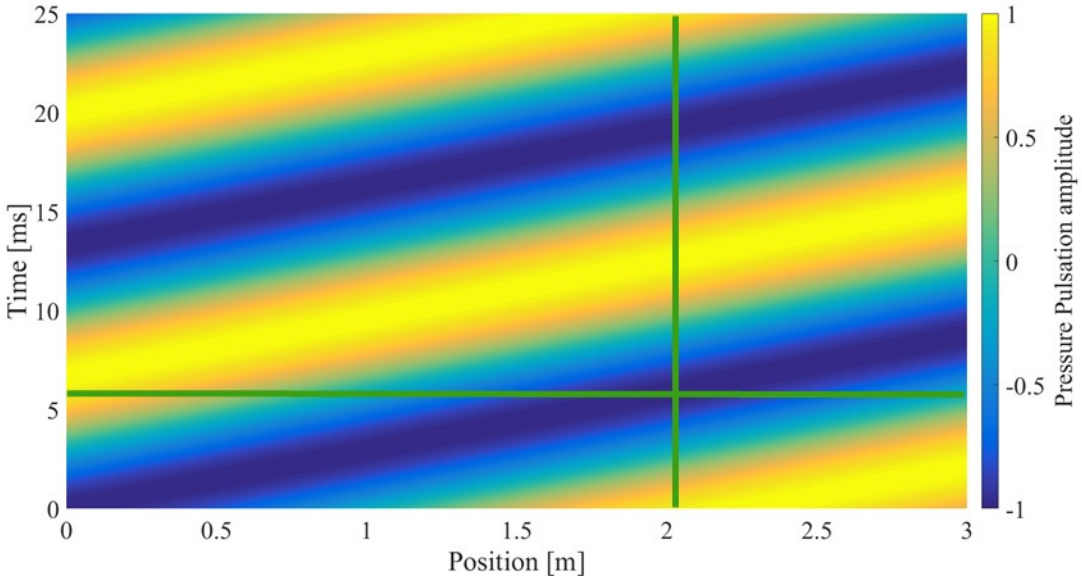


**Figure 123: Wave propagation in time and space**

The aim is to create a direct interaction between the different cylinders. Then the firing order gives the cylinder interaction. For instance the considered engine has the sequence of 1 - 3 - 4 - 2. The shortest time between two events is obtained when the cylinder 1 interacts with the 3, the 3 with the 4, the 4 with the 2, and finally the 2 with the 1. As short is the time between the event as short is duct which ensure the expected delay. Because of the regular sequence, the cylinders 1 and 4 are connected as well as cylinders 2 and 3. Then a folded duct of 2m is connected between those two blocks. The comparison between the Figure 124 base line and the Figure 125 concept exhibits this expansion length between this two blocs.

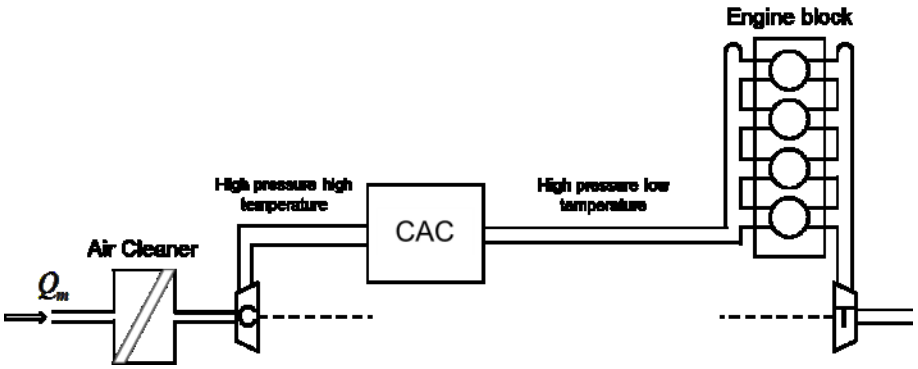


**Figure 124: Base line configuration**

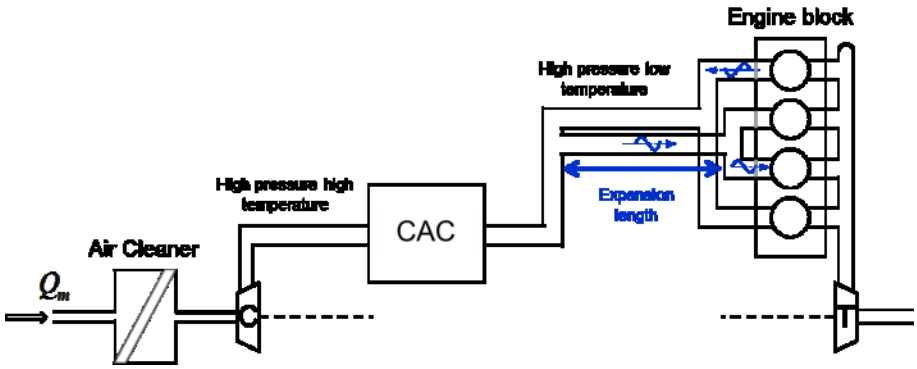


**Figure 125: Description of the concept**

The reflection and resonance system are not used here, the only effect is the propagation distance. Indeed, as with Herschel-Quincke system, the phase is directly defined by the duct length [144].

The first investigations are carried out with intake line only. The first uses the dynamic flow bench described in a previous part. The Figure 126 shows the simulation results, the abrupt reduction of the air flow induces a pressure increase at the cylinder 1 location. Later the pulse propagates to the cylinder 2 location. This simulation provides a good understanding of the delay between an event created at the cylinder 1/4 to propagate to the cylinder 2/3. Nevertheless the aim is here to propagate an expansion and be able to understand properly its thermal effect.

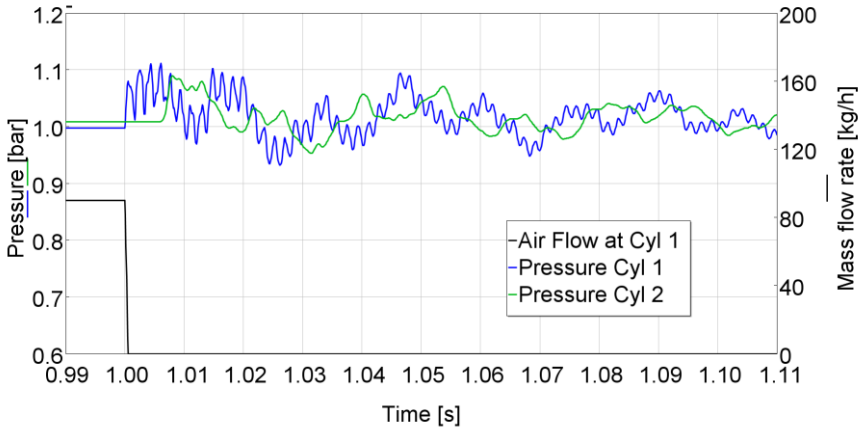


**Figure 126: Air intake response to dynamic flow bench.**

The next attempt has then been to create an airflow pulse so that the expansion can be observed. The Figure 127 shows the expansion produced when the air flow takes place. In the same way the previous figure shows the delay between the pressure at the cylinder 1 location compared to what happens at the cylinder 2. The air flow modeled that way does not well represent what actually happen on engine. The movement of the piston in the cylinder creates the flow motion relative to its velocity and the valve position. At the end of the intake process the valve closes abruptly the port creating also pulse in pressure known as “ram effect”. The two phenomena create a pressure wave with almost a sinus shape. With the same instantaneous airflow before the shutdown the pressure wave amplitude is higher for the heavy side airflow (Figure 127) than for a steady airflow (Figure 126). The pressure wave created can be then tuned or evaluated through a various

methodologies like proposed for racing engine by Winterborne *et al* [107], Harrison *et al* [147] or Payri *et al* [148]. Usually the authors works consider the complete engine meaning all cylinders as one acoustic source and not the interactions between cylinders.

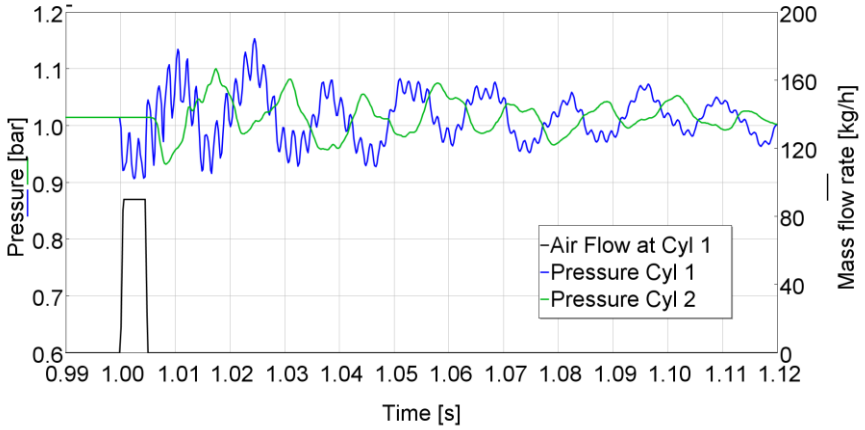


**Figure 127: Air intake response to an air mass flow impulse step.**

The boundary condition could be defined in pressure. Actually this would be easily defined when the flow is taking place but more difficult when the valve is closed. Indeed a pressure wave amplitude imposed null would much more defined an opened end than a closed end as discussed in section 3.1.1.

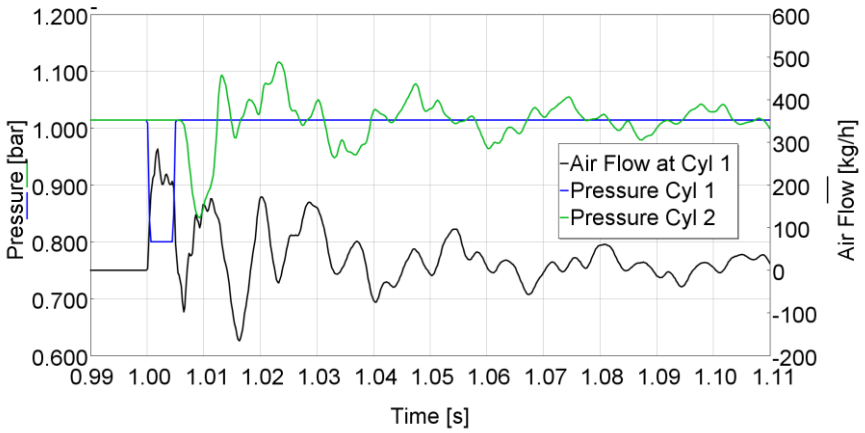


**Figure 128: Air intake response to an air pressure impulse step.**

The Figure 128 shows the response to pressure pulse at the cylinder 1. It is still possible to evaluate the travel time between the cylinder 1 to the cylinder 2. Nevertheless the air flow is not quite plausible as the air flow is far from zero out of the pulse. Furthermore it is not possible to define any clear wave after this first travel to cylinder 2. All the rest seems quite chaotic.

Considering the engine as a volumetric pump, the Figure 129 shows the volumetric air flow condition imposed at each valve position according the firing order. The analysis is made easier through a volumetric flow imposed with a shape of half a sinus. This is helpful has the frequency content of such a shape is restricted. During the time when the valve would be closed the null flow is consistent with the actual boundary condition on engine.

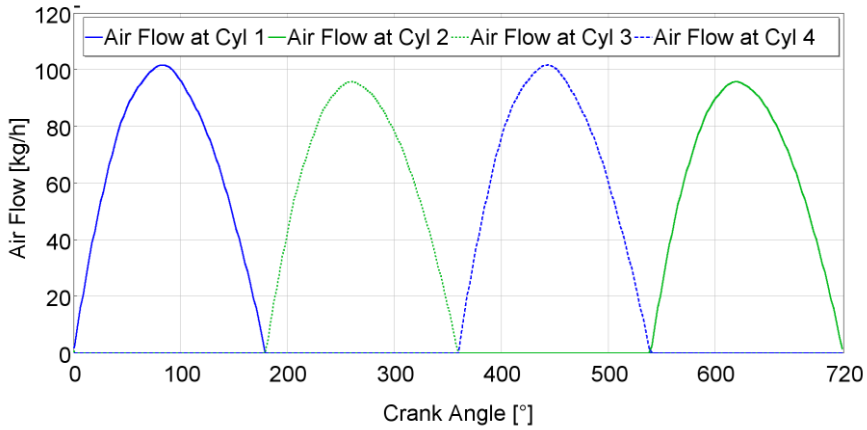


**Figure 129: Volume Air Flow imposed at each cylinder intake valve position**

The pressure and temperature can be observed on the Figure 130 at the same positions.

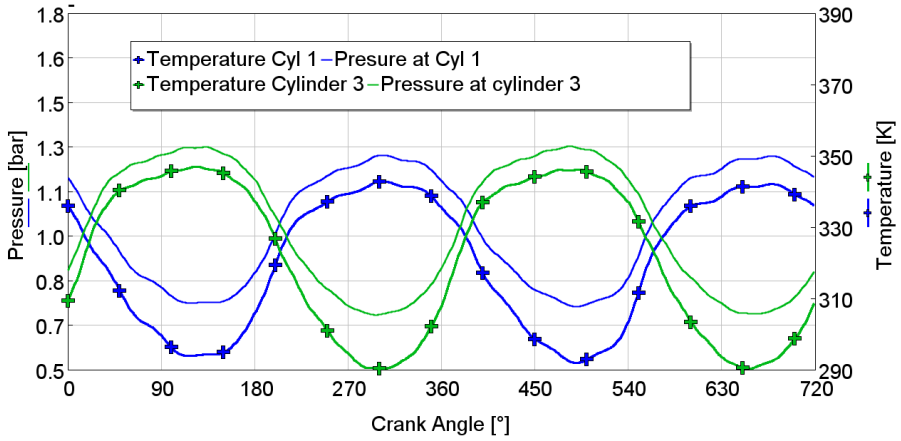


**Figure 130: Pressure resulting from half sinus air flow source with a length of 1000mm**

The comparison between the Figure 130 and Figure 131 shows the pressure and the temperature upstream the valve for two different expansion lengths at an equivalent to 4500RPM. It is noticeable that the length of 1000mm gives the highest amplitude but not the lower temperature when the airflow stops at 180° CA for the Cylinder 1 or 360° CA for the cylinder 3. For this engine speed the best should be 1200mm.

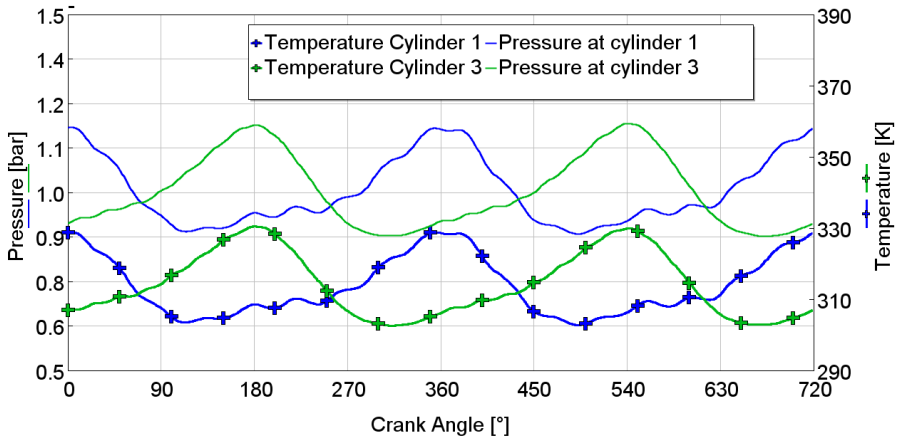


**Figure 131: Pressure resulting from half sinus air flow source with a length of 1200mm**

Those results demonstrate the potential of temperature reduction coming from wave interactions. Equivalent to a Herschel-Quincke principle the upstream intake valve pressure results from the superposition between pressure created by the air flow at this position and the pressure previously created at another location.
The engine evaluation is first handled with a 1D simulation model, explicited in the next part.

## 5.3 Simulation model assumption and objectives

A one dimensional simulation tool is used to understand and layout the device. Knocking and the intake wave propagation will play a key role to well represent the actual physics.
The UserCylinder model developed by the Forschungsinstitut für Kraftfahrwesen und Fahrzeugmotoren Stuttgart (FKFS) is used to simulate the cylinder behavior [141]. This two zones model is tuned to cope with available data. The later investigations require the model to react at different input variations and this is the reason why the predictive model is used. The aim of this predictive model is to be able to take into account the effect of pressure and temperature not only on the cylinder pressure and resulting torque, but also on the risk of knocking. Actually the model calculates the activation energy as explained by Fandakov *et al* [124]. In this case, the main parameters will be the cylinder temperature and pressure.

### 5.3.1 Model set up

First the combustion model is set to give the same output as the reference model. The test bench measurements data were not available at the beginning of the study. The simulation model has been set up with another Renault simulation model as reference. The reference model uses Wiebe law based on measurement carried out prior to this study.
Only a set of a few parameters will be used to fit on the entire operating conditions. Once all geometrical dimensions are defined and the thermal boundaries are set, the turbulence model has to be defined. The turbulence is set to fit the best with the full load curve, it remains constant for the complete engine operating conditions. The Ck value, from the

equation ( 3.42 ), is set at 1.51. The Figure 132 shows how the combustion duration is affected by the predictive model set with this parameter. At high engine speed the duration is lower than the reference but for low engine speed the reference is lower, the overall results fits within less than 2°CA except the very low engine speed, such as 1000RPM and 1100 RPM. Those points are not the main interest for this study.

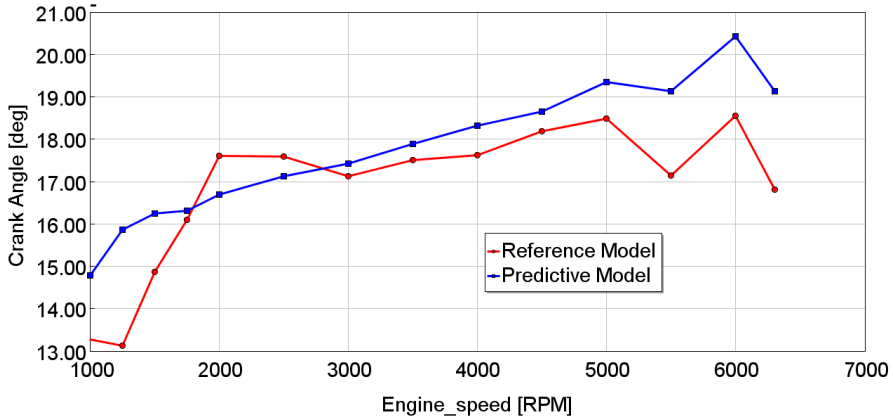


**Figure 132: Combustion duration from 10 to 90% mass fraction burnt**

The in-cylinder pressure depicted on Figure 133 and the heat release shown on Figure 134 at 5000RPM demonstrate the very good agreement between the predictive model and the reference one.

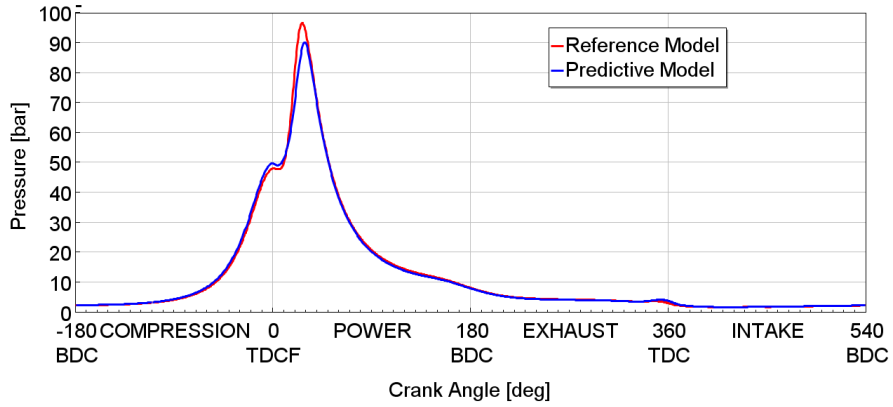


**Figure 133: In-cylinder pressure at 5000RPM**

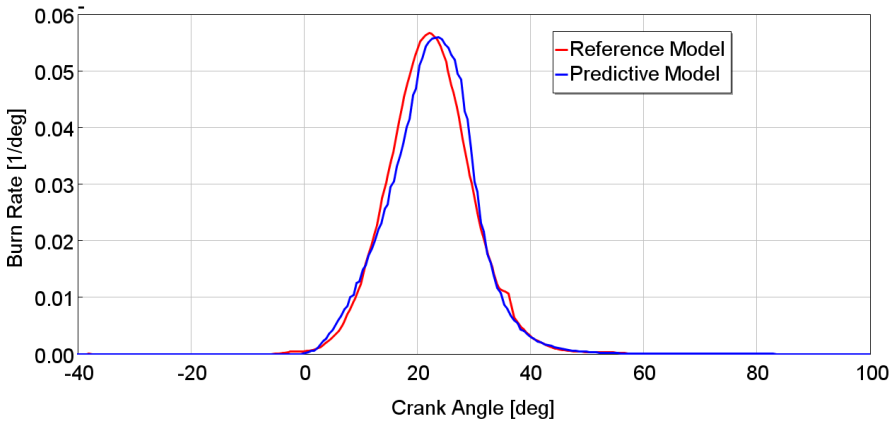


**Figure 134: Heat release at 5000RPM**

Then the knocking model needs to be set. It is quite complicated to adequately define all the 3D thermal conditions and turbulence in the cylinder. And thus the activation energy defined for the knocking process initiation is corrected with a coefficient for the different engine speeds but will remain the same for all the presented investigations. The knock model uses the knock integral $I_k$ from equation ( 3.48 ). The target value represented on the Figure 135 defines the upper limit. The model needs to take into account the protection of the exhaust line components. This control can be done on the fuel injection to maintained the exhaust temperature lower than 1250K as shown on Figure 136.

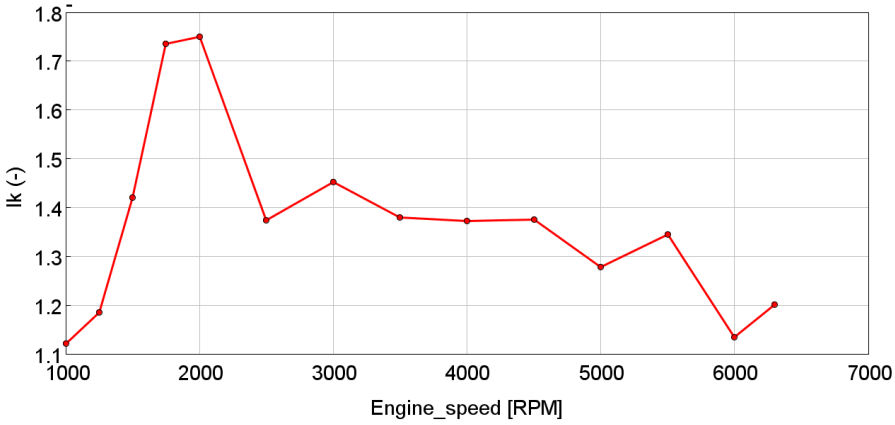


**Figure 135: Knock integral limits**

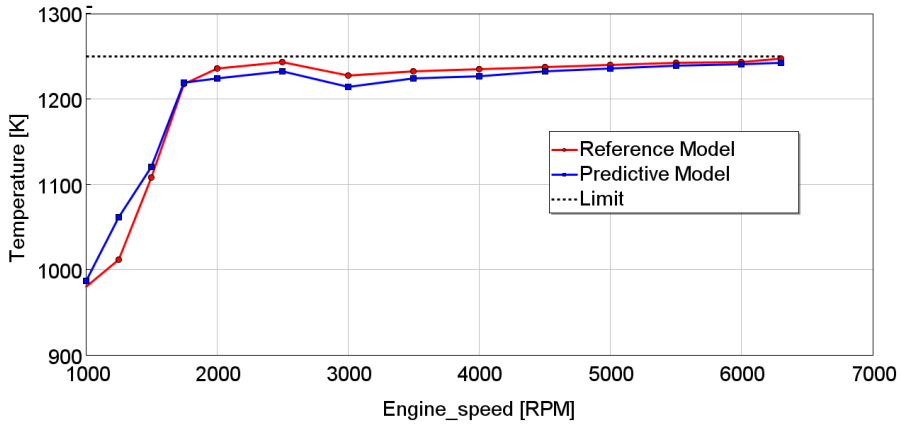


**Figure 136: Exhaust temperature at Full Load**

The exhaust temperature is kept under the limits and the enrichment is applied. The Figure 137 shows how the enrichement is required from 2000RPM to the maximum engine speed. The predictive model reproduces quite well the required enrichement quantity. The ability of the model to estimate the knock is validated.

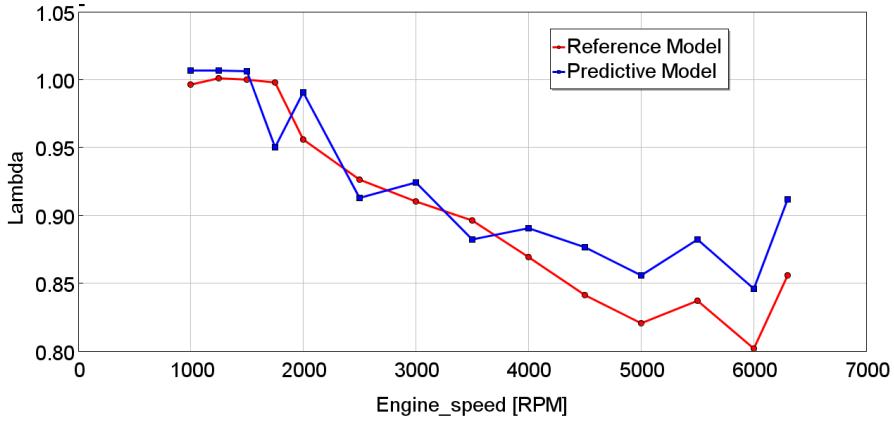


**Figure 137: Lambda at Full Load**

The MFB50, represented on Figure 138, is accurately simulated by the predictive model too.

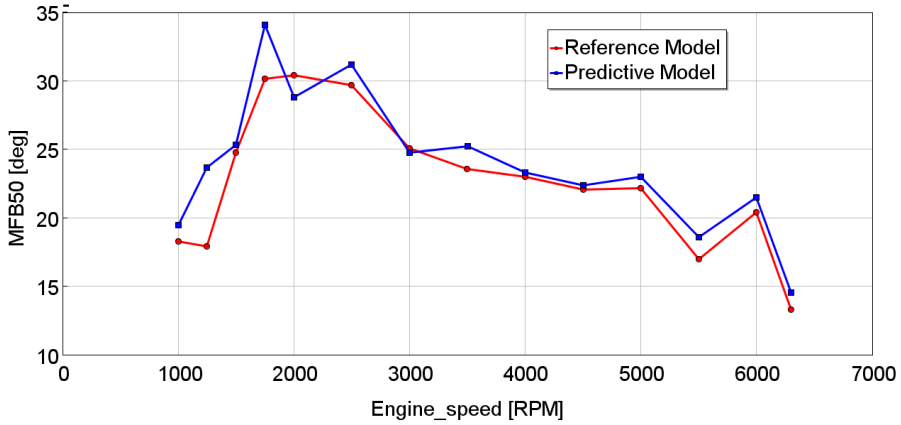


**Figure 138: MFB50 at Full Load**

The Figure 139 and Figure 140 show the good agreement of the two models on the exhaust and intake mean pressure at full load. The two models are using the same compressor and turbine maps.

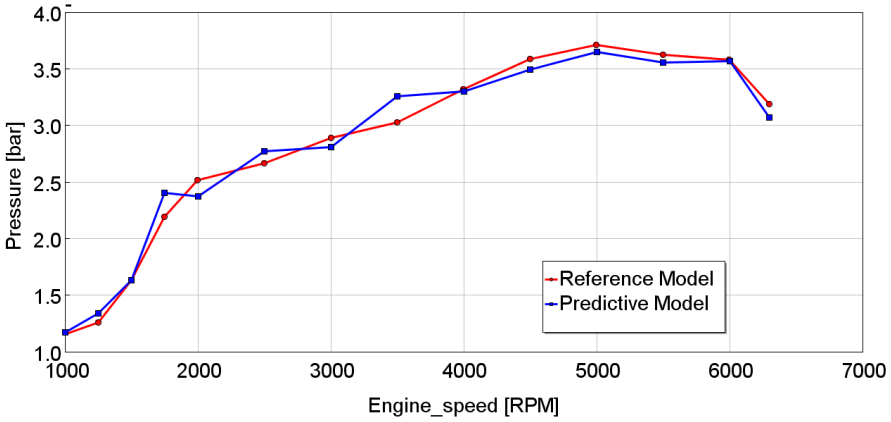


**Figure 139: Exhaust mean pressure**

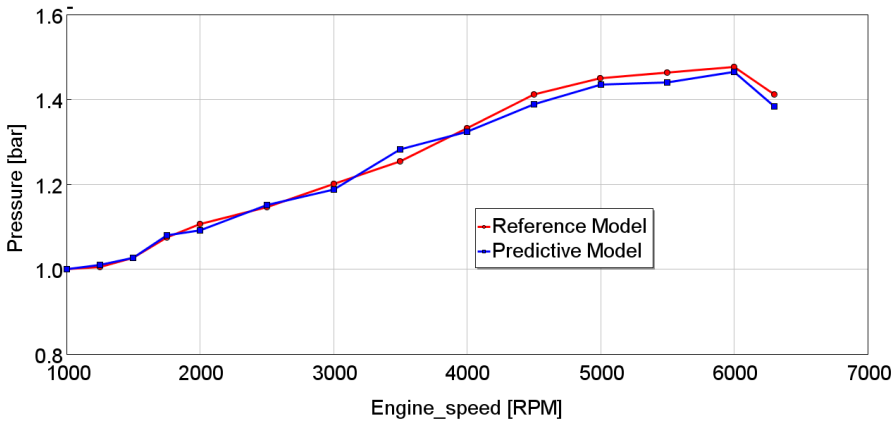


**Figure 140: Intake mean pressure**

The resulting torque depicted on Figure 141 is quite accurately simulated. There is a small gap between the two configurations, the output torque is higher with the reference model. This can be explained by the combustion duration. Nevertheless the Ck value is maintained constant over the whole engine operating condition to make the comparison easier. The model will be used in comparison between different air intake architectures, the model is considered accurate enough to launch the investigation.

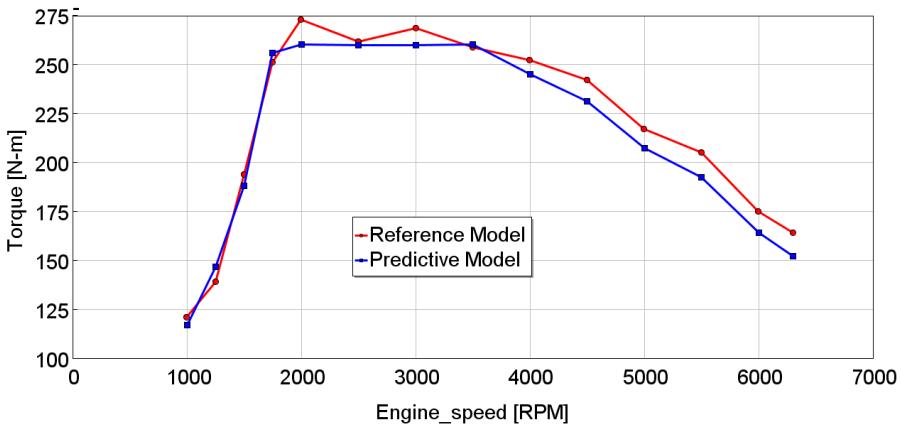


**Figure 141: Full load curve**

### 5.3.2 Adaptation to λ=1

The European commission pushes strongly to keep emissions controlled in real driving conditions [2]. Furthermore the catalyst can convert properly the main part of the raw emissions such as carbon monoxide, hydrocarbon or nitrogen oxide when the mixture ratio at the catalyst inlet remains stoichiometric. To cope with it, the model is now tuned with lamba=1 injection as depicted in the Figure 142. The Ik target value are not modified so that the knock risk assessment remains the same.

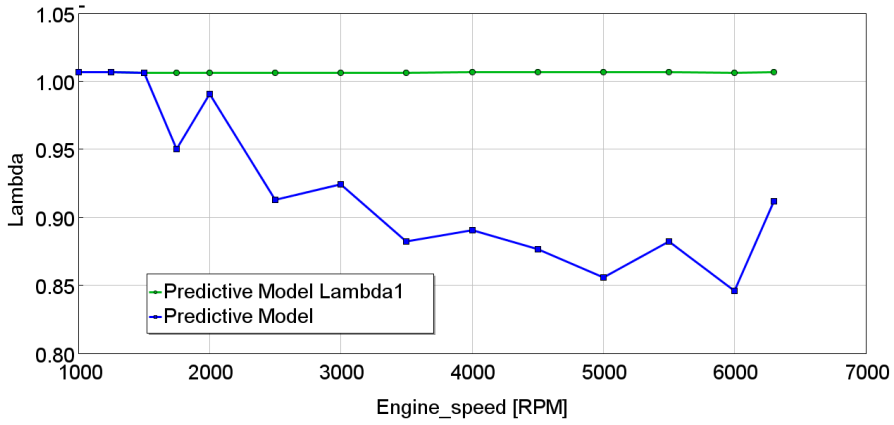


**Figure 142: Lambda at full load conditions**

The exhaust temperature still needs to be maintained under 1250K as shown on the Figure 143. Its control is then handled through a WG opening control. Indeed the exhaust pressure, depicted on the Figure 144, is reduced because of the WG opening.

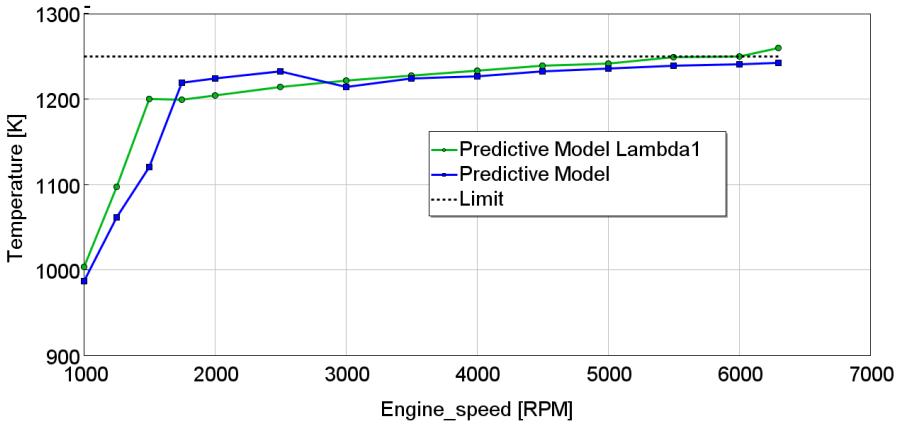


**Figure 143: Exhaust temperature at Full Load**

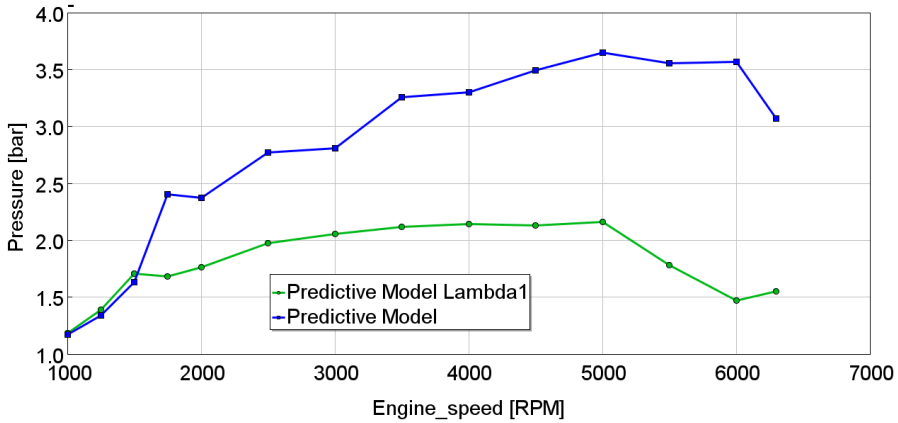


**Figure 144: Exhaust pressure at Full Load**

The reduction of the turbine inlet pressure induces a reduction of power recovering at the exhaust and thus reduces the intake pressure as depicted on Figure 145.

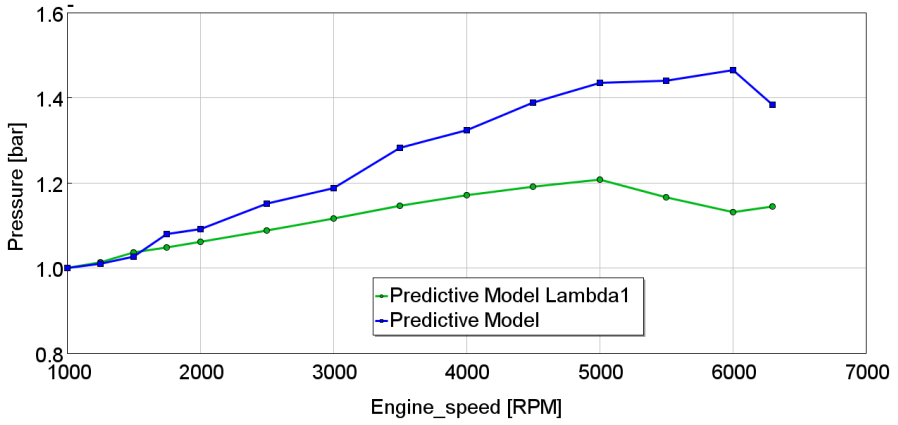


**Figure 145: Intake pressure at Full Load**

The combustion model reacts to these changes with an earlier combustion which results from lower knock risk. The Figure 146 shows the earlier in-cylinder pressure peak at 5000RPM. The MFB50 depicted on the Figure 147 demonstrates the effect of the reduced pressure with an earlier combustion.

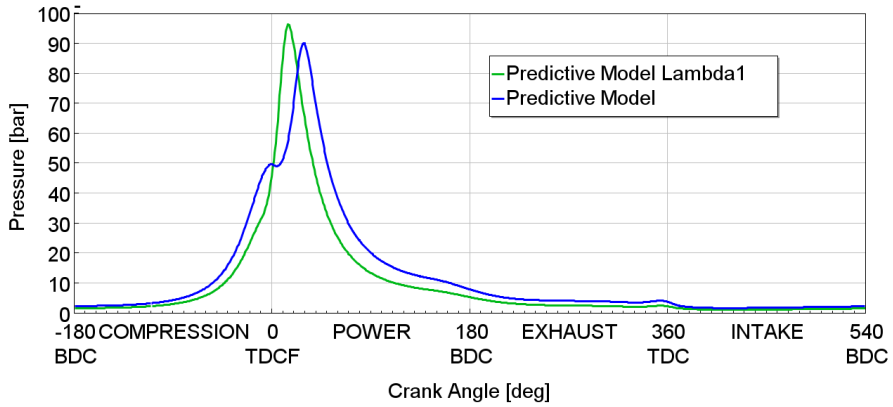


**Figure 146: in-cylinder pressure at 5000RPM**

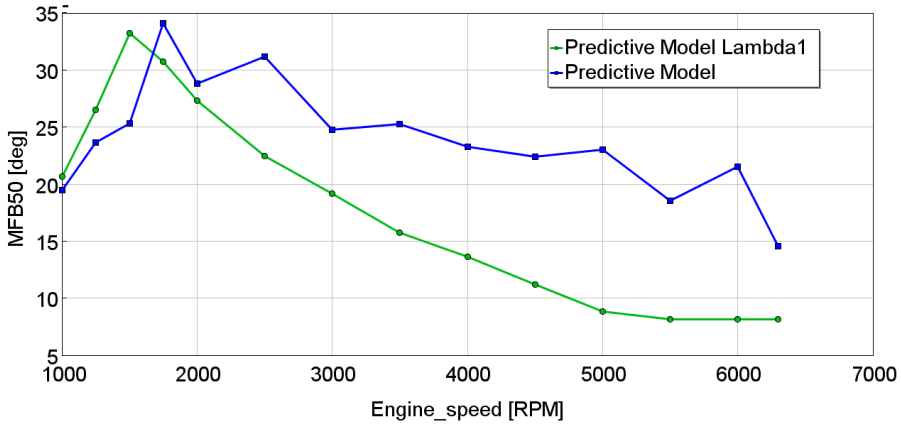


**Figure 147: MFB50 at Full Load**

Obviously the reduction of the air intake pressure leads to the reduction of the torque and cannot be compensated by the earlier combustion. The Figure 148 shows that suppressing the enrichment leads to a reduction of almost 50N.m from 2000RPM till maximum engine speed.

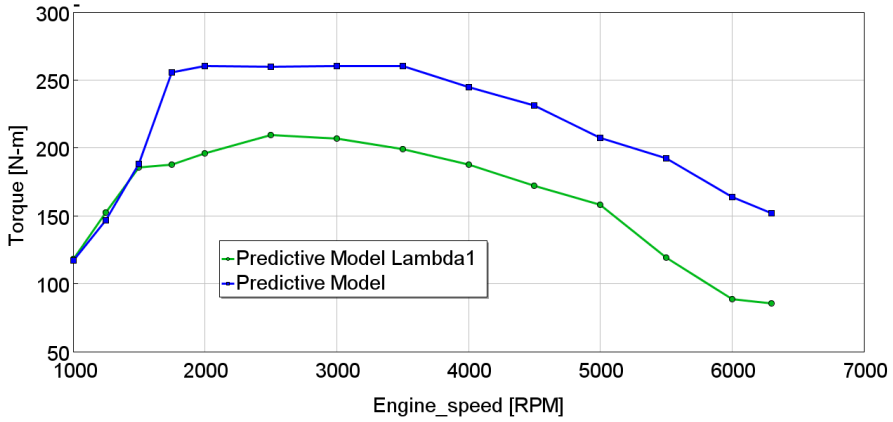


**Figure 148: Full torque torque**

This model is used firstly to define the potential of the different tested configurations and to help defining the layout. The simulation results are used to rank the solution by comparing the output power with the base line set up.

## 5.4 Simulation results on complete engine

The base line configuration is compared with the expansion device. Engine conditions are kept constant. The mixture stays stoichiometric in all conditions. The boost pressure is regulated to keep the exhaust temperature lower than 1250K. The spark advance is controlled to keep the same knocking risk as the base line. The output power and torque can be directly compared with two different expansion lengths (1000 and 1200 mm) in each side (as described in Figure 125).

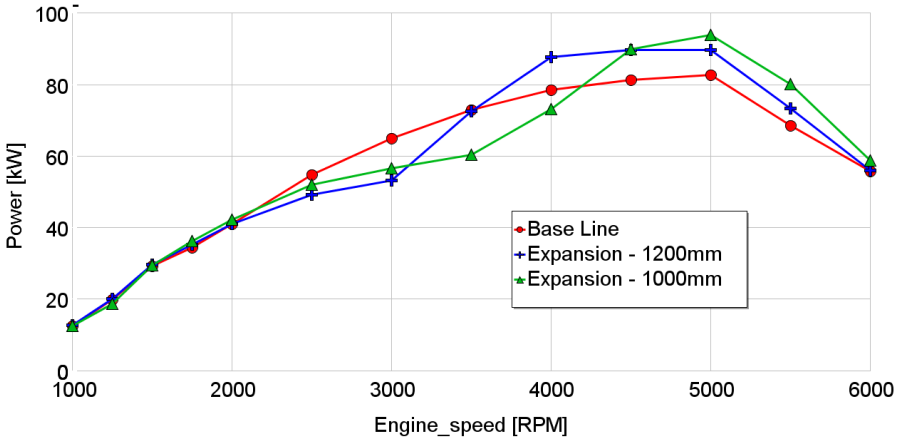


**Figure 149: Power variation with and without expansion effect**

As depicted in Figure 149, the benefit is about 10kW at maximum power which is more than a 10% increase. The configuration with the 1000mm gives the best output power at 5000 RPM. However, with the 1200mm, it is possible to improve the situation in a wider engine speed range. The range around 3000RPM reveals lower power with the expansion device compared to the base line. This issue will be addressed with a damping system in the investigation and will be investigated later.

The power increase is not coming from the volumetric efficiency enhancement as shown on Figure 150. Actually the volumetric efficiency is lower with expansion. Around 3000RPM, where the expansion provides better volumetric efficiency, the power is lower.

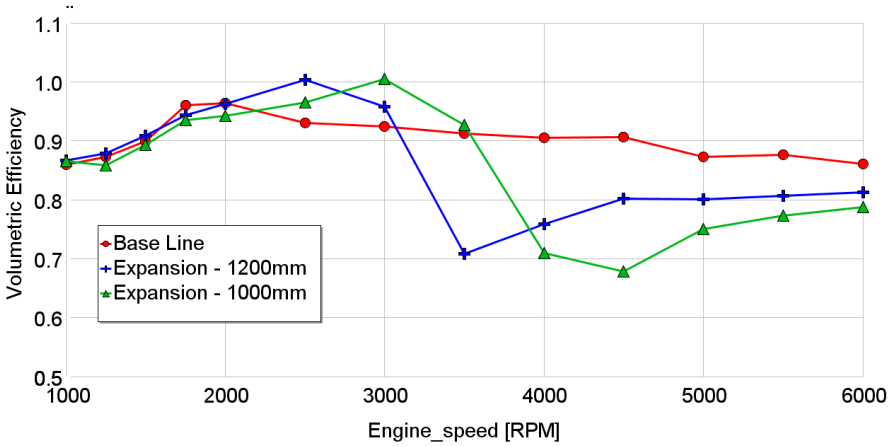


**Figure 150: Volumetric efficiency with and without expansion effect**

Figure 151 clearly shows the reason of the volumetric efficiency reduction hence the pressure wave exhibites a minimum when valves are closing. The waves phase difference between one branch (cylinders 1-4) and the other (cylinders 2-3) is 180° CA. The frequency is the same as the engine and not twice as usually is the case for a four cylinder engine.

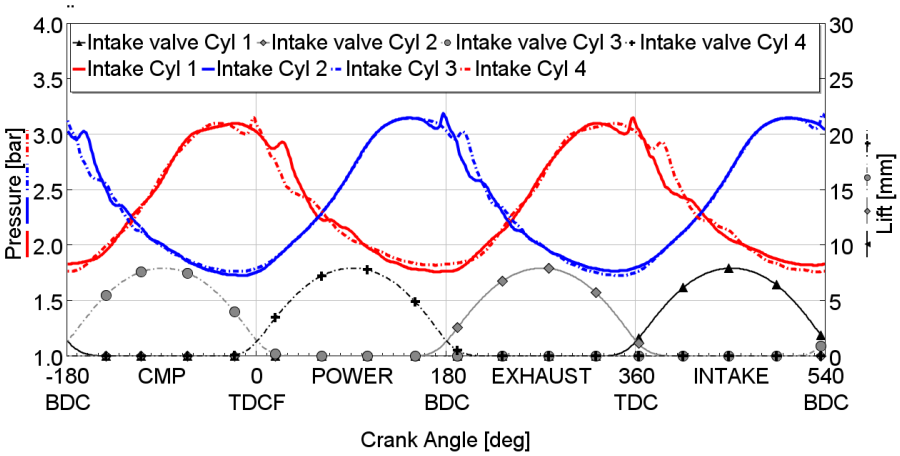


**Figure 151: Pressure upstream the intake valve with 1000mm at 4500RPM**

The pressure gets to a minimum each time the corresponding intake valve is closing. This expansion will profit the engine as it cools down the intake air as depicted on Figure 152. The intake temperature varies with the same shape as the pressure. The oscillation of temperature is about 25K from mean temperature to peak.

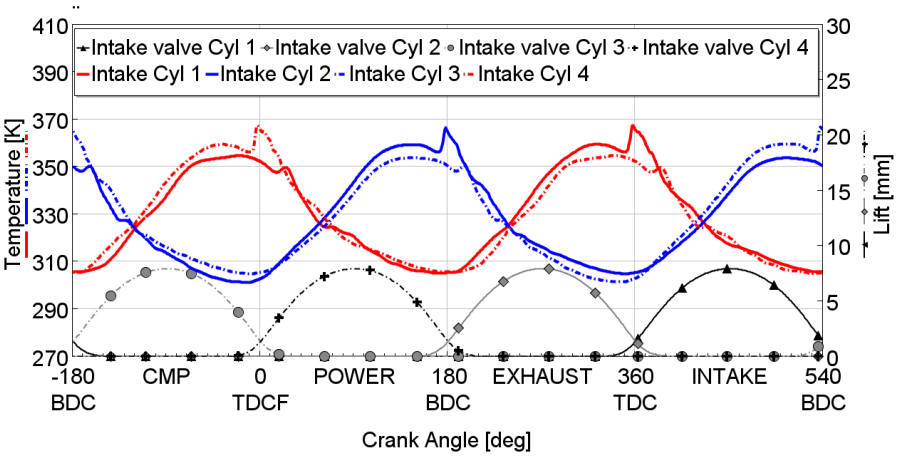


**Figure 152: Temperature upstream the intake valve with 1000mm at 4500RPM**

The Figure 153 shows the comparison with the Base Line. The variation of the mean pressure compensates the volumetric efficiency reduction. The Base Line does not exhibit high oscillation.

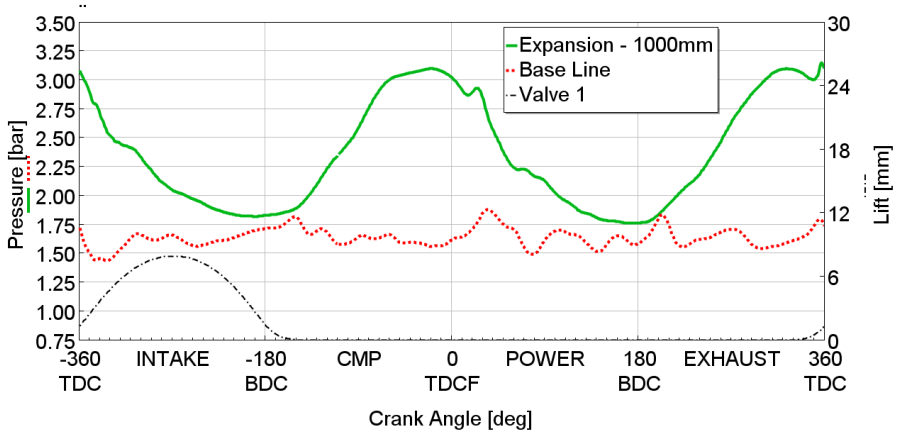


**Figure 153: Cylinder 4 intake pressure with 1000mm length at 4500RPM**

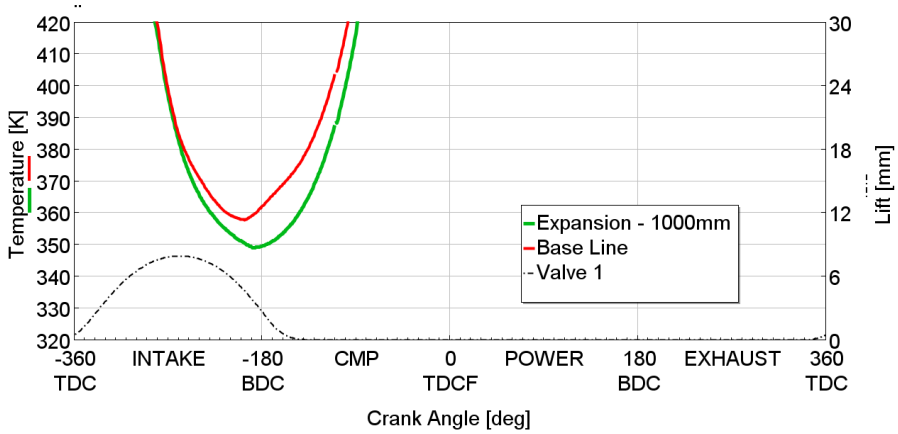


**Figure 154: Cylinder 4 temperature with 1000mm length at 4500RPM**

The in-cylinder temperatures, on Figure 154, are in a good agreement with the observed temperature at the intake and show a temperature reduction of about 15K compared to the base line. This helps for an earlier combustion and so reduces the exhaust temperature. In this investigation this potential is used to increase the boost pressure while keeping the same knocking tendency. Thus more output power around 4500RPM can be produced while the exhaust temperature stays below 1250K as shown in Figure 155.

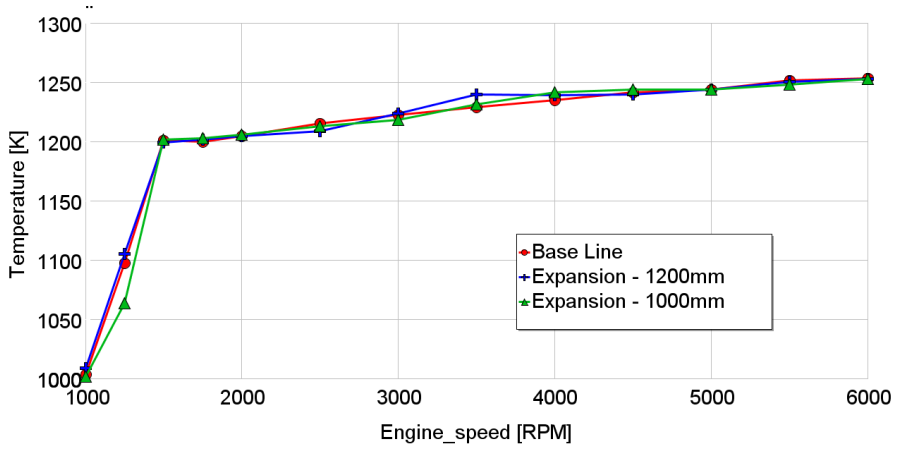


**Figure 155: Exhaust gas temperature**

Nevertheless some parameters need to be adapted to actually benefits from the expansion device. The Figure 156 shows that the maximum in-cylinder pressure increases by 10% which is anyway lower than current Diesel engines but would require an engine adaptation compared with the base line.

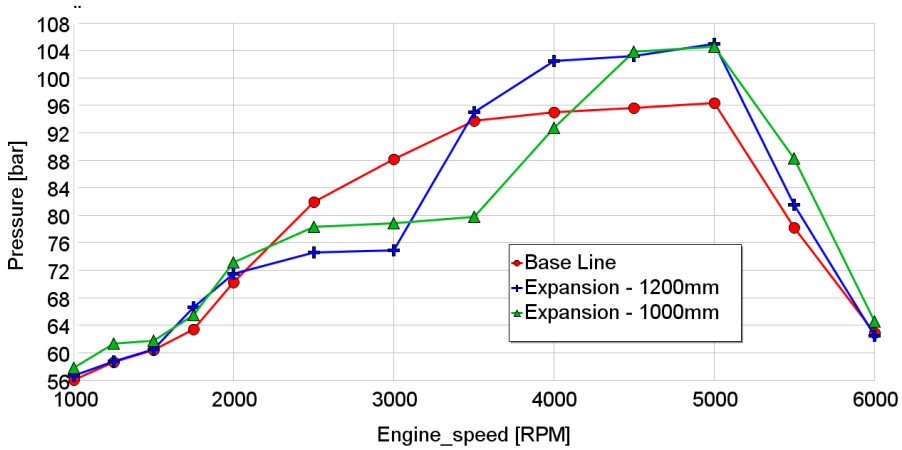


**Figure 156: Maximum in-cylinder pressure**

Furthermore as mentioned earlier the volumetric efficiency reduction needs to be compensated with a higher boost pressure (Figure 157) which is usually achievable with turbocharger at this operating condition.

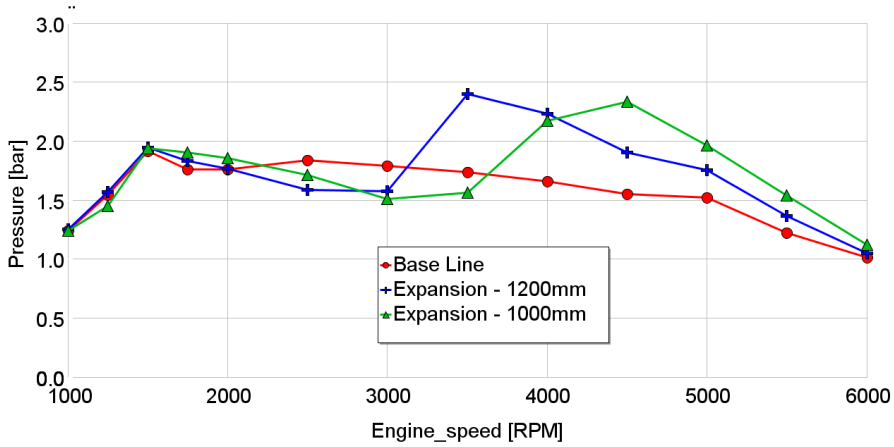


**Figure 157: Compressor outlet pressure**

The impact of the upstream ducts has been investigated through a DOE at 4500RPM by varying both the expansion length and the connection pipe between the cooler and the T pipe connecting the cooler to the expansion length.

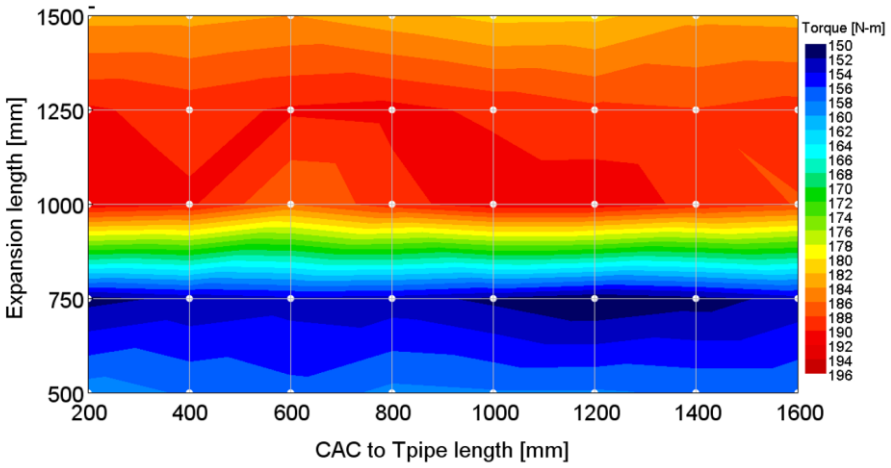


**Figure 158: DOE - piping length variation impact on torque output**

Figure 158 and Figure 159 reveal that the upstream and downstream CAC ducts lengths barely affect the output torque. So the system can be easily tuned only through a variation of the expansion lengths.

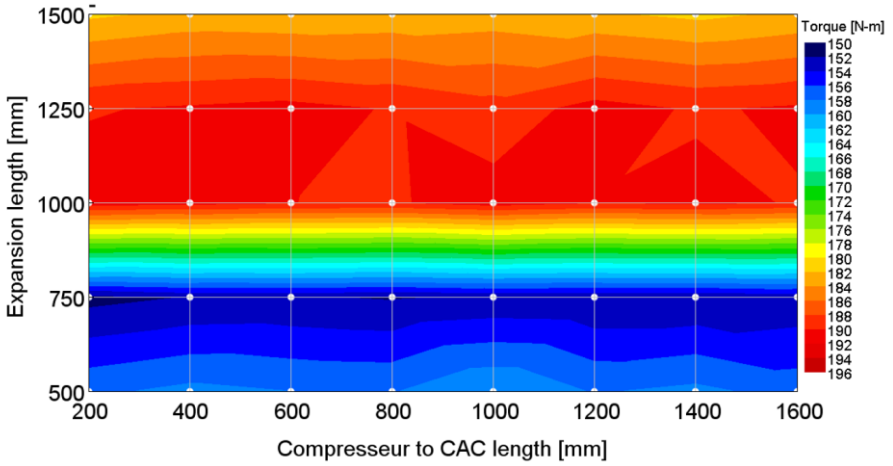


**Figure 159: DOE - piping length variation impact on torque output**

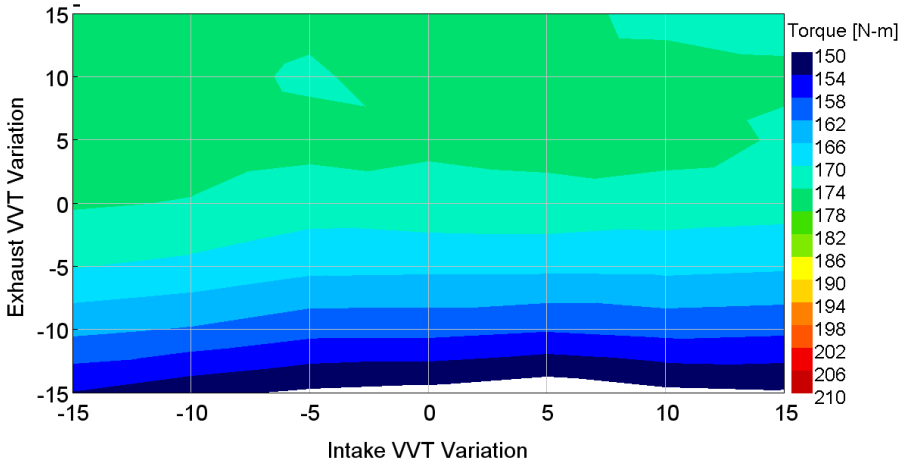


(a)

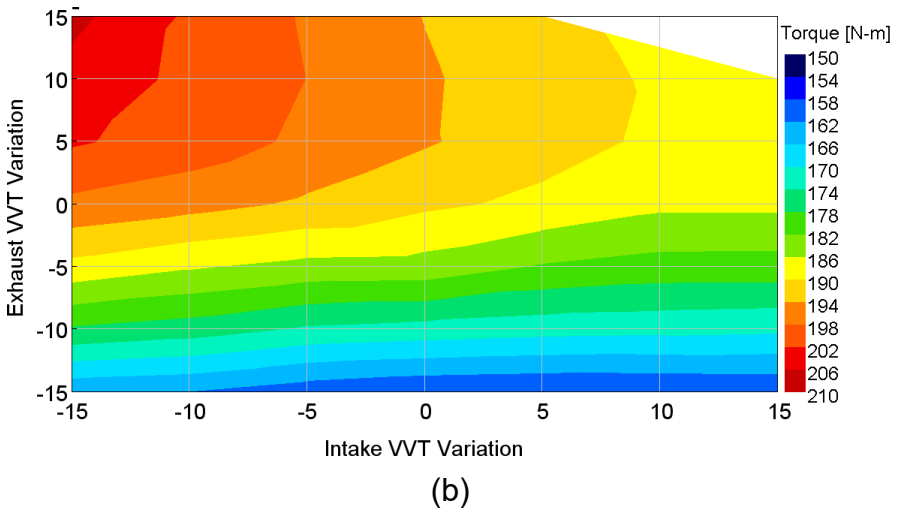


(b)

**Figure 160: Torque output with different intake and exhaust valve timing on base line (a) with expansion 1200mm (b)**

The Figure 160 shows that the valve timing variation does not provide much improvement for the base line. Indeed the exhaust valve timing is quite sensitive whereas the intake valve timing doesn't modify much the performance. With the expansion manifold there is room to increase the output torque with earlier intake valve closing and later exhaust valve closing.

The simulations have shown 10% increase in power and the compressor ability compensate the volumetric efficiency reduction. High pressure pulsation level has been provided with expansion length. The validation of those results is handled through engine tests reported in the next part.

## 5.5 Engine test

### 5.5.1 Engine set up

The engine has been mounted at the CMT Valencia. An opened Electronic Control Unit (ECU) has been used to take the control of the different parameters of the engine such as the injection quantity through the injector opening time, the spark timing control the start of combustion. The turbocharger operating point can be adjusted with the regulated waste gate.

The engine runs in safe operating conditions thanks to different limits (as described in Table 14). Those limits have been defined by Renault to ensure no damage on the system for all normal operating conditions.

**Table 14. Limits**

| | Limits |
|---|---|
| Maximum cylinder pressure | 100 bar |
| Intake pressure | 2,6 bar |
| Compressor outlet temperature | 170°C |
| Turbine inlet pressure | 2,8bar |
| Turbine inlet temperature | 950ºC |
| Turbocharger speed | 255 000RPM |

The turbocharger speed limit is defined by the supplier it is usually related to the speed of the blade, for this turbocharger it is set at 255000RPM.
The in-cylinder pressure is measured with instrumented spark plugs. The maximum pressure can be controlled. The knock is also evaluated with the in-cylinder high frequency pressure amplitude, as described in the paragraph 2.4.1.
The Figure 161 exhibits the positions of the sensors used on engine test bench. A Kistler 4007C pressure sensor has been positioned in each branch of the expansion system upstream the intake valve at cylinder 1 and cylinder 2. The simulation has demonstrated that the pressure at the cylinder 4 intake valve is equal to cylinder 1 and the same between cylinder 2 and 3. Two K type thermocouples (Ø1mm) have been monted at each branches of the expansion device.

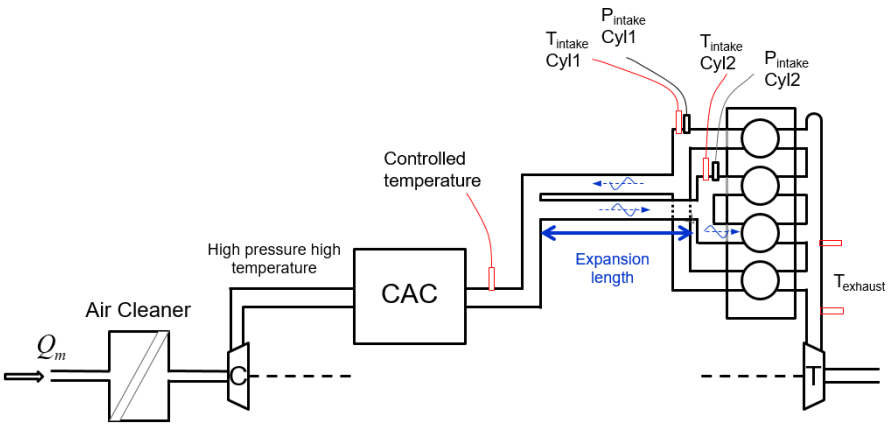


**Figure 161: Measurement sensors positions**

The temperature at the exhaust is evaluated through two thermocouples located in exhaust manifold and at the turbine inlet. The maximum of those two needs to stay lower than the limit. This is required to ensure the exhaust line won't melt neither the turbine would be damaged.

### 5.5.2 Results

#### 5.5.2.1 Installation

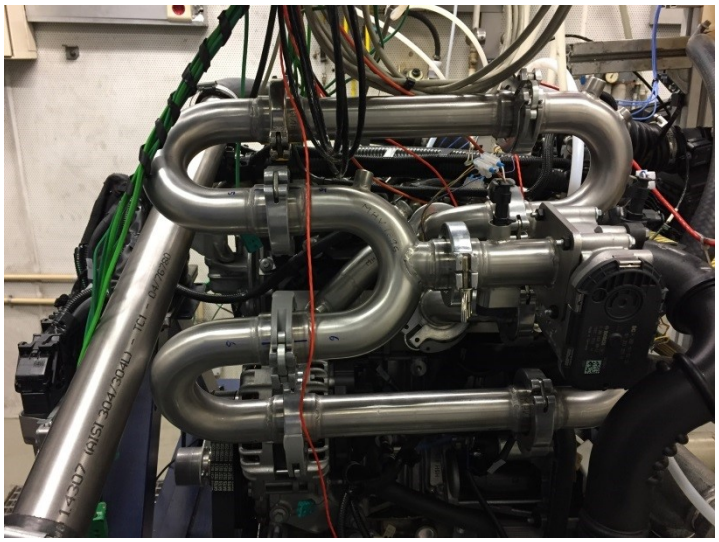

**Figure 162: Prototype installation**

The prototype made of stainless steel is placed instead of the mass production plastic air intake manifold, as depicted on Figure 162.
The sensor used for ECU control are placed directly downstream the throttle body and thus farer from the intake valves. The controlled of the air fuel mixture are handled manually. The ECU has been tuned for the volumetric efficiency of the mass production line injected too much fuel as the air mass trap in the cylinder is much lower with the gas expansion concept for the same mean pressure value. The installation of this concept on an engine requires an adaptation of the parameter used for air flow evaluation in the ECU. The operator used the lambda sensor at the exhaust to control the injection duration and thus ensure combustion at lambda 1 till there is no scavenging.
The measurement are carried out on engine test bench, the displacement of the vehicle cannot provide the air through the charge air cooler to cool down the air coming from the compressor. The mass production air to air cooler has been replaced by a water charge air cooler. The water flow is controlled to keep the outlet air temperature constant.

#### 5.5.2.2 Mean values analysis

The Figure 164 shows the output torque with the expansion length of 1200 mm and 1000mm. Those two configurations can be compared to the base line and the configuration presented in Figure 163, where a bypass duct has been placed between the ducts connected the cylinder 1-4 and 2-3. This last configuration stands for a deactivation of the expansion device.

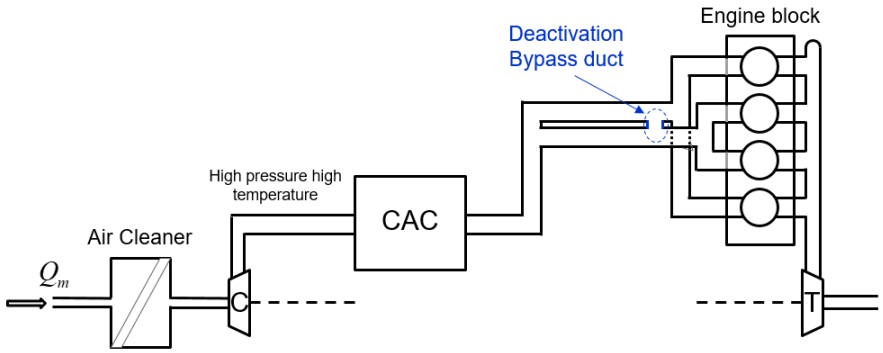


**Figure 163: Deactivation system**

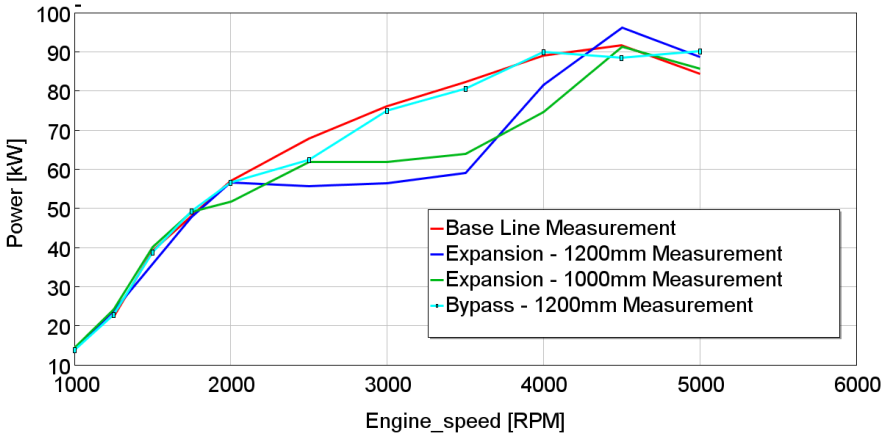


**Figure 164: Output power with the expansion length compared to base line**

The measurements are in good agreement with simulation and show the drawback of the system with both 1000 and 1200mm length from 2000 to 4000 RPM. The aim of the interaction between the cylinders is to increase the maximum power and this is shown on the graph at 4500RPM. The simulation, Figure 149, demonstrated an increase of about 10% from 81kW to 93kW. The measurement shows a bit less enhancement of the power with 5.5% from 91kW to 96kW at 4500RPM and almost the same ratio at 5000RPM.
To understand the differences, the exhaust temperature can be checked on the Figure 165.

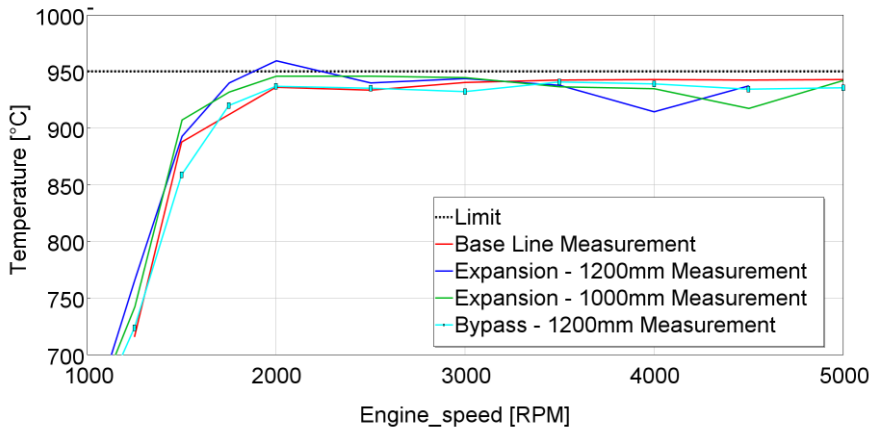


**Figure 165: Exhaust temperature measurement**

The exhaust temperature has been well controlled. It can be noticed that the exhaust temperature remains lower than the limit with the expansion 1200mm at 4000RPM and with 1000mm.

The air fuel mixture can be checked through the Figure 166. The measurement shows the same mixture for all which is almost stoichiometric.

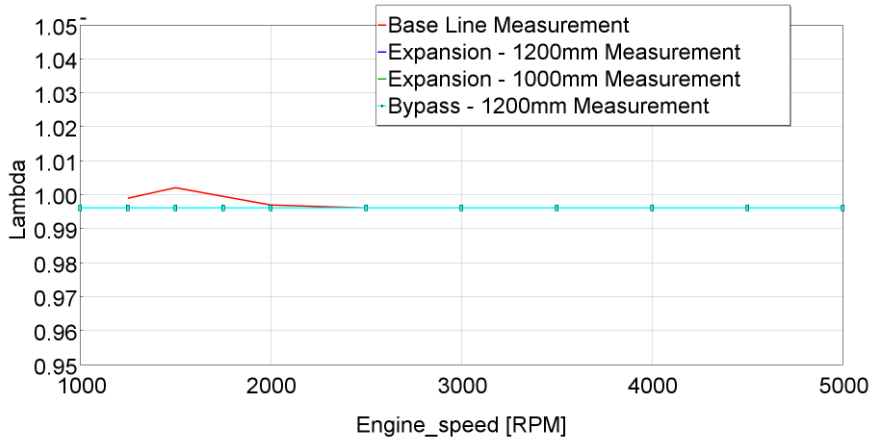


**Figure 166: Lambda measurement**

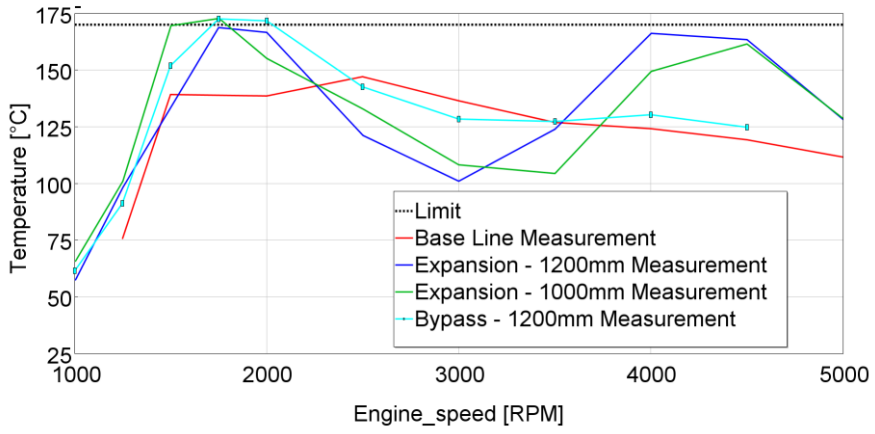


**Figure 167: Compressor outlet temperature**

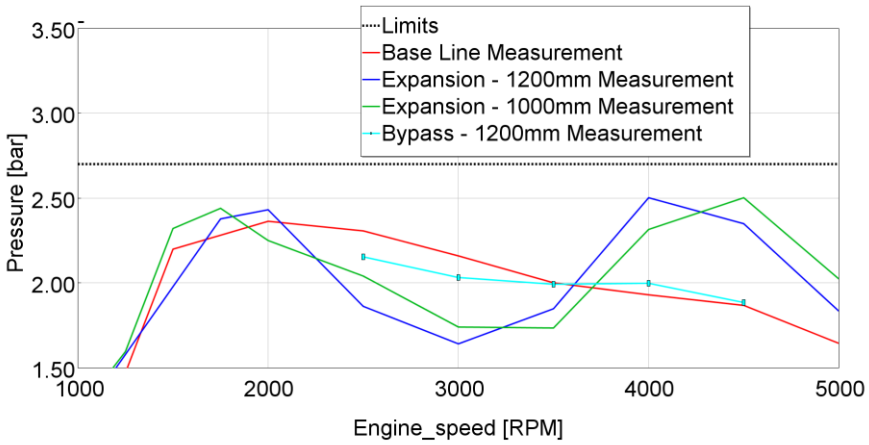


**Figure 168: Compressor outlet pressure**

The volumetric efficiency has been affected by the expansion device. Its decrease needs to be compensated by the boosting system which can be seen through the outlet temperature (Figure 167) and pressure (Figure 168). The outlet compressor temperature hits the limit for the operating points where the exhaust temperature limit was not reached. The turbocharger speed is also limited at 255 000RPM. The Figure 169 indicates that this limit has not been overpassed even a reasonable margin has been maintained.

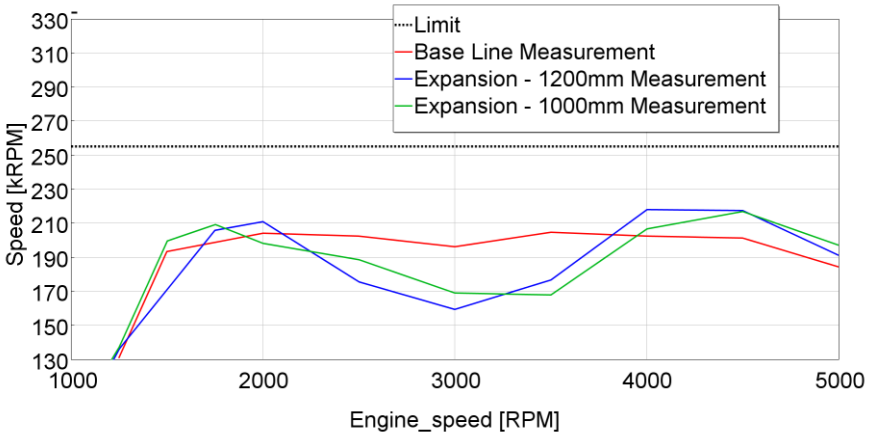


**Figure 169: Turbocharger speed.**

Another critical area consists of the turbine inlet. Not only needs the temperature to be controlled but also the pressure. The Figure 170 pressure shows that a margin is maintained only the short expansion hits the limit at 4500RPM which explained that no benefice at 4500RPM has been gained.

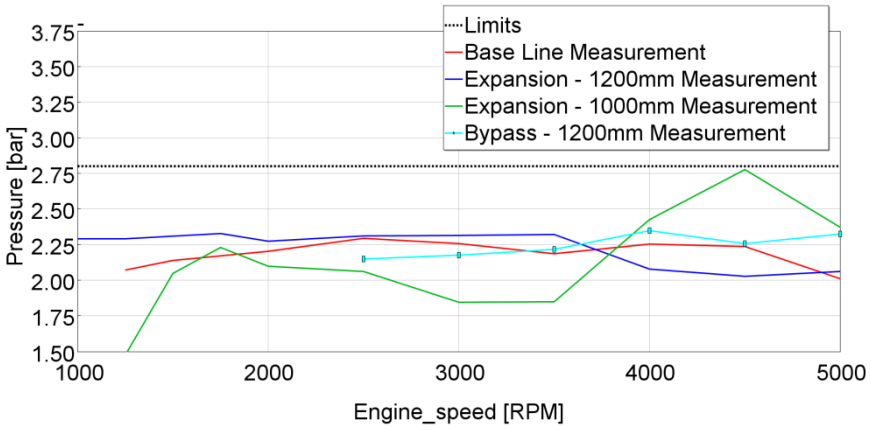


**Figure 170: Exhaust pressure**

5.5.2.3 Unsteady quantities

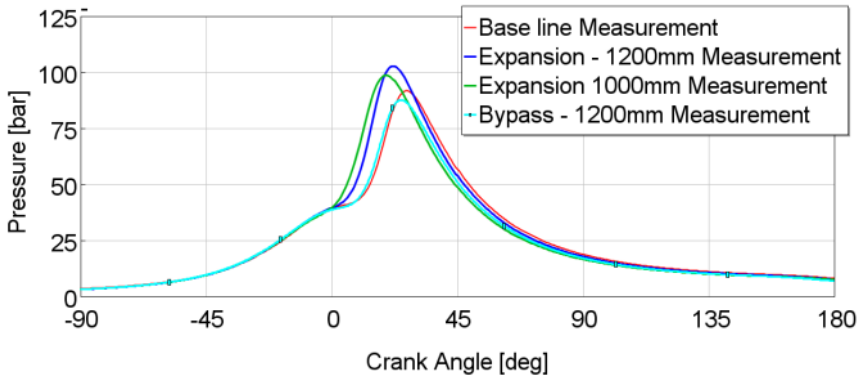


**Figure 171: In-cylinder 1 pressure at 4500RPM**

The in-cylinder 1 pressure reported in Figure 171 shows that both configurations with the expansion device present earlier combustion peak compared to the configuration with base line or bypass configuration. The reduction in temperature aims to go in that direction. Nevertheless it has be considered that the intake and exhaust temperatures and pressures are not the same. The recorded pressure is not only the direct effect of the unsteady expansion but by the mean values changes as well. As an example the compressor works with higher compression ratio with higher outlet pressure and temperature (Figure 168 and Figure 167).

The comparison between simulation and measurement, in Figure 172, shows some differences in both the combustion timing and in the compression phase not only a shift but also the slope during the compression. The timing is mainly related to the knocking assessment.

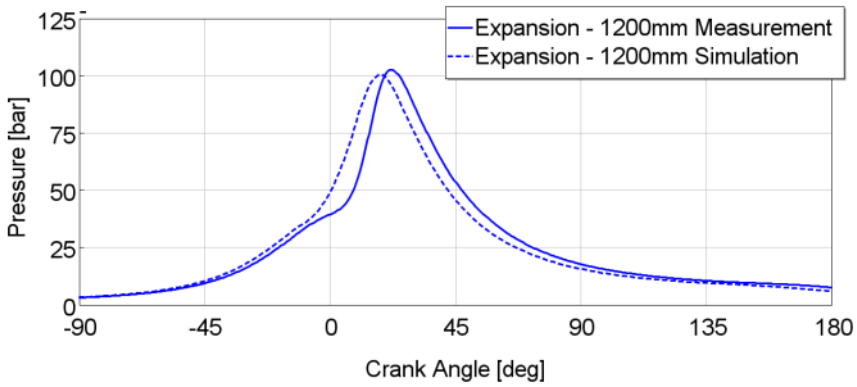


**Figure 172: In-cylinder pressure - comparison between simulation and measurement**

The available test facilities for this study do not integrate any possibility to get the temperature with a crank angle resolution. Nevertheless the effect of the dynamic expansion can be assessed through the pressure pulsation upstream the intake valve (as depicted in Figure 173).

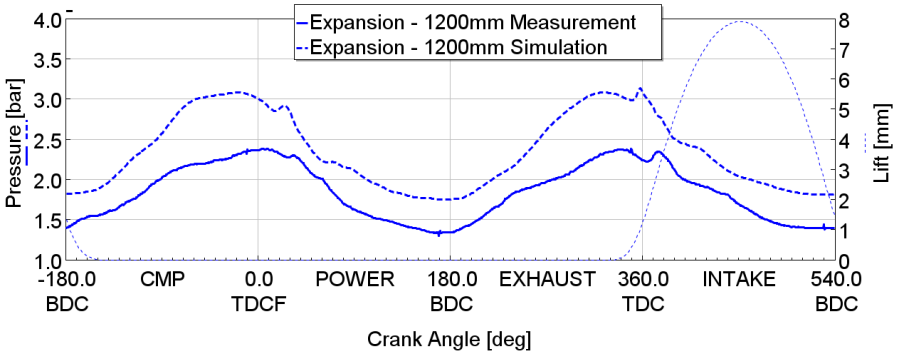


**Figure 173: Pressure at 4500RPM upstream cylinder 1 intake valve.**

The pressure recorded upstream the cylinder 1 intake valve (Pintake Cyl1 from the **Error! eference source not found.**) shows the optimum effect of the expansion when the minimum of the pressure wave happened at the intake valve closing. The comparison between the simulation and the measurement present a shift in boost pressure. Nevertheless the dynamic behavior of the line is pretty well predicted by simulation. The difference in the boost pressure is coming from some discrepancies between the measurements and the simulation as already shown on the cylinder pressure trace (Figure 172). Those differences can be explained by differences in the cylinder wall heat exchange which has not been set but just assessed from another model. Furthermore there is remaining differences in the combustion timing which can result from an inaccurate evaluation of the knocking. This latter effect is also sensitive to the heat losses through the cylinder wall. The simulation and measurement have not been carried out at the same time and the aim of the simulations was to evaluate the potential on the torque and measurement used later to validate the potential. The wall heat loss model could be adapted with the right coolant jacket geometries and more advanced heat model models than the Woschni [31]. This work has not been handled during this PhD Thesis.

### 5.5.3 Valve timing effect

The valve timing effect shown through the simulation has also been investigated with few valves timing variation. The benefit shown Figure 164 at 4500 and 5000RPM was given for an VVT at intake of 30.4 CA and 6.8 CA at the exhaust. The Figure 174 shows the effect of an earlier intake valve closing. The exhaust valve closing variation decrease the output power.

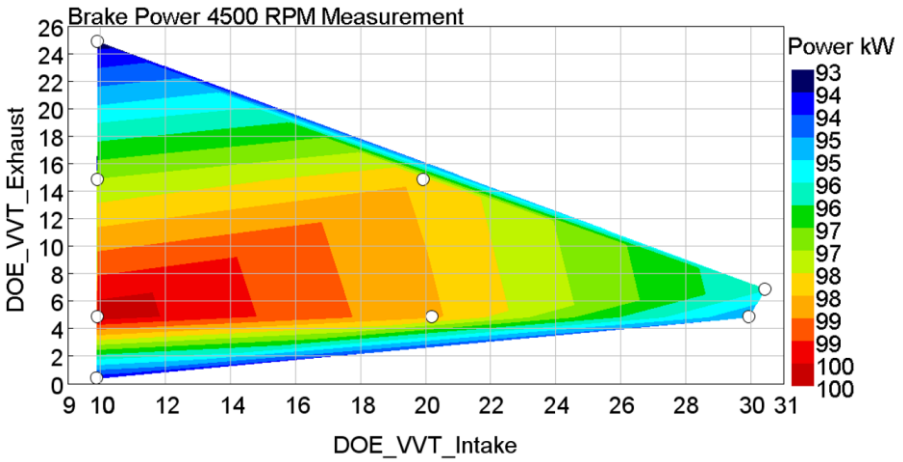


**Figure 174: Effect of the intake and exhaust valve timing on the output power**

The valve timing adjustement gives the chance for 4.5% further increase. A total of 9.5% of power increase can then be obtained.

## 5.6 Discussions

The direct effect of the temperature reduction is quite difficult to evaluate. The crank angle resolution temperature measurement has not been possible during this investigation. The effect can be seen through the earlier combustion. Even the observed difference include the complete system loop effect. Indeed the lower intake temperature gives the chance for an earlier combustion leading to lower exhaust temperature. Actually having an earlier combustion, as shown in chapter 2, gives more expansion in-cylinder. But the exhaust temperature is also controlled through the waste gate position. The exhaust temperature reduction potential is directly used to close a bit more the waste gate and thus keep the exhaust temperature at the same level but providing higher boost pressure. This higher boost pressure will also affect the combustion as the knocking tendency is directly related to the temperature and pressure in-cylinder. Finally a new equilibrium is found which has been shown to give more output power for the engine.

### 5.6.1 Comparison with early intake valve closing – Miller cycle

A common way to achieve an increased expansion in-cylinder, like proposed in the Miller cycle, is to close the intake valve before the piston reaches the bottom dead center. A 1D simulation has been launched to evaluate the difference between the proposed concept

and the early valve closing. The target for the exhaust temperature is maintained. The result of the exhaust temperature controlled is reported on the Figure 175.

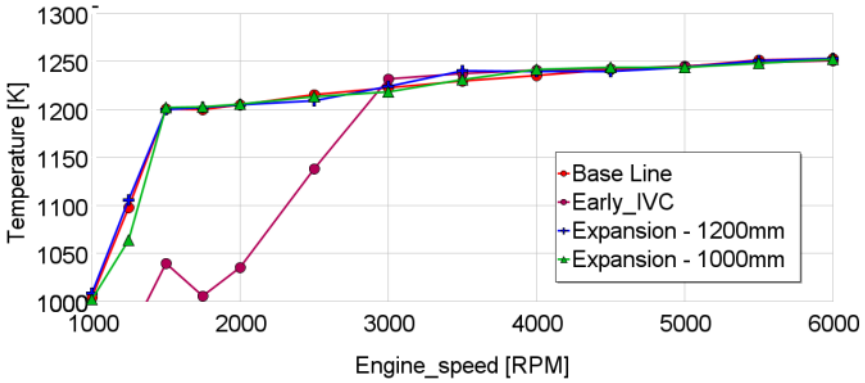


**Figure 175: Exhaust temperature**

The knocking tendency is maintain through the same activation energy target. The intake valve timing is varied as well as the opening duration thanks to scaling shown on the Y axis of the Figure 176. The resulting output power is painted with reddest color for the highest power.

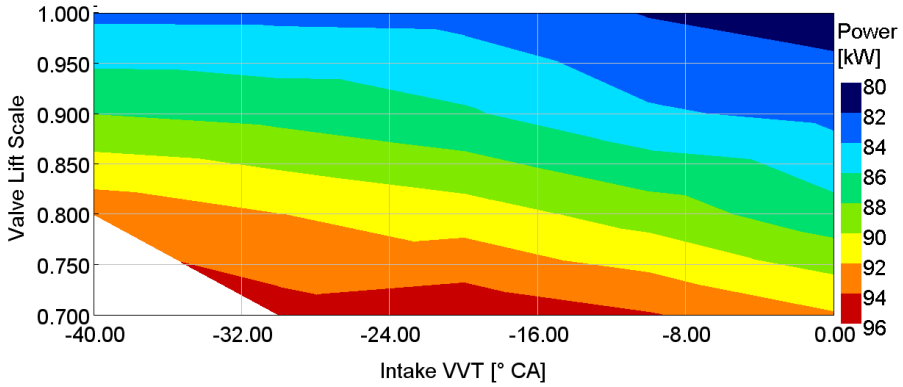


**Figure 176: DOE results of the IVC timing and opening angle on the output power at 4500RPM**

The results show that it is possible to reach higher torque while moving the valve opening earlier. The reduction of the opening time lessens the overlap with the exhaust process. The comparison with the wave action has been handled on the configuration with opening time reduced by 15% (0.85 on Valve Lift Angle scale) and an advance of the intake valve closing of 30° compared to the base line as presented on the Figure 177.

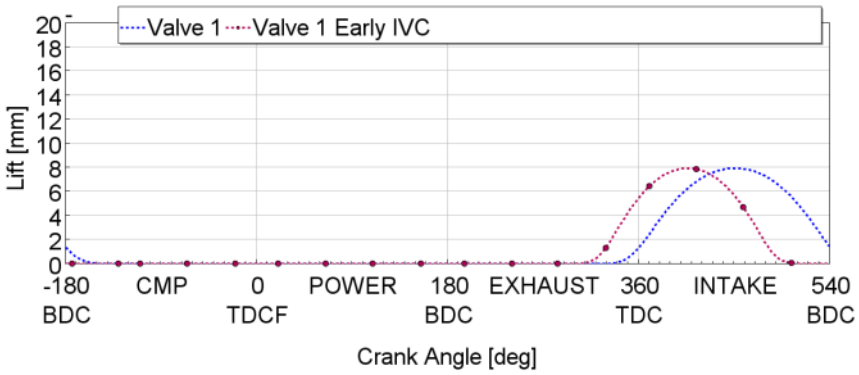


**Figure 177: Cylinder 1 intake valve lift with early intake valve closing set up compared to base line**

The power benefit provided by this early intake valve closing is equivalent to the expansion provided by the wave action at 4500RPM. The engine speed range of benefit is higher with also a great increase at 3000RPM as well as higher in engine speed (Figure 178). For lower engine speed, the pressure losses cost cannot be compensated by the turbocharger and shows reduction on the output power.

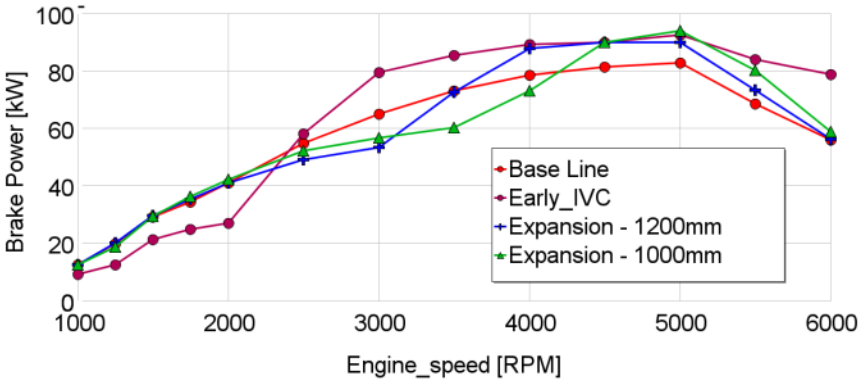


**Figure 178: Output Power with early intake valve closing set up**

Boost pressure reported on the Figure 179 shows the needs for the compressor to increase the boost pressure in order to compensate the reduction in volumetric efficiency.

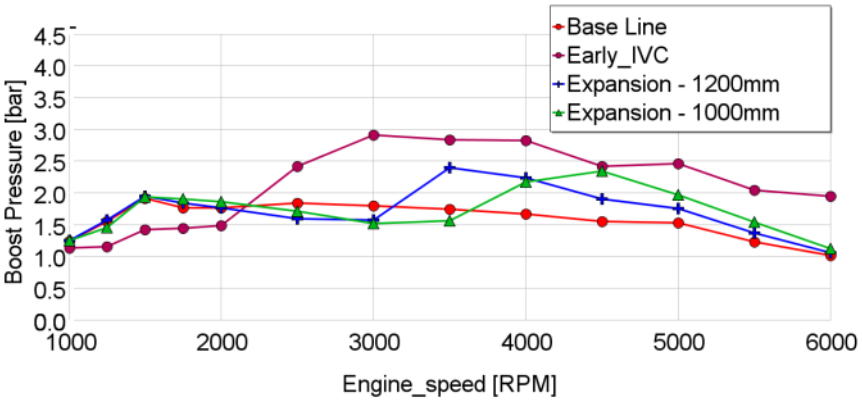


**Figure 179: Boost pressure induced by early intake valve closing**

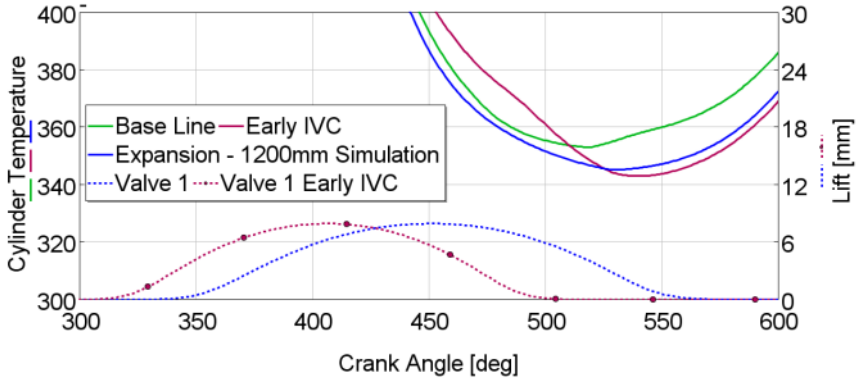


**Figure 180: In-cylinder temperature at the end of the intake process**

The Figure 180 shows clearly the reduction in temperature with both wave action and early intake valve closing just before and during the compression phase which starts at 540° CA.
The cooling is provided in both cases by the expansion in the cylinder. With the early intake valve closing the piston displacement provides the expansion whereas the wave makes it with expansion length. That means also that part of the work as to be provided by the compressor and so the turbine has to recover more energy from the exhaust gases. The higher boost pressure increases, the higher temperature at the compressor outlet is, the CAC has to compensate and provide the same temperature at the intake valve. The cooler has to be layout accordingly.

### 5.6.2 Temperature increase with high wave amplitude

During the measurement the intake temperature is controlled at the outlet of the cooler and two thermocouples have been placed in the intake duct close to the valve approximately at 200mm from the valves of the cylinder 1 and 2. Those thermocouples provided the temperature reported in the Figure 181. As expected the average temperature is not decreased by the expansion effect as it appears only when the intake valve closes. In average for the engine speed lower than 2000RPM there is no difference between the Base Line configuration and the Expansion device. At the speed of 3500RPM the average temperature increases by 25°C.

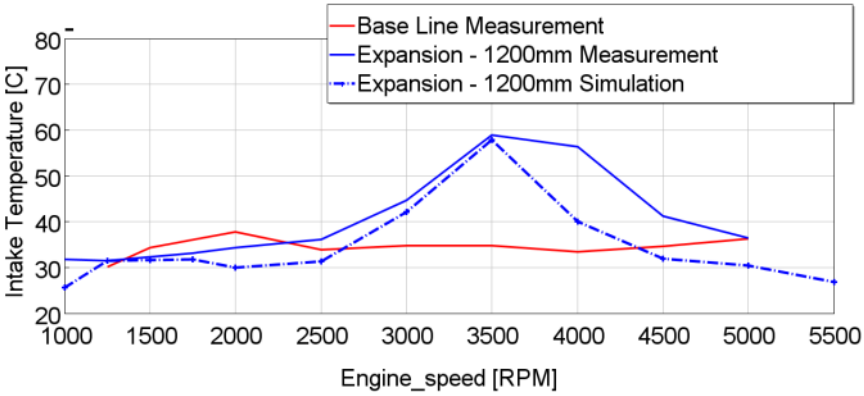


**Figure 181: Effect of the pressure pulsation on the mean intake temperature**

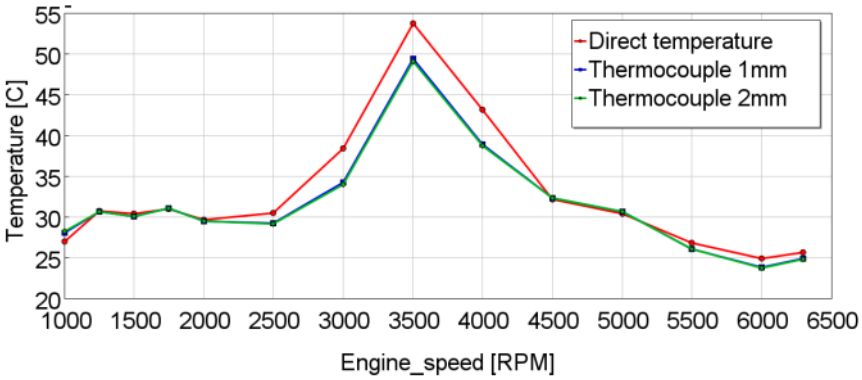


**Figure 182: Temperature from native GT Power simulation and through simulated thermocouple**

As the measurement results comes from thermocouples and there is known inertia and delay provided by such a device. The estimation of the effect of the sensors effect is given on the Figure 182 which shows the bias which can come from the thermocouple. The thermocouple is clearly not the only reason of the increase even if a difference can be observed of about 4°C. The variation of the thermocouple diameter from 1mm to 2mm provides very similar results.

A back flow from the cylinder may bring high temperature gases in the intake ducts. The Figure 183 shows the airflow through the air intake valve at cylinder 1. There is very few air flow at the beginning of the intake process but this does not bring much effect on the upstream temperature recorded too.

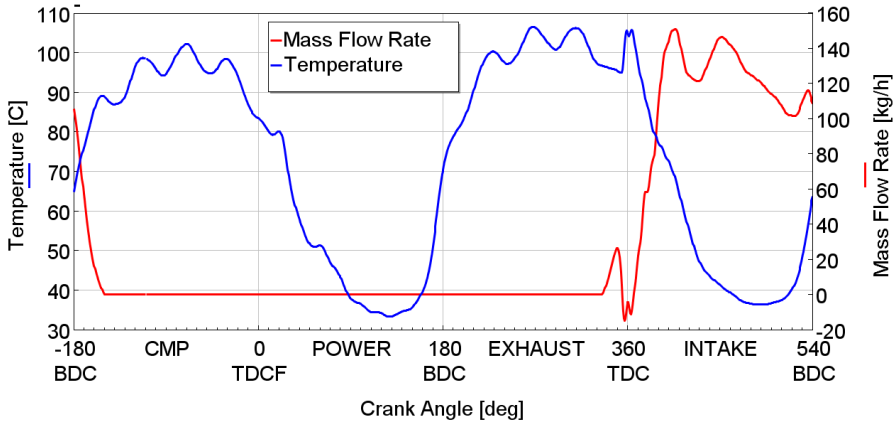


**Figure 183: Airflow at cylinder 1 valve and upstream intake duct temperature at 3500RPM**

The increase in temperature is due to the viscous effect. The Figure 184 shows the same trends between the temperature and the pressure wave amplitude. The viscosity can explain this increase of temperature. The dynamic viscosity and the intake temperature reported in the Figure 185 have pretty similar trend. The high velocity generated by the high wave amplitude leads to high viscous effect.

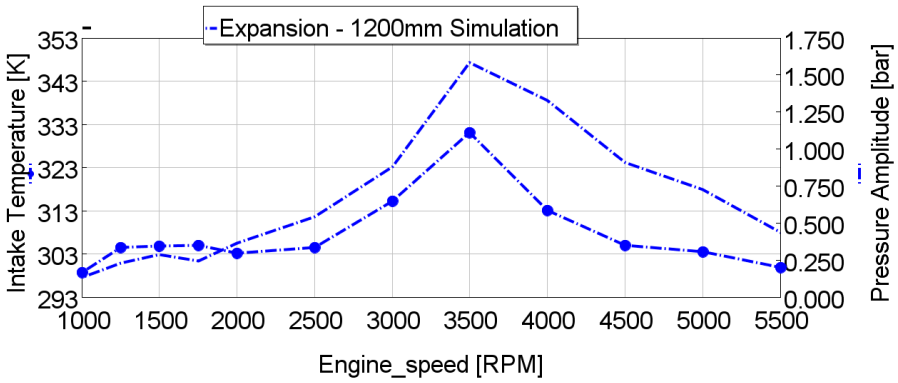


**Figure 184: Temperature and pressure wave amplitude at the intake**

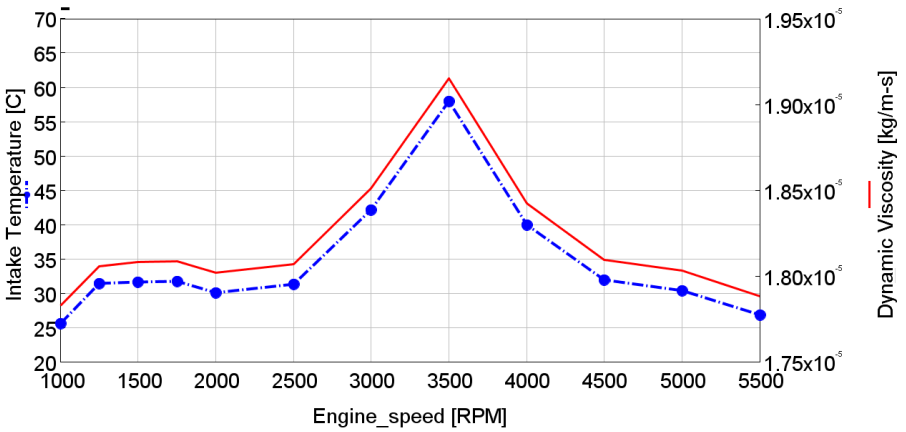


**Figure 185: Dynamic viscosity comparison to temperature**

The mean temperature and the dynamic viscosity increase at 3500RPM explain the power decrease around 3500RPM.

## 5.7 Conclusion

The intake pressure waves effect on the exhaust temperature, and thus on the maximum power, has been demonstrated. An architecture enabling the interaction between the waves coming from the different cylinders has been developed. The expansion can then be obtained at the intake valve closing which reduce the volumetric efficiency but provide the intake temperature cooling. The cooler trapped air reduces directly the combustion temperature and provides a better knock resistance. The lower knock tendency permits an earlier combustion, providing a higher expansion in the cylinder and thus a lower exhaust gas temperature.

The reduced temperature at the exhaust allows to increase the turbine inlet pressure by closing the wastegate. Then the intake pressure increases which tends to increase the knock risk and so a new combustion timing is obtained. The new equilibrium allowed 10% increase on the maximum power.

The simulation and measurement have shown some discrepancies. The reduced availability of the engine test bench did not give the chance for further investigations. First

a longer expansion length should be tested, indeed the best power increase has been obtained at higher engine speed than on simulation. Furthermore the simulation assumes that the trapped air has an homogenous temperature which is equal to the intake temperature at the valve closing. This hypothesis should be validated, this could be handled through 3D CFD simulation.
The early valve closing is a strong competitor to this wave action. The required package volume is much lower. The main drawback of the early intake valve closing is increased pressure losses induced by the cam shape modification to reduce the valve opening range in crank angle. This can increase the part load consumption. Further investigations could quantify this on real driving cycle.

# 6 Conclusion and outlook

The literature survey has shown the relationship between the thermal efficiency of the spark ignition engine and the compression ratio. Original equipment manufacturers have increased this compression ratio to reach low fuel consumption at low load. This consequently increases the knocking risk. In the same time the downsizing has allowed to increase the engine load during real driving and so improve the BSFC as well. The full load performance with those downsized can be maintained with wider application of boosting systems and mainly the turbochargers. At low engine speed the turbocharged engines can suffer from the lack of enthalpy at the exhaust and compressor surge risk. The three way catalyst used since decades to efficiently convert the CO, HC and NOx requires a stoichiometric mixture at its inlet. This is challenging for maximum power operating conditions where the exhaust temperature becomes high and can lead to mechanical damage on the turbine and the exhaust line. An overview of the available technologies to overcome this challenge has been presented. The water injection or the EGR allows to increase the heat capacity of the mixture and thus reduce the combustion temperature. The Miller cycle with early and late intake valve closing reduces the apparent compression ratio for full load, the variable compression ratio systems allowing the same effect through the mobile part of the engine. Those technologies can be efficient but require a highly complex adaptation on engine.

This PhD thesis has focused the investigation on wave propagation control to either improve the low end torque or the power. The chapter 3 has investigated the linear acoustic theory to understand the effect of the simple geometries such as expansion or a volume in the wave propagation. The reflection and transmission has been calculated and the dynamic flow bench used for impedance measurement was detailed. The combustion model and the knocking risk assessment method have been presented. The combustion is evaluated through a two zones calculation method with a calculation of flame front speed as a combination of a laminar velocity model and turbulent speed model. This modelling cannot take into account any 3D effect neither the turbulence nor the hotspot. The advantage is low time consuming. This method is well suited with the next investigations as there is no variation of the cooling system and low variation in the turbulence. The fast calculations allow high number of tests.

The low end torque is addressed in the chapter 4 with an acoustic charging system composed of an added volume. At first the simulation is used to evaluate how this concept can modify the output torque of the engine. Then the optimal configuration is defined. A prototype has been produced and tested on engine test bench.
The experiments have demonstrated the 10% output torque increase. The direct wave action have been exhibited almost half of the gain, the second half has been produced through the turbocharger which has been able to provide more boost pressure. The transient behavior has been tested by load step evaluation. The direct benefit from the

wave action can be observed instantaneously whereas the loop effect is observed as soon as the turbocharger speeds up. The benefit has been observed whether the scavenging is applied or not. Another configuration aiming in using a higher frequency Eigen mode has been showing good results with the simulation. The benefit has not been confirmed when tested on actual engine. This configuration would have been beneficial for the packaging volume.
This study could be completed by a finer acoustic analysis. Indeed the volume and connection duct are not behaving as a Helmholtz resonator or quarter wave or half wave. The interaction with the rest of the line could also be further investigated. The knocking sensitivity should also be deeper investigated. An analysis until the knock limit would allow a proper evaluation of the knock margin for the different configurations.

The chapter 5 has been dedicated to enhance the power while keeping the stoichiometric mixture. At this operating point the main limitations are the exhaust temperature limitation which rises over 1200K and the knocking which tends to delay the combustion. The reduction of the air intake temperature is a way to reduce the knock risk. This enables an earlier combustion and thus more expansion in the cylinder leading to lower the exhaust temperature. The proposed concept aimed to use the pressure waves to expand the air intake and thus cool it down at the valve closing. Commonly the resonance systems are reacting completely at the opposite for volumetric efficiency enhancement. The tested device aims to create the pressure wave interaction between cylinders. The connecting duct length defines pressure wave phase and thus the expansion at the intake valve closing. The system has firstly been evaluated with a simulation. The model has been set to control the spark timing to keep the same knock risk and the waste gate is controlled to avoid any over temperature at the exhaust. The power increase has been about 10% compared to the base line. The expansion has also been observed on engine test bench. The benefit has been lower than simulation but, with an adjustment of the valve timing, the gain reached 9.5%. The comparison with the early intake valve closing has shown the lower pressure drop with the expansion length.
The benefit of the expansion has been demonstrated however this study could be conducted further with deeper analysis on the effect at lower engine speed. The deactivation strategy should be also evaluated with a standard cycle. The integration of this device in engine compartment will be another challenge.
The simulations have been efficient to define the behavior of the complete system and to layout the expansion device. However further investigations on engine could identify the reason of the observed discrepancies. Some further measurement could be carried out with the same boost pressure in order to compare the effect on combustion timing. The assumed homogeneous temperature in the cylinder at the intake valve closing could be evaluated with three dimensional fluid dynamic simulations.

# 7 Publications

## 7.1 Patent

- V. Raimbault, T. Günther, D. Chalet, J. Migaud – Air duct arrangement and internal combustion engine, European Patent 17290162.1-1004, accepted in April 2018, in Press

## 7.2 International conferences with proceedings

- V. Raimbault, J. Migaud, D. Chalet, M. Bargende, E. Revol, Q. Montaigne – Resonance charging applied to a turbo charged gasoline engine for transient behavior enhancement at low engine speed – 13th International Conference on Engines & Vehicles, SAE Technical Paper, 2017-24-0146, DOI: 10.4271/2017-24- 0146, Capri, Italy, September 10-14, 2017
- V. Raimbault, J. Migaud, S. Guilain, D. Chalet, T. Gunther, B. Peressini, M. Bargende – Exhaust temperature reduction with intake pressure wave action control – Thiesel 2018, Thermo and fluid dynamic processes in direct injection engines, Valencia, Spain, September 11-14, 2018
- V. Raimbault, J. Migaud, H. Buhl, S. Guilain, D. Chalet, M. Bargende – Air intake temperature cooling thanks to pressure waves action and adapted air intake geometry – 19th Stuttgart International Symposium, Automotive and Engine Technology, Stuttgart, Germany, March 19-20, 2019

## 7.3 Seminar

- V. Raimbault, D. Chalet, J. Migaud – Air intake temperature reduction due to pressure wave action – 24ème Colloque de Recherche Inter-Ecoles Centrales – Nantes, France, June 25-28, 2018

# 8 References


[1] J. B. Heywood, D. MacKenzie, I. Bonde Akerlind, P. Bastani, I. Berry, K. Bhatt, A. Chao, E. Chow, V. Karplus, D. Keith, M. Khusid, E. Nishimura, and S. Zoepf, “On the Road toward 2050: Report Massachusetts Institute of Technology Potential for Substantial Reductions in Light-Duty Vehicle Energy Use and Greenhouse Gas Emissions,” 2015.

[2] Commission European, “Directive of the european parliament and of the council,” 2017.

[3] “Reducing CO2 emissions from passenger cars | Climate Action.” [Online]. Available: https://ec.europa.eu/clima/policies/transport/vehicles/cars_en#tab-0-0. [Accessed: 14-Nov-2018].

[4] G. Pitron, La guerre des métaux rares : la face cachée de la transition énergétique et numérique, LLL Les Liens qui Libèrent, 2018.

[5] S. Amant, H.-M. Aulanier, C. Ramos, A. Schuller, and S. Timsit, “La France Amorce Le Virage Vers Le Véhicule Électrique,” 2018.

[6] D. D. Davis, G. M. Stokes, D. Moore, and G. L. Stevens, “Global EV Outlook 2018 - Towards cross-modal electrification.”

[7] “Simulateur Renault - Zoe.” [Online]. Available: https://group.renault.com/RCW_BINARIES/ZE_Simulator/autonomy.php?country=france&locale=fr. [Accessed: 27-Nov-2018].

[8] R. Amirante, E. Cassone, E. Distaso, and P. Tamburrano, “Overview on recent developments in energy storage: Mechanical, electrochemical and hydrogen technologies,” Energy Convers. Manag., vol. 132, pp. 372–387, Jan. 2017 doi:10.1016/j.enconman.2016.11.046.

[9] C. F. Shih, T. Zhang, J. Li, and C. Bai, “Powering the Future with Liquid Sunshine,” Joule, vol. 2, no. 10, pp. 1925–1949, Oct. 2018 doi:10.1016/j.joule.2018.08.016.

[10] V. R. J. H. Timmers and P. A. J. Achten, “Non-exhaust PM emissions from electric vehicles,” Atmos. Environ., vol. 134, pp. 10–17, 2016 doi:10.1016/j.atmosenv.2016.03.017.

[11] “Coradia iLint – le premier train à hydrogène au monde | Alstom.” [Online]. Available: https://www.alstom.com/fr/coradia-ilint-le-premier-train-hydrogene-au-monde. [Accessed: 27-Nov-2018].

[12] V. Subramanian, R. Gillet, G. De Paola, and C. Ternel, “Future evolutions of diesel engine technology and its powertrain trends influencing CO2 emissions in Europe,” in SIA Powertrain Congress, Rouen, France, 16-17 May, 2018.

[13] M. Schudeleit, C. Sieg, and F. Küçükay, “The Potential of 48V HEV in Real Driving The Potential of 48V HEV in Real Driving,” Int. J. Mech. Manuf. Eng. vol9,No10,2015., vol. 9, no. November, pp. 1662–1671, 2015 doi:10.13140/RG.2.1.3183.5368.

[14] S. Lauer and F. Graf, “Next gen 48 Volt hybrids by new architectures and connectivity,” in SIA Powertrain Congress, Versailles, France, 7-8 June, 2017.

[15] C. Harter, L. Eckstein, I. Olschewski, and C.-S. Ernst, “CO2 Technology Strategies for OEM in Europe until 2025,” 23. Aachener Kolloquium Fahrzeug- und Mot. 2014, pp. 661–678, Aachen, Germany, 6-8 october, 2014.

[16] N. Marc, “Méthodologie de dimensionnement d’un véhicule hybride électrique sous contrainte de minimisation des émissions de CO2,” PhD Thesis Université d’Orléans, 2013.

[17] “Car occupancy rates — European Environment Agency.” [Online]. Available: https://www.eea.europa.eu/data-and-maps/figures/term29-occupancy-rates-in-passenger-transport-1. [Accessed: 27-Nov-2018].
[18] C. Brace, “Engine modelling and optimisation for RDE,” in FPC2015 Future Powertrain Conference, Solihull, UK, 25-26 February, 2015.
[19] Horiba, “RLS Editor STARS User Manual.” .
[20] J. Pavlovic, A. Tansini, G. Fontaras, B. Ciuffo, M. Garcia Otura, G. Trentadue, R. Suarez Bertoa, and F. Millo, “The Impact of WLTP on the official fuel consumption and electric range of Plug - in Hybrid Electric Vehicles in Europe,” 13th International Conference on Engine and Vehicle, no. 2017-24–0133, pp. 1–10, 2017 doi:10.4271/2017-24-0133, Capri-Napoli, Italy, 10-14 September, 2017.
[21] J. Pavlovic, A. Marotta, and B. Ciuffo, “CO2 emissions and energy demands of vehicles tested under the NEDC and the new WLTP type approval test procedures,” Appl. Energy, vol. 177, pp. 661–670, 2016 doi:10.1016/j.apenergy.2016.05.110.
[22] D. M. Thewes, H. Baumgarten, J. Dohmen, T. Uhlmann, J. Seibel, A. Balazs, F. Hoppe, M. Krieck; P. Hoppe, “Gasoline Combustion Systems Beyond 2020,” 23rd Aachen Colloq. Automob. Engine Technol., pp. 267–292, Aachen, Germany, 6-8 October, 2014.
[23] O. Perrot, “Cours de thermodynamique,” IUT Saint Omer Dunkerque, 2010.
[24] J. B. Heywood, Internal Combustion Engine Fundamentals, MacGraw-Hill Higher Education, 1988.
[25] R. C. Costa and J. R. Sodré, “Compression ratio effects on an ethanol/gasoline fuelled engine performance,” Appl. Therm. Eng., vol. 31, no. 2–3, pp. 278–283, Feb. 2011 doi:10.1016/J.APPLTHERMALENG.2010.09.007.
[26] D. Tsokolis, S. Tsiakmakis, A. Dimaratos, G. Fontaras, P. Pistikopoulos, B. Ciuffo, and Z. Samaras, “Fuel consumption and CO2emissions of passenger cars over the New Worldwide Harmonized Test Protocol,” Appl. Energy, vol. 179, pp. 1152–1165, Oct. 2016 doi:10.1016/j.apenergy.2016.07.091.
[27] W. Bryzik and R. Kamo, “TACOM/Cummins Adiabatic Engine Program,” SAE Int., 1983 doi:10.4271/830314, SAE International Congress and Exposition, 1983.
[28] K. Fukui, Y. Wakisaka, K. Nishikawa, Y. Hattori, H. Kosaka, and A. Kawaguchi, “Development of Instantaneous Temperature Measurement Technique for Combustion Chamber Surface and Verification of Temperature Swing Concept,”, 2016-01–0675, doi:10.4271/2016-01-0675, SAE 2016 World Congress and Exhibition, Detroit, USA, 12-14 April, 2016.
[29] H. Kosaka, Y. Wakisaka, Y. Nomura, Y. Hotta, M. Koike, K. Nakakita, and A. Kawaguchi, “Concept of ‘Temperature Swing Heat Insulation’ in Combustion Chamber Walls, and Appropriate Thermo-Physical Properties for Heat Insulation Coat,” SAE Int. J. Engines, vol. 6, no. 1, 2013-01–0274, pp. 142-149 doi:10.4271/2013-01-0274, 2013.
[30] P. Hölz, T. Böhlke, and T. Krämer, “Determining water mass flow control strategies for a turbocharged SI engine using a two-stage calculation method,” Appl. Therm. Eng., vol. 146, pp. 386–395, Jan. 2019 doi:10.1016/J.APPLTHERMALENG.2018.09.133.
[31] G. Woschni, “A Universally Applicable Equation for the Instantaneous Heat Transfer Coefficient in the Internal Combustion Engine,” doi:10.4271/670931, SAE 670931, National Fuels and Lubricants, Powerplants, Transportation Meetings, 1967.
[32] S. Le Guen, A. Maiboom, S. Bougrine, and X. Tauzia, “Analysis of Systematic Calibration of Heat Transfer Models on a Turbocharged GDI Engine Operating Map,” doi:10.4271/2018-01-0787, WCX World Congress Experience, pp. 1–13, Detroit, USA, 10-12 April, 2018.
[33] G. Salameh, “Caractérisation expérimentale d’une turbine de suralimentation automobile et modélisation de ses courbes caractéristiques de fonctionnement,” PhD Thesis, Ecole Centrale de Nantes , 2016.
[34] R. Kurz, R. K. Marechale, E. J. Fowler, and M. J. Cave, “Operation of Centrifugal

Compressors in Choke Conditions," Asia Turbomachinery & Pump symposium, Singapore, 22-25 February, 2016.
[35] N. Watson and M. S. Janota, Turbocharging the Internal Combustion Engine. London: Macmillan Education UK, doi:10.1007/978-1-349-04024-7, 1982.
[36] N. Morand, G. Agnew, N. Bontemps, and D. Jeckel, "Variable Nozzle Turbine Turbocharger for Gasoline ' Miller ' Engine," MTZ Worldw., vol. 78, pp. 40–50, 2017 doi:10.1007/s38313-016-0148-5.
[37] R. Christmann, N. Buhl, and H. Breitbach, "Turbocharger Development with Variable Turbine Geometry for Gasoline Applications," in 25th Aachen Colloquium Automobile and Engine Technology, pp. 1157–1171, 10-12 October, 2016.
[38] A. Lefebvre and S. Guilain, "Modelling and Measurement of the Transient Response of a Turbocharged SI Engine," in SAE International, 2005 doi:https://doi.org/10.4271/2005-01-0691, SAE 2005 World Congress and Exhibition, Detroit, USA, 11-14 April, 2005.
[39] Eaton, "Roots Based Supercharger Technologies and its Application to Gasoline and Diesel Engines," in 6th International Conference Advanced Downsizing & Turbocharging, Dusseldorf, Germany, 27-27 March, 2014.
[40] M. Lau, R. Suteekarn, G. Lautrich, M. Pannwitz, and T. Tietze, "Concept for lower raw engine emission covering full engine map operation," in Internationaler Motorenkongress, 2016, pp. 195–216 doi:10.1007/978-3-658-13255-2, Baden Baden, Germany, 23-24 February, 2016.
[41] R. Aymanns, T. Uhlmann, C. Nebbia, and T. Plum, "Electric Supercharging New Opportunities with Higher System Voltage," MTZ Worldw., vol. 7, pp. 4–11, 2014.
[42] M. Bassett, J. Hall, B. Hibberd, S. Borman, S. Reader, K. Gray, and B. Richards, "Heavily Downsized Gasoline Demonstrator," doi:10.4271/2016-01-0663, SAE 2016 World Congress and Exhibition, Detroit, USA 12-14 April, 2016.
[43] E. Droulez, "AC cooler for electrical supercharger compressed air," International Congress SIA Powertrain, Versaille, France, 7-8 June, 2017.
[44] M. Bassett, J. Hall, T. Cains, R. Wall, M. P. Limited, C. House, S. James, and M. Road, "Extremely Downsized Gasoline Demonstrator Vehicle," International Congress SIA Powertrain, Versaille, France, 7-8 June, 2017.
[45] M. Fleiss, G. Almkvist, R. Burenius, and J. Björkholtz, "The Pneumatic Turbocharger Support System PowerPulse," MTZ Worldw., vol. 77, no. 6, pp. 10–15, 2016 doi:https://doi.org/10.1007/s38313-016-0042-1.
[46] A. Capetti, "Effects of intake pipe on the volumetric efficiency of an internal combustion engine," National Advisory Committee for Aeronotics, Washington DC, USA, 1st February, 1929.
[47] M. Takizawa, T. Uno, T. Oue, and T. Yura, "A Study of Gas Exchange Process Simulation of an Automotive Multi-Cylinder internal Combustion Engine," doi:https://doi.org/10.4271/820410, SAE International Congress and Exposition, 1982.
[48] R. J. Tabaczynski, J. Rodney, and F. M. Co, "Effects of Inlet and Exhaust System Design on Engine Performance," pp. 71–81, 1982 doi:https://doi.org/10.4271/821577, SAE International Congress and Exposition, 1982.
[49] I. Matsumoto and A. Ohata, "Variable Induction Systems to Improve Volumetric Efficiency at low and / or Medium Engine Speeds," doi:https://doi.org/10.4271/860100, SAE International Congress and Exposition, 1986.
[50] H. Bühl, M. Kratzsch, M. Günther, and H. Pietrowski, "Potential of variable intake manifolds to reduce CO2 emissions in part load," MTZ Worldw., vol. 74, no. 11, pp. 24–29, 2013 doi:https://doi.org/10.1007/s38313-013-0111-7.
[51] J. Migaud, V. Raimbault, D. Chalet, and H. Mezher, "Variable Charge Air Duct for Low-end Torque Enhancement and High Speed Performance," MTZ Worldw., vol. 76, pp. 20–25, 2015.

[52] S. L. Winkler, J. E. Anderson, L. Garza, W. C. Ruona, R. Vogt, and T. J. Wallington, “Vehicle criteria pollutant ( PM , NO x , CO , HCs ) emissions : how low should we go ?,” npj Clim. Atmos. Sci., 2018 doi:10.1038/s41612-018-0037-5.
[53] A. Zschutschke, J. Neumann, D. Linse, and C. Hasse, “A systematic study on the applicability and limits of detailed chemistry based NOx models for simulations of the entire engine operating map of spark-ignition engines,” Appl. Therm. Eng., vol. 98, pp. 910–923, 2016 doi:10.1016/j.applthermaleng.2015.12.093.
[54] P. Giansetti, “Contrôle moteur à allumage commandé. Estimation / prédiction de la masse et de la composition du mélange enfermé dans le cylindre,” PhD Thesis, Université d’Orléans, 2006.
[55] M. Keenan, ”Exhaust Emissions Control : 60 Years of Innovation and Development,” doi:10.4271/2017-24-0120, SAE 2015 World Congress and Exhibition, Detroit, USA, 21-23 April, 2015.
[56] T. Leroy, “Cylinder filling control of variable valve actuation equipped internal combustion engines,” PhD Thesis, Ecole Nationale Supérieure des Mines de Paris, 2010.
[57] N. Al-Hasan, J. Beer, J. Ehrhard, T. Lorenz, and L. Stump, “Charging Technologies for CO 2 Optimization by Millerization,” doi:10.4271/2015-01-1250, SAE 2015 World Congress & Exhibition, Detroit, USA, 21-23 April, 2015.
[58] M. Hubbard, P. D. Dobson, and J. D. Powell, “Closed Loop Control of Spark Advance Using a Cylinder Pressure Sensor,” J. Dyn. Syst. Meas. Control, vol. 98, no. 4, pp. 414–420, 1976 doi:10.1115/1.3427059.
[59] A. Businaro, N. Cavina, E. Corti, G. Mancini, D. Moro, F. Ponti, and V. Ravaglioli, “Accelerometer Based Methodology for Combustion Parameters Estimation,” Energy Procedia, vol. 81, pp. 950–959, Dec. 2015 doi:10.1016/J.EGYPRO.2015.12.152.
[60] E. Corti, N. Cavina, A. Cerofolini, C. Forte, G. Mancini, D. Moro, F. Ponti, and V. Ravaglioli, “Transient Spark Advance Calibration Approach,” Energy Procedia, vol. 45, pp. 967–976, Jan. 2014 doi:10.1016/J.EGYPRO.2014.01.102.
[61] J. Trapy, “Moteur à allumage commandé,” Tech. l’Ingénieur, vol. BM2 540, 2000.
[62] P. Bares, D. Selmanaj, C. Guardiola, and C. Onder, “A new knock event definition for knock detection and control optimization,” Applied Thermal Engineering, Volume 131, pp80-88, doi:10.1016/j.applthermaleng.2017.11.138, 2018.
[63] D. P. V. Doria, A. Stroppiana, M. Ferrera, F. Millo, M. Mirzaeian, “Knock Mitigation Techniques for highly boosted downsized SI engines,” Internaltional Congress SIA Powertrain, Versailles, France, 7-8 June, 2016.
[64] A. Robert, S. Richard, O. Colin, L. Martinez, and L. De Francqueville, “LES prediction and analysis of knocking combustion in a spark ignition engine,” Proc. Combust. Inst., vol. 35, no. 3, pp. 2941–2948, 2015 doi:10.1016/j.proci.2014.05.154.
[65] G. Töpfer, J. Reissing, H. Weimar, and U. Spicher, “Optical Investigation of Knocking Location on S . I . -Engines with Direct-Injection,” Journal of Engines, Volume 109, pp 156-168, 2000.
[66] Y. Qi, Z. Wang, J. Wang, and X. He, “Effects of thermodynamic conditions on the end gas combustion mode associated with engine knock,” Combust. Flame, vol. 162, pp. 4119–4128, 2015 doi:10.1016/j.combustflame.2015.08.016.
[67] N. Peters, B. Kerschgens, and G. Paczko, “Super-Knock Prediction Using a Refined Theory of Turbulence,” Journal of Engines, vol. 6, no. 2, pp. 953-957, 2013 doi:10.4271/2013-01-1109.
[68] M. Rothe, T. Heidenreich, U. Spicher, and A. Schubert, “Knock Behavior of SI-Engines: Thermodynamic Analysis of Knock Onset Locations and Knock Intensities,” doi:10.4271/2006-01-0225, Journal of Engines, vol 115, pp 165-176, 2006.
[69] C. Dahnz and U. Spicher, “Irregular combustion in supercharged spark ignition engines-pre-ignition and other phenomena” doi:10.1243/14680874JER609,

International Journal of Engine Research, Volume 11, pp 485-498, 2010.
[70] C. Hudson, X. Gao, and R. Stone, “Knock measurement for fuel evaluation in spark ignition engines,” Fuel, vol. 80, no. 3, pp. 395–407, Feb. 2001 doi:10.1016/S0016-2361(00)00080-6.
[71] M. Mirzaeian, “Analysis of combustion phenomena and knock mitigation techniques for high efficient spark ignition engines through experimental and simulation investigations,” PhD Thesis, Politecnico di Torino, 2017 doi:10.6092/polito/porto/2675370.
[72] E. Balducci, L. Ceschini, N. Rojo, N. Cavina, R. Cevolani, and M. Barichello, “Knock induced erosion on Al pistons: Examination of damage morphology and its causes,” Eng. Fail. Anal., vol. 92, pp. 12–31, Oct. 2018 doi:10.1016/J.ENGFAILANAL.2018.05.002.
[73] E. Galloni, G. Fontana, and S. Staccone, “Numerical and experimental characterization of knock occurrence in a turbo-charged spark-ignition engine,” Energy Convers. Manag., vol. 85, pp. 417–424, 2014 doi:10.1016/j.enconman.2014.05.054.
[74] M. Sjerić, I. Taritaš, R. Tomić, M. Blažić, D. Kozarac, and Z. Lulić, “Efficiency improvement of a spark-ignition engine at full load conditions using exhaust gas recirculation and variable geometry turbocharger – Numerical study,” Energy Convers. Manag., vol. 125, pp. 26–39, 2016 doi:10.1016/j.enconman.2016.02.047.
[75] E. Corti, C. Forte, G. M. Bianchi, and L. Zoffoli, “A Control-Oriented Knock Intensity Estimator,” SAE Int. J. Engines, vol. 10, no. 4, pp. 2017-24–0055, 2017 doi:10.4271/2017-24-0055.
[76] N. Kawahara, E. Tomita, and Y. Sakata, “Auto-ignited kernels during knocking combustion in a spark-ignition engine,” Proc. Combust. Inst., vol. 31 II, pp. 2999–3006, 2007 doi:10.1016/j.proci.2006.07.210.
[77] L. Ceschini, A. Morri, E. Balducci, N. Cavina, N. Rojo, L. Calogero, and L. Poggio, “Experimental observations of engine piston damage induced by knocking combustion,” Mater. Des., vol. 114, pp. 312–325, Jan. 2017 doi:10.1016/J.MATDES.2016.11.015.
[78] J. Zhao, “Research and application of over-expansion cycle (Atkinson and Miller) engines – A review,” Appl. Energy, vol. 185, pp. 300–319, Jan. 2017 doi:10.1016/J.APENERGY.2016.10.063.
[79] J. Atkinson, “Gas Engine, US367496A,” US367496A, 02-Aug-1887.
[80] R. Budack, R. Wurms, G. Mendl, and T. Heiduk, “The New Audi 2 .0-l I4 TFSI Engine,” MTZ Worldw., vol. 77, no. 5, pp. 16–23, 2016.
[81] R. Aymanns, F. Xia, B. Franzke, and D. Lückmann, “Combining Miller Cycle and VTG - A promising concept for future gasoline engines?” ATK Aufladetechnische Konferenz, Dresden, Germany, 15-16 September, 2016.
[82] S. Luisi, V. Doria, A. Stroppiana, F. Millo, and M. Mirzaeian, “Experimental Investigation on Early and Late Intake Valve Closures for Knock Mitigation through Miller Cycle in a Downsized Turbocharged Engine,” doi:10.4271/2015-01-0760, SAE 2015 World Congress & Exhibition, Detroit, USA, 21-23 April, 2015.
[83] L. Teodosio, D. Pirrello, F. Berni, V. De Bellis, R. Lanzafame, and A. D’Adamo, “Impact of intake valve strategies on fuel consumption and knock tendency of a spark ignition engine,” Appl. Energy, vol. 216, pp. 91–104, Apr. 2018 doi:10.1016/J.APENERGY.2018.02.032.
[84] W. Demmelbauer-Ebner, H. Middendorf, A. Birkigt, M. Ganzer, D. Hagelstein, and K. Persigehl, “EA211 TSI ® evo – The New 4-Cylinder Gasoline Engines from Volkswagen.” 25th Aachen Colloquium Automobile and Engine Technology, Aachen, Germany, 10-12 October, 2016.
[85] A. Maiboom, X. Tauzia, and J. F. Hétet, “Experimental study of various effects of exhaust gas recirculation (EGR) on combustion and emissions of an automotive direct injection diesel engine,” Energy, vol. 33, no. 1, pp. 22–34, 2008 doi:10.1016/j.energy.2007.08.010.

[86] S. Potteau, P. Lutz, S. Leroux, S. Moroz, and E. Tomas, “Cooled EGR for a Turbo SI Engine to Reduce Knocking and Fuel Consumption,” 2007-01-3978, doi:10.4271/2007-01-3978, Powertrain & Fluid Systems Conference and Exhibition, Rosemont, USA, 29 October-1st November, 2017.
[87] K. Siokos, R. Koli, R. Prucka, J. Schwanke, and J. Miersch, “Assessment of Cooled Low Pressure EGR in a Turbocharged Direct Injection Gasoline Engine,” SAE Int. J. Engines, vol. 8, no. 4, pp. 2015-01–1253, 2015 doi:10.4271/2015-01-1253.
[88] K. Kumano and S. Yamaoka, “Analysis of Knocking Suppression Effect of Cooled EGR in Turbo-Charged Gasoline Engine,” doi:10.4271/2014-01-1217, SAE 2014 World Congress & Exhibition, Detroit, USA, 8-10 April, 2014.
[89] T. Alger, S. Hanhe, C. E. Roberts, and T. W. Ryan, “The Heavy Duty Gasoline Engine – A Multi-Cylinder Study of a High Efficiency, Low Emission Technology,” doi:10.4271/2005-01-1135, Journal of Fuels and Lubricants, Volume 114, N°4, pp 628-638, 2005.
[90] T. Alger, T. Chauvet, and Z. Dimitrova, “Synergies between High EGR Operation and GDI Systems,” SAE Int. J. Engines, vol. 1, no. 1, pp. 2008-01–0134, 2008 doi:10.4271/2008-01-0134.
[91] F. Bozza, V. De Bellis, L. Teodosio, B. Fabio, D. B. Vincenzo, T. Luigi, F. Bozza, V. De Bellis, and L. Teodosio, “EGR systems employment to reduce the fuel consumption of a downsized turbocharged engine at high-load operations,” Energy Procedia, vol. 81, pp. 866–873, Dec. 2015 doi:10.1016/j.egypro.2015.12.134.
[92] G. Fontana and E. Galloni, “Experimental analysis of a spark-ignition engine using exhaust gas recycle at WOT operation,” Appl. Energy, vol. 87, no. 7, pp. 2187–2193, Jul. 2010 doi:10.1016/J.APENERGY.2009.11.022.
[93] F. Bozza, V. De Bellis, and L. Teodosio, Daniela Tufano, Enrica Malfi “Techniques for CO2 Emission Reduction over a WLTC. A Numerical Comparison of Increased Compression Ratio, Cooled EGR and Water Injection,” doi:10.4271/2018-37-0008, SAE CO2 Reduction for transport systems Conference, Torino, 6-8 June, 2018.
[94] F. Liu and J. Pfeiffer, “Estimation Algorithms for Low Pressure Cooled EGR in Spark-Ignition Engines,” doi:10.4271/2015-01-1620, International Journal of Engine, vol. 8, no. 4, pp. 1652–1659, 2015.
[95] F. Hoppe, M. Thewes, H. Baumgarten, and J. Dohmen, “Water injection for gasoline engines: Potentials, challenges, and solutions,” Int. J. Engine Res., vol. 17, no. 1, pp. 86–96, 2016 doi:10.1177/1468087415599867.
[96] C. Käppner, N. Garrido Gonzalez, J. Drückhammer, H. Lange, J. Fritzsch, and M. Henn, “On board water recovery for water injection in high efficiency gasoline engines,” 17th Internationals Stuttgarter Symposium, Automotive and Engine Technology, pp 867-887, Stuttgart, Germany, 14-17 March, 2017.
[97] M. Battistoni, C. N. Grimaldi, V. Cruccolini, G. Discepoli, and M. De Cesare, “Assessment of Port Water Injection Strategies to Control Knock in a GDI Engine through Multi-Cycle CFD Simulations,” 2017-24–0034, doi:10.4271/2017-24-0034, 13th International Conference on Engine and Vehicle, Capri, Italy, 10-14 September, 2017.
[98] T. Pauer, M. Frohnmaier, J. Walther, P. Schenk, A. Hettinger, and S. Kampmann, “Optimierung von Ottomotoren durch Wasser-Einspritzung Optimization of gasoline engines by water injection,” 37. Internationales Wiener Motorensymposium, Wien, Austria, 28-29 April, 2016.
[99] D. Tomazic, H. Kleeberg, S. Bowyer, J. Dohmen, K. Wittek, and B. Hakke, “Two-Stage Variable Compression Ratio (VCR) System to Increase Efficiency in Gasoline Powertrains,” doi:10.4271/2013-01-0288, 2012 Directions in Engine-Efficiency and Emissions Research (DEER) Conference, Dearborn, USA, 16-19 October, 2012.
[100] U. Walther, M. Hunger, J. Mueller, S. Nicklitzsch, M. Sens, and S. Zwahr, “Combination of Variable Compression Ratio and Early Intake Valve Closing as a Basis for Future Highly Efficient Gasoline Engines,” International Congress SIA Powertrain, pp 1-15, Versaille, France, 7-8 June, 2017.

[101] M. Schwaderlapp, K. Habermann, and K. I. Yapici, “Variable Compression Ratio-A Design solution for Fuel Economy Concepts,” 2002-01-1103, no. 724, doi:10.4271/2002-01-1103, Journal of Engines, Volume 111, 2002.
[102] S. Kiga, K. Moteki, and S. Kojima, “The New Nissan VC-Turbo with Variable Compression Ratio,” MTZ Worldw., vol. 78, no. 11, pp. 42–49, 2017.
[103] Y. Gazeau, “Les solutions techniques des F1 actuelles sont-elles implémentables sur les voitures ?,” Auto-Innovation, vol. April, 2018.
[104] M. Bunce and H. Blaxill, “Sub-200 g / kWh BSFC on a Light Duty Gasoline Engine,” doi:10.4271/2016-01-0709, SAE 2016 World Congress and Exhibition, Detroit, USA, 12-14 April, 2016.
[105] C. E. C. Alvarez, G. E. Couto, V. R. Roso, A. B. Thiriet, and R. M. Valle, “A review of prechamber ignition systems as lean combustion technology for SI engines,” Appl. Therm. Eng., vol. 128, pp. 107–120, Jan. 2018 doi:10.1016/J.APPLTHERMALENG.2017.08.118.
[106] H. Mezher, J. Migaud, V. Raimbault, J. G. Lelong, D. Chalet, N. Perrot, A. Hunault, P. Chesse, and B. Huurdeman, “Optimized Air Intake for a Turbocharged Engine Taking into Account Water-Cooled Charge Air Cooler Reflective Properties for Acoustic Tuning,” doi:10.4271/2013-01-0575, SAE 2013 World Congress, Detroit, USA, April 16-18, 2013.
[107] D. E. Winterbone and R. J. Pearson, Design techniques for engine manifolds : wave action methods for IC engines. Professional Engineering Pub. Limited, 1999.
[108] D. E. Winterbone and R. J. Pearson, Theory of engine manifold design : wave action methods for IC engines. Professional Engineering Pub, 2000.
[109] M. Bruneau, Manuel d’acoustique fondamentale. Hermes, 1998.
[110] M. L. Munjal, Acoustics of ducts and mufflers. Wiley, 1987.
[111] J.-P. Dalmont, C. J. Nederveen, and N. Joly, “Radiation impedance of tubes with different flanges: numerical and experimental investigations,” Journal of Sound and Vibration, vol. 244, no. 3, pp. 505–534, 2001 doi:10.1006/jsvi.2000.3487.
[112] J.C. Pascal, “Cours Vibration et Acoustique,” Ecole Nationale Supérieure d’Ingénieurs de Mans – Université du Maine, 2008.
[113] M. F. Harrison, I. De Soto, and P. L. R. Unzueta, “ARTICLE IN PRESS A linear acoustic model for multi-cylinder IC engine intake manifolds including the effects of the intake throttle,” vol. 278, pp. 975–1011, 2004 doi:10.1016/j.jsv.2003.12.009.
[114] D. Chalet, A. Mahe, J. Migaud, and J. F. Hetet, “A frequency modelling of the pressure waves in the inlet manifold of internal combustion engine,” Appl. Energy, vol. 88, no. 9, pp. 2988–2994, 2011 doi:10.1016/j.apenergy.2011.03.036.
[115] V. Raimbault, J. Migaud, D. Chalet, M. Bargende, E. Revol, and Q. Montaigne, “Resonance Charging Applied to a Turbo Charged Gasoline Engine for Transient Behavior Enhancement at Low Engine Speed,” doi:10.4271/2017-24-0146, 13 International Conference on Engines & Vehicle, Capri, Italy, 10-14 September, 2017.
[116] H. Mezher, “Caractérisation du comportement dynamique d’un circuit d’admission. Incidence sur le remplissage d’un moteur à combustion interne suralimenté.,” PhD Thesis, Ecole Centrale de Nantes, 2013.
[117] A. Torregrosa, F. Arnau, P. Piqueras, M. Reyes-Belmonte, M. Knutsson, and J. Lennblad, “Acoustic One-Dimensional Compressor Model for Integration in a Gas-Dynamic Code,” doi:10.4271/2012-01-0834, SAE 2012 World Congress & Exhibition, Detroit, USA, 24-26 April, 2012.
[118] L. Kaprielian, “Modélisation 0D pour la combustion dans les moteurs à allumage commandé : développements en proche paroi et dans le front de flamme,” PhD Thesis, Arts et Métiers Paris Tech, 2015.
[119] M. Wenig, M. Grill, and M. Bargende, “A New Approach for Modeling Cycle-to-Cycle Variations within the Framework of a Real Working-Process Simulation,” SAE Int. J. Engines, vol. 6, no. 2, pp. 2013-01–1315, Apr. 2013 doi:10.4271/2013-01-1315.
[120] M. Grill, T. Billinger, and M. Bargende, “Quasi-Dimensional Modeling of Spark

Ignition Engine Combustion with Variable Valve Train," doi:10.4271/2006-01-1107, SAE 2006 World Congress & Exhibition, Detroit, USA, 3-6 April, 2006.
[121] "Operating Instructions for the GT-Power expansion UserCylinder," FKFS - Research Institute of Automotive Engineering and Vehicle Engines Stuttgart, 2018.
[122] "Engine Performance - Application Manual VERSION 2017." 2016.
[123] S. Hann, L. Urban, M. Grill, and M. Bargende, "Prediction of burn rate, knocking and cycle-to-cycle variations of binary compressed natural gas substitutes in consideration of reaction kinetics influences," Int. J. Engine Res., vol. 19, no. 1, pp. 21–32, Jan. 2018 doi:10.1177/1468087417732883.
[124] A. Fandakov, M. Bargende, M. Grill, and A. C. Kulzer, "Investigation of thermodynamic and chemical influences on knock for the working process calculation," 17 International Stuttgarter Symposium Automotive and Engine Technology, pp. 107–122, Stuttgart, Germany, 14-17 March, 2017, doi:10.1007/978-3-658-16988-6.
[125] P. Leduc, B. Dubar, A. Ranini, and G. Monnier, "Downsizing of Gasoline Engine: an Efficient Way to Reduce CO 2 Emissions," Oil Gas Sci. Technol. – Rev. IFP, vol. 58, no. 1, pp. 115–127, 2003 doi:10.2516/ogst:2003008.
[126] C. Glahn, M. Kluin, I. Hermann, and A. Königstein, "Requirements for the Boosting System of Future Engine Concepts," MTZ Worldw., vol. 78, no. 4, pp. 16–21, Apr. 2017 doi:10.1007/s38313-017-0022-0.
[127] L. De Francqueville, G. De Paola, L. Noel, I. F. P. Énergies, D. Bois-préau, and R. Cedex, "Evaluation of Downsizing and Downspeeding Concepts to Reduce Fuel Consumption of Diesel Engines," pp. 1–11, International Congress SIA Powertrain, Rouen, France, 21-22 May, 2014.
[128] J. Scharf, H. Baumgarten, T. Uhlmann, M. Thewes, A. Balazs, A. Sehr, G. Ney, and U. Schaffrath, "High Performance and High Efficiency Powertrains," in FISITA 2016 World Automotive Congress, Busan, Korea, 26-30 September, 2016 doi:10.1007/978-3-642-24772-9_8.
[129] F. Payri, E. Reyes, and J. Galindo, "Analysis and Modeling of the Fluid-Dynamic Effects in Branched Exhaust Junctions of ICE," J. Eng. Gas Turbines Power, vol. 123, no. 1, p. 197, 2001 doi:10.1115/1.1339988.
[130] A. Ohata, Y. Ishida, "The Engineering Resource For Advancing Mobility Dynamic Inlet Pressure and Volumetric Efficiency of Four Cycle Four Cylinder Engine," no. 820407, SAE International Congress and Exposition, Detroit, USA, 22-26 February, 1982.
[131] J. J. Silvestri, T. Morel, and M. Costello, "Study of Intake System Wave Dynamics and Acoustics by Simulation and Experiment," 1doi:10.4271/940206, International Congress & Exposition, Detroit, USA, 28 February-3 March, 1994.
[132] P. Pogorevc and B. Kegl, "Intake system design procedure for engines with special requirements," Proc. Inst. Mech. Eng. Part D J. Automob. Eng., vol. 220, no. 2, pp. 241–252, Feb. 2006 doi:10.1243/095440706X72763.
[133] R. Royo, J. Corberan, and A. Perez, "Optimal design of the intake system in 4-S I.C.E.," doi:10.4271/940210, International Congress & Exposition, Detroit, USA, 28 February-3 March, 1994.
[134] J. Taylor, D. Gurney, P. Freeland, R. Dingelstadt, J. Stehlig, and V. Bruggesser, "Intake Manifold Length Effects on Turbocharged Gasoline Downsizing Engine Performance and Fuel Economy," doi:10.4271/2012-01-0714, SAE 2012 World Congress & Exposition, Detroit, USA, 24-26 April, 2012.
[135] P. Marez, P. System, and M. Challenges, "New PSA (Peugeot Citroen) EB Turbo Puretech 1,2l gasoline engine," RWTH AACHEN, Aachen, Germany, 9 December, 2013.
[136] D. S. Mokhtari, D. P. Souhaité, D. A. Tellier, S. Mokhtari, P. Souhaité, and A. Tellier, "Combustion System Design of the New PSA Peugeot Citroën PureTech 1 . 2 e-THP Engine," 23rd Aachen Colloq. Automob. Engine Technol., pp. 893–912,, Aachen, Germany, 6-8 October, 2014.

[137] H. Kleeberg, S. Bowyer, and D. T. Fev, “Combustion Development Methodologies and Challenges for Smaller Boosted Engines,” 2012 Directions in Engine-Efficiency and Emissions Research (DEER) Conference, Dearborn, USA, 16-19 October, 2012.
[138] “Fuel Balance Operating Manuel,” AT0905E, 2005.
[139] “T40B Caractéristiques techniques,” B3901−5.0.
[140] D. H. Schnüpke, T. Maass, and S. Zimmer, A. Rehberger, M. May, T. Langer, M. Proust, O. Mohsen, P. Trochet, and A. Arandyelovitch “Modern, Compact and Efficient : M 282 – The New 1.4-Liter Gasoline Engine from Mercedes-Benz,” in in 26th Aachen Colloquium Automobile and Engine Technology, pp. 875–894, 2017.
[141] M. T. Keskin, M. Bargende, and M. Grill, “Fast predictive burn rate model for Gasoline- HCCI,” W. Springer, Ed. 2016, pp. 155–169 doi:10.1007/978-3-658-13255-2.
[142] L. Theilemann, J. Scheiba, and F. Seiler, “Internal combustion engine,” Patent, EP 2 179 153 B1, 2016.
[143] M. E. S. Martins and T. D. M. Lanzanova, “Full-load Miller cycle with ethanol and EGR: Potential benefits and challenges,” Appl. Therm. Eng., vol. 90, pp. 274–285, Nov. 2015 doi:10.1016/J.APPLTHERMALENG.2015.06.086.
[144] J. M. Desantes, A. J. Torregrosa, H. Climent, and D. Moya, “Acoustic performance of a Herschel–Quincke tube modified with an interconnecting pipe,” J. Sound Vib., vol. 284, pp. 283–298, 2005 doi:10.1016/j.jsv.2004.06.016.
[145] B. Poirier, C. Maury, and J. M. Ville, “The use of Herschel-Quincke tubes to improve the efficiency of lined ducts,” Appl. Acoust., vol. 72, no. 2–3, pp. 78–88, 2011 doi:10.1016/j.apacoust.2010.09.010.
[146] M. Karlsson, “Aeroacoustics studies of duct branches with application to silencers.” , PhD Thesis, School of Engineering Sciences, KTH Royal Institute of Technology, 2010.
[147] M. F. Harrison and A. Dunkley, “The acoustics of racing engine intake systems,” J. Sound Vib., vol. 271, no. 3–5, pp. 959–984, Apr. 2004 doi:10.1016/S0022-460X(03)00773-9.
[148] F. Payri, A. J. Torregrosa, and R. Payri, “Evaluation through pressure and mass velocity distributions of the linear acoustical description of I. C. engine exhaust systems,” Appl. Acoust., vol. 60, no. 4, pp. 489–504, Aug. 2000 doi:10.1016/S0003-682X(00)00006-2.

# 9 French summary

## 9.1 Introduction

Le transport connaît, aujourd'hui, une période de tension importante. En effet il est devenu rapide, efficace et abordable. Le nombre de véhicules vendus a augmenté significativement dans les dernières décennies. Dans le même temps les enjeux liés aux gaz à effet de serre (GHG) et la qualité de l'air sont devenus critiques. Notamment le $CO_2$ est considéré comme un contributeur important du réchauffement climatique. D'autre part, les émissions de particules (PM), d'oxyde d'azotes (NOx), hydrocarbures (HC) et de monoxyde de carbone (CO) participent à la dégradation de la qualité de l'air.
La production de gaz à effet peut être estimée sous la forme d'une équation ( 9.1 ) présentée par Heywood [1].

$$GHG = km\ /\ personne\ \frac{km\ /\ vehicle}{km\ /\ personne}\ \frac{Energie}{km/\ véhicule}\ \frac{GHG}{Energie} \qquad (9.1)$$

Ainsi les émissions dépendent du nombre de kilomètres parcourus par personne, du nombre de personne par véhicule, de la consommation de d'énergie par kilomètre parcouru et enfin de la quantité de gaz à effet de serre produite par unité d'énergie. Les personnes étant libre de circuler, il n'est pas possible de limiter le nombre de kilomètres parcourus par personne. Les pouvoirs publics essaient de favoriser les transports en commun et ainsi d'augmenter le nommbre de voyageurs par véhicule. Les constructeurs automobiles sont attachés à rendre l'énergie consommée par véhicule la plus faible possible et la moins émetrice de gaz à effet de serre. D'autant plus que la réglementation européenne [2] a fixé la limite de $CO_2$ émis, par véhicule vendu, à 90g/km en moyenne pour chaque constructeur. Le gramme excédentaire sera alors taxé jusqu'à 95€/g au-dessus de 93g($CO_2$)/km. L'ambition est même de réduire les niveaux autorisés de 30% en 2030 et 50% en 2050. La réglementation a aussi sévérisée le cycle d'homologation afin de le rendre plus représentatif d'un usage réel. Celui-ci est devenu plus transitoire et requiert des niveaux de charge moteur plus élevés.
Cette thèse a donc pour objectif d'étudier les moyens d'améliorer la performance du moteur à allumage commandé en prenant en compte les enjeux des prochaines réglementations.

## 9.2 Recherche bibliographique

La recherche bibliographique est focalisée sur le moteur à allumage commandé. Elle a pour objectif de déterminer les leviers permettant de réduire la consomation et d'augmenter les performances, tout d'abord au travers du cycle de Beau de Rochas / Otto.

### 9.2.1 Ideal Beau de Rochas / Otto cycle

La Figure 186 décrit le cycle Beau de Rochas / Otto idéal. Celui-ci commence au point mort haut (A), l'admission d'air se fait alors jusqu'au point mort bas de manière isobare (AB). Ensuite, l'air admis est compressé par une transformation adiabatique (BC). Une combustion instantanée isochore (CD) est suivie d'une détente adiabatique (DE) et l'ouverture de la soupape d'échappement démarre par une détente isochore (EB) qui est suivie de l'échappement isobare des gaz jusqu'au point mort haut (A).

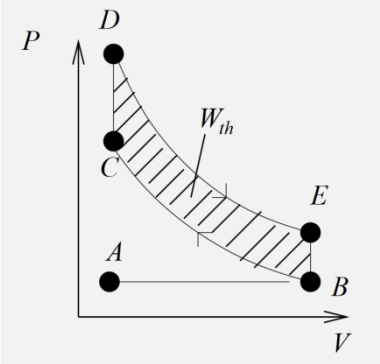


**Figure 186: Cycle idéal de Beau de Rochas / Otto** [23]

Le travail généré pendant le cycle correspond à la surface hachurée. Heywood [24] and Costa *et al* [25] ont présenté le lien entre le taux de compression et le rendement moteur suivant l'équation ( 9.2 ). Le taux de compression est défini comme le rapport du volume du cylindre au point mort bas et le volume du cylindre au point mort haut. Ainsi l'augmentation du taux de compression permet une amélioration de la conversion de la chaleur calorifique potentielle du carburant en travail.

$$\eta_{f,i} = \frac{W_{th}}{m_f Q_B} = 1 - \frac{1}{r_c^{\gamma-1}} \qquad (9.2)$$

Un rendement élevé permet d'obtenir une consommation spécifique réduite. La consommation spécifique est caractérisée par l'équation ( 9.3 ).

$$BSFC = \frac{\dot{m}_f}{P} \qquad (9.3)$$

Ce cycle est idéalisé et, notamment, ne prend pas en compte les variations de pression qui ont lieu lors des phases d'admission et d'échappement.

### 9.2.2 Charges partielles

La partie basse pression du cycle réel Beau de Rochas, correspond au travail de pompage. Les pertes par pompage peuvent être évaluées en mesurant la surface entre la phase d'échappement et la phase d'admission dans le diagramme PV de la Figure 187.

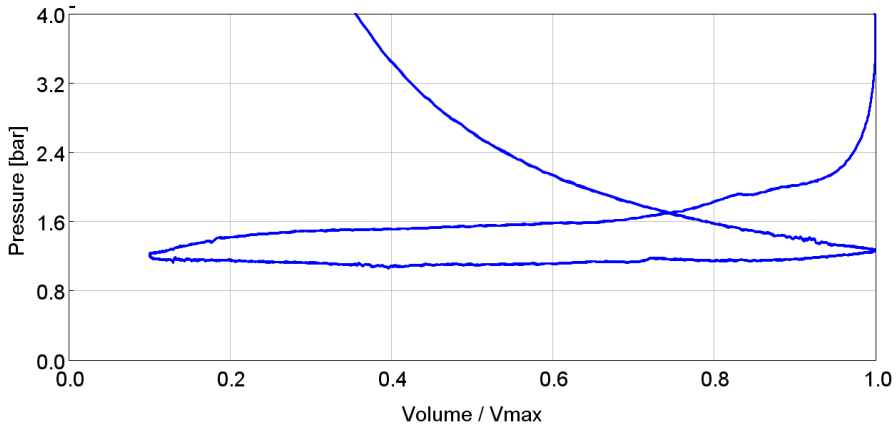


**Figure 187: Diagramme PV basse pression – Pertes par pompage**

Les pertes par pompage peuvent être interprétées comme le travail nécessaire, fournit par le piston, pour assurer le remplissage en air du cylindre et à l'expulsion des gaz brulés. Ces pertes sont particulièrement sensibles aux charges partielles. En effet, contrairement aux moteurs Diesel qui fonctionnent en excès d'air, la plupart des moteurs à allumage commandé fonctionnent avec un mélange stœchiométrique. Celui-ci définit le rapport des masses d'air et de carburant mélangées dans le cylindre. Il permet de garantir la combustion complète du mélange. Ainsi ce rapport, défini par l'équation ( 9.4 ), doit être maintenu à 14,7 pour de l'essence standard.

$$AFR = \frac{\dot{m}_{air}}{\dot{m}_{fuel}} \qquad (9.4)$$

La stœchiométrie est aussi évaluée au travers du coefficient lambda définit par l'équation ( 9.5 ) qui doit être maintenu à 1.

$$\lambda = \frac{AFR_{actual}}{AFR_{stoïc}} \qquad (9.5)$$

La quantité de carburant étant liée à la demande de couple, la quantité d'air doit être contrôlée. A charge partielle, la quantité d'air est réduite par l'intermédiaire du boitier papillon qui réduire la pression et donc la densité de l'air admis dans le cylindre. La Figure 188 montre comment la pression d'admission diminue lorsque la demande de couple est réduite. Le couple est ici représenté par la pression moyenne effective (PME/BMEP) définit par l'équation ( 9.6 ).

$$BMEP = \eta_m \frac{W}{V_{cyl}} = \frac{4\pi T}{V_{cyl}} \qquad (9.6)$$

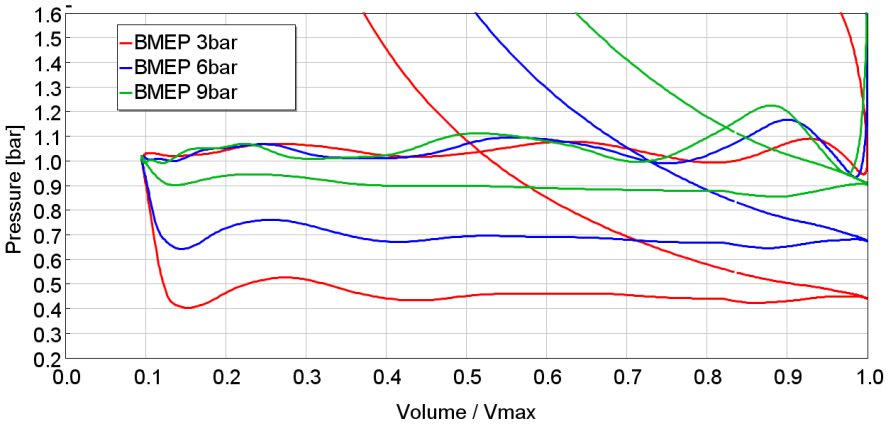


**Figure 188: Pertes par pompage pour différentes charges**

Les pertes par pompage contribuent à consommation spécifique. Le Tableau 15 montre l'augmentation significative de la consommation spécifique lorsque la demande de couple diminue et que la pression moyenne effective des pertes par pompage (PMEP) augmente.

**Tableau 15: Travail de pompage pour différentes charges moteur**

| BMEP [bar] | 3 | 6 | 9 |
|---|---|---|---|
| Mean pressure in the intake manifold [bar] | 0.46 | 0.71 | 0.93 |
| PMEP [bar] | 0.57 | 0.35 | 0.16 |
| BSFC [g/kWh] | 330 | 264 | 241 |

Pour une demande de couple donnée, un moteur de petite cylindrée à une pression moyenne effective (BMEP) plus élevée. Ainsi les pertes par pompage à charge partielle ont tendance à diminuer. La Figure 189 donne un exemple de couple demandé pour les cycles NEDC et WLTC, la taille des bulles représente la durée. Ainsi la demande est principalement située à bas régimes et basses charges pour ces cycles d'homologation. Ainsi les moteurs de faibles cylindrées peuvent bénéficier de la réduction des pertes par pompage.

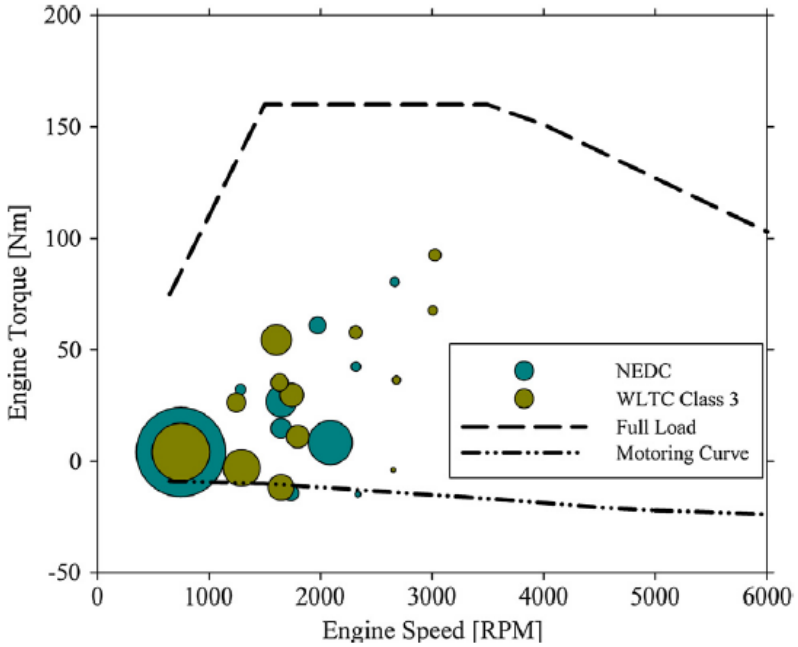


**Figure 189: Points de fonctionnement pour les cycles NEDC et WLTC pour une moteur à allumage commandé de 1,2l** [26]

C'est ainsi que le "downsizing" a permis de réduire significativement la consommation sur les cycles d'homologation.

### 9.2.3 Pleine charge

A pleine charge, le boitier papillon est complètement ouvert les pertes par pompage sont moins influentes. La partie haute pression du cycle devient prépondérante. Le cycle réel se différencie du cycle idéal par des pertes thermiques aux parois durant les phases de compression et de détente, ce qui tend à diminuer les pressions et températures. Ce flux de chaleur peut être décrit par l'équation ( 9.7 ). Il dépend ainsi de la surface d'échange, de la différence de température entre les gaz et les parois du cylindre et d'un coefficient d'échange.

$$\frac{Q_w}{dt} = \alpha_w \, A_W \, (T_w - T) \qquad (9.7)$$

Ce coefficient d'échange peut prendre en compte différents paramètres dont la turbulence. Ainsi Woschni [31] a proposé de le modéliser en intégrant la vitesse du piston, ainsi que les conditions de pression et de température dans le cylindre comme décrit par l'équation ( 9.8 ).

$$\alpha_w = 110 \, d^{-0.2} \, p_{cyl}^{0.8} \, T_b^{-0.53} (C_1 Vp + C_2 \frac{V_{Cyl} T_{1_{ref}}}{P_{1_{ref}} V_{1_{ref}}} (P_{cyl} - p_0))^{0.8} \qquad (9.8)$$

Ces pertes doivent être prises en compte pour pouvoir évaluer performances réelles du moteur.
Lors de la combustion, la masse de mélange brulé et le dégagement de chaleur sont liés par l'équation ( 9.9 ).

$$\frac{dm_t}{dt} = \frac{dQ_B}{d\emptyset} \cdot \frac{1}{H_u} \frac{d\emptyset}{dt} \qquad (9.9)$$

Le dégagement de chaleur peut être évalué, via la mesure de pression et l'estimation du volume de la chambre de combustion, en utilisant l'équation ( 9.10 ).

$$\frac{dQ_B}{dt} = \frac{\gamma}{\gamma - 1}\, p\, \frac{dV}{dt} + \frac{1}{\gamma - 1}\, V\, \frac{dp}{dt} \qquad (9.10)$$

Pour obtenir plus de dégagement de chaleur et donc plus de pression, il faut donc augmenter la quantité de carburant et d'oxygène. Ceci est limité par la masse d'air enfermée dans le cylindre. Celle-ci peut être augmentée par l'apport d'un système de suralimentation qui permet d'augmenter la densité de l'air d'admission.

### 9.2.4 Les systèmes de suralimentation

Avec la réduction des cylindrées, les motoristes ont eu recours à des systèmes de suralimentation pour maintenir les puissances développées. Le plus répandu est le turbocompresseur.

#### 9.2.4.1 Le turbocompresseur

Le turbocompresseur est composé d'une turbine à l'échappement et d'un compresseur à l'admission. La turbine permet une détente des gaz d'échappement et entraine le compresseur qui comprime l'air d'admission et en d'augmente la densité.
En faisant l'hypothèse d'une transformation adiabatique et d'un gaz parfait, les performances de la turbine et du compresseur peuvent être caractérisées respectivement par le taux de détente défini par l'équation ( 9.11 ) et par le taux de compression explicité par l'équation ( 9.12 ).

$$\tau = \frac{P_{i,t}}{P_{o,t}} = \left(\frac{T_{is,o,t}}{T_{i,t}}\right)^{\frac{\gamma}{1-\gamma}} \qquad (9.11)$$

$$\varphi = \frac{P_{o,c}}{P_{i,c}} = \left(\frac{T_{is,o,c}}{T_{i,c}}\right)^{\frac{\gamma}{\gamma-1}} \qquad (9.12)$$

La puissance à la turbine s'exprime via l'équation ( 9.13 ) en fonction du débit qui la traverse et de la variation de température à ses bornes.

$$\dot{w}_t = \dot{m}_a\, C_p\, (T_{i,t} - T_{o,t}) \qquad (9.13)$$

Son rendement est défini par l'équation ( 9.14 ), comme le rapport du travail isentropique et du travail réel.

$$\eta_t = \frac{w_t}{w_{is,t}} = \frac{T_{i,t} - T_{o,t}}{T_{i,t} - T_{is,o,t}} \qquad (9.14)$$

De même, les équations ( 9.15 ) et ( 9.16 ) définissent respectivement la puissance consommée par le compresseur et son rendement isentropique.

$$\dot{w}_c = \dot{m}_a C_p (T_{o,c} - T_{i,c}) \quad (9.15)$$

$$\eta_c = \frac{w_{is,c}}{w_c} = \frac{T_{is,o,c} - T_{i,c}}{T_{o,c} - T_{i,c}} \quad (9.16)$$

En combinant ces équations, il est possible d'écrire l'équation ( 9.17 ) qui définit le rapport de compression en fonction de la détente au niveau de la turbine et de la variation de température à ses bornes.

$$\varphi = \left(1 + \frac{T_{i,t}}{T_{i,c}} \eta_c \, \eta_m \, \eta_t \left(1 - \tau^{\frac{1-\gamma}{\gamma}}\right)\right)^{\frac{\gamma}{\gamma-1}} \quad (9.17)$$

Cette analyse permet une estimation grossière du potentiel de compression en fonction des conditions à l'échappement. Il faut, toutefois, noter que les hypothèses retenues ne prennent pas en compte les échanges thermiques qui ont lieu au niveau du compresseur et de la turbine. De même, les gaz d'échappement ne sont pas uniquement constitués d'air. Ainsi l'hypothèse d'un $\gamma$ constant génère une erreur. Néanmoins cette équation permet de montrer que le rapport de compression est lié au taux de détente à la turbine. Elle démontre aussi l'influence des températures à l'entrée de la turbine et du compresseur aini que l'effet du rendement mécanique du turbocompresseur, des rendements isentropiques du compresseur et de la turbine.

La Figure 190 (a) représente ainsi le rendement de la turbine en fonction du taux de détente. Le rendement est, pour cette turbine, optimum pour un taux de détente de 2,2 et plus faible lorsque le taux de détente est de 4,5. De même lorsque le régime turbine est élevé, par exemple à 250 000RPM, le rendement est plus faible. La Figure 190 (b) montre le débit corrigé pour différents taux de détente, définit par l'équation ( 9.18 ), les courbes montrent bien la réduction du taux de détente lorsque le débit est réduit.

$$q_c = q_1 \frac{\sqrt{T_1 / T_{ref}}}{P_1 / P_{ref}} \quad (9.18)$$

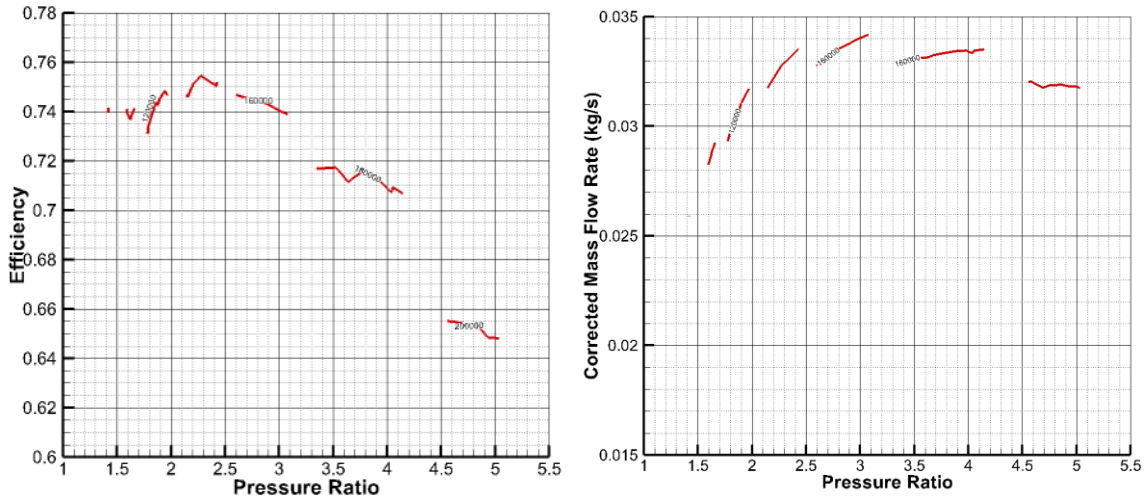


**Figure 190: Exemple de champ turbine map en rendement (a) en débit massique corrigé (b)**

Le dimensionnement de la turbine permet d'obtenir l'efficacité maximum pour les points de fonctionnement moteur critiques, ainsi il peut permettre d'obtenir le couple maximal à plus bas régime. L'interaction avec le compresseur doit être prise en compte. La Figure 191 montre un exemple de champ compresseur décrivant le rapport de compression en fonction du débit d'air corrigé. Ce champ est limité à gauche pour les faibles débits par la ligne de pompage. Ce pompage est caractérisé par des instabilités aérodynamiques au niveau des aubages de compresseur. Le passage dans la zone de pompage se caractérise par des oscillations de pression de basses fréquences et dans les cas les plus sévères, par une inversion de débit. Le pompage peut causer des dommages mécaniques, c'est pourquoi cette zone est soigneusement évitée en fonctionnement normal. La zone haute est limitée par la survitesse. Enfin la partie droite est limitée par le risque d'aspiration d'huile.

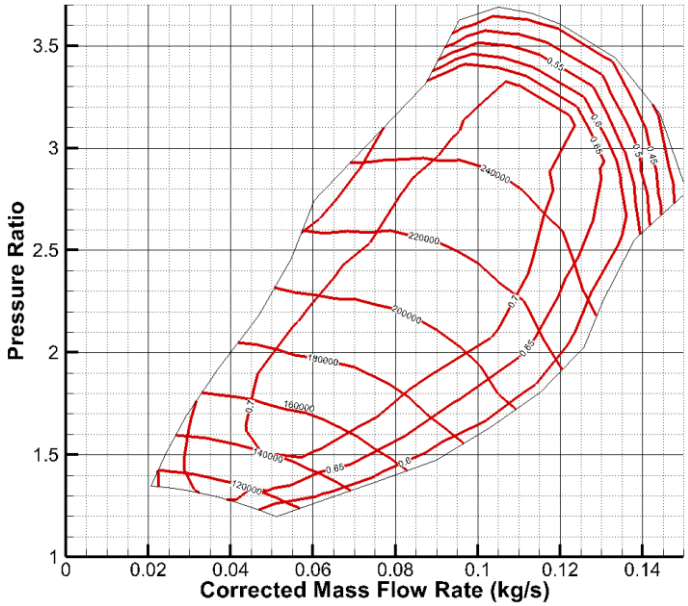


**Figure 191: Exemple de champ compresseur**

Par ailleurs, les turbines ne peuvent pas supporter des températures d'échappement dépassant, en général, 1200 K. Les températures excessives engendrent des oxydations des matériaux comme présenté sur la Figure 192.

**Figure 192: Dommage provoqué par l'excès de température sur une turbine** [36]

Les turbocompresseurs permettent donc de récupérer une partie de la chaleur des gaz d'échappement. La pression dans la ligne d'échappement peut être augmentée et donc les pertes par pompage, ce qui est en partie compensée par l'augmentation de pression d'admission. Les deux principaux inconvénients connus des moteurs à allumage commandé équipés d'un turbocompresseur est le défaut de couple à bas régime et le temps nécessaire pour obtenir la performance maximale à cause, notamment, des inerties mécaniques et thermiques.
Le compresseur mécanique et les e-booster ont pour vocation de limiter ces difficultés.

#### 9.2.4.2 Compresseur mécanique et E-booster

Afin de limiter la dépendance à l'enthalpie disponible à l'échappement, le compresseur mécanique utilise directement l'énergie mécanique provenant du vilebrequin. Deux vis contra rotative, représentée sur la Figure 193, sont alors entrainées et permettent la compression de l'air d'admission.

**Figure 193: Exemple de compresseur mécanique** [39]

Ce système permet donc d'obtenir une pression de suralimentation dès les bas débits et donc aux bas régimes. Toutefois, il utilise de l'énergie qui pourrait permettre d'entrainer les roues même s'il permet de développer plus de couple et de puissance qu'un moteur

atmosphérique. La consommation spécifique est moins favorable que la suralimentation par turbocompresseur. Certains constructeurs l'ont associé au turbocompresseur, il ne fonctionne alors qu'à très bas régime et permet d'améliorer le brio du moteur. Toutefois Lau *et al* [40] ont mentionné l'augmentation de niveau acoustique engendré avec notamment des pics correspondant aux harmoniques de la vitesse de rotation du compresseur mécanique.
Le e-booster n'utilise pas directement d'énergie issue du vilebrequin. En effet il est entrainé par un moteur électrique. Il est composé d'un compresseur similaire à celui du turbocompresseur comme représentée sur la Figure 194.

**Figure 194: Principe du E-Booster** [42]

Aymanns *et al* [41] ont montré que le couple maximum peut être obtenu plus rapidement. Sur la Figure 195, le couple atteint par les e-booster 12V et 48V est obtenu après moins d'une seconde alors que l'usage du seul turbocompresseur requiert 2.5 secondes.

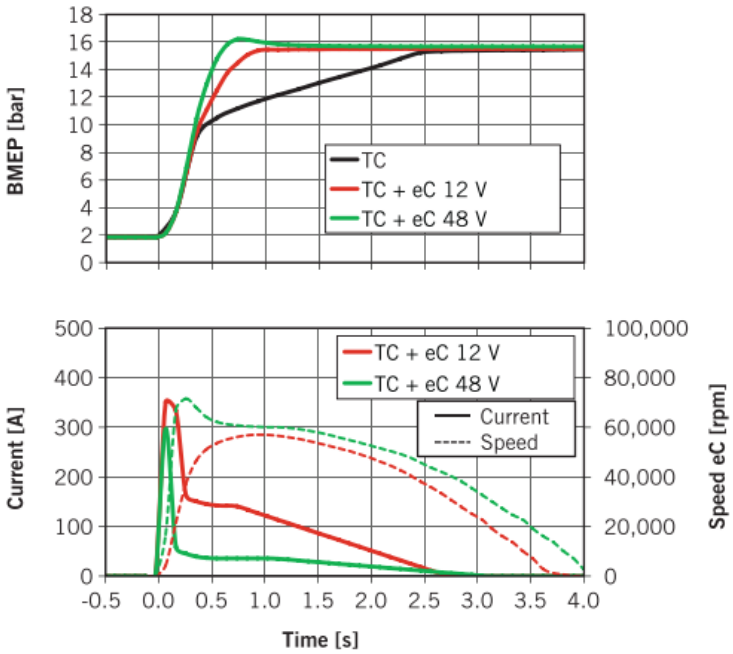


**Figure 195: Bénéfice du E-booster en transitoire de charge** [41]

Cette solution est très pertinente pour améliorer certaines performances mais l'utilisation d'électricité requiert un stockage d'électricité suffisant. De plus, il est nécessaire de prévoir un système de récupération d'énergie. Par conséquent, il est en concurrence avec les

systèmes de propulsion hybride thermique/électrique. Ces derniers présentent un avantage lors des faibles vitesses véhicules.
Il est donc recherché une méthode permettant d'améliorer les performances moteur qui n'utilisent ni de systèmes auxiliaires ni d'énergie mécanique du vilebrequin. L'utilisation des ondes de pression de la ligne d'air remplit ces objectifs.

#### 9.2.4.3 Remplissage acoustique

Les ondes de pression sont depuis longtemps utilisées pour augmenter la quantité d'air enfermée dans le cylindre. Ainsi Capeti [46], en 1929, a cherché à dimensionner des conduits permettant d'obtenir une onde phasée avec la fermeture de la soupape d'admission. Les ondes ont été modélisées en utilisant une approche thermodynamique qui sont performante mais lourde à mettre en œuvre [24] [47]. L'application des théories d'acoustique linéaire permet des calculs rapides et un bon positionnement fréquentiel des phénomènes.

Les effets sur le moteur ont été démontrés à de nombreuses reprises. Par exemple, Tabaczynski *et al* [48] ont montré, sur la Figure 196, l'effet de la longueur d'admission sur le rendement volumétrique. Il est notable que pour une longueur de 826 mm, ce rendement excède 1.

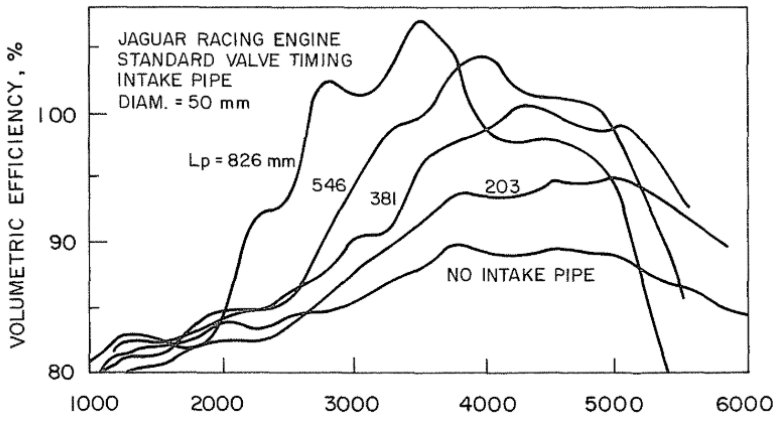


**Figure 196: Incidence de la longueur du conduit d'admission sur le rendement volumétrique**

En 1986, Matsumoto *et al* [49] ont proposé un système innovant composé de conduits de différentes longueurs connectés ou déconnectés de l'admission grâce à des volets afin d'optimiser le rendement volumétrique. La Figure 197 montre le bénéfice de ce système d'admission variable qui excède 10% sur une large étendue de régime.

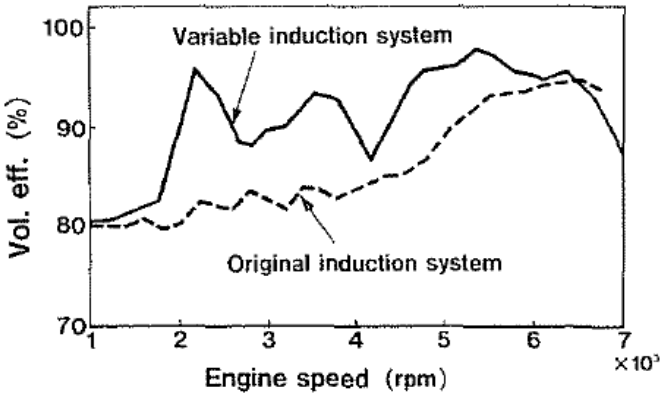


**Figure 197: Amélioration du rendement volumétrique par l'utilisation d'un système d'admission variable** [49]

#### 9.2.4.4 Conclusion

Les moteurs à allumage commandé utilisent de plus de turbocompresseurs. En effet ceux-ci permettent d'augmenter la puissance spécifique du moteur. Il permet d'utiliser des moteurs de plus petites cylindrées ce qui est bénéfique lorsqu'il opère à basse charge (ce qui est le cas de cycle d'homologation). L'utilisation des turbocompresseurs augmente pourtant le temps pour atteindre le couple maximum. De plus les moteurs suralimentés ont tendance à avoir un couple à bas régime inférieur à un moteur atmosphérique de puissance équivalente.
Pour compenser ces défauts, des solutions de suralimentation n'utilisant pas l'enthalpie à l'échappement sont disponibles. Le compresseur mécanique et le e-booster permettent d'améliorer significativement les performances à bas régime. Néanmoins ils utilisent de l'énergie qui pourrait soit être directement utilisée pour propulser le véhicule, soit utilisé par un système d'hybridation permettant un gain en consommation supplémentaire à charges partielles et dans les cycles d'homologation.
Par ailleurs, le remplissage par onde acoustique a montré de un potentiel important d'amélioration de rendement volumétrique. Cette optimisation peut avoir un impact sur la perte de charge mais n'utilise pas directement de l'énergie qui pourrait directement propulser le véhicule. De plus les pertes de charge ne sont pas problématiques sur les charges partielles puisque ces points sont papillonnés (utilisant le boitier papillon pour réduire la pression d'admission).
Un autre aspect important du controle moteur est la maîtrise des émissions polluantes.

### 9.2.5 Emissions polluantes

Les émissions polluantes sont principalement constituées des hydrocarbures (HC), du monoxyde de carbone (CO) et des oxydes d'azote (NOx). Ces émissions sont limitées par la réglementation depuis les années 1970 notamment aux Etats Unis. En Europe, la norme Euro 1 a été mise en application en juillet 1992. Comme indiqué dans le Tableau 16, l'évolution a rendu la règlementation plus stricte notamment sur les oxydes d'azote. La dernière évolution limite aussi les particules en nombre et en masse.

**Tableau 16: Réglementation européenne concernant les émissions polluantes [2]**

| | date | CO | HC | HC+NOx | NOx | NMHC | PM | PN |
|---|---|---|---|---|---|---|---|---|
| **Euro 1** | juil.-92 | 2,72 | - | 0,97 | - | | - | - |
| **Euro 2** | janv.-96 | 2,2 | - | 0,5 | - | | - | - |
| **Euro 3** | janv.-00 | 2,3 | 0,20 | - | 0,15 | | - | - |
| **Euro 4** | janv.-05 | 1,0 | 0,10 | - | 0,08 | | - | - |
| **Euro 5** | sept.-09 | 1,0 | 0,10 | - | 0,06 | 0,068 | 0,005 | - |
| **Euro 6** | sept.-17 | 1,0 | 0,10 | - | 0,06 | 0,068 | 0,005 | $6{,}0\times10^{11}$ |

Ces normes ont permis de réduire les émissions notamment d'oxydes d'azote comme le démontre la Figure 198.

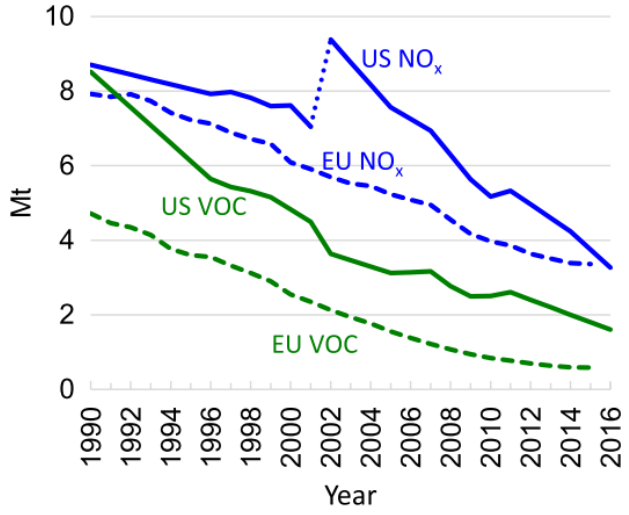


**Figure 198: Emission de NOx des véhicules routiers en Europe et aux Etats Unis** [52]

Les moyens de contrôler les émissions polluantes commencent par une bonne compréhension des causes racines.

### 9.2.1 Production des oxydes d'azote

Les émissions d'oxydes à l'échappement des moteurs à combustion interne proviennent de l'oxydation de l'azote présent dans l'air comme le rapporte les équations ( 9.19 ), ( 9.20 ) et ( 9.21 ).

$$O + N_2 \leftrightarrow NO + N \qquad (9.19)$$

$$N + O_2 \leftrightarrow NO + O \qquad (9.20)$$

$$N + OH \leftrightarrow NO + H \qquad (9.21)$$

Les opérations se font dans les deux sens lors de la combustion mais pas à la même vitesse. De plus, ces transformations dépendent de la température et la tendance suit la courbe présentée sur la Figure 199. Les émissions montent de manière exponentielle lorsque la température augmente.

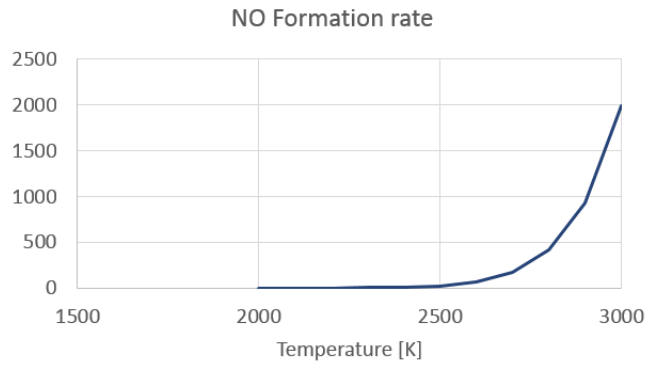


**Figure 199: Dépendance de la formation du monoxyde d'azote avec le température**

Dans le cylindre, la température est notamment liée et à la richesse. Ainsi Giansetti [54] a montré le lien entre la constitution du mélange et la production de polluant comme reporté dans la Figure 200. Ainsi le compromis entre les différents polluants est obtenu quand le mélange est stoechiométrique.

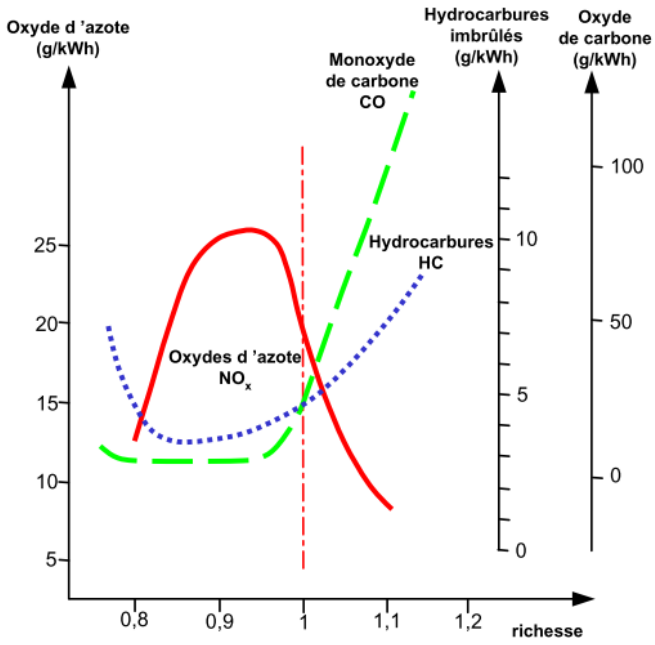


**Figure 200: Emissions polluantes en function de la richesse** [54]

### 9.2.2 Le catalyseur trois voies

Depuis plus de vingt ans les moteurs automobiles à allumage commandé sont de plus en plus équipés de pots catalytiques trois voies qui permettent de convertir les émissions polluantes issues du moteur.

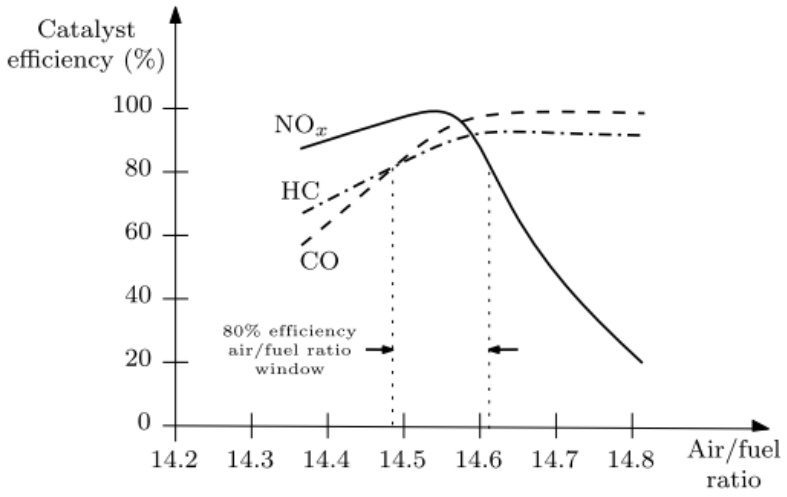


**Figure 201: Efficacité de conversion d'un catalyseur trois voies** [56]

La Figure 201 représente l'efficacité de conversion en fonction de la composition du mélange air/carburant à l'échappement. La figure montre que pour un mélange autour de 14,5 le taux de conversion est supérieur à 80% pour les trois polluants. Ce taux correspond à la stœchiométrie pour l'essence.

La limitation des polluants à l'échappement est optimum lorsque le mélange en amont du catalyseur est stœchiométrique. En effet cette proportion permet de limiter les émissions à la source et de mieux les traiter dans le système en aval.
Néanmoins, le cliquetis est aussi un paramètre important dans le controle du mélange air / carburant.

### 9.2.3 Cliquetis

La combustion est modélisée comme une flamme sphérique qui prend naissance à l'allumage de la bougie et qui se propage jusqu'à ce que tout le mélange air carburant soit brulé. Contrairement à ce que suggère le cycle Beau de Rochas / Otto idéal, la combustion n'a donc pas lieu de manière instantanée. Elle s'étend ainsi de part et d'autre du point mort haut (PMH). Si elle ne débute qu'au point mort haut, la combustion se termine alors que le piston a commencé sa descente et ainsi limite la détente, réduisant le travail et le rendement. A l'inverse une combustion qui démarre très tôt avant le PMH augmente le travail de compression. Ainsi l'optimum de MFB50 où 50% de la masse de carburant est brulé doit se situer entre 6 et 16 °CA [24] [58] [59] [60] [61]. Cet optimum varie avec la durée de combustion et des pertes aux parois.
Pourtant, comme le révèle la Figure 202, tous les points au-dessus de 10bar de BMEP ont une combustion après 8°CA.

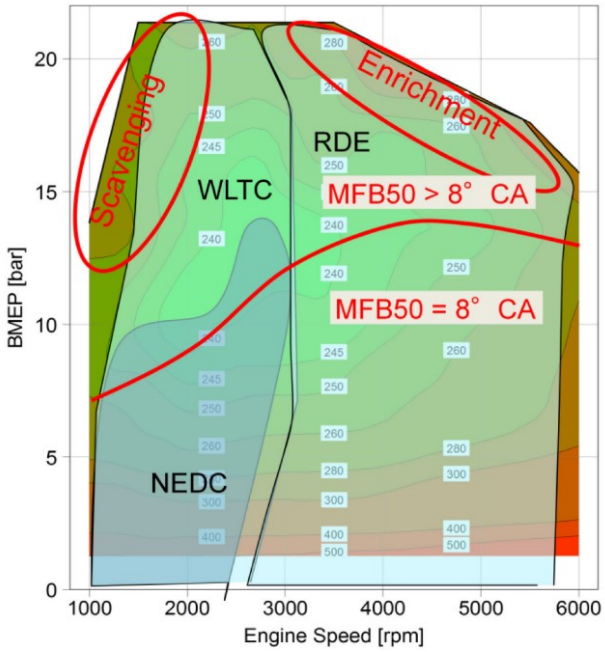


**Figure 202: Champ moteur et stratégie d'un moteur GTDI** [57]

Ceci est expliqué par le cliquetis. En effet lorsque les conditions de température et de pression sont élevées des points chauds peuvent entrainer l'auto inflammation du mélange avant que le front de flamme, créé par la bougie, ne l'ait atteint.
Le cliquetis est caractérisé par l'apparition d'oscillation de pression dans le cylindre autour la pression maximum du cylindre. La pression et la température augmentent de manière importante et peuvent causer des dommages sur les parties mobiles qui doivent supporter des contraintes plus élevées mais aussi pour les pistons qui peuvent être très oxydés et même percés dans quelques cas extrêmes.
Le décalage du point de MFB50 permet de décaler le point où la pression est maximum alors que la détente a commencé. Le retard à allumage permet ainsi de contrôler le risque de cliquetis. Dans certains cas, retarder l'allumage n'est pas suffisant et l'injection de carburant supplémentaire dans la chambre permet d'augmenter la capacité calorifique du mélange et de réduire la température, c'est l'enrichissement. Dans ces conditions, la consommation est plus élevée et la production de HC est importante à la source, mais aussi à la sortie du catalyseur puisqu'en mélange riche les HC ne peuvent pas être converties efficacement.

Cette thèse s'est donc focalisée sur ces deux objectifs que sont l'amélioration de la réponse des moteurs à allumage commandé turbocompressé à bas régime et la puissance moteur en maintenant un mélange stœchiométrique.

## 9.3 Moyens de simulation

Le système d'admission permet de fournir l'air au moteur. Sa performance peut être augmentée de différentes manières. La première consiste à limiter les pertes de charge et ainsi augmenter la densité de l'air admis comme le révèle la loi des gaz parfait ( 9.2 ).

$$\rho = \frac{PV}{rT} \qquad (9.22)$$

Le flux d'air dans l'admission est très oscillant. En effet la succession des ouvertures de soupapes et le mouvement sinusoïdal du piston rendent la pression et le débit dans l'admission très dynamique. Ainsi Mezher *et al* [106] ont montré que les ondes de pression peuvent aussi contribuer à l'amélioration du rendement volumétrique.
Ces ondes de pressions peuvent être modélisées au travers de l'approche d'acoustique linéaire.

### 9.3.1 Eléments d'acoustique linéaire

Les ondes de pression sans amortissement s'écrivent suivant l'équation ( 9.23 ) en utilisant le principe fondamental de la dynamique [109].

$$\rho \frac{d\vec{v}}{dt} = -\overrightarrow{grad}\, P + \rho \vec{F} \qquad (9.23)$$

La conservation de la masse permet d''écrire l'équation ( 9.24 ).

$$\frac{\partial \rho}{\partial t} + div(\rho \vec{v}) = \rho q \qquad (9.24)$$

Pour une transformation isentropique idéale la variation de pression s'écrit suivant l'équation ( 9.25 ).

$$dP = \frac{1}{\rho \chi_T} d\rho \qquad (9.25)$$

Une linéarisation de premier ordre de l'équation ( 9.23 ) permet d'écrire l'équation d'onde ( 9.26 ).

$$\Delta p - \frac{1}{{c_0}^2} \frac{\partial^2}{\partial t^2} p = \rho_0 \left[ div\, \overrightarrow{F} - \frac{\partial q}{\partial t} \right] \qquad (9.26)$$

Les variables de cette équation ne représentent que les oscillations autour de la valeur moyenne. Lors de l'application de cette équation à une propagation monodirectionnelle, en l'absence de source d'excitation, cette dernière peut s'écrire sous la forme ( 9.27 ) [110].

$$\left( \frac{\partial^2}{\partial t^2} - {c_0}^2 \frac{\partial^2}{\partial x^2} \right) p = 0 \qquad (9.27)$$

${c_0}^2$ est la vitesse du son qui est décrite par l'équation ( 9.28 )

$${c_0}^2 = \frac{\gamma RT}{M} \qquad (9.28)$$

Les solutions de l'équation ( 9.27 ) peuvent s'écrire sous la forme décrite par l'équation ( 9.29 ).

$$p\,(x,t) = \left(A\,e^{-jkx} + B\,e^{jkx}\right)e^{j\omega t} \qquad (9.29)$$

En condition de pulsation harmonique, la simplification donne l'équation ( 9.30 ).

$$p\,(x) = A\,e^{-jkx} + B\,e^{jkx} \qquad (9.30)$$

L'impédance acoustique s'écrit comme le rapport de la pression sur la vitesse comme décrit par l'équation ( 9.31 ).

$$Z = \frac{p}{v} \qquad (9.31)$$

### 9.3.2 Propagation d'onde dans des géométries simples

#### 9.3.2.1 Saut de section

Pascal [112], Munjal [110] et Harrison *et al* [113] ont décrit la propagation d'ondes dans les sauts de section. La Figure 203 représente la forme du changement de section de $S_1$ vers $S_2$.

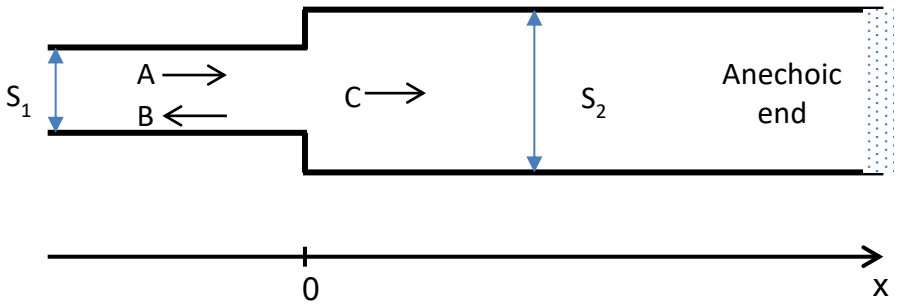


**Figure 203: Schéma d'un d'un saut de section** [112]

La pression dans la première partie peut s'écrire sous la forme de l'équation ( 9.30 ). Alors que la condition anéchoïque du bout de conduit permet d'écrire une forme plus simple, équation ( 9.32 ), pour la partie située au-delà de x=0.

$$p_2\,(x) = C\,e^{-jkx} \qquad (9.32)$$

De plus la conservation de la masse se traduit par l'équation ( 9.33 ).

$$\rho S_1 u_1 = \rho S_2 u_2 \qquad (9.33)$$

L'application de l'équation ( 9.23 ) permet de calculer les vitesses acoustiques (équations ( 9.34 ) et ( 9.35 )) pour les deux zones.

$$u_1 = \frac{A}{\rho_0 c_0} e^{-jkx} - \frac{B}{\rho_0 c_0} e^{jkx} \qquad (9.34)$$

$$u_2 = \frac{C}{\rho_0 c_0} e^{-jkx} \qquad (9.35)$$

En combinant ces dernières au point x=0, il est possible de déterminer les équations ( 9.36 ) et ( 9.37 ).

$$S_1(A - B) = S_2\, C \qquad (9.36)$$

$$A + B = C \qquad (9.37)$$

Ces dernières permettent de déterminer le coefficient de réflexion décrit par l'équation ( 9.38 ) qui est le rapport de l'amplitude de l'onde réfléchie sur celle de l'onde incidente. Le coefficient de transmission décrit par l'équation ( 9.39 ) est le rapport l'amplitude de l'onde transmise sur celle de l'onde incidente.

$$\frac{B}{A} = \frac{S_1 - S_2}{S_1 + S_2} \qquad (9.38)$$

$$\frac{C}{A} = \frac{2\,S_1}{S_1 + S_2} \qquad (9.39)$$

Ces coefficients montrent qu'un fort saut de section contribue à une forte réflexion et une diminution de la transmission des ondes. Ces équations peuvent aussi être appliquées à un double changement de section ou chambre d'expansion de la Figure 204 [112].

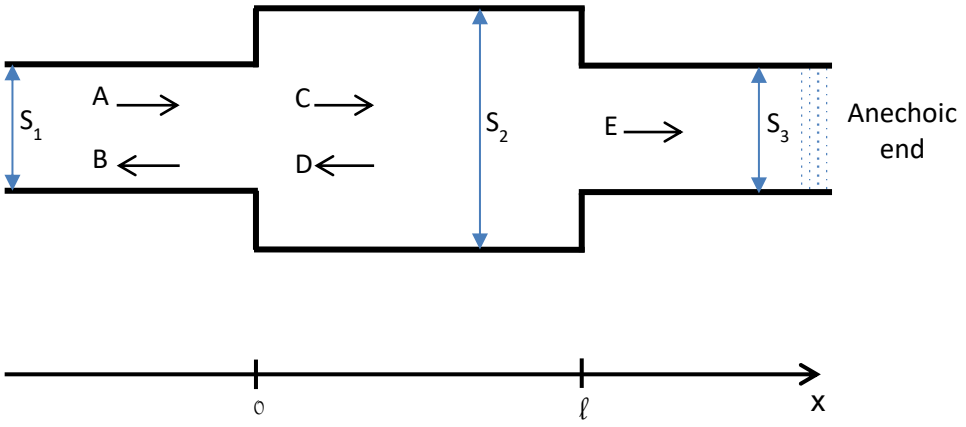


**Figure 204: Schéma d'une chambre d'expansion**[112]

Les coefficients de réflexion et de transmission s'expriment avec les équations ( 9.40 ) et ( 9.41 ).

$$\frac{B}{A} = \frac{j\left(\frac{S_1}{S_2} - \frac{S_2}{S_1}\right) sin(kl)}{2\cos(kl) + j\left(\frac{S_1}{S_2} + \frac{S_2}{S_1}\right) sin(kl)} \qquad (9.40)$$

$$\frac{E}{A} = \frac{2\,e^{jkl}}{2\cos(kl) + j\left(\frac{S_1}{S_2} + \frac{S_2}{S_1}\right) sin(kl)} \qquad (9.41)$$

Pour conduit de 0,05m de diamètre et une chambre d'expansion de de 0,5m de longueur et de diamètre égale à 0,15m, les équations ( 9.40 ) et ( 9.41 ) peuvent être représentées

par la Figure 205. La réflexion est de 1 pour les fréquences qui ne correspondent pas à la résonance du volume en demi-onde à 342Hz.

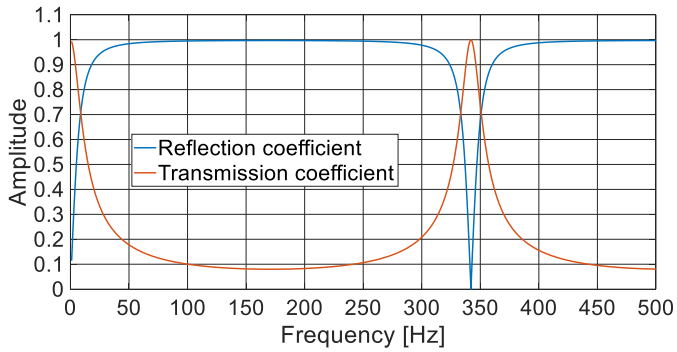


**Figure 205: Module des coefficients de transmission et de reflexion d'une chambre d'expansion**

#### 9.3.2.2 Le résonateur de Helmholtz

Le résonateur de Helmholtz est un artifice acoustique très utilisé. Il est composé d'un volume et d'un conduit de section et de longueur connu comme décrit dans la Figure 206.

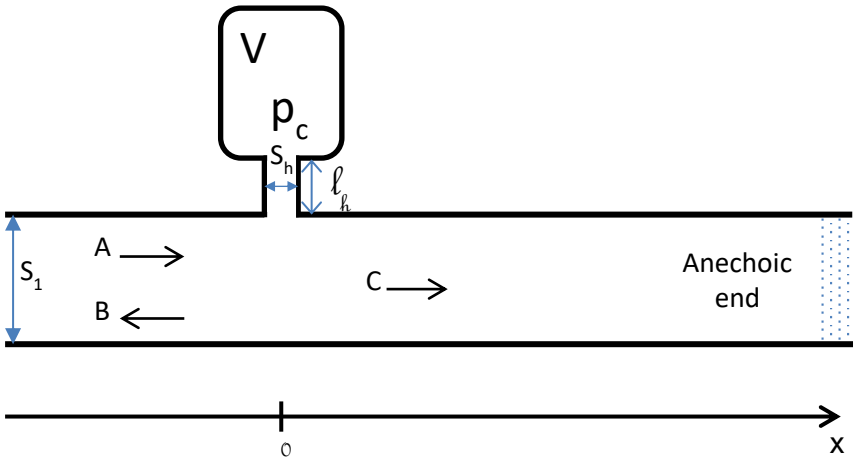


**Figure 206: Schéma d'un conduit equipé d'un résonateur de Helmholtz** [112]

Le débit au niveau du col du résonateur de Helmholtz peut être écrit comme indiqué dans l'équation ( 9.42 ).

$$Q_h = j\,\omega\,\rho\,V \qquad (9.42)$$

Les coefficients de réflexion et de transmission peuvent être calculés par les équations ( 9.43 ) et ( 9.44 ) [112].

$$\frac{B}{A} = \frac{jc_0\omega S_h}{2S_1 l_h\left(\omega^2 - \frac{{c_0}^2 S_h}{V l_h}\right) - jc_0\omega S_h} \qquad (9.43)$$

$$\frac{C}{A} = \frac{1}{1 - j\dfrac{\omega c_0 S_h}{2S_1 l_h\left(\omega^2 - \dfrac{{c_0}^2 S_h}{V l_h}\right)}} \qquad (9.44)$$

La Figure 207 présente les résultats des modules des coefficients de réflexion et de transmission. Le résonateur de Helmholtz est composé d'un volume de 1l, d'un col de 15mm de rayon et d'une longueur de 100mm. Le graphe montre la résonance au-dessous de 150Hz. A la résonance le coefficient de transmission est bas et la réflexion maximum.

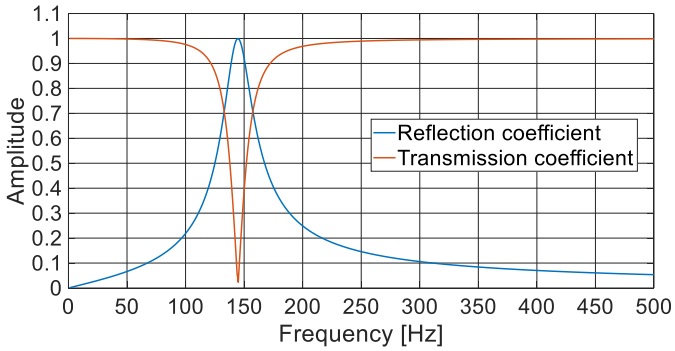


**Figure 207: Module des coefficients de transmission et de reflexion d'un conduit equipé d'un résonateur de Helmholtz.**

L'approche d'acoustique linéaire permet de comprendre et d'évaluer le comportement acoustique de simples géométries. Pour des géométries plus compliqués et des conditions de pression et température plus variées l'utilisation d'outils de simulation permet d'obtenir des résultats plus rapides. Toutefois une phase de comparaison entre simulation et essais est nécessaire pour garantir la bonne représentativité des modèles. Ainsi le banc dynamique est un moyen rapide qui permet de valider la réponse fréquentielle du modèle.

### 9.3.3 Banc dynamique et mesure d'impédance

Le banc dynamique est outil permettant de faire la mesure de l'impédance acoustique [114]. La Figure 208 montre le système d'obturation permettant la rupture de débit en 0,5ms et le montage d'une ligne d'admission d'air.

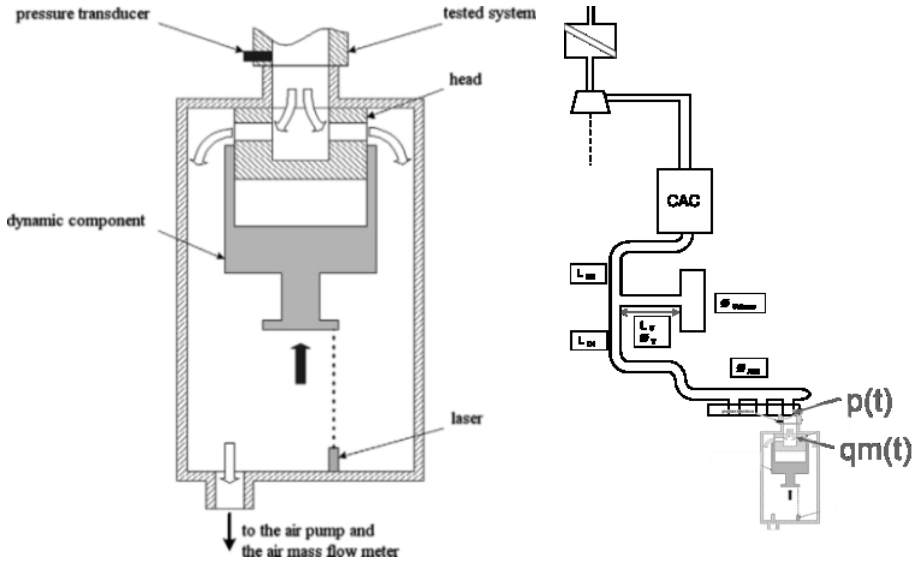


**Figure 208: Sytème permettant une reduction linéaire de debit en 0,5ms et une description d'une ligne d'admission montée** [115]

Ainsi après la stabilisation d'un débit, la Figure 209 (a) montre, à 1s, sa réduction linéaire de 90kg/h à 0 en 0,5ms. La pression, Figure 209 (b), est alors mesurée dans la ligne d'admission d'air. Pour un conduit de 2,5m et d'un diamètre de 40mm les oscillations ont une fréquence principale de 34Hz correspondant à la résonance en quart d'onde, facile à observer sur cet exemple simple. Pour des géométries plus complexes une analyse fréquentielle est menée.

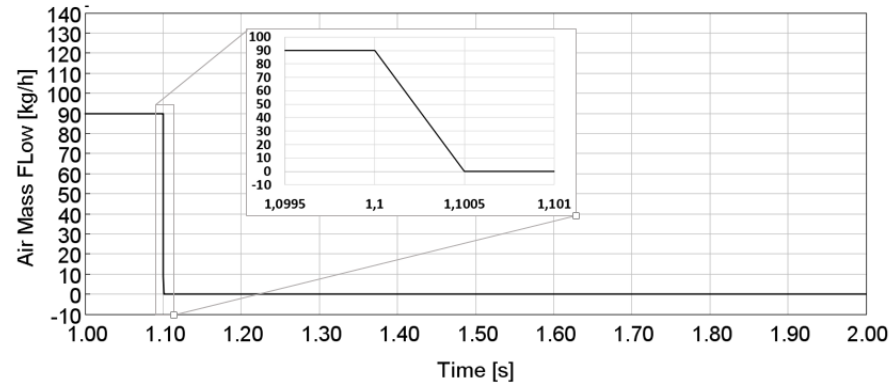


(a)

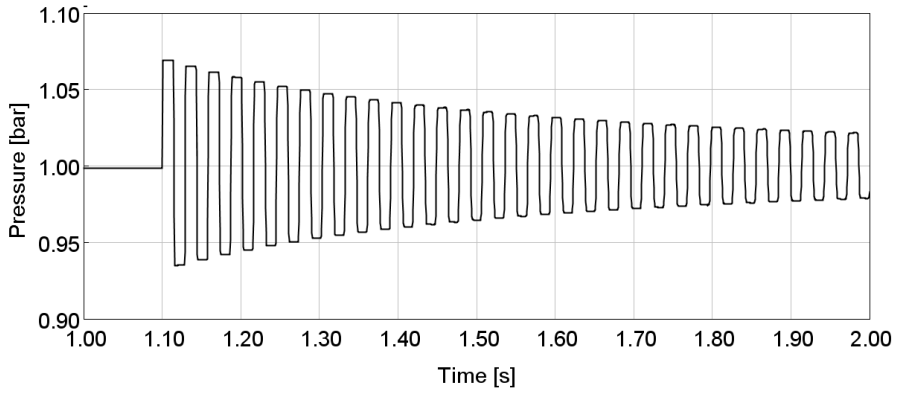


(a)

**Figure 209: Simluation GT Power du banc dynamique, débit massique $\dot{m}_a$(t) (a) and pression p(t) (b)**

Le calcul de l'impédance dans le domaine fréquentiel est réalisé par l'équation ( 9.45 ).

$$Z(j\omega) = \frac{FFT\ [p(t)]}{FFT[\dot{m}_a(t)]} = \frac{P(j\omega)}{\dot{m}_a(j\omega)} \qquad (9.45)$$

Z(jω) est l'impédance acoustique, son module est reporté sur la Figure 210.

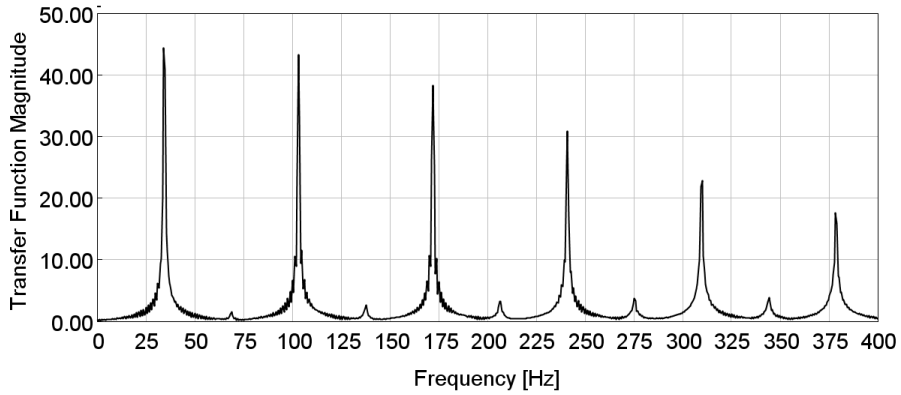


**Figure 210: Fonction de transfert simulée**

Cette approche a été validé pour une grande variété de géométrie [116]. Elle permet de comparer rapidement le comportement dynamique simulé et réel.

## 9.4 Simulation moteur

L'objectif de cette thèse est de prendre en compte les effets du changement de l'admission sur le système moteur complet. La simulation doit donc permettre de montrer les effets sur les différents éléments contribuant à la performance moteur tels que la combustion ou le turbocompresseur.
Le logiciel commercial GT Power a été utilisé pour prendre en compte les différents éléments du moteur.

### 9.4.1 Modélisation des composants

Les différents conduits sont modélisés en utilisant les géométries le plus précisément possibles. Les différents changements de section et les longueurs sont pris en compte. L'utilisation de pertes de charge additionnelles, au travers de coefficients de décharge ou de pertes de charge singulières, est proscrite. L'objectif est que le modèle puisse rester prédictif lors de changements importants de géométrie.
Le compresseur et la turbine sont modélisés au travers de champs. Leurs géométries est néanmoins prise en compte par l'addition de conduits les représentant comme proposé par Torregrosa *et al* [117].

### 9.4.2 Modèle de combustion

La combustion est un élément clé dans la conversation de l'énergie potentielle chimique en travail mécanique. Les simulations 3D permettent une meilleure précision mais les temps de calculs et de modélisation sont importants. Ainsi le choix a été fait d'une modélisation quasi dimensionnelle. Kaprielian [118] a listé différentes méthodes de modélisations de la combustion tel que la loi de Wiebe. Une méthode permettant de prendre en compte les variations importantes des conditions d'admission et d'échappement. Ainsi une méthodologie de modélisation à deux zones est choisie. Elle consiste a considéré la zone dites des gaz brulés et la zone des gaz frais. La Figure 211 présente ces deux zones ainsi que la flamme qui les séparent.

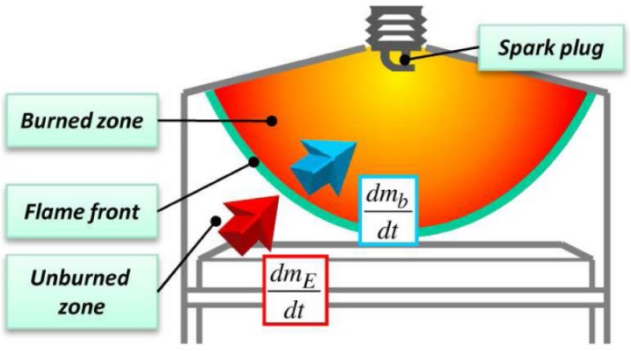


**Figure 211: Descritpion du modèle à deux zones** [119]

Grill *et al* [120] ont définit la vitesse de flamme comme l'addition d'une vitesse laminaire et d'une vitesse turbulente qui sont définies respectivement par les équations ( 9.46 ) et ( 9.50 ).

$$u_L = u_{L,0}\left(\frac{T_{ub}}{T_0}\right)^{\alpha}\left(\frac{p_{cyl}}{p_0}\right)^{\beta}\left(1 - 2.06\ {x_{r,st}}^{\xi}\right) \quad (9.46)$$

$\alpha$, $\beta$ et $u_{L,0}$ sont spécifiques au carburant utilisé. $x_{r,st}$ est le rapport air/carburant spécifique au niveau de la flamme et est défini à 0,97. $\xi$ est défini empiriquement à 0,973 [121]. $\alpha$, $\beta$ et $u_{L,0}$ sont définis pour l'essence par les équations ( 3.39 ), ( 3.40 ) and ( 3.41 ) [120].

$$\alpha = 2.18 - 0.8\left(\frac{1}{\lambda} - 1\right) \quad (9.47)$$

$$\beta = -0.16 + 0.22\left(\frac{1}{\lambda} - 1\right) \quad (9.48)$$

$$u_{L,0} = 0.305 - 0.549\left(\frac{1}{\lambda} - 1.21\right)^2 \quad (9.49)$$

L'équation ( 9.50 ) définit la vitesse turbulente. Elle est liée à l'énergie turbulente cinétique $k_e$ qui est dissipé suivant l'équation ( 9.52 ). Sa valeur de départ est définie empiriquement suivant l'équation ( 9.51 ).

$$u_{Turb} = C_k\sqrt{\frac{2}{3}\cdot k_e} \quad (9.50)$$

$$k_{start} = C_k\left(\frac{c_m d_{Cyl}^2}{n_{IV}\ d_{IV}\ h_{IV}}\right)^2 \quad (9.51)$$

$$\frac{dk}{dt} = -\frac{2}{3}\frac{k}{Vcyl}\frac{dVcyl}{dt} - \varepsilon_{Diss}\frac{k^{1.5}}{l} + \left(\varepsilon_q\frac{k_q^{1.5}}{l}\right) \quad (9.52)$$

$C_k$ permet d'ajuster les résultats de simulation aux essais. Sa valeur doit varier entre 0.02 et 5, il est conseillé de d'utiliser une valeur de 0,35 lorsqu'aucune information n'est disponible. Cette valeur peut permettre de prendre en compte des systèmes augmentant la turbulence.

Par ailleurs la surface de la flamme, considérée sphérique, dépend de la position du piston et donc de la position vilebrequin et du volume brulé par rapport au volume du cylindre comme rapporté dans la Figure 212.

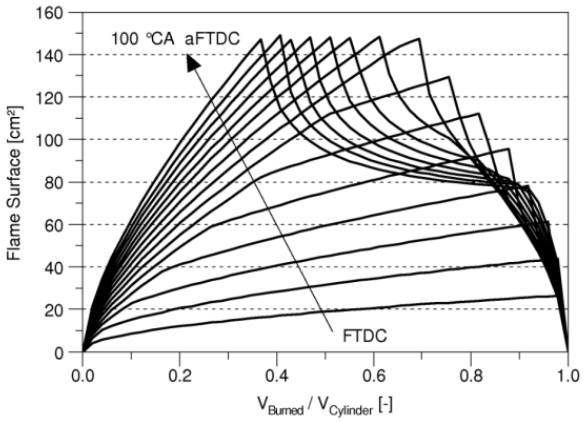


**Figure 212: Surface de la flame avec une bougie centrée en function du taux volume brulé** [120]

Connaissant la surface et la vitesse de flamme il est possible de définir la variation de masse de mélange brulé ( 9.53 ) [121].

$$\frac{dm_E}{dt} = \rho_{uv} \cdot A_{fl} \cdot u_E \qquad (9.53)$$

La combustion du mélange est liée par la relation ( 9.54 ) à la chaleur dégagée.

$$\frac{dQ_B}{d\emptyset} \cdot \frac{1}{H_u} \frac{d\emptyset}{dt} = \frac{dm_f}{dt} \qquad (9.54)$$

Le dégagement de chaleur peut ainsi être évalué ainsi que les températures de gaz brulés et imbrulés. Cette dernière et la pression cylindre sont utilisés pour évaluer le risque de cliquetis.

### 9.4.3 Modélisation du cliquetis

Le cliquetis est caractérisé par l'auto inflammation d'une partie des gaz imbrûlés. Ainsi une partie des gaz s'enflamme alors que la flamme créée par la bougie ne l'a pas atteinte. Ce cliquetis est influencé par le carburant et par les conditions cylindres [123]. Fandakov *et al* [124] ont présenté la  Figure 56 montrant l'influence de la pression cylindre, du λ et du taux d'EGR sur le retard à l'allumage. Un mélange riche augmente le retard à l'allumage c'est pourquoi l'enrichissement est parfois utilisé.

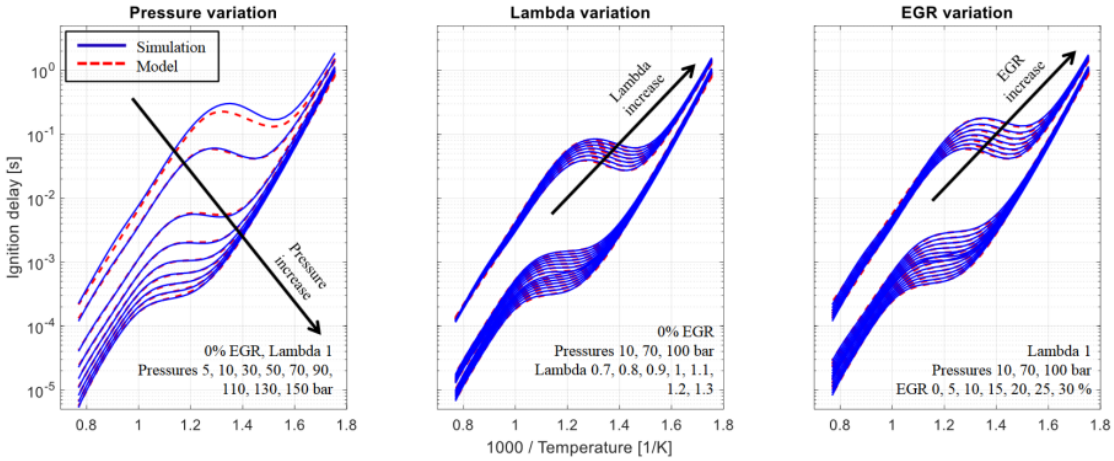


**Figure 213: Délai d'inflammation haute température de la composition du mélange**

Ces courbes associées à la connaissance de la pression, de la température et de la composition des gaz imbrulés à chaque instant permettent de calculer $I_k$ qui intègre l'inverse du délai d'allumage comme indiqué par l'équation ( 9.55 ). Cette valeur est alors proportionnelle au risque de cliquetis.

$$I_k = \int_{t=0}^{t=t_k} \frac{1}{\tau} dt \qquad (9.55)$$

### 9.4.4 Conclusion

Cette partie a permis de caractériser la propagation d'onde de pression pour différentes géométries. Les outils de simulations et d'essais ont été présentés. La modélisation de la combustion et du risque cliquetis sera mis en œuvre pour évaluer différentes architectures d'admission. Celle qui est présentée dans la prochaine partie a pour objectif d'augmenter le couple à bas régime et de réduire le temps nécessaire pour atteindre le couple maximum.

## 9.5 Amélioration du couple à bas régime

La recherche bibliographique a montré l'importance du couple à bas régime et de la réduction du temps de réponse. Les nouvelles normes et les enjeux écologiques poussent vers le maintien d'un mélange air / carburant stœchiométrique.
L'effet des ondes acoustiques est donc étudié ici pour contribuer à ces objectifs. Cette étude est appliquée à un moteur 3 cylindres de dernière génération. Sa version de base utilise une stratégie largement adoptée : « le balayage », qui consiste à bas régime à ouvrir en même temps des soupapes d'admission et d'échappement alors que la pression échappement est inférieure à la pression d'admission. Un débit d'air frais passe donc directement à l'échappement. Dans ces conditions l'excèse d'oxygène au niveau du catalyseur ne permet pas la bonne conversion des NOx.
L'architecture d'admission est ainsi modifiée pour pouvoir augmenter l'amplitude des ondes de pression. Pour un moteur 3 cylindres, les fréquences mises en jeu sont plus

faible que pour les moteurs équipés de plus de cylindres, ce qui constitue aussi un challenge car les dimensions devront être plus importantes.
Un modèle moteur a été élaboré pour faire une évaluation de différentes architectures et, au final, pour en retenir une.

### 9.5.1 Description du concept

Différentes configurations ont été envisagées. La solution retenue consiste en un volume connecté au conduit entre le refroidisseur d'air suralimenté et le répartiteur. Les différentes dimensions sont ensuite évaluées afin de définir une configuration permettant d'obtenir le meilleur couple.
La Figure 214 décrit une ligne d'admission standard avec notamment un conduit reliant le refroidisseur d'air suralimenté (RAS/CAC) au répartiteur et aux soupapes.

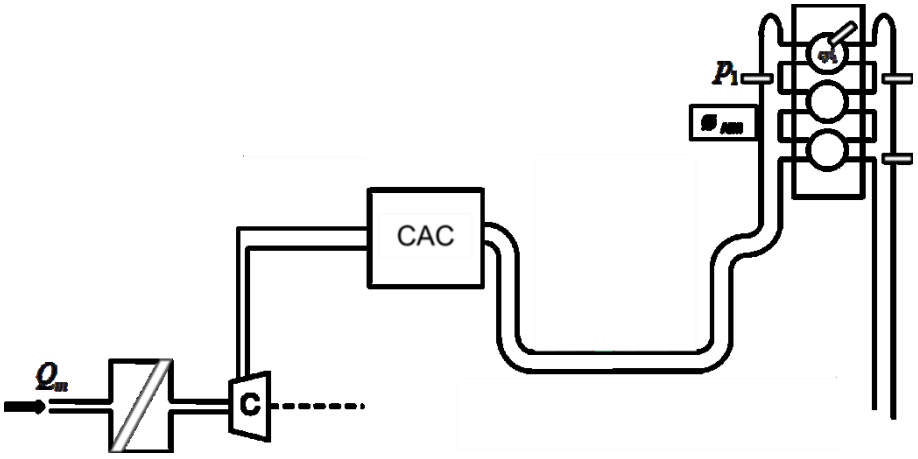


**Figure 214: Schéma de la ligne d'admission de référence**

Le concept présenté Figure 215 est composé d'un volume qui est connecté au conduit aval CAC. Ce volume est un lieu privilégié de résonance. Les dimensions des différents composants, synthétisés dans le Tableau 17, permettent d'en définir la fréquence. Les interactions entre le volume du répartiteur, ainsi que les différentes longueurs sont évaluées.

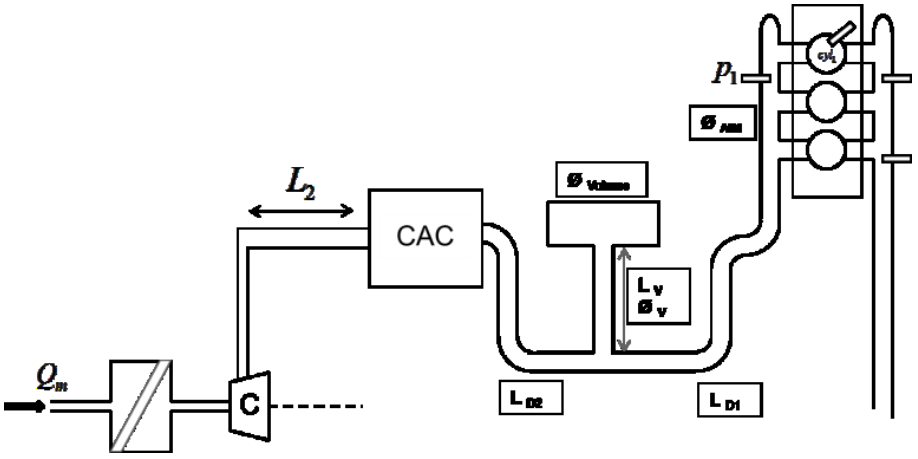


**Figure 215: Shéma de la ligne équipée du système resonant**

**Tableau 17: Paramêtre pouvant varier sur la ligne d'admission d'air**

| | **Parameters** |
|---|---|
| Ø AIM | AIM plenum Diameter |
| Ø Volume | Added Volume size |
| LV / ØV | Length & Ø pipes to DRS volume |
| LD1 / LD2 | Length to the Charge Air Cooler |

### 9.5.2 Dimensionnement par simulation

Le modèle permet de tester les différentes dimensions tout en maintenant les autres paramètres constants. Le modèle est calibré de manière à maintenir le mélange stœchiométrique. Dans cette première phase la distribution variable est ajustée afin d'éviter le balayage. Le volume du système résonant (DRS) est cylindrique avec une longueur de 440mm. Le plénum du répartiteur (AIM Vol) est maintenu avec un diamètre de 55mm.

La Figure 216 montre le couple obtenu pour différents diamètres de volume DRS, diamètres et longueurs entre le volume DRS et le répartiteur. Cette dernière est répartie à 60% dans la connexion entre le volume et la jonction avec le conduit turbo et à 40% dans le conduit turbo. Les résultats montrent qu'il y a dans chaque configuration un couple longueur diamètre qui permet d'augmenter le couple au vilebrequin. La longueur nécessaire augmente lorsque le volume diminue. Le diamètre optimum est obtenu, pour les 4 volumes DRS, entre 33 et 35mm.

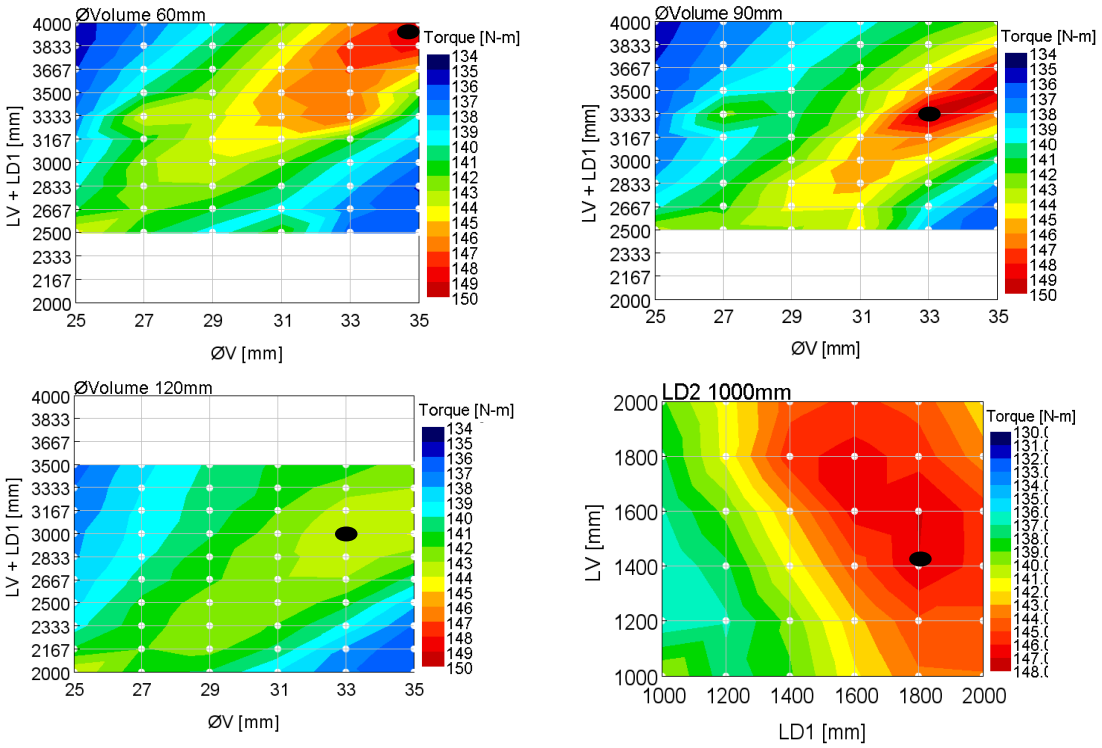


**Figure 216: Couple en fonction du diamètre de volume additionnel et des longueurs et diamètres de conduits**

Pour l'optimum de chaque point symbolisé par un point noir, une représentation de la pression statique est représentée Figure 217. Ces évaluations de pression sont réalisées en amont des soupapes d'admission du cylindre 1. Elles montrent que pour chacun de ces points le maximum de pression est atteint lors de la fermeture soupape. En effet un tel calage des ondes de pression permet d'augmenter la pression et donc la densité de l'air enfermé dans le cylindre.

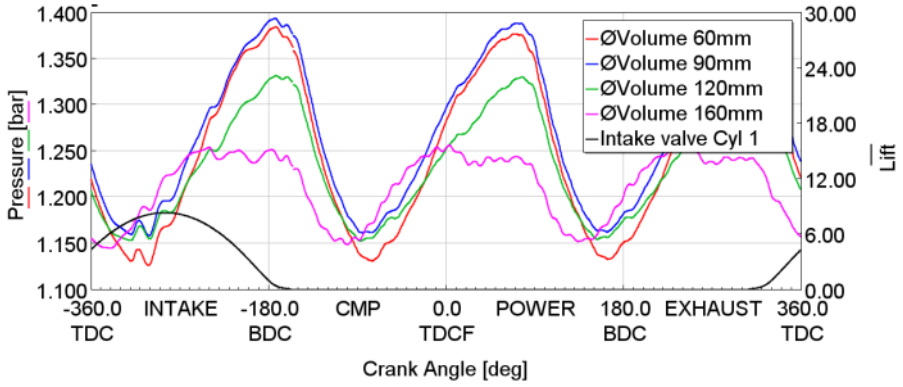


**Figure 217: Pressions obtenues en amont de la soupape d'admission aux points de couple maximum du DOE**

### 9.5.3 Mesure sur banc moteur

Un prototype est ensuite réalisé sur base des résultats précédents. La configuration permettant d'obtenir un bon compromis entre l'espace requis et la performance est retenue d'autant qu'elle permet aussi un gain sur une plus large étendue de régime moteur. Celle-ci correspond donc à un volume de 120mm de diamètre et de une longueur de conduit de 3000mm. Elle permet d'obtenir des ondes fort niveau pour l'harmonique 1,5, et est nommée E.O 1.5.

Les mesures, reportées sur la Figure 218, confirment l'amplitude des ondes de pression et leurs phasage. Afin de mieux comprendre l'impact direct et indirect de cette amélioration de remplissage, une première mesure est réalisée en maintenant la pression moyenne dans le répartiteur. Dans ce cas, la WG est alors ouverte ce qui n'est pas le cas de la configuration initiale. En effet, l'amélioration de remplissage permet une augmentation de débit à la turbine et donc offre l'opportunité d'augmenter la pression répartiteur lorsque la WG est fermée.

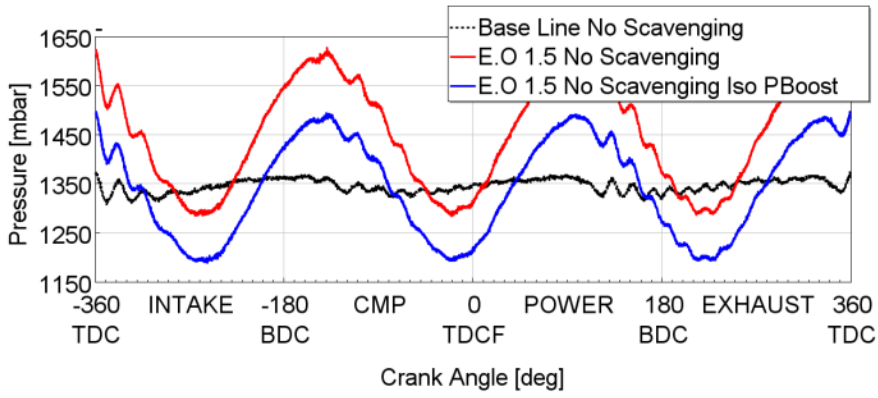


**Figure 218: Runner dynamic pressure at 1200RPM**

Le Tableau 18 montre un gain de PME de 4,4%, qui est directement lié à l'amélioration de remplissage fournie par les ondes de pression. Lorsque la WG est maintenue fermée, comme dans la configuration de base, le gain est 6% plus élevé pour atteindre un total de 10%.

**Tableau 18: Comparaison du couple**

| | Version de référence | Avec le volume additionnel Iso pression répartiteur | Avec volume additionnel |
|---|---|---|---|
| PME (bar) | 12,7 | 13,3 | 14,0 |
| Augmentation relative de PME | 0,0 % | 4,4 % | 10,4 % |
| Pression répartiteur | 1,36 | 1,36 | 1,43 |
| Position WG | Fermé | Controlé | Fermé |
| Lambda | 1,02 | 1,02 | 1,02 |
| Débit d'air (kg/h) | 65,2 | 70,5 | 74,9 |

L'effet transitoire est évalué au travers d'un « enfoncé de pédale », simulé par un maintien d'une charge initiale très faible de 20N.m de couple, puis d'une demande de pleine charge instantanée pour un régime moteur de 1200 $tr.min^{-1}$. Pour ne pas refaire une optimisation de distribution variable en transitoire, les essais sont d'abord évalués avec balayage comme dans la stratégie série.

Les résultats, en terme de pression dans le répartiteur, sont représentés sur les Figure 219 pour la configuration de base et la Figure 220 avec le volume additionnel. La comparaison montre, dans les deux cas, une augmentation rapide à l'ouverture du boitier papillon. La configuration avec le volume additionnel montre que les oscillations de pression sont de plus grandes amplitudes juste après avoir procédé à l'ouverture du boitier papillon, ce qui démontre que le bénéfice des ondes acoustiques est quasi instantané. La pression moyenne est ensuite plus grande avec le volume additionnel jusqu'à un point où le calculateur ouvre la WG car il détecte une pression trop élevée.

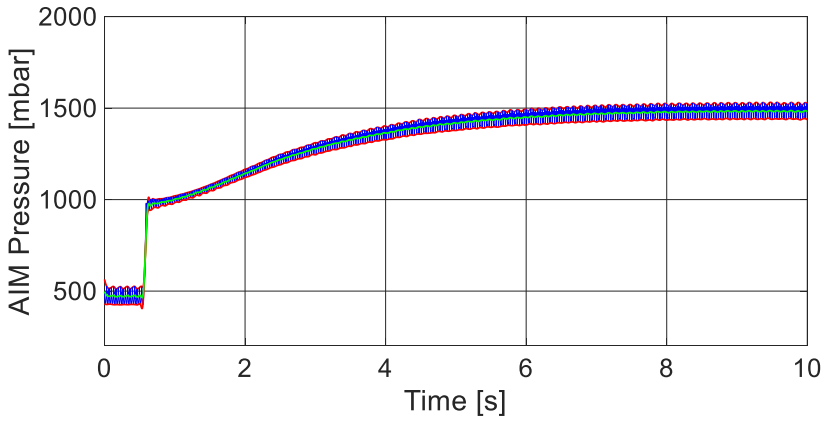


**Figure 219: Pression dans le répartiteur durant un transitoire de charge à 1200tr.min$^{-1}$ avec la ligne de référence**

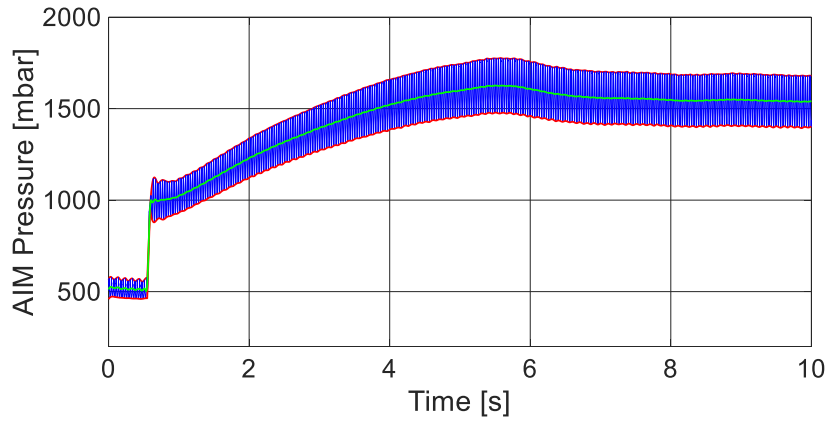


**Figure 220: Pression dans le répartiteur durant un transitoire de charge à 1200tr.min$^{-1}$ avec le volume additionnel**

Le bénéfice sur le couple est reporté dans la Figure 221. Le couple obtenu juste à l'ouverture du boitier papillon est un peu plus élevé avec le volume additionnel ce qui démontre, à nouveau, le rapide bénéfice de l'onde de pression. Enfin le couple, avant que le calculateur ne reprenne la main, est plus élevé avec le volume additionnel.

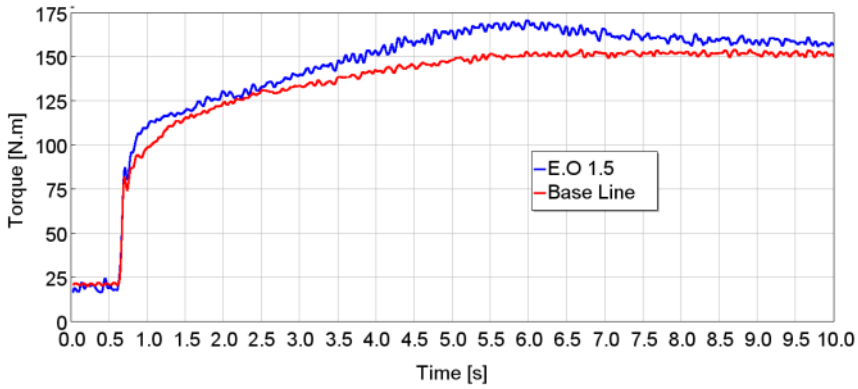


**Figure 221: Evolution du couple durant un transitoire de charge à 1200 tr.min$^{-1}$**

Cette partie a permis de démontrer le bénéfice de l'action des ondes acoustiques sur le couple à bas régime d'un moteur à allumage commandé suralimenté. L'intérêt est direct et accentué via le turbocompresseur. De plus, il permet une réponse plus rapide dans les phases transitoires.

## 9.6 Augmentation de la puissance

La suppression de l'enrichissement pour obtenir la puissance maximale contraint la température d'échappement et le risque de cliquetis. En effet, le risque de cliquetis pour les points de pleine charge est important. Le collecteur d'échappement et la turbine sont alors soumis à des températures qui peuvent nettement dépasser les 1200K.
Les émissions polluantes doivent, de plus, être limitées en maintenant un mélange stœchiométrique.

### 9.6.1 Effet des ondes acoustiques à l'admission sur l'échappement

Theilemann *et al* [142] ont proposé d'utiliser les ondes de pression afin de réduire la température de l'air d'admission. En effet, les ondes de pression véhiculent aussi une onde thermique, la succession des compressions et détentes provoquent aussi des variations de températures instantanées associées.
Ainsi le phasage d'une onde qui provoquerait une détente à la fermeture de la soupape d'admission permettrait une réduction de la température des gaz admis. Theilemann *et al* ont proposé un système composé de volumes permettant une réflexion des ondes de pression afin d'atteindre cet objectif. L'étude, présentée ci-après, est focalisée sur une interaction cylindre à cylindre directe.

### 9.6.2 Description du concept

L'interaction directe entre deux cylindres peut être obtenue si la distance entre ces deux cylindres en maîtrisée. L'interaction dépend donc de la longueur et de la vitesse de propagation qui est celle du son. Pour limiter les longueurs il faut que les temps entre l'émission et la réception attendue soit le plus court possible. Ainsi un conduit de longueur connue est disposé entre les conduits d'admission des cylindres consécutifs dans l'ordre d'allumage. Comparée à une ligne d'admission classique, représentée sur la Figure 222, la configuration testée, ici présente une longueur dite « longueur de détente » entre les soupapes des cylindres 1-4 et les soupapes des cylindres 2-3. Ainsi le cylindre 1 peut interagir avec le cylindre 3 et ainsi de suite avec le 4 puis le 2.

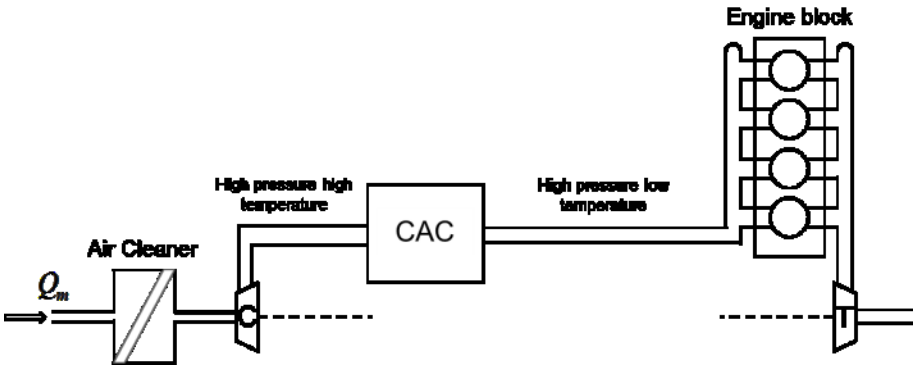


**Figure 222: Ligne de référence**

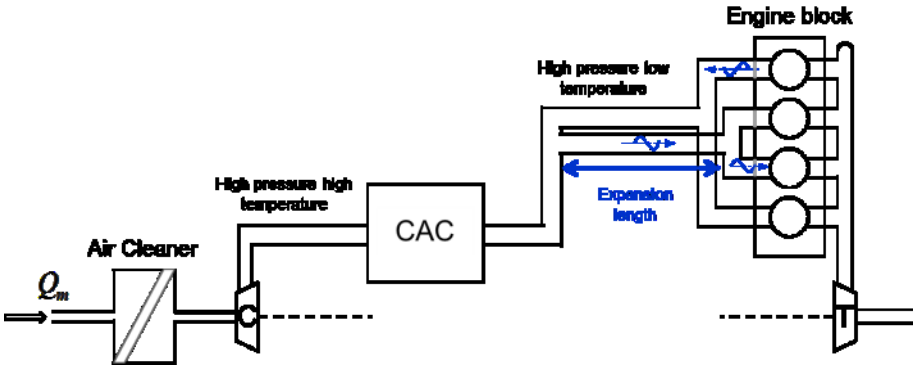


**Figure 223: Description du système d'expansion**

L'objectif est d'utiliser la détente provoquée par la descente du piston pendant l'admission. En effet, comme le montre la Figure 224, cette détente se propage dans la « longueur de détente » jusqu'à la position de l'entrée du cylindre 2 et 3.

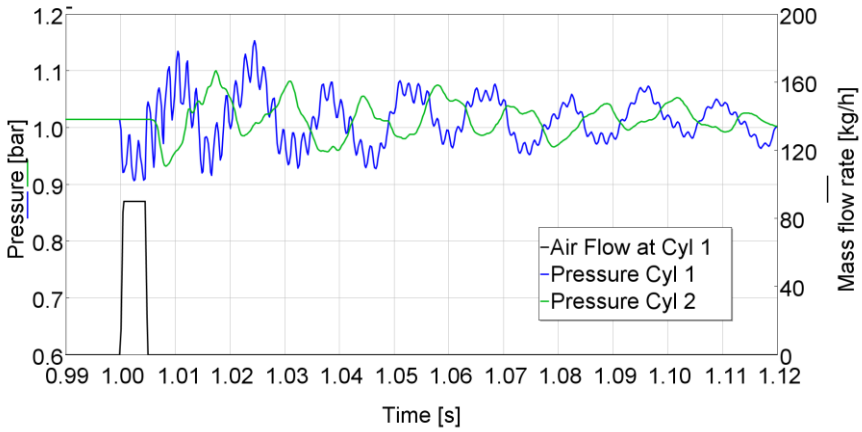


**Figure 224: Réponse en pression de l'admission d'air à un échelon de débit.**

En réalité, le débit au travers des soupapes ressemble à celui représenté sur la Figure 225. Ainsi la source est entretenue par les débits successifs au travers de toutes les soupapes.

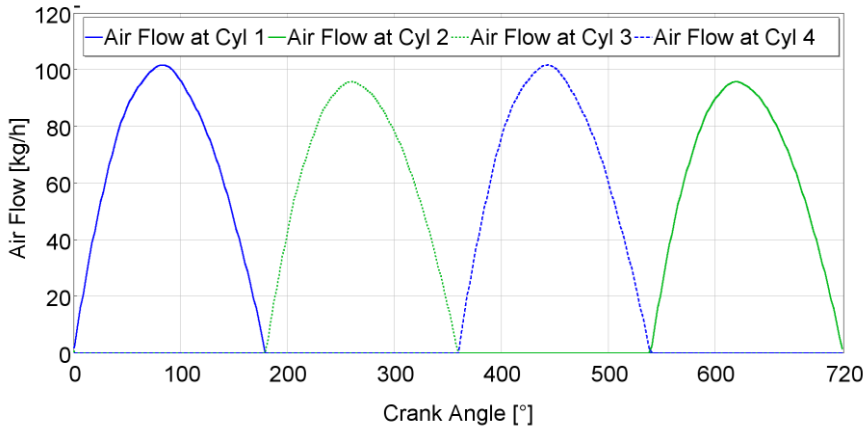


**Figure 225: Débit massique imposé à la position de la soupape**

La pression dans le conduit est donc très oscillante avec un déphasage de 180° entre le bloc des cylindres 1-4 et celui des cylindres 2-3. Comme le représente la Figure 226, la température oscille à la même fréquence et la même phase que la pression. L'amplitude de l'oscillation de température est de l'ordre de 50K crête à crête.

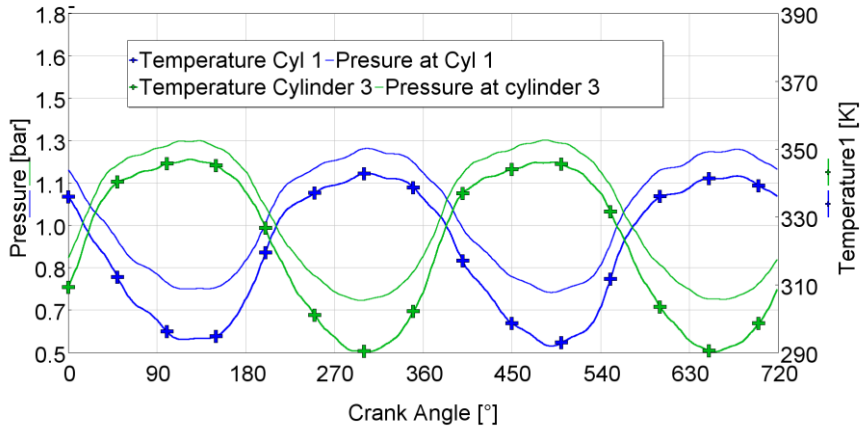


**Figure 226: Pression et température obtenues pour un conduit de 1000mm**

Pour évaluer le gain en puissance, un modèle moteur est construit pour simuler le comportement du moteur avec ce système de détente. Il intègre les champs du compresseur et de la turbine. L'injection permet de maintenir le mélange stœchiométrique. La pression de suralimentation est régulée par la température d'échappement via le controle de l'ouverture de la WG. Enfin, l'avance à l'allumage est contrôlée afin de maintenir un risque de cliquetis constant. Le risque de cliquetis est estimé par le calcul de l'intégrale d'énergie d'activation. Les valeurs sont estimées pour la configuration de base et maintenues pour toutes les autres configurations. La base utilisée est un moteur 4 cylindres avec une puissance spécifique élevée, dont les caractéristiques sont reportées dans la Tableau 19.

**Tableau 19. Engine characteristics**

| | |
|---|---|
| Aspiration | Turbocharged |
| Injection | Directe |

| Carburant | Essence |
|---|---|
| Soupape d'admission | 2 par cylinder<br>Distribution variable |
| Soupape d'échappement | 2 par cylinder<br>Distribution variable |
| Cylindrée | 1,3 l |
| Température d'échappment maximale | 1250 K |
| Charge | Pleine charge |
| Rapport de compresion | 10.5 |
| Alésage | 72 mm |
| Course | 81 mm |

La Figure 227 montre les résultats obtenus dans la configuration initiale et avec une longueur de détente de 1000mm et de 1200mm. Les simulations montrent le bénéfice de la réduction de température par l'utilisation d'ondes de pression. En effet, la puissance augmente dès 4000 $tr.min^{-1}$ pour le conduit le plus long et à 4500 $tr.min^{-1}$ pour la version de 1000mm. Le gain apporté est de l'ordre de 10% en puissance. Toutefois, la puissance a été réduite autour de 3000 et 3500 $tr.min^{-1}$. A ces points, l'onde de pression présente un maximum de pression au moment de la fermeture soupape. Cet inconvénient peut être surmonté en plaçant un conduit court-circuitant la longueur de détente.

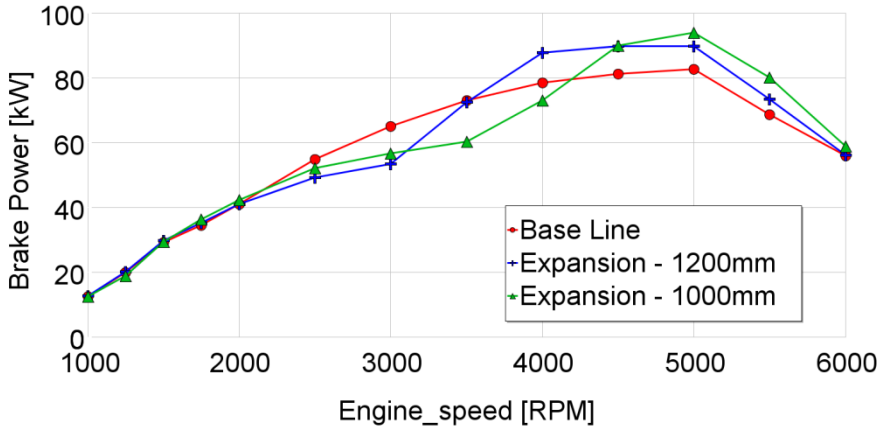


**Figure 227: Puissance obtenue avec et sans le système de détente**

Les limites de fonctionnement ont été prises en compte et sont répertoriées dans la Tableau 20.

**Tableau 20. Limites**

| | Valeur maximale |
|---|---|
| Pression cylindre | 100 bar |
| Pression d'admission | 2,6 bar |
| Température de sortie compresseur | 170°C |
| Pression d'entrée turbine | 2,8bar |

| | |
|---|---|
| Température d'entrée turbine | 950ºC |
| Vitesse du turbocompresseur | 255000RPM |

### 9.6.3 Essais moteur

A l'issue de cette première phase simulation, des prototypes ont été produits et montés sur un moteur de caractéristiques similaires aux simulations. La Figure 228 montre un gain en puissance avec la longueur de 1200mm. L'augmentation des performances est un peu inférieure aux résultats de simulation, une évaluation de l'effet de la distribution a donc été menée. D'autre part, il est montré que le dispositif de désactivation connectant les deux branches admissions permet de supprimer la perte de puissance autour de 3000 tr.min$^{-1}$.

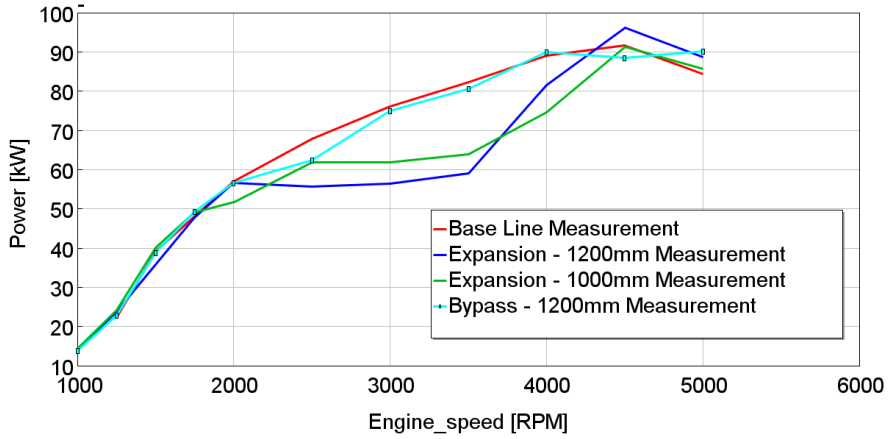


**Figure 228: Puissance mesurée avec le système de détente comparé à la référence**

La Figure 229 montre l'effet de la variation de distribution sur la puissance délivrée. La configuration initiale avait un calage de 30° à l'admission et de 7° à l'échappement. Le passage à 10° à l'admission permet d'obtenir un gain supplémentaire de 5kW supplémentaires.

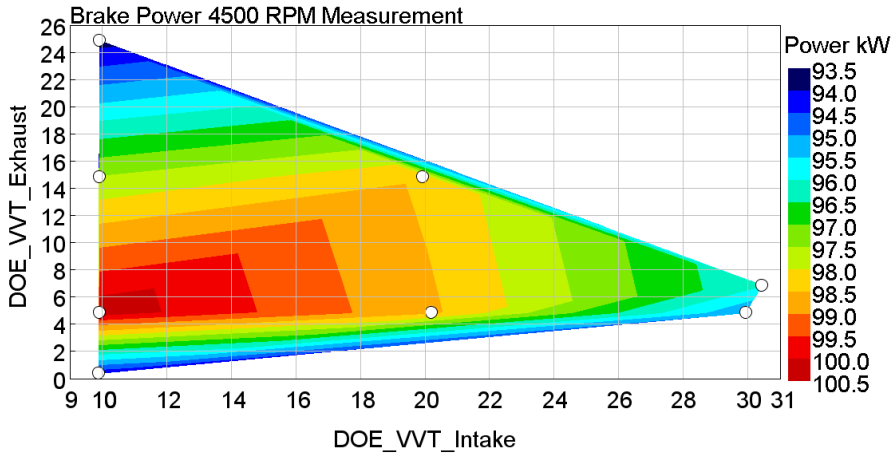


**Figure 229: Effet de la variation de distribution admission et échappement sur la puissance**

Ces résultats de simulation et d'essais ont permis de développer une nouvelle architecture réduisant la température d'admission. Cette réduction de température permet de limiter le risque de cliquetis et ainsi d'augmenter la détente dans le cylindre et donc de réduire la température d'échappement. La WG peut ainsi être refermée et permet d'augmenter la pression de suralimentation. Ceci modifie à nouveau le risque de cliquetis et donc l'avance à l'allumage. Un nouvel équilibre est donc atteint autorisant une augmentation de puissance.

## 9.7 Conclusion et perspective

La recherche bibliographique a permis de montrer le lien entre le rendement du moteur thermique et le rapport de compression. Les constructeurs automobiles l'ont donc augmenté pour améliorer la consommation à charges partielles. Le risque de cliquetis a, par contre, été augmenté à pleine charge. De plus le « Downsizing » a conduit à une réduction de la cylindrée des moteurs pour permettre de diminuer les pertes par pompage. Cette réduction de cylindrée a été compensée par l'adoption massive de turbocompresseur. Les augmentations de pression et de température dans le cylindre ont impacté le risque de cliquetis. Par ailleurs, à bas régime, l'enthalpie à l'échappement est faible. Le turbocompresseur ne peut donc pas fournir de forte pressions de suralimentation. Le couple à bas régime est donc limités.

Durant cette thèse les travaux se sont focalisés sur la propagation des ondes dans le but d'augmenter le couple à bas régime d'une part et la puissance d'autre part. La partie 9.3 a eu pour objectif de montrer le comportement en réflexion et transmission de quelques géometries simples. L'utilisation de la théorie acoustique linéaire a permis de modéliser leurs comportements. D'autre part, la simulation de la combustion et du cliquetis a été détaillée. La modélisation de la combustion est réalisée au travers de modèles à deux zones. La partie « gaz frais » d'une part et la partie gaz brulé d'autre part sont séparées par la flamme dont la vitesse est calculée comme le cumul des vitesses turbulente et laminaire. La composition ainsi que la température et la pression des gaz frais permet d'évaluer le risque de cliquetis. Ces méthodes permettent une évaluation rapide de l'impact des modifications d'admission ou d'échappement.

Pour augmenter le couple à bas régime un système résonant a été utilisé afin d'augmenter le rendement volumétrique. Le système résonant est constitué d'un volume et d'un conduit de connexion. Celui est tout d'abord dimensionné au travers de simulations moteur. Celles-ci ont permis de montrer un gain potentiel de 10% de couple. Un prototype a ensuite été réalisé et testé sur moteur. Ces essais ont permis de confirmer le gain en couple à bas régime. L'onde de pression permet un gain direct par l'augmentation de la pression et donc de la densité de l'air dans le cylindre au moment de la fermeture soupape d'admission. L'augmentation de la masse d'air enfermée permet d'augmenter l'énergie récupérée par la turbine et ainsi d'augmenter la pression à l'admission, le cumul des deux effets a permis de confirmer les 10% d'augmentation de couple. De plus les ondes de pression s'établissent très rapidement, ainsi lors des transitoires de couple le bénéfice de la pulsation est observable quasi instantanément.

L’implantation de ce système résonant dans un compartiment moteur va être un défi car l’espace disponible est souvent restreint et le volume nécessaire assez important. Par ailleurs le dimensionnement du système n’a pas montrer un comportement de type Helmholtz ni une réflexion liée à une expansion. Une autre étude pourrait évaluer l’effet acoustique du volume dans la ligne d’admission et les éventuelles interactions avec les autres éléments de la ligne d’admission.

Les enjeux liés à la puissance maximale sont liées à la fois au cliquetis et aux températures d’échappement élevées. Le maintien de mélange stœchiométrique contraint d’autant plus la température d’échappement. Le système développé a permis d’obtenir une détente des gaz d’admission à la fermeture soupape diminuant ainsi la température. Les simulations ont permis de définir les dimensions du système et de montrer un potentiel en terme d’augmentation de puissance. Le refroidissment de 15K de l’admission permet une augmentation de 10% de puissance. Le système a ensuite été testé sur moteur. Les gains ont été inférieurs aux simulations avec 5% d’augmentations de puissance. Une variation de la distribution, principalement à l’admission, a permis d’augmenter la puissance de presque 5% de plus.
L’implantation de ce système dans un environnement moteur va aussi être difficile. Néanmoins les autres systèmes permettant d’augmenter la puissance requièrent aussi un volume additionnel. Par exemple, l’injection d’eau requiert des injecteurs et un réservoir. L’accès limité au banc moteur n’a pas permis d’investiguer une longueur de détente plus importante pour atteindre une amélioration de puissance à un régime moteur inférieur. Par ailleurs l’homogénéité de température dans le cylindre pourrait être évaluer par une analyse de dynamique des fluides en trois dimensions par exemple.

Titre : **Optimisation de la ligne d'admission d'air de moteurs suralimentés à allumage commandé**.

**Mots clés :** Moteur à allumage commandé, dynamique des gaz, écoulement compressible, lambda 1, brio, cliquetis.

**Résumé :** Ces dernières années les ventes de moteurs à allumage commandé sont croissantes. Pourtant les exigences en termes d'émissions de $CO_2$ et d'émissions polluantes sont devenues plus contraignantes, taxant lourdement les dépassements. De plus le cycle d'homologation a évolué vers un élargissement de la fenêtre d'utilisation du moteur ou les émissions sont réglementées. La réduction de cylindrée « downsizing » opérée ces dernières années a permis de réduire les consommations notamment grâce à la réduction des pertes par pompage. Les performances ont pu être maintenues par l'adoption de système de suralimentation et notamment du turbocompresseur. Celui-ci présente toutefois une lacune à bas régime où il ne peut fournir une réponse instantanée et où la pression de suralimentation est limitée.

De même à plus haut régime le fort taux de compression utilisé pour augmenter le rendement du moteur rend difficile le contrôle du cliquetis. Cette thèse s'est focalisée sur l'utilisation des ondes de pression pour améliorer la réponse du moteur à bas régime. Tout d'abord avec des outils de simulation puis en validation sur banc moteur. Une seconde partie a permis de développer une architecture de ligne d'admission d'air permettant de réduire la température d'admission afin d'augmenter la résistance au cliquetis et d'augmenter l'avance à l'allumage. La température d'échappement est ainsi réduite. Celle-ci est un élément dimensionnant de la stratégie moteur qui a maintenu, dans ces travaux, un mélange stœchiométrique afin de limiter les émissions polluantes.

Title : **Benefit of air intake optimization for new turbocharged gasoline engine**

**Keywords :** spark-ignition engine, gas dynamic, compressible flow, Lambda 1, low end torque, knock

**Abstract:** The last years have witnessed a strong increase of the sold spark ignition engines. Furthermore the new regulations are formally constraining pollutant emissions and $CO_2$ with high fines. In the same time the new homologation driving cycle extends the engine operating conditions where the emissions need to be controlled. The downsizing has been a strong lever over the last years to improve the fuel consumption with reduction of the throttling and thus the pumping losses. With the downsizing, the turbocharger has been widely adopted to maintain the output performance. The implementation of turbocharger challenges the time to torque and the low end torque at low engine speed. In the same time the increase of boost pressure associated to high compression ratio confront the knock controls at maximum power operating conditions.

This thesis focuses on acoustic boosting with volumetric efficiency enhancement to improve the low end torque and the time to torque. Firstly a simulation model allows taking into account the combustion behavior as well as the turbocharger characteristics. The intake geometry has been optimized to enhance the engine response time and low end torque. The second part deals with the pressure wave action used to reduce the intake temperature and thus improve the knock resistance being beneficial for exhaust gas temperature reduction. The interaction between the waves created the different cylinder is demonstrated. The test has confirmed the power increase while maintaining lambda 1 and thus keeping the three way catalyst efficient.